



Copyright Statement

The digital copy of this thesis is protected by the Copyright Act 1994 (New Zealand). This thesis may be consulted by you, provided you comply with the provisions of the Act and the following conditions of use:

- Any use you make of these documents or images must be for research or private study purposes only, and you may not make them available to any other person.
- Authors control the copyright of their thesis. You will recognise the author's right to be identified as the author of this thesis, and due acknowledgement will be made to the author where appropriate.
- You will obtain the author's permission before publishing any material from their thesis.

To request permissions please use the Feedback form on our webpage.
<http://researchspace.auckland.ac.nz/feedback>

General copyright and disclaimer

In addition to the above conditions, authors give their consent for the digital copy of their work to be used subject to the conditions specified on the Library [Thesis Consent Form](#)

Buckling and Growth of Disbonds in Honeycomb Sandwich Structure

Temoana Southward

Supervisors:

Assoc. Prof. Gordon D. Mallinson

Dr. Krishnan Jayaraman

Dr. Damian P.W. Horrigan

A thesis submitted in partial fulfilment of the requirements for the
degree of

Doctor of Philosophy in Engineering

The University of Auckland

July 2005

I have no special talents. I am only passionately curious.

Albert Einstein

ABSTRACT

The response of honeycomb sandwich structure to disbond damage, in a compressive stress field, has been assessed. Two types of disbond were considered; those extending through the full width of a panel (through-width) and those enclosed within the panel boundaries (embedded). For each type of disbond the failure process was established through four-point bend testing of 56 sandwich specimens. For both types of disbond, failure was found to be governed by buckling-driven disbond growth and, consequently, models of buckling and disbond growth were developed.

All of the models decoupled the face-sheets of the sandwich and treated the core as a spring foundation having a stiffness determined from equilibrium of a two-dimensional orthotropic solid.

A linear Winkler beam model was used to predict buckling of a through-width disbond. The model buckling loads agreed with specimen test results with an average difference of 1.7%. A non-linear Winkler beam model was then developed to predict post-buckling behaviour and the initiation of disbond growth, through a fracture mechanics analysis. A characteristic growth curve, defining the work input required to initiate disbond growth, was developed and agreed with specimen test results with an average difference of 3.3%. The model also verified that disbond growth occurs in discrete increments approximately equal to the diameter of the honeycomb cells.

A linear Winkler plate model was used to predict buckling of an embedded disbond. The model buckling loads agreed with specimen test results with an average difference of 3.7%. A non-linear Winkler plate model was then developed to predict post-buckling behaviour of a sandwich panel containing an embedded disbond. The model considered contact conditions and modelled disbond growth by releasing fractured nodes during load incrementation. Disbond growth initiation loads agreed with specimen test results with an average difference of 15.8%. Failure loads consistently over-predicted specimen test results by an average of 13.9%. It was concluded that the growth initiation loads should be used as a conservative estimate of failure.

The models developed may be used to assess the criticality of disbond damage in sandwich structure having thin-gauge, composite face-sheets.

ACKNOWLEDGEMENTS

Many thanks to the Foundation for Research Science & Technology for providing the Technology in Industry Fellowship (TIF) scholarship that supported me for the first three years of this research.

Many thanks also to Air New Zealand Engineering Services for providing resources and support as well as the initial concept for the research.

The following people were instrumental in the completion of this project:

Dr. Damian Horrigan: Without your encouragement and infectious passion for a good mathematical problem I would not have even considered doing PhD research. Thank you for your expert guidance and input to the technical direction of the research and for your continuous support from start to finish.

Assoc. Prof. Gordon Mallinson: Thank you for your friendly supervision and wise input to, not only the direction of the research but also several key technical aspects. Thank you also for the encouragement when it was needed and for your manner of not dwelling on past mistakes, it was appreciated. Also, this thesis would not have been written nearly as well were it not for your input, thank you.

Dr. Krishnan Jayaraman: Thank you for the honest and constructive feedback on not only the written work but also the research methodology and structure.

Mike Pervan: For initially defining the problem that this research set out to solve and providing further information when it was required.

Dr. Mark Battley: Thank you for generously providing the equipment and support required to successfully complete the panel specimen testing.

Andy Skeates: For your time and effort to provide the test data without which a large portion of this thesis would not have been possible.

ANZES Composites Shop: Thanks for being so helpful at every step and making the manufacture of test specimens as easy as possible for me.

Jos Geurts, Rex Halliwell, Barry Fullerton and Ivan Bailey: Thanks guys for all your willing technical support.

Finally, to those friends and family who convinced me to keep at it when the going was tough, particularly *Teresa Behrens*, thank you.

CONTENTS

ABSTRACT	<i>i</i>
ACKNOWLEDGMENTS	<i>iii</i>
CONTENTS	<i>v</i>
LIST OF FIGURES	<i>ix</i>
LIST OF TABLES	<i>xiii</i>
SYMBOLS AND ABBREVIATIONS	<i>xv</i>
1. INTRODUCTION TO SANDWICH STRUCTURE	1
1.1 Introduction	1
1.2 Damaged Sandwich Structure	5
1.2.1 <i>A General Discussion of Damage Tolerance</i>	5
1.2.2 <i>Damage Tolerance of Sandwich Structure</i>	8
2. DISBOND DAMAGE IN SANDWICH STRUCTURE	9
2.1 Disbond Damage in Sandwich Structure	9
2.1.1 <i>Identifying the Critical Loading Method</i>	10
2.1.2 <i>Damage Tolerant Design of Disbonded Sandwich Structure</i>	12
2.1.3 <i>Summary of the Reviewed Literature</i>	14
2.2 Properties of Honeycomb Cores	21
2.2.1 <i>In-Plane Honeycomb Properties</i>	21
2.2.2 <i>Fracture Properties of Honeycomb</i>	23
2.3 Thesis Structure	24
3. TESTING OF DISBONDED SANDWICH BEAM SPECIMENS	25
3.1 Introduction	25
3.2 Literature Review	25
3.2.1 <i>Compression Loading of Disbonded Sandwich Beams</i>	26
3.2.2 <i>Compression of Delaminated Solid Laminates</i>	27
3.2.3 <i>Interfacial Fracture Toughness Test Methods</i>	28
3.2.4 <i>Review Conclusion</i>	29
3.3 Manufacture of Test Specimens	30
3.4 Four-Point Loading of Specimens	32
3.4.1 <i>Acoustic Emission Measurement</i>	33
3.5 Material Properties	34
3.5.1 <i>Face-sheet Properties</i>	34
3.5.2 <i>Honeycomb Core Properties</i>	37
3.5.3 <i>A New Method for Determining Fracture Toughness of the Face-Core Interface</i>	38

3.6	Conclusions	45
4.	MODELLING DISBOND BUCKLING IN SANDWICH BEAMS	47
4.1	Introduction	47
4.2	Refined Winkler Beam Model	52
4.2.1	<i>Analysis Procedure</i>	52
4.2.2	<i>The Modified Foundation Stiffness</i>	53
4.3	Results and Discussion	57
4.3.1	<i>Non-dimensional Analysis</i>	57
4.3.2	<i>Comparison of Model and Experimental Buckling Loads</i>	61
4.4	Conclusions	63
5.	MODELLING DISBOND GROWTH IN SANDWICH BEAMS	65
5.1	Introduction	65
5.2	Large Displacements of a Refined Winkler Beam	68
5.2.1	<i>Post-buckling Model</i>	68
5.2.2	<i>Validation Process</i>	70
5.2.3	<i>Disbond Growth Criterion</i>	71
5.3	The Characteristic Disbond Growth Curve	74
5.3.1	<i>Comparing the Characteristic Curve to Test Results</i>	78
5.3.2	<i>Analysis of Continued Disbond Growth</i>	80
5.4	Conclusions	85
6.	TESTING OF DISBONDED SANDWICH PANEL SPECIMENS	87
6.1	Introduction	87
6.2	Specimen Manufacture	91
6.3	Four-Point Loading of Panel Specimens	93
6.3.1	<i>Buckling and Failure Load Results</i>	94
6.4	Laser Gauging to Measure Buckle Height	97
6.5	Acoustic Emission Monitoring to Identify Disbond Growth Events	101
6.5.1	<i>Analysis of Acoustic Emission Data</i>	101
6.6	Conclusions	115
7.	MODELLING DISBOND BUCKLING IN SANDWICH PANELS	117
7.1	Introduction	117
7.1.1	<i>Literature Review</i>	118
7.2	A Winkler Plate Model	119
7.2.1	<i>Panel Buckling</i>	119
7.3	Comparison with Specimen Test Results	124
7.4	Non-dimensional Analysis	125
7.4.1	<i>Effects of an Orthotropic Face Material</i>	128
7.5	Edge Effects and Disbond Shape Effects	129
7.5.1	<i>Proximity to a Restrained Edge</i>	129

7.5.2	<i>Disbond Shape</i>	133
7.6	Conclusions	136
8.	MODELLING DISBOND GROWTH IN SANDWICH PANELS	137
8.1	Introduction	137
8.2	Literature Review	137
8.2.1	<i>Laminated Plates Containing Delaminations</i>	139
8.2.2	<i>Literature Review Conclusions</i>	140
8.3	Non-linear Winkler Plate Model	141
8.3.1	<i>Governing Equations</i>	141
8.3.2	<i>Boundary Conditions</i>	142
8.3.3	<i>Non-linear Solution Procedure</i>	143
8.3.4	<i>Validation Process</i>	147
8.3.5	<i>Convergence Checks</i>	149
8.4	Comparison with Specimen Test Results	152
8.4.1	<i>Post-buckling Stiffness Comparison</i>	152
8.4.2	<i>Disbond Growth Initiation Comparison</i>	163
8.4.3	<i>Prediction of Continued Disbond Growth</i>	167
8.4.4	<i>Summary of Critical Load Predictions</i>	169
8.5	Conclusions	171
9.	CONCLUSIONS	173
9.1	Research Summary in Damage Tolerance Terms	173
9.1.1	<i>Sandwich Beams</i>	174
9.1.2	<i>Sandwich Panels</i>	178
9.2	Summary of Original Contributions	181
9.3	Suggestions for Further Research	182
	REFERENCES	185
	APPENDICES	191
	Appendix A - Specimen Manufacture and Testing	191
	Appendix B - Derivation of Non-dimensional Parameters	196
	Appendix C - Strain Energy Release Rate Definitions for a Winkler Beam Model	200
	Appendix D - Core Support Function at Disbond Boundaries	203
	Appendix E - Derivation of Plane Strain Stiffness Terms used in Effective Core Stiffness Function	206
	Appendix F - Non-linear Winkler Plate Modelling	209
	Appendix G - Two Measures of Scatter in Experimental Results	215
	Appendix H - Criterion for Assessing the Validity of a Small Rotations Assumption	216

LIST OF FIGURES

Figure 1.1.1	Honeycomb-core sandwich construction	1
Figure 1.1.2	The Mosquito bomber, one of the earliest structures incorporating sandwich panels	2
Figure 1.1.3	The Boeing 787 will be in production by 2008 and will be 58% composite structure by weight with sandwich used extensively for interiors, fairings and some control surfaces	3
Figure 1.1.4	Sandwich failure modes; (a) face yielding/fracture, (b) core shear failure, (c-d) face wrinkling, (e) global buckling, (f) shear crimping, (g) face dimpling and (h) local indentation	3
Figure 1.2.1	Residual strength curve showing the allowable damage limit at ultimate load	5
Figure 1.2.2	Damage tolerance curves with two static allowable damage limits	6
Figure 1.2.3	Damage tolerance graph including static failure, damage growth and endurance limit	7
Figure 2.1.1	A disbond in a sandwich beam	9
Figure 2.1.2	Four-point bend sandwich specimen with disbond location as used by Burman (1998). The bending moment and shear force diagrams are also shown	11
Figure 2.1.3	Damage tolerance curve specific to disbond damage	13
Figure 2.1.4	Through-width (left) and embedded (right) disbonds in sandwich panels	14
Figure 2.1.5	Method of modelling entire sandwich beam, with typical sectioning method shown	15
Figure 2.1.6	Decoupled face-sheet method used to model local behaviour	16
Figure 3.2.1	Delaminated composite beam	27
Figure 3.2.2	The three basic modes of fracture	29
Figure 3.3.1	Statistical confidence, expressed as a half range (defined as the number of sample standard deviations either side of the sample mean within which the population mean is expected to lie with X% confidence), for various sample sizes	31
Figure 3.4.1	Sandwich beam specimen under load in the four-point bending test rig (Arrows indicate the location of the strain gauge and acoustic emission sensor)	32
Figure 3.4.2	Loading geometry (outer span = 290mm, inner load span = 110mm) and arrangement of the strain gauge and accelerometer on the test specimen	32
Figure 3.4.3	Overlaid load and acoustic output profiles (used to determine when disbond growth initiated)	33
Figure 3.5.1	Facesheet lay-up sequences and materials	35
Figure 3.5.2	The test rig used to evaluate the bending stiffness of the face laminates	36
Figure 3.5.3	Honeycomb core geometry, showing the ribbon (R) and transverse (T) directions as 'x' and 'y', respectively.	38
Figure 3.5.4	Typical specimen loading and reloading profiles used to determine the critical strain energy release rate (G_c)	39
Figure 3.5.5	Variation of G_c with disbond length (Ural et al. 2003)	40
Figure 3.5.6	Variation of G_c with disbond length (Cantwell et al. 1999)	41

Figure 3.5.7	Post-testing photograph of the underside of a disbonded face-sheet (with the Teflon release film used to create the disbond shown also)	44
Figure 4.1.1	Through-width disbond in a sandwich beam	47
Figure 4.1.2	Illustration of the wrinkling wavelength and load for a sandwich beam	49
Figure 4.2.1	A compressively loaded Winkler beam with a central disbond region	52
Figure 4.2.2	Definition of deformed sandwich shape used by previous authors	53
Figure 4.2.3	Deformed shape and axes of refined core stiffness solution	54
Figure 4.3.1	Plot of Π_1 versus core thickness normalised with respect to the natural half-wavelength of the face-sheet	58
Figure 4.3.2	Characteristic curve for the Euler buckling load coefficient as a function of the disbond length normalised to the natural half-wavelength	60
Figure 5.2.1	Lagrangian formulation for the post-buckling Winkler beam model	68
Figure 5.2.2	Lagrangian co-ordinate system used for the post-buckling model	69
Figure 5.2.3	Post-buckling behaviour of an end loaded column with built-in ends (Comparison between the present model and the solution presented by Timoshenko (1936))	70
Figure 5.2.4	Range of large deflections over which the non-linear beam model is verified by comparison to an exact solution	71
Figure 5.2.5	Notation used in the general Virtual Crack Closure technique derivation	71
Figure 5.2.6	The displacements in the disbond region are assumed to be at the undeformed reference state (dotted line) for the purpose of evaluating the strain energy release rate at node n	72
Figure 5.3.1	Load-displacement profile predicted by the post-buckling model	74
Figure 5.3.2	Disbond in a sandwich beam	76
Figure 5.3.3	The characteristic disbond growth curve	77
Figure 5.3.4	Load-displacement profile of a sample test specimen (shaded area indicates work done up to the point of growth initiation)	79
Figure 5.3.5	Characteristic curve with model results included	79
Figure 5.3.6	The load-displacement profile for continuous disbond growth (shaded areas represent the strain energy stored in the beam at each point)	80
Figure 5.3.7	Comparison of predicted growth profile with a specimen test profile	82
Figure 5.3.8	Comparison to specimen test results of the predicted growth profile, incorporating discrete growth increments equal to the cell diameter	83
Figure 6.1.1	Pure compression loading of a disbonded sandwich panel	89
Figure 6.1.2	Bending of a disbonded sandwich panel	89
Figure 6.2.1	Plan view of general panel specimen dimensions	91
Figure 6.3.1	Specimen layout (top surface shown). The Acoustic Emission sensors are located halfway between the load application line and the disbond edge.	93
Figure 6.3.2	Buckling and failure loads versus disbond diameter for all of the test specimens	95
Figure 6.4.1	The laser gauge mounting rig used on all panel specimens	97
Figure 6.4.2	Typical plot of face-sheet load versus buckled disbond height	98
Figure 6.4.3	Typical plot of buckled disbond height in the case of 'snap' buckling	99
Figure 6.4.4	Plot of buckled disbond height with the parabolic post-buckling function overlayed to find the approximate buckling load	100

Figure 6.5.1	Acoustic profile features recorded for every acoustic event	102
Figure 6.5.2	Typical plot of cumulative acoustic event count during a test	103
Figure 6.5.3	Distribution of AvF values for the highest-energy events in each specimen test	105
Figure 6.5.4	Location of the zones from which transient files were taken	107
Figure 6.5.5	Sample waveform of a zone four transient files	107
Figure 6.5.6	Sample FFT of a zone four transient	108
Figure 6.5.7	Examples of binomial distribution curves for different probabilities	111
Figure 6.5.8	Buckling, growth initiation and failure loads with G-type face-sheets	114
Figure 6.5.9	Buckling, growth initiation and failure loads with GH-type face-sheets	114
Figure 7.1.1	Embedded face-core disbond in a sandwich panel	117
Figure 7.2.1	Winkler plate in uni-axial compression	119
Figure 7.4.1	Characteristic buckling curve for a sandwich panel with an embedded circular disbond of diameter L_d	126
Figure 7.4.2	Master buckling curve for an embedded disbond in a sandwich panel	127
Figure 7.4.3	Characteristic curves for three different orthotropy ratios	128
Figure 7.5.1	Edge effects for each of the five configurations	130
Figure 7.5.2	Edge effect comparison with the modified width ratio	131
Figure 7.5.3	An illustration of the minimum required panel size, to avoid edge effects.	131
Figure 7.5.4	Illustration of the reason for the varying edge effects in the parallel and transverse directions	132
Figure 7.5.5	Minimum separation required for disbonds to act independently (extension of the edge effects analysis to the interaction of multiple disbonds)	133
Figure 7.5.6	Effect of disbond aspect ratio on the buckling load	134
Figure 8.3.1	Winkler plate in uni-axial compression	141
Figure 8.3.2	Boundary conditions applied to the Winkler plate model	143
Figure 8.3.3	A typical method of enforcing contact between two bodies	144
Figure 8.3.4	Location at which fracture criterion was measured	146
Figure 8.3.5	Load versus strain energy release rate for various mesh densities	150
Figure 8.3.6	Load versus disbond buckle height for various mesh densities	150
Figure 8.3.7	Load versus disbond buckle height for various load increment sizes	151
Figure 8.4.1	Comparison between test and model in-plane stiffness results where the strain is the average value at the loaded boundary	152
Figure 8.4.2	Deformed shapes and load profiles of two panels having circular regions of reduced stiffness subjected to different boundary conditions	153
Figure 8.4.3	Exaggerated deformed shape of a disbonded panel with a 75mm disbond and length ratios $R = Q = 2$ (see 8.4.1)	154
Figure 8.4.4	Panel geometry definitions	155
Figure 8.4.5	Illustration of the increased in-plane stiffness resulting from an increased panel length ratio, R .	155
Figure 8.4.6	Model versus specimen test results (25mm disbond diameter and Gtype face-sheet)	156
Figure 8.4.7	Model versus specimen test results (50mm disbond diameter and Gtype face-	157

	sheet)	
Figure 8.4.8	Model versus specimen test results (50mm disbond diameter and GH-type face-sheet)	158
Figure 8.4.9	Model versus specimen test results (75mm disbond diameter and G-type face-sheet)	158
Figure 8.4.10	Model versus specimen test results (75mm disbond diameter and GH-type face-sheet)	159
Figure 8.4.11	Buckling modes of a specimen configuration with 75mm disbond diameter and GH-type face-sheet	161
Figure 8.4.12	Out-of-plane displacement at growth initiation for a specimen with 25mm disbond diameter and G-type face-sheet	162
Figure 8.4.13	Out-of-plane displacement at growth initiation for a specimen with 50mm disbond diameter and G-type face-sheet	162
Figure 8.4.14	Illustration of the elliptical profile observed in post-buckling, particularly for large disbonds, and the region of core contact	163
Figure 8.4.15	Normalised disbond growth initiation loads for the G-type face-sheet (specimen test data also displays the 95% confidence range)	164
Figure 8.4.16	Normalised disbond growth initiation loads for the GH-type face-sheet (specimen test data also displays the 95% confidence range)	165
Figure 8.4.17	Normalised load versus strain energy release rate for different disbond sizes	166
Figure 8.4.18	Face-sheet displacements at various stages during loading	168
Figure 8.4.19	Growth initiation and failure loads, from model and test results, for the G-type face-sheet material (test data includes the 95% confidence range)	169
Figure 8.4.20	Growth initiation and failure loads, experimental and model results, for the GH-type face-sheet material (test data includes the 95% confidence range)	169
Figure 9.1.1	Through-width (left) and embedded (right) disbonds	173
Figure 9.1.2	A damage tolerance graph for disbonded sandwich structure	174
Figure 9.1.3	Characteristic buckling curve for disbonded sandwich beams	175
Figure 9.1.4	Characteristic disbond growth curve for disbonded sandwich beams	176
Figure 9.1.5	Comparison between continued disbond growth analysis and a typical specimen test result	177
Figure 9.1.6	Characteristic buckling curve for a sandwich panel with an embedded circular disbond of diameter L_d	178
Figure 9.1.7	An illustration of the minimum required panel size, to avoid edge effects.	179
Figure A.1	Lay-up sequence of sandwich test specimens	192
Figure A.2	Sample temperature profile of a specimen cure (note: least controlled profile is the air temperature)	193
Figure A.3	Manufacturer supplied face-sheet properties for 120 and 1581 (also labelled 181) glass fabric laminates	194
Figure C.4	Reference for general strain energy release rate expression	200
Figure C.5	Discretised Winkler beam model	201
Figure D.6	Method of defining stiffness at circular disbond boundary	204
Figure E.7	Sandwich beam in which the core stress function is being considered	206

LIST OF TABLES

Table 2.1.1	Categorised list of the reviewed literature	18
Table 2.3.1	Thesis chapter structure	24
Table 3.3.1	Experimental design (full factorial test plan with three parameters and two variations on each)	30
Table 3.5.1	Manufacturer-supplied material properties	34
Table 3.5.2	Face laminate properties	37
Table 3.5.3	Honeycomb core properties	38
Table 3.5.4	Fracture properties (G_c) for all specimens	41
Table 3.5.5	Fracture properties for each combination of face material and core orientation	43
Table 4.3.1	Comparison of buckling load results from specimen testing and the present buckling model	61
Table 5.3.1	Parameters ranges used in the regression analysis	76
Table 5.3.2	Comparison between actual and predicted final disbond lengths	84
Table 6.2.1	Half-factorial test plan for panel specimens	92
Table 6.3.1	Dimensions of each specimen configuration	94
Table 6.3.2	Buckling and failure load result averages for each configuration	94
Table 6.3.3	Average reduction in load carrying capacity for each specimen	95
Table 6.3.4	Power coefficients of buckling and failure curves	96
Table 6.5.1	Fibre fracture frequencies (Pappas et al. 2004)	104
Table 6.5.2	Dominant frequencies ordered from most to least common	108
Table 6.5.3	Propagation and damage frequencies identified by Pappas et al. for fibre types similar to those in the present sandwich constituent materials	109
Table 6.5.4	Comparison of fibre propagation and damage frequencies	109
Table 6.5.5	Probabilities of the disbond growth frequency occurrences being random	111
Table 6.5.6	Loads for buckling, growth initiation and failure events for all specimens	112
Table 6.5.7	Fraction of post-buckling load at which growth initiates	113
Table 7.2.1	Foundation stiffness definitions from three methods	122
Table 7.3.1	Comparison of Experimental and Model Buckling Loads	124
Table 7.5.1	Configurations used to examine edge effects	129
Table 7.5.2	Comparison between Circular and Square Disbonds	134
Table 8.3.1	Non-linear controls used in the present model	147
Table 8.3.2	Comparison of circular plate displacements due to pressure loading	148
Table 8.4.1	Comparison of disbond growth initiation loads obtained from the model and specimen testing	164
Table 8.4.2	Comparison of experimental failure loads (Chapter Six) with model-predicted growth initiation loads	166

Table 8.4.3	Comparison of model-predicted failure loads with experimental results	167
-------------	---	-----

LIST OF SYMBOLS AND ABBREVIATIONS

Latin Symbol	Description
A	Component sectional area
$A\nu F$	Average frequency of transient acoustic events
C	Constant
C_E	Coefficient of Euler beam buckling
C_{PE}	Coefficient of Euler panel buckling
D_f	Face-sheet bending stiffness
D_{ij}	Row i , column j of the face-sheet bending stiffness matrix
E	Young's modulus of elasticity
E_{eff}	Homogenised (effective) Young's modulus of honeycomb in through-thickness direction
G	Shear modulus of elasticity
G_c	Critical strain energy release rate
$G_{total}, G_I, G_{II}, G_{III}$	Strain energy release rate; total, Mode I, Mode II and Mode III, respectively
J	Core modulus expression used in Airy's stress function
L_{cr}	Wrinkling half-wavelength (sandwich beam)
L_d	Disbond Size (length for through width disbonds, diameter for circular disbonds and edge length for square disbonds)
L_{dy}, L_{dx}	Rectangular disbond side lengths in x and y directions
L_x, L_y	w -displacement face-sheet wavelengths in x and y coordinates
L_X, L_Y	Panel dimensions in x and y directions
M	Number of laminae in a laminate
N_{cr}	Panel buckling load
N_{grow}	Load at which disbond growth initiates in a panel
N_{ult}	Panel failure load (ultimate load)
P	Beam Load
P_{cr}	Beam buckling load
P_{wr}	Wrinkling load of perfectly bonded sandwich beam
Q	Ratio of panel length to disbond diameter
R	Ratio of panel width to disbond diameter
S	Shear stiffness
THA	Ratio of threshold to maximum amplitude (regarding acoustic events)
U	Strain energy
U_s	Surface energy
W	Specimen width in direction transverse to loading

LIST OF SYMBOLS AND ABBREVIATIONS

X_1, X_2, X_3, \dots	Constants
[]	Defines variable within brackets as a matrix
c_1, c_2, c_3, \dots	Constants
$f()$	Function of the bracketed variables
h	Maximum out-of-plane face-sheet displacement (disbond buckle height)
k	Elastic foundation stiffness in z-direction
l	Length of regular honeycomb cell wall
n	Node number
n_s	Sample size
p	Binomial probability
s	Sample standard deviation
t	Thickness
u, v, w	Displacement functions in x, y and z directions, respectively

Greek Symbol Description

Δ	Beam end-shortening
Δ_s, Δ_b	Beam shear and bending deflections, respectively
Δ_{sx}	Nodal spacing in s-coordinate (Lagrangian) approximated by projected length in x-coordinate (Cartesian), i.e. assuming small displacements
Δ_x	Spacing between nodes in the x-direction
P_1, P_2, P_3, \dots	Dimensionless parameters
$(1-a)$	Confidence level
q, s	Lagrangian coordinates
k	Beam curvature
l_1, l_2	Constants
ν	Poisson's ratio
ρ	Component density
σ	Stress
s_s	Sample mean
s_p	Population mean
f	Airy's stress function

Subscripts Description

c	Core property
f	Face-sheet property
L	Laminate property
m	m^{th} layer lamina property
x, y, z	Property refers to Cartesian coordinate
n	Node number
cw	Refers to honeycomb cell wall property

Superscripts	Description
<i>c</i>	Core property (used when subscript specifies x, y, z orientation)
<i>f</i>	Face-sheet property (used when subscript specifies x, y, z orientation)
<i>e</i>	End value, i.e. after testing
<i>o</i>	Original value, i.e. before testing

Abbreviations	Description
ADL	Allowable damage limit
AE	Acoustic emission
CDF	Cumulative density function
COV	Coefficient of variance
CSB	Cracked sandwich beam fracture test
DCB	Double cantilever beam fracture test
ENF	End-notch flexure fracture test
FAR	Federal aviation regulation
FFT	Fast Fourier transform
LEFM	Linear elastic fracture mechanics
PMF	Probability mass function
SERR	Strain energy release rate
SRM	Structural repair manual
TPBS	Three-point bend sandwich fracture test
VCCT	Virtual crack closure technique

CHAPTER ONE

Introduction to Sandwich Structure

1.1 INTRODUCTION

The concept behind sandwich constructions is relatively simple and has been exploited in the design of common Ibeams. The concept developed from consideration of the most materially efficient method of providing a high-stiffness structure, having as much material stiffness located as far from the neutral axis of bending as possible. Sandwich structure achieves this by bonding high-density, high-strength material to either side of a low density core material (Figure 1.1.1). This structure is ideally suited to applications requiring high stiffness-to-weight ratios. For example, a typical aircraft sandwich construction (as used on Boeing 747-400 aircraft) weighs only 1kg for every 1000kg of a homogeneous material of equivalent stiffness.

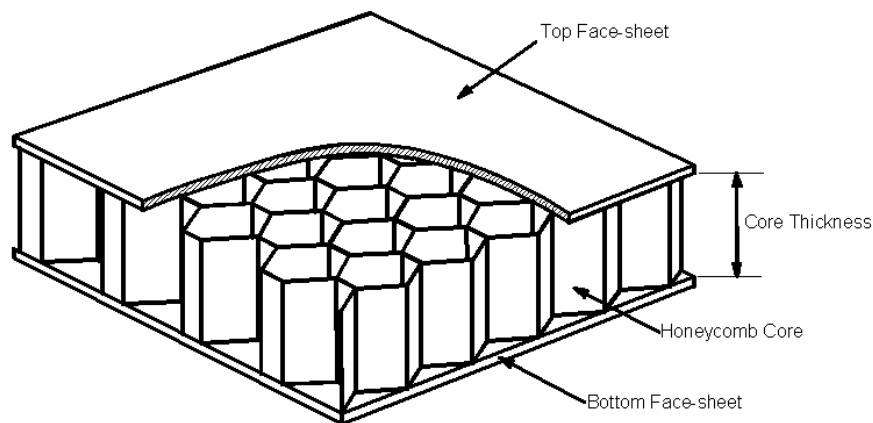


Figure 1.1.1 – Honeycomb-core sandwich construction

The World War II Mosquito bomber (Figure 1.1.2) is often quoted as the first structure to incorporate sandwich panels (Bitzer 1997). Sandwich construction is now used in many high performance structures, such as military and commercial aircraft, Navy vessels and high-performance yachts. Aircraft in particular are very weight-critical and consequently the aircraft industry is a primary user of sandwich structure. Most commercial aircraft use sandwich materials

extensively on secondary areas of aircraft structure and many of the flight control surfaces (Figure 1.1.3). Flight control surfaces include flaps, spoilers, ailerons, horizontal stabilisers, elevators, rudders, and winglets. Aircraft interior structure, such as floors and bulkheads, are also primarily sandwich construction. Future aircraft designs, such as NASA's HSCT (High Speed Civil Transport) program, are attempting to maximise the usage of sandwich structure in primary load carrying areas such as wing structures, to achieve maximum weight savings and provide more efficient, cheaper flight.

The development and usage of sandwich structures has largely been led by the evolution of high-strength materials over the last 50 years and while developments in materials continue to improve sandwich strength, there is now more focus on efficient usage of available constructions. A large part of this process is developing a more complete understanding of the behaviour of sandwich structure.



Figure 1.1.2 – The Mosquito bomber, one of the earliest structures incorporating sandwich panels

Sandwich structure is a composite material in that the core and facings, even though they may not be composed of different materials, always have different overall material properties. Additionally, fibre-composite laminates are frequently used for both core and facing material. The most weight-efficient structure available (in terms of providing bending stiffness) is sandwich structure with laminated composite facings and cellular composite core. Zenkert (1997) provides an excellent review of the behaviour of sandwich beams and panels.



Figure 1.1.3 – The Boeing 787 will be in production by 2008 and will be 58% composite structure by weight with sandwich used extensively for interiors, fairings and some control surfaces

One of the features of sandwich structure is a broad and complex range of failure modes (Figure 1.1.4). While the failure behaviour of undamaged sandwich structure is currently quite well understood and predicted, there are still aspects that attract research. The behaviour of sandwich structure containing damage is much more complex and one of the key factors limiting the optimum usage of sandwich structure is the current inability to accurately predict its damage tolerance behaviour.

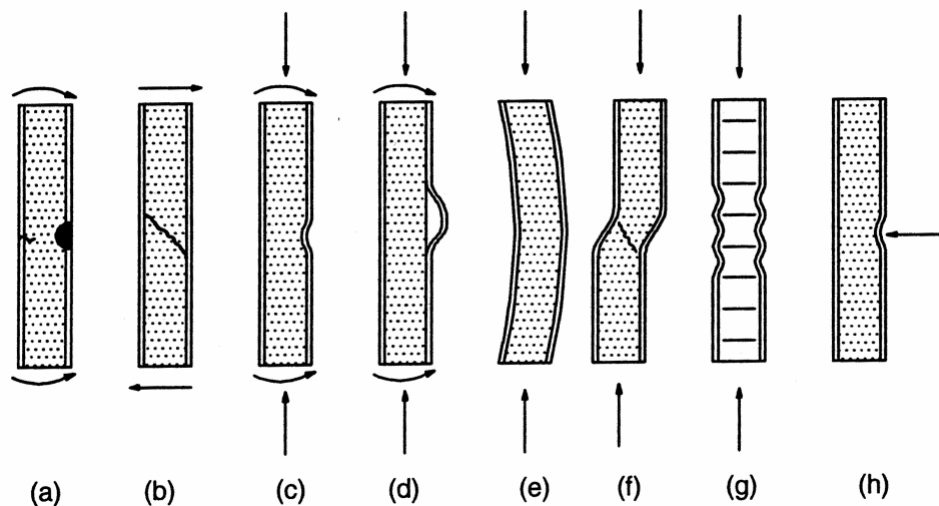


Figure 1.1.4 – Sandwich failure modes; (a) face yielding/fracture, (b) core shear failure, (c-d) face wrinkling, (e) global buckling, (f) shear crimping, (g) face dimpling and (h) local indentation

So, while sandwich construction has some great benefits it also has drawbacks such as a wide variety of failure modes and complexity of analysis. Unless a better understanding of sandwich

behaviour is developed, it will be relegated to secondary applications, especially in safety critical structure. Hence the current research, which aims to develop the understanding of damage tolerance of sandwich structure, specifically considering disbond damage (one of the most common types of damage). The next section is a brief introduction to damage tolerance and the next chapter discusses disbond damage in detail.

1.2 DAMAGED SANDWICH STRUCTURE

1.2.1 A GENERAL DISCUSSION OF DAMAGE TOLERANCE

Studies of damage can be divided into two categories: damage resistance and damage tolerance. Damage resistance is concerned with the development of damage in a structure, whereas damage tolerance is concerned with the loading of a structure containing some prior damage. The present research considers pre-existing damage in a sandwich structure and therefore it is relevant to provide an overview of damage tolerance. Damage tolerance is a complex field and an in-depth review of the whole field is not relevant here. For a more detailed review of damage tolerant design concepts refer to AFRL (2002).

Damage tolerant design requires knowledge of the variation of residual strength with damage size which can be characterised by length, area or volume. The present overview considers a simple structure (i.e. single load path) in which damage growth is stable. Figure 1.2.1 illustrates how the residual strength profile is used to determine an allowable damage limit (ADL).

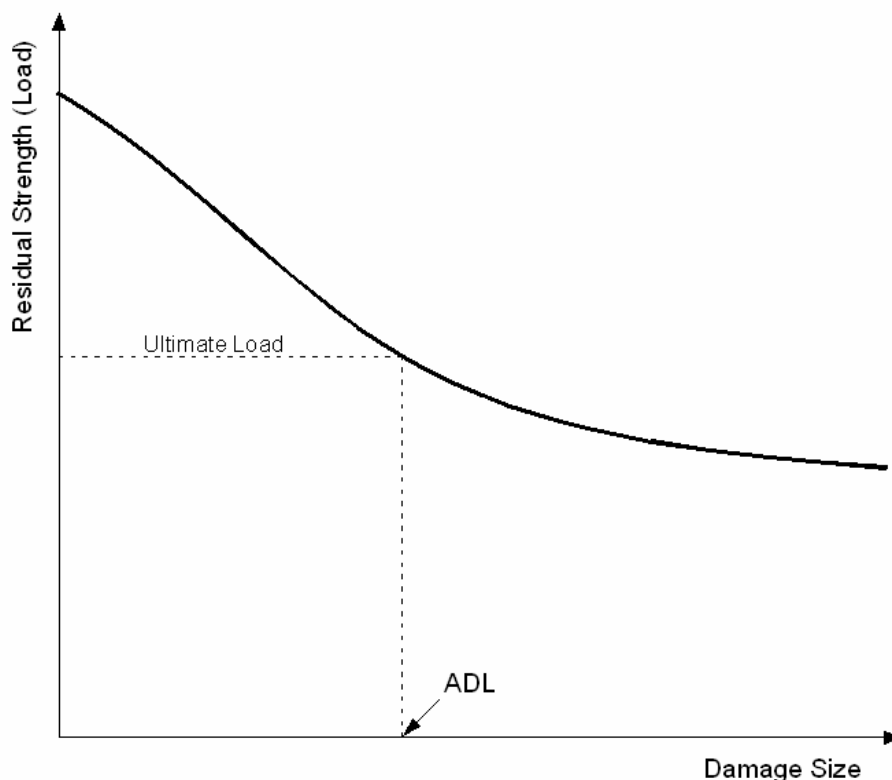


Figure 1.2.1 – Residual strength curve showing the allowable damage limit at ultimate load

One of the initial design considerations is the minimum size of damage that can be detected through non-destructive evaluation methods. The structure must be designed to carry the ultimate load

indefinitely with this level of damage present. Part 25 of the United States Federal Aviation Regulations (FAR) defines the design standards with which any aircraft flying in US airspace must comply. These regulations define ultimate load as limit load multiplied by a safety factor, typically 1.5 (FAR 25.303). Limit load is defined as the maximum load the structure is expected to be subjected to during its service life (FAR 25.301). The actual operating load is lower again than limit load and varies considerably during flight. An aircraft might be subjected to limit load only once or twice in its service life, due to factors such as extreme turbulence or emergency landing.

Damage tolerant design of aircraft requires that any structure must carry ultimate load without failure and must carry limit load without any detrimental permanent deformation (FAR 25.305). Damage growth, which typically reduces the residual load carrying capacity of the structure containing it, is considered here to be detrimental permanent deformation. Therefore, a structure must support the limit load without damage growth. This defines another allowable damage limit as shown in Figure 1.2.2, in which the damage growth curve defines the static load at which damage growth initiates. The maximum allowable damage size is defined as the smaller of the two allowable damage limits (i.e. ADL 1 in Figure 1.2.2). These are the static load considerations to design a damage tolerant structure.

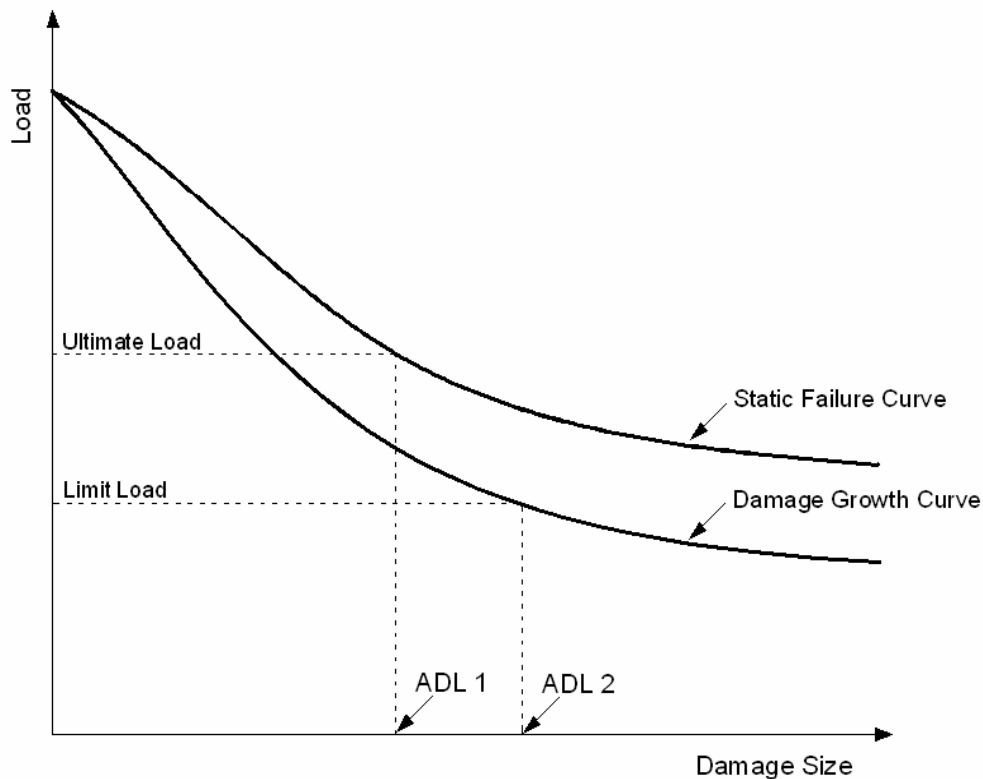


Figure 1.2.2 – Damage tolerance curves with two static allowable damage limits

Cyclic loading may also cause damage. Structural inspection intervals are determined with knowledge of the damage growth rate due to cyclic loading of the operational load (i.e. fatigue considerations). Within an inspection interval, damage must not be able to grow to the maximum allowable damage size. The region of the damage tolerance curve in which cyclic damage growth must be considered is illustrated in Figure 1.2.3 by including a lower cyclic load limit, the endurance limit. This is defined as the maximum load that could be applied cyclically and indefinitely to the damaged structure without damage growth occurring. Whether or not this limit exists in practice depends on the material type and configuration.

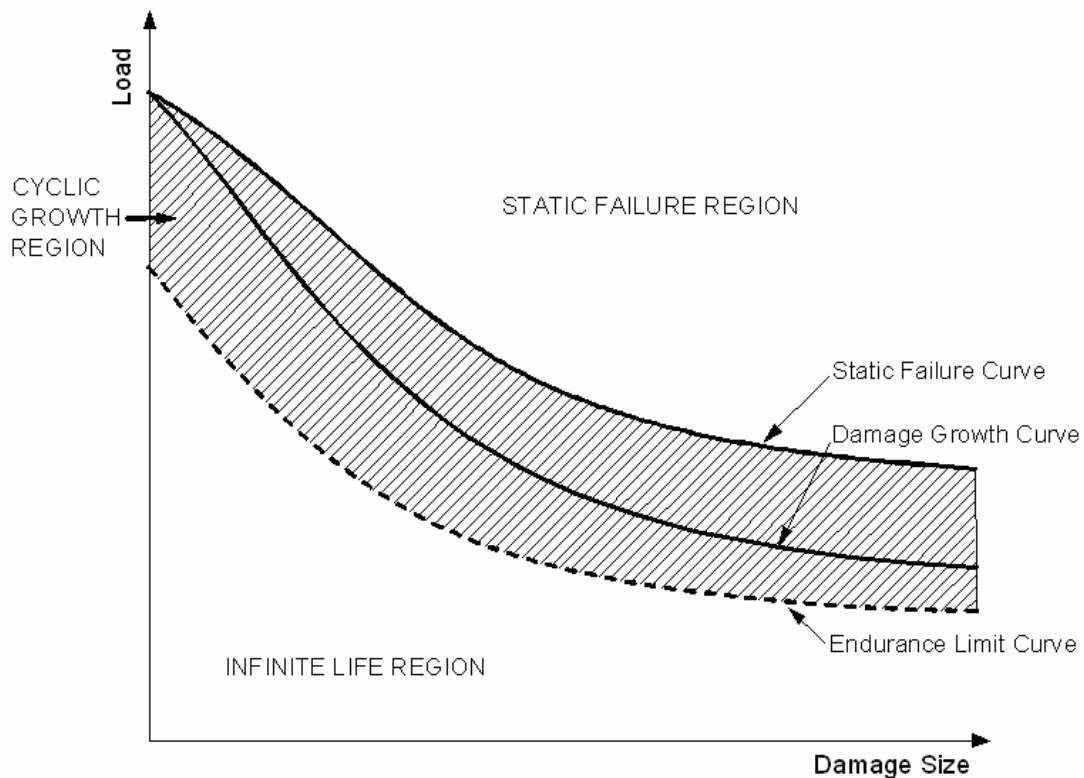


Figure 1.2.3 – Damage tolerance graph including static failure, damage growth and endurance limit

Below the endurance limit there is no failure for an infinite (or practically infinite, i.e. the design life of the structure) number of load cycles. Above the static failure curve failure occurs immediately. Between the endurance limit and static failure curve is the region in which damage growth may occur due to cyclic loading. Within this region lies the damage growth initiation curve, which is required along with the static failure curve in order to determine the maximum allowable damage size. These concepts are used in Chapter Three with specific reference to disbanded sandwich structure. For now it is important to recognise that without a complete knowledge of damage tolerance characteristics a structure must be conservatively (sub-optimally) designed.

1.2.2 DAMAGE TOLERANCE OF SANDWICH STRUCTURE

The nature of sandwich structure is such that it may contain sub-surface damage that is not easily detectable. Damage can be caused during manufacture or in service. Current aircraft design regulations ensure that aircraft structure is tolerant to a detectable level of damage, ensuring that components will not fail between regular inspection intervals. Consequently, knowledge of the damage tolerance of sandwich structure is critical to its increased usage in aircraft. Regarding the most critical damage types, Buebl (2004) states:

“A wide collection of damage sources, failures and damage types for typical aeronautical, naval and automotive applications has been catalogued. Low velocity impact damage and debonding of skins were identified as damages which occur most frequently and affect the structural behaviour most severely.”

The majority of research into damage of sandwich structures has been concerned with impact events. Disbonding (also referred to as debonding) of the face-core interface has received a relatively minor amount of consideration, both in terms of modelling and experimental investigation.

The motivation for the research presented in this thesis is to improve the knowledge of the tolerance of sandwich structure to disbonding. The next chapter will describe what disbond damage is and how it affects the integrity of sandwich structure.

CHAPTER TWO

Disbond Damage in Sandwich Structure

2.1 DISBOND DAMAGE IN SANDWICH STRUCTURE

Sandwich structure relies on the adhesive bond between the face-sheet and core for its overall integrity. A region where there is no bond is called a disbond (Figure 2.1.1). A disbond can occur during manufacture or can be caused by a variety of in-service loading conditions, such as foreign body impact (Aitken 2000, Burman 1998). Water trapped within honeycomb core under thermo-cyclic loading can also cause a disbond Han *et al.* (2002). Often there are discontinuities present in sandwich structures (such as fastener inserts) that are high stress gradient areas and potential nucleation sites for disbonds.

Minguet *et al.* (1988) conducted an experimental study of undamaged sandwich panels in compression (including both honeycomb and foam core materials) and observed disbonding, core failure and face fracture as the three failure modes in post-buckling. Disbonding has also been identified as the first stage of fatigue failure of undamaged foam-core sandwich beams (Kulkarni *et al.* 2003) and occurs at approximately 85% of the total fatigue life.

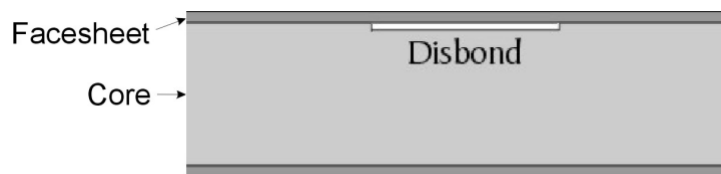


Figure 2.1.1 – A disbond in a sandwich beam

Some of the documented failure processes of sandwich structures containing pre-existing disbonds are described below, according to the loading condition.

Disbonded face-sheet loaded in compression:

- The disbond may buckle and grow in size (typically in an unstable manner (Han *et al.* 2002)) until failure by either face-sheet fracture or a gross loss of stiffness.

- The disbond may buckle and initiate global buckling of the sandwich (Avery and Sankar 2000; Hansen 1998)

Structure loaded in shear:

- Failure may be initiated by crack growth through the core, and lead to disbonding of both face-sheets. This process is very dependant on the type of core used (Burman 1998).

It should be noted that in many applications where sandwich construction is used, failure is considered to be a reduction in global stiffness below a certain threshold, rather than ultimate load failure. For example, control surfaces on aircraft must maintain their shape (remain sufficiently stiff) for safe and efficient flight.

2.1.1 IDENTIFYING THE CRITICAL LOADING METHOD

An initial consideration when undertaking research into the failure of disbonded honeycomb sandwich is determination of the critical loading scenario. Sandwich construction typically takes the form of a flat or curved panel, in which the thickness is small relative to the length and width. Any general panel load application can be resolved into shear, bending and membrane forces within the panel.

The typical assumptions used in analysis of sandwich panels are that the face-sheets carry all bending and membrane forces as tensile and compressive stresses, while the core carries all of the transverse forces as shear stresses. These assumptions are valid for most sandwich configurations, in which the core modulus is much less than the face-sheet modulus and the core thickness is at least 5.77 times the face-sheet thickness (Zenkert 1997).

Two doctoral theses (Burman 1998, Shipsha 2001) have investigated the static and fatigue growth of disbonds in foam and honeycomb core sandwich beams under shear loading. Shipsha focussed on fatigue loading of undamaged and impact damaged foam core sandwich. Burman focussed on foam core sandwich but also performed static four-point bend testing of undamaged and damaged honeycomb core sandwich. Damaged specimens contained a pre-existing disbond located so as to be in the centre of the shear loaded region of the beam (Figure 2.1.2).

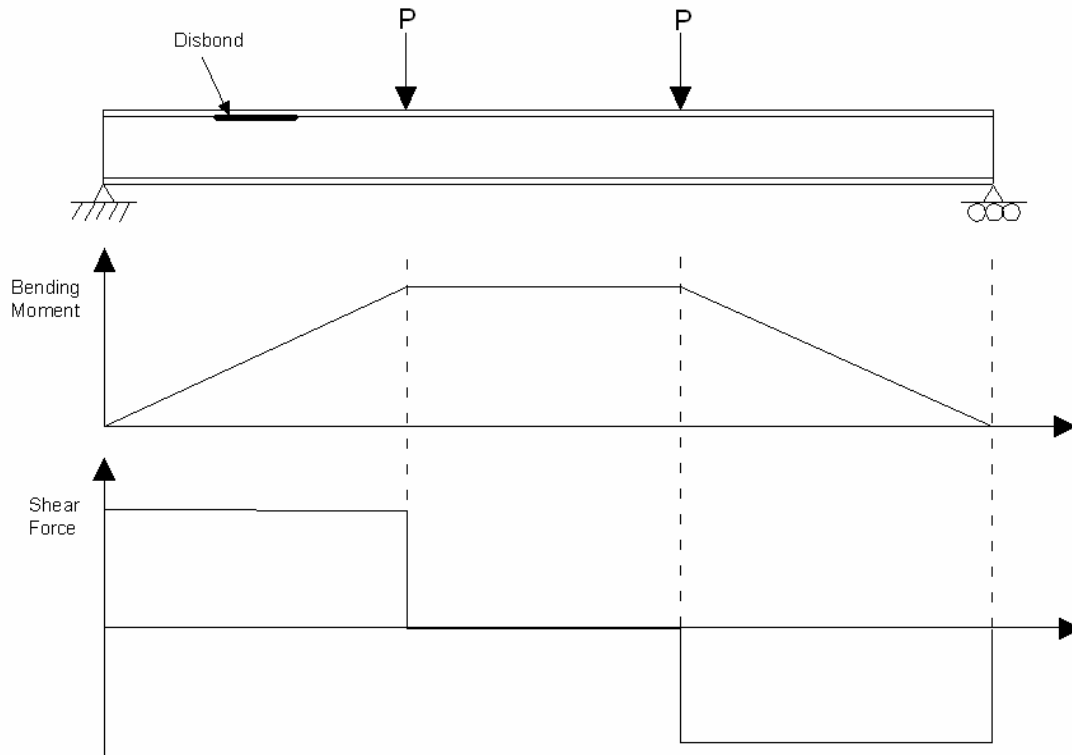


Figure 2.1.2 – Four-point bend sandwich specimen with disbond location as used by Burman (1998). The bending moment and shear force diagrams are also shown

In testing conducted by Burman (1998) the failure mode varied depending on the orientation of the core, but in all cases failure was due to crack propagation through the core, beginning at the disbond tips. Two disbond sizes were tested, 15mm and 30mm. The core was a 15mm thick Nomex honeycomb and the faces were four ply carbon-epoxy laminates. The average reduction in load carrying capacity was 73% for the 30mm disbonds and 26% for the 15mm disbonds. Note that the failure mode for the undamaged specimens was core shear failure.

The remainder of the reviewed studies of disbonded sandwich considered compressive loading of the face-sheet as the critical loading scenario. Avery and Sankar (2000) conducted testing of sandwich beams in pure compression. They showed that in this load scenario there is significant interaction of local and global buckling modes and there are a variety of failure modes depending on the specimen configuration. These results cannot be compared to those of Burman (1998) because there were no undamaged tests performed and therefore the reduction in load carrying capacity is unknown. It is also difficult to estimate the failure loads because there are several possible modes of failure (e.g. global buckling, face-sheet wrinkling and face-sheet fracture). There are no published studies of bending tests of disbonded sandwich in which the disbonded face-sheet is compressively loaded. However, there are various models of buckling of disbonded sandwich in which the face-

sheet is treated as a beam on an elastic foundation (Cheng *et al.* 1997, Niu and Talreja 1999, Sleight and Wang 1995, Vizzini and Lagace 1987). Assuming the buckling load to be a reasonable estimate of the failure load (which subsequent testing presented in Chapter Four has proven it to be) and that failure of an undamaged specimen would occur due to face-sheet wrinkling (Aitken 2000) it is possible to estimate the reduction in load carrying capacity of a disbonded sandwich beam in bending. Using results of Niu and Talreja (1999), the reduction in load carrying capacity of 15mm and 30mm disbonds, in the same specimen configuration as that of Burman (1998), is approximately 62% and 90% respectively. This indicates that a compressive stress field is more critical for a disbonded sandwich than a shear stress field. The actual failure mode (shear or compressive) will depend on the specimen geometry as well as the loading conditions. This can be explained considering Figure 2.1.2, in which the maximum shear force is simply equal to load P and the maximum bending moment (which causes the compressive stress in the face-sheet) is a function of the load span and beam length. From this review it is concluded that, in most cases, compression loading is the critical load type for disbonded sandwich structure.

Tensile loading of disbonded sandwich panels has not been addressed by any published papers. It is not a critical load case for disbonded sandwich as the tensile strength does not rely significantly on the face-core interfacial bond strength.

2.1.2 DAMAGE TOLERANT DESIGN OF DISBONDED SANDWICH STRUCTURE

Damage tolerant design concepts will now be discussed further, specifically in relation to disbond damage. The previous discussion identified three load curves that define the damage tolerance behaviour of a single load path structure; endurance limit, damage growth curve and static failure curve. Knowledge of these curves provides the design engineer with all the tools required to design damage tolerant structure and to assess the criticality of damage (i.e. whether or not it must be repaired). This research is focussed towards developing and validating tools to predict these three curves.

Han *et al.* (2002) found that the failure process of a compressively loaded disbonded sandwich panel begins with buckling and concludes with unstable disbond growth. It has been demonstrated analytically and experimentally that disbond growth does not occur until the disbond region has buckled because growth is dominated by Mode I (peel) fracture (Han *et al.* 2002, Niu and Talreja 1999, Peck and Springer 1991, Whitcomb 1992). Whitcomb (1992) found that the peel stresses induced after buckling are the primary mechanism driving disbond growth. This means that the

buckling load may be viewed as an endurance limit (see Chapter One), defining the lower bound on the cyclic failure load.

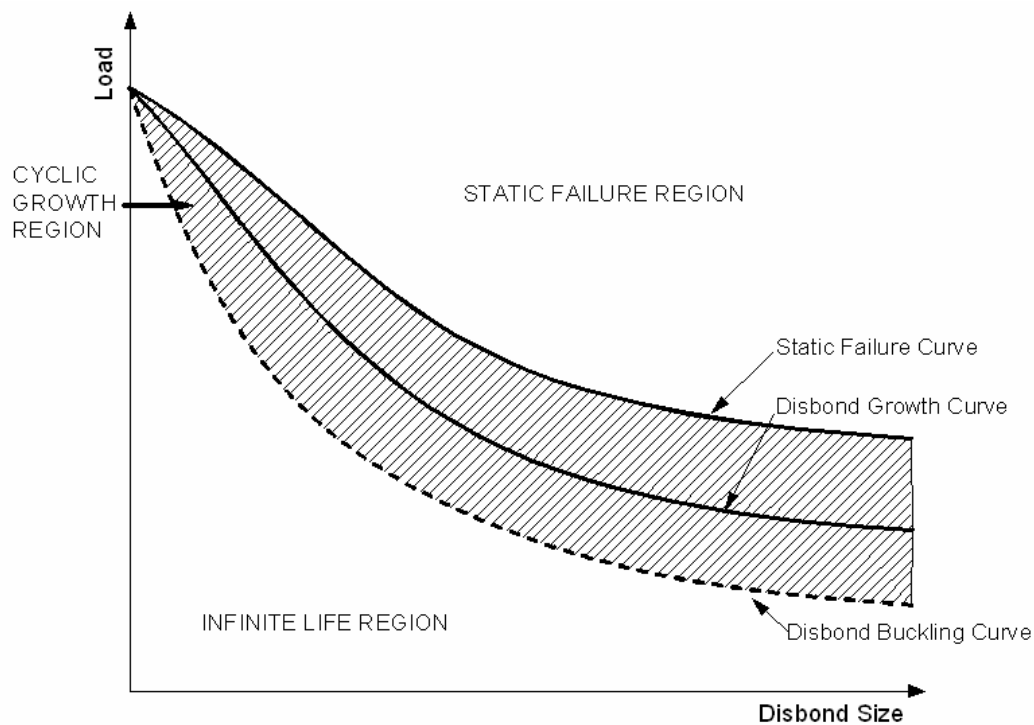


Figure 2.1.3 – Damage tolerance curve specific to disbond damage

Note that in Figure 2.1.3 the buckling curve intersects the static failure curve at zero disbond length. The assumption made here is that failure of an undamaged sandwich beam or panel in compression is due to face-sheet wrinkling (Aitken 2000).

Unlike homogeneous Engineering materials, there is little understanding of the fatigue behaviour of sandwich composites. This understanding is even less for sandwich composites containing damage. Burman (1998) presented the only published study of the fatigue behaviour of disbanded honeycomb-cored sandwich. Fatigue studies of undamaged honeycomb sandwich structure are also scarce. Kulkarni *et al.* (2003) and Sheno *et al.* (1995) have studied fatigue of undamaged foam core sandwich beams. Shipsha (2000) studied fatigue of foam core sandwich beams containing damage and Aitken (2000) performed fatigue testing of honeycomb sandwich beams with impact damage.

Establishing the buckling load (endurance limit) and static failure load identifies the limits within which cyclic loading can result in failure. Cyclic loading is not addressed in the present research other than to establish these limits.

2.1.3 SUMMARY OF THE REVIEWED LITERATURE

Each of the chapters in this thesis begins with a detailed review of the relevant literature. An overview of the complete body of literature is presented here.

2.1.3.1 DEFINITIONS OF DISBOND TYPES

Before continuing, the distinction between through-width and embedded disbonds will be made. A through-width disbond has constant length and extends through the full width of a sandwich panel. An embedded disbond may be any shape and is defined as having a single enclosed boundary within the sandwich structure. Authors typically treat embedded disbonds as being circular, elliptical or rectangular. Herein a sandwich structure with a through-width disbond is referred to as a disbonded beam and sandwich with an embedded disbond is referred to as a disbonded panel.

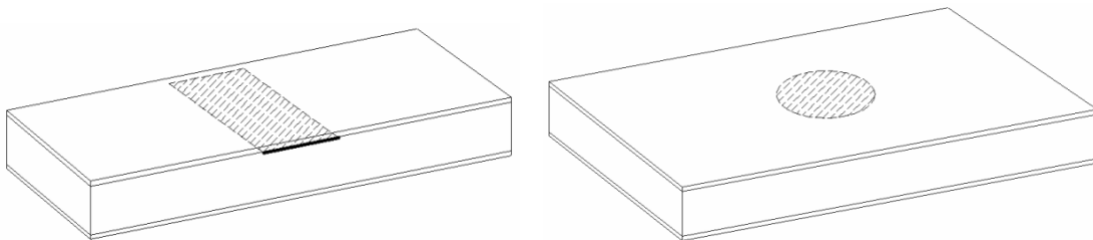


Figure 2.1.4 – Through-width (left) and embedded (right) disbonds in sandwich panels

2.1.3.2 STUDIES BASED ON ANALYSIS OF SOLID LAMINATES

There are a considerable number of studies concerned with the buckling and post-buckling of through-width and embedded delaminations in solid laminates (where the substrate is treated as being infinitely stiff out-of-plane, i.e. built-in edge conditions around the delamination). This is a sufficiently similar scenario to disbonding in sandwich structure that these studies have some relevance and indeed some authors have developed models of sandwich structure maintaining the assumption of built-in conditions at the disbond boundary. Many of the studies of disbond buckling in beams (Gaudenzi *et al.* 1998, Hwu and Hu 1992, Somers, *et al.* 1991, Yin *et al.* 1986) have maintained this assumption, as well as one study of embedded disbond post-buckling (Chen and Bai 2002). However, Hansen (1998) has shown that this assumption is very crude when modelling any realistic sandwich structure and that the transverse flexibility of the core must be considered.

2.1.3.3 SUMMARY OF DISBOND ANALYSIS METHODS

Of all the published studies of disbonded sandwich structure reviewed here, only Zenkert (1991) and later Burman (1998) and Shipsha (2000) considered a disbond loaded in a shear stress field, resulting in core fracture initiated at the disbond boundary. All other studies have considered compression loading of the disbonded face-sheet leading to disbond buckling and growth. This topic was addressed in Section 2.1.1 and, consequently, the load type of interest here is compressive face-sheet loading.

A feature of the reviewed literature is the scarcity of experimental studies regarding the failure of disbonded sandwich structure. Of the earlier research, most of the analysis was of sandwich beams (i.e. having a through-width disbond). This is a simpler analysis case than sandwich panels (i.e. having an embedded disbond) which must be modelled in three-dimensional space. These are the two groups into which the literature can be initially divided, analyses of sandwich beams and analyses of sandwich panels, and for categorising experimental studies these groupings are sufficient. Regarding the modelling approaches in the literature each of these groups can be further categorised into three analysis groups:

- Disbond buckling analyses
- Post-buckling analyses without disbond growth
- Post-buckling analyses with disbond growth

2.1.3.4 DISBOND BUCKLING ANALYSES

Within the disbond buckling analyses of sandwich beams there are two general approaches. The first considers the effect of a disbond on the global response of a sandwich beam in pure compression and as such the entire structure is modelled, two face-sheets and a core (Figure 2.1.5).

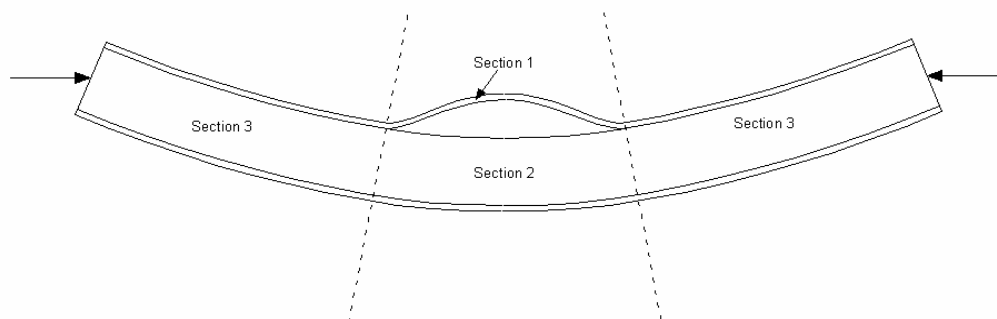


Figure 2.1.5 – Method of modelling entire sandwich beam, with typical sectioning method shown

Notice in Figure 2.1.5 that global beam buckling occurs simultaneously with local disbond buckling. This kind of buckling interaction always occurs for sandwich beams in pure compression (Frostig and Sokolinsky 1999). With the exception of Frostig and Sokolinsky (1999), authors who have developed this type of model have typically modelled the core as having infinite out-of plane stiffness (Hwu and Hu 1992, Somers *et al.* 1991, Yin *et al.* 1986). They then divide the beam into regions (Figure 2.1.5) with compatibility enforced where sections join. The other approach is to decouple the face-sheets and consider only the localised effects of the disbond, but to incorporate the transverse flexibility of the core (Cheng *et al.* 1997, Niu and Talreja 1999, Sleight and Wang 1995, Vizzini and Lagace 1987).

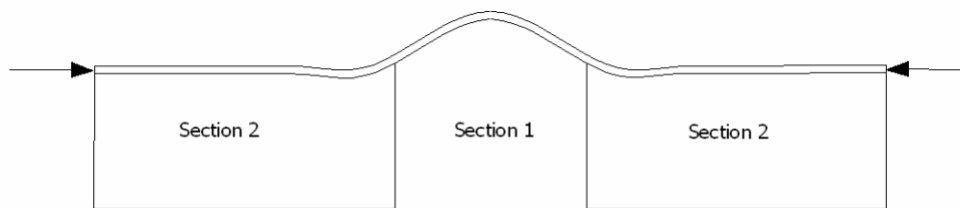


Figure 2.1.6 – Decoupled face-sheet method used to model local behaviour

Niu and Talreja (1999) presented a characteristic curve defining the buckling load for any given sandwich beam configuration. However, all of the models that incorporate transverse flexibility of the core have assumed a simplistic constant strain state in the core. Frostig and Sokolinsky (1999) argued that this method does not accurately account for the complex interaction of local and global buckling modes for sandwich beams in pure compression. However, for beams subjected to bending, in which global buckling of the sandwich beam cannot occur, this argument does not apply and the approach is reasonable.

There are only three studies of disbond buckling analyses of sandwich panels in which the transverse flexibility of the core is considered (Lin *et al.* 1996, Hansen 1998, Han *et al.* 2002).

Avery and Sankar (2000) compared the failure loads obtained through specimen testing of sandwich beams in pure compression with buckling load predictions of Hwu and Hu (1992). The comparison showed significant differences for the majority of cases. The buckling load was not specifically isolated in the tests, which precluded a direct comparison with the model predictions.

The only specimen test study in which the buckling load was isolated for comparison to model results was performed by Hansen (1998). The test specimen configuration was quite complex, consisting of a sandwich panel in pure compression containing two separate rectangular disbonds and consequently it is difficult to compare it with results of any existing models. Therefore, despite

the number of disbond buckling models available, their agreement with actual test specimen results has not been shown. This is the motivation for the specimen testing described in Chapter Three.

2.1.3.5 *POST-BUCKLING ANALYSES WITHOUT DISBOND GROWTH*

Both of the studies described in this section considered a complete sandwich beam, with coupling between the face-sheets, as in Figure 2.1.5.

Sankar and Narayanan (2001) developed a non-linear, plane strain finite element model of a sandwich beam to predict the failure loads observed in the specimen testing of Avery and Sankar (2000). The model did not incorporate a growth criterion but predicted the maximum load carrying capacity of the disbonded beam in post-buckling. The model results agreed with the specimen test result with less than 10% difference in 50% of the cases. The remainder of the test cases exhibited failure modes that caused failure prior to the maximum load predicted by the model. This model considers pure compression loaded specimens and is not appropriate for modelling sandwich beams in bending.

Frostig and Thomsen (2004) considered sandwich beams in bending, caused by application of a central transverse load (i.e. three-point bending). The model is based on a High-Order Sandwich Panel Theory and incorporates a transversely flexible core with contact between the core and face-sheet. The effect of applying load directly to the disbonded face-sheet was considered and it was noted that there were tensile stresses generated at the disbond tip, but an analysis of disbond growth was not included. There was no comparison made with specimen test results.

2.1.3.6 *POST-BUCKLING ANALYSES WITH DISBOND GROWTH*

Han *et al.* (2002) presented the most effective model of sandwich structure containing an embedded disbond to date, predicting an experimental disbond growth initiation load to within 9%. The purpose of the study was to investigate the accuracy of a cohesive zone model of disbond growth. The study involved only a single test specimen and a single corresponding model result. Therefore, while the predictive capabilities of the model were very good, a more detailed study is required to provide insight into the problem and validate the model against a wider range of test configurations.

Disbond growth in sandwich beams was addressed by Kim and Dharan (1992) by incorporating a strain energy release rate term into a linear model of an Euler beam on an elastic foundation. This model is limited by the assumption of small displacements and when compared with specimen test results of Kim *et al.* (1993) the error was approximately 150%. There were no non-linear post-buckling models of sandwich beams including growth analysis found in the literature.

2.1.3.7 IDENTIFIED GAPS IN THE BODY OF KNOWLEDGE

The following points summarise the main gaps in the body of research as they appear from the current review:

- Disbond buckling in sandwich beams has been extensively modelled but there are no comparisons with experimental results.
- Disbond buckling in sandwich panels has been modelled by only two authors and neither developed a general understanding of the problem.
- The transverse flexibility of a sandwich core is typically orders of magnitude lower than the face-sheet modulus and it should be considered when modelling sandwich panels (Hansen 1998). Of the models that do incorporate a transversely flexible core, all assume a simple constant strain state in the core.
- No studies have been found that considered the transverse flexibility of the core in a non-linear post-buckling model of the growth of through-width disbonds.
- The most advanced model developed to study embedded disbond growth (Han *et al.* 2002) agreed closely with specimen test results but was for one specific case and referenced only a single experiment, therefore it was of limited use in deepening the understanding of the principles governing disbond behaviour.

2.1.3.8 TABLE OF REFERENCED PAPERS

In the following table, modelling studies have been categorised as relating to sandwich only if they treated the core as having finite transverse flexibility, otherwise they have been grouped with the models of solid laminates. The list of references regarding delaminations in solid laminates contains only those papers referenced in the body of the thesis and is not a thorough review of each subject area.

Table 2.1.1 – Categorised list of the reviewed literature

Subject Area:	References:
Sandwich Beam Experiments	Avery and Sankar (2000) Burman (1998) Kim and Dharan (1992) Shipsha (2000)
Sandwich Panel Experiments	Falk (1994) Han <i>et al.</i> (2002) Hansen (1998) Kassapoglou (1988)

Subject Area:	References:
	Peck and Springer (1991)
Sandwich Beam Buckling Analysis	Cheng <i>et al.</i> (1997) Frostig (1992) Frostig and Sokolinsky (1999) Hetenyi (1946) Niu and Talreja (1999) Sleight and Wang (1995) Vizzini and Lagace (1987)
Sandwich Beam Post-Buckling Analysis – Without Growth	Frostig and Thomsen (2004) Sankar and Narayanan (2001)
Sandwich Beam Post-Buckling Analysis – With Growth	Kim and Dharan (1992) Kim <i>et al.</i> (1993)
Sandwich Panel Buckling Analysis	Han <i>et al.</i> (2002) Hansen (1998) Lin <i>et al.</i> (1996)
Sandwich Panel Post-Buckling Analysis – Without Growth	
Sandwich Panel Post-Buckling Analysis – With Growth	Han <i>et al.</i> (2002)
Solid Laminate Experiments	Davidson (1991) Kardomateas (1990) Pradhan and Tay (1998)
Solid Laminates with Through-Width Delaminations; Buckling, Post-Buckling and Growth Analyses	Gaudenzi <i>et al.</i> (2001) Hwu and Hu (1992) Kyoung and Kim (1995) Somers <i>et al.</i> (1991) Yin (1988) Yin <i>et al.</i> (1986)
Solid Laminates with Embedded Delaminations; Buckling, Post-Buckling and Growth Analyses	Chen and Bai (2002) Kassapoglou (1988) Klug <i>et al.</i> (1996) Krueger and O'Brien (2000) Peck and Springer (1991) Pradhan and Tay (1998) Riccio <i>et al.</i> (2000) Rinderknecht and Kroplin (1997) Tafreshi and Oswald (2003) Thomson and Scott (2000) Whitcomb (1989) Whitcomb (1992)
Test Methods for Face-Core Interfacial Fracture Toughness	Cantwell <i>et al.</i> (1999) Carlsson <i>et al.</i> (1991) Ural <i>et al.</i> (2003) Zenkert (1991)

Subject Area:	References:
Numerical Fracture Methods	Kim and Dharan (1992) Mackerle (1995) Raju (1987) Toya <i>et al.</i> (1997) Ural <i>et al.</i> (2003)
Fatigue Testing of Damaged and Undamaged Sandwich	Aitken (2000) Burman (1998) Kulkarni <i>et al.</i> (2003) Shenoi <i>et al.</i> (1995) Shipsha (2000)

2.2 PROPERTIES OF HONEYCOMB CORES

One of the particularly complex aspects of honeycomb-cored sandwich behaviour is the cellular nature of the core. In general, honeycomb is assumed to be an anisotropic solid because of the computational expense of modelling it as cellular structure. The properties of honeycomb are usually taken as the global effective properties with the assumption that there are a sufficient number of cells in the structure for this to be valid. Authors have concerned themselves with accurately determining the global effective properties of honeycomb core since it first became widely used as a core materials. For example Penzien and Didriksson (1964) evaluated the effective shear modulus of honeycomb with a unit cell approach. However, these models have typically been simplistic representations, treating the honeycomb cell walls as beams and until recently none had considered the effect of the restraint provided by a face-sheet bonded to the core.

2.2.1 IN-PLANE HONEYCOMB PROPERTIES

The work of Ashby and Gibson (1997) is the most common reference for determining effective properties of cellular materials. However, Ashby and Gibson (1997) do not give the effective properties for cellular core when it is restrained by a bonded face-sheet. While this has very little if any influence on the out-of-plane properties, it can significantly affect the in-plane properties. This effect is typically ignored because of the standard assumption, when modelling sandwich structure, that the face-sheets carry the entire in-plane and bending load while the core carries only shear and out-of-plane loads. However, when considering localised effects such as wrinkling or when modelling damage regions, the in-plane properties of the core can be significant and critical to model accuracy as determined by Vonach and Rammerstorfer (2000).

The effect of the skin-core bond on the core properties was first investigated by Becker (1998). The in-plane properties of unrestrained honeycomb (i.e. not bonded to a face-sheet) are given by manufacturers and standard tests exist to determine the in-plane moduli. These values are very low (approximately 0.1% of the out-of-plane moduli) because the stiffness depends almost entirely on the flexible joints at the corners of the hexagonal cells. The geometry dependence of the in-plane moduli is noticeably reduced when the core deformation is restrained by a rigid face-sheet, and the moduli increase significantly. Becker (2000) developed a model of a unit cell of honeycomb core and investigated the effects of core thickness (t_c) on the in-plane moduli, ultimately concluding that the moduli of face-restrained honeycomb can increase by up to 100% as the core thickness decreases to zero. However, the simple fact Becker (2000) does not mention out of his results is that

regardless of core thickness, the in-plane moduli of face-restrained honeycomb is orders of magnitude larger than unrestrained honeycomb. A comparison between the analytical models of Ashby and Gibson (1997) and Becker (2000) shows this fundamental difference:

$$\begin{aligned} \text{Ashby and Gibson : } \quad E_{eff} &= E_{cw} \left(\frac{t_{cw}}{l} \right)^3 14.9 \\ \text{Becker : } \quad E_{eff} &= E_{cw} \left(\frac{t_{cw}}{l} \right) f(t_c) \end{aligned} \tag{2.2.1}$$

The ratio of cell wall thickness, t , to cell wall length, l , has its power reduced from three down to one when the core is bonded to a face-sheet. This ratio is typically in the order of 3%, so the model of Becker (2000) will result in much larger modulus values. Using the model of Becker (2000) for a typical honeycomb core sandwich gives an in-plane modulus for the core of 20 MPa (assuming a very thick core). This compares to a modulus of 1.5 MPa derived using the model of Ashby and Gibson (1997). The experimentally determined modulus of unrestrained core (which is what authors studying sandwich structure typically use), in this case, is 0.4 MPa. As commented by Xu and Qiao (2002),

“The practice of neglecting skin effect is prevalent in today’s sandwich research and design, wherein the equivalent core properties are simply taken from those formulas based on pure cellular models. Besides other unscrupulous uses causing erroneous Poisson’s ratios and singularities, this neglect yields underestimates of stiffness and subsequent inconsistencies between modeling and reality, although only few of them were noticed in experiments (e.g., the study by Cunningham and White, 2001).”

The result of this is that the experimental values for unrestrained honeycomb moduli commonly in use are often inappropriate, although in the majority of cases it will have little effect on the overall sandwich stiffness. For example, a ten-fold increase in core stiffness for a typical sandwich construction results in an increase in the sandwich bending stiffness of approximately 0.1% and an increase in the tensile stiffness of less than 0.4%. This is why this behaviour has either gone unrecognised or been ignored. However, in the field of damage in sandwich construction, where local core deformations require accurate modelling and core orthotropy is important (Vonach and Rammerstorfer 2000), the effect of face restraint on the core should be considered.

This effect is mentioned because the model of Vonach and Rammerstorfer (2000) is used in the models described in Chapters Four, Five, Seven and Eight to determine the effective core stiffness

and this model incorporates orthotropic core properties. The model of Becker (2000) was not recreated to determine the in-plane moduli of face-restrained honeycomb, but the influence of core stiffness is determined for each model so that the effect of an increased core stiffness can be evaluated.

2.2.2 FRACTURE PROPERTIES OF HONEYCOMB

Crack propagation through honeycomb is another important behaviour that is not at all well understood. A disbond front grows through the cellular core and hence the fracture properties at the crack front are very important in the analysis of disbond growth. Avery and Sankar (2000) noted that fracture properties vary with core orientation but, to date, there is no clear explanation of why this is so. Avery and Sankar (2000) proposed that it is due to delamination of the cell walls during fracture. Goswami and Becker (2000) described the stress concentration points that are found at the triple points (where three cell walls meet) of a honeycomb sandwich when it is modelled using shell elements. They noted that in this scenario there is a finite value for the strain energy release rate at this point even when no crack is present. They studied the strain energy release rate along the interface of the face and core cell walls when a crack is initiated and propagated radially outwards from the triple point. This does not, however, provide insight into the propagation of an arbitrary crack front through honeycomb. Chen and Huang (1998) studied fracture through cellular materials, but they considered the crack front to be parallel to the cell walls (as in delamination of the cell walls themselves). This is an entirely different plane of fracture to that of disbonding and therefore the results do not apply. All methods of experimentally determining the fracture toughness of honeycomb are macroscopic, global methods providing large-scale effective fracture properties. There are currently no methods of measuring the fracture toughness for a crack propagating through a cellular material. It would be useful in developing an understanding of the qualitative behaviour of a crack in a cellular medium to perform some kind of basic analysis of the problem. Because no relevant papers were found to aid in the understanding of this problem, in this research the global fracture properties were experimentally determined and the effect of core orientation was investigated to provide some insight into the cellular level of fracture. Finally, this area of research is included in the list of recommended future research topics.

2.3 THESIS STRUCTURE

The approach of this research has been to consider sandwich beams and sandwich panels separately. The former is a simpler analysis case and provides insight into parameters governing behaviour, while the latter is a more realistic case. For each of these cases the modelling has been divided further into linear disbond buckling models and non-linear disbond growth models.

The layout of this thesis is such that each chapter is self-contained, with reference to other relevant chapters where necessary. The first two chapters are a general introduction to sandwich structures and disbond damage. The methodology of considering through-width and embedded disbonds separately, is represented in the chapter structure of the rest of the thesis (Table 2.3.1), where the two central sections describe the beam and panel testing and modelling.

Table 2.3.1 – Thesis chapter structure

Introduction	CHAPTER ONE Introduction to sandwich structure	CHAPTER TWO Introduction to disbond damage	
Sandwich Beams (Through-width disbonds)	CHAPTER THREE Sandwich beam specimen testing	CHAPTER FOUR Through-width disbond buckling model	CHAPTER FIVE Through-width disbond post-buckling and growth
Sandwich Panels (Embedded Disbonds)	CHAPTER SIX Sandwich panel specimen testing	CHAPTER SEVEN Embedded disbond buckling model	CHAPTER EIGHT Embedded disbond post-buckling and growth
Discussion and References	CHAPTER NINE Conclusions and Discussion	REFERENCES	APPENDICES

Each chapter begins with a review of the relevant literature and concludes with a summary and discussion of the findings. Chapter Nine presents a summary of the results of the research and places them in the broader context of the field of study.

CHAPTER THREE

Testing of Disbonded Sandwich Beam Specimens

3.1 INTRODUCTION

One of the features of the current body of literature regarding disbonds in sandwich beams is a lack of specimen test studies. This chapter begins with a review of the existing specimen test studies and then describes the manufacture and testing of sandwich beam specimens with disbonds. Some of the results of the specimen tests are presented in this chapter, although the majority will be given in Chapters Four and Five for comparison with the models in those chapters. A new test for the fracture strength of the interfacial bond (between core and face-sheet) is developed and described in this chapter and the initiation of disbond growth during the test is identified with the aid of acoustic emission monitoring.

3.2 LITERATURE REVIEW

The scarcity of sandwich beam specimen test results is highlighted by the fact that Kim and Dharan (1992) compared a fracture model (described in Chapter Five) with results of compression tests performed 23 years earlier by Harris and Nordby (1969). Further to this, the specimens utilised by Harris and Nordby (1969) were made from 6mm thick plywood facings on a 76mm thick foam core, which is not a material configuration representative of the majority of sandwich construction used today or in 1992. There have been minimal additions to the literature since then. All of the experimental studies of disbonded sandwich beams (Avery and Sankar 2000, Burman 1998, Shipsha 2001) used either pure compression or shear-loaded test specimens, there are none that have considered compression loading due to bending. It was stated in Chapter Two that the critical loading scenario for honeycomb sandwich is generally compressive loading of the disbonded face and this is the focus of this thesis. Therefore the shear loaded beam tests of Shipsha (2001) and Burman (1998), while extensive studies in terms of shear loading, are not relevant to the present work. Numerous experimental studies of delaminations in solid laminated beams exist, some of

which provide useful information regarding the general failure process of that type of damage, and these are reviewed in the following sections.

3.2.1 COMPRESSION LOADING OF DISBONDED SANDWICH BEAMS

Avery and Sankar (2000) performed a series of axial compression tests on 16 different configurations of disbonded sandwich beams with graphite/epoxy face-sheets and aramid fibre honeycomb core. The tests were performed to determine the ultimate axial load carrying capacity of the beams and they identified four different buckling modes leading to failure. This result highlights the interaction of local and global buckling in a pure compression load field and validates the argument of Frostig and Sokolinsky (1999) that buckling modes cannot be separated when considering disbonded sandwich in pure compression. Avery and Sankar (2000) developed an empirical formula for the compressive failure load of a sandwich beam, using their test results. They considered four parameters and assumed an expression for the failure load of the form:

$$F = C f_1(t_f) f_2(L_d) f_3(r_c) f_4(t_c) \quad (3.2.1)$$

The face-sheet modulus was not varied in the test plan and the core stiffness is dependant on its density, which was a variable in the test plan. The functions were assumed to be polynomial and were fitted to the experimental data with the following results:

$$\begin{aligned} f_1(t_f) &= -1.17 \times 10^7 (t_f)^3 + 1.63 \times 10^6 (t_f)^2 - 2.20 \times 10^4 (t_f) + 226 \\ f_2(L_d) &= -336 (L_d)^3 + 1631 (L_d)^2 - 2640 (L_d) + 2035 \\ f_3(r_c) &= -43 (r_c)^2 + 422 (r_c) - 109 \\ f_4(t_c) &= -9447 (t_c)^2 + 8174 (t_c) - 932 \end{aligned} \quad (3.2.2)$$

These are rather unwieldy equations from which to draw conclusions about the effect of each parameter. The results are expressed here by fitting a power curve to each of the expressions in (3.2.2) using the least squares method. This provides the following definition of failure load:

$$F = C (t_f)^{1.58} (L_d)^{-0.49} (r_c)^{0.39} (t_c)^{0.56} \quad (3.2.3)$$

The main assumption of (3.2.3) is that the constants in the first, third and fourth equations of (3.2.2) are negligible. This implies that the failure load is zero when either t_f , r_c or t_c are zero, which is considered to be a reasonable assumption. The assumption that the second equation of (3.2.2) approaches infinity when the disbond length is zero is not as reasonable but the power curve can still be used to approximate the polynomial curve fit of (3.2.2).

The magnitude of each of the powers in (3.2.3) indicates the amount of influence of the corresponding variable. Clearly the face-sheet thickness has the most effect on failure load and the relationship to disbond length is inverse (i.e. as the disbond length increases the failure load decreases, as expected). The relatively large influence of core thickness is due to the fact that loading was done in pure compression and failure was initiated by a combined global buckling of the beam (strongly influenced by core thickness) and local buckling of the disbond (strongly influenced by face-sheet thickness). One of the most important results of the tests performed by Avery and Sankar (2000) is the observation of four distinct failure modes in disbonded sandwich beams loaded in pure compression.

Avery and Sankar (2000) also determined the relationship between the same four parameters and the fracture toughness of the face-core interface, using Double Cantilever Beam (DCB) test results. In all cases it was found that the fracture toughness was sufficient to prevent disbond growth in the axial compression tests.

3.2.2 COMPRESSION OF DELAMINATED SOLID LAMINATES

There are many experimental studies of laminated beams with delaminations between various plies and, while the results are not directly relevant to sandwich materials, the damage propagation mechanism is similar and provides an established reference point for comparison. Of all the studies reviewed, Kardomateas (1990) outlined the typical insights available from laminate testing. He performed a series of compression tests on laminated Kevlar/epoxy specimens with through-width delaminations at various depths from the top of the specimen (Figure 3.2.1).

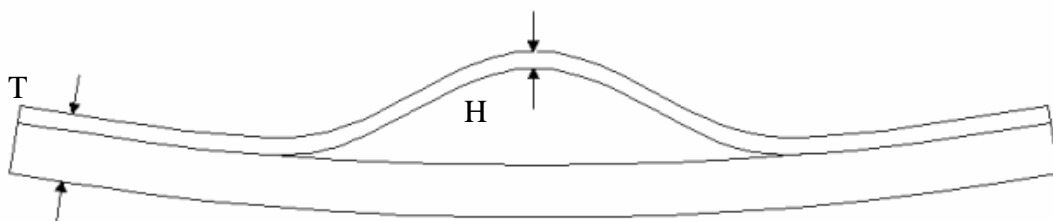


Figure 3.2.1 – Delaminated composite beam

He found that when the ratio of delamination thickness (H) to total laminate thickness (T) is $1/15$, then there is no delamination growth. Increasing H/T to $2/15$ gave a finite, but small, resistance to growth and this decreased exponentially as H/T was increased. Note that because the disbond length was held constant, this increase in H/T corresponds to an increase in the slenderness ratio (sub-laminate thickness to length) of the delaminated region. In some cases the growth continued along

the full length of the specimen as the load was increased, in others the delamination closed up at one end and grew only in the other direction. This is most likely due to the fact that as the delamination becomes more slender it has less ability to generate high peel stress at the ends. Because this is the mode of fracture (peeling of the buckled sub-laminate from the main laminate) there is a maximum slenderness ratio beyond which no delamination growth can occur.

Kardomateas (1990) found that the load deflection profiles consist of two phases: “(1) a rising stage that includes the initial post-buckling deflections, and for most cases is free of growth, and (2) a falling load stage that includes mostly growth of the delamination and accumulated damage”. There are a number of similarities between these results and the sandwich beam results presented later in this chapter.

3.2.3 INTERFACIAL FRACTURE TOUGHNESS TEST METHODS

There are a number of methods of determining the interfacial fracture toughness of laminated specimens. The critical strain energy release rate, G_c , is generally accepted as the most useful fracture parameter for input into numerical fracture simulations (Han *et al.* 2002, Kim and Dharan 1992, Sankar and Narayanan 2001, Ural *et al.* 2003). There are also strength-based approaches but they have been found to be less accurate (Ural *et al.* 2003). The experimental methods used to determine this parameter can be grouped by the mode of fracture that they measure. The total strain energy release rate is the sum of the value for each of the three fracture modes (Figure 3.2.2):

$$G_{total} = G_I + G_{II} + G_{III} \quad (3.2.4)$$

The Double Cantilever Beam (DCB) specimen is the most common method of measuring the Mode I fracture toughness. Ural *et al.* (2003) demonstrated that, when carefully performed, this method provides consistent and accurate Mode I fracture toughness properties for sandwich structure with honeycomb core. Cantwell *et al.* (1999) proposed and tested an alternative mode one fracture test for sandwich structure called the three-point-bend sandwich (TPBS) specimen. This was compared to a finite element model of the test geometry and it was found that the ratio of Mode I to Mode II in the test method was always greater than 10.

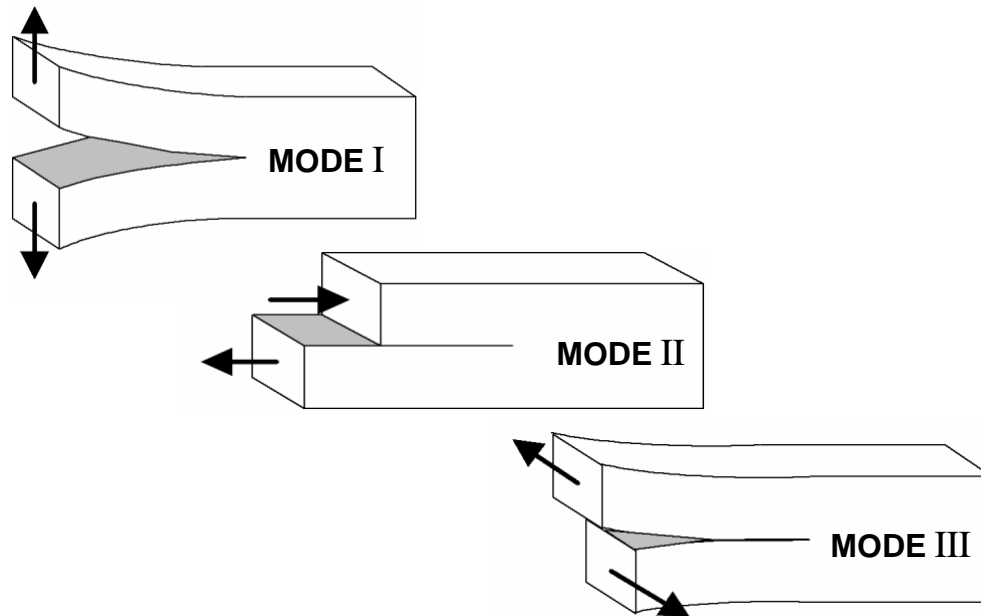


Figure 3.2.2 – The three basic modes of fracture

Carlsson *et al.* (1991) proposed and tested a modified version of the End-Notch Flexure (ENF) specimen, called the Cracked Sandwich Beam (CSB) test to measure the Mode II fracture toughness of the face-core interface. Mode III fracture is so rarely a consideration that there is no standard test method to measure this parameter in isolation. The drum peel test is a standardised method of evaluating the toughness of the interfacial bond in sandwich structures but it is difficult to extract the strain energy release rate accurately from the test results and it can be difficult to perform for very thin or very thick faces (Cantwell and Davies 1994). The general theory behind these methods is described in Section 3.5.3, where an alternative, buckling-driven fracture toughness test is proposed. The proposed test method provides fracture properties based on the actual buckling-driven fracture mode under consideration and it is simpler to perform than other fracture tests.

3.2.4 REVIEW CONCLUSION

Because of the scarcity of test results in the literature this research had to begin with specimen testing. This established the basic failure process and identified those aspects of the problem that needed to be modelled, while also providing insight into how they might best be modelled (i.e. which assumptions are reasonable and which are not). Sandwich beams were considered before sandwich panels so that the simpler case was well understood before approaching the more complex case.

3.3 MANUFACTURE OF TEST SPECIMENS

A total of 32 specimens were manufactured from thin laminated face sheets and Nomex honeycomb core. All specimens were manufactured according to aerospace recommended practices (SAE ARP5144 and ARP5143). The sandwich was laid-up on a platen (refer Appendix A for details), vacuum bagged to 12psi and cured at 120°C for 90 minutes per the face-sheet manufacturer's specification. The specimen configurations were designed with disbond length, face-sheet stiffness and core orientation as the variable parameters because these were considered to be the variables having the largest effect on the structural behaviour. Table 3.3.1 shows the full factorial specimen test plan, having three variables and two variations on each. This was developed with reference to Mason *et al.* (1989).

Table 3.3.1 – Experimental design (full factorial test plan with three parameters and two variations on each)

Specimen Designation	Disbond Length	Facesheet Layup	Core Orientation
25-G-R	25 mm	1581 Glass	Ribbon
25-G-T	25 mm	1581 Glass	Transverse
40-G-R	40 mm	1581 Glass	Ribbon
40-G-T	40 mm	1581 Glass	Transverse
25-GH-R	25 mm	120/1581 Hybrid	Ribbon
25-GH-T	25 mm	120/1581 Hybrid	Transverse
40-GH-R	40 mm	120/1581 Hybrid	Ribbon
40-GH-T	40 mm	120/1581 Hybrid	Transverse

This test configuration is called a full factorial because all of the possible combinations of the three variables are considered. Four repetitions were done for each configuration to obtain a statistically significant average (Figure 3.3.1). The population mean can be inferred from the sample mean, standard deviation and size by means of a two-sided T-test. The half range, quoted on the vertical axis of Figure 3.3.1, is the number of sample standard deviations either side of the sample mean within which, 95% or 98% of the time (depending on the chosen confidence range), the population mean will lie. This analysis is based on a t-distribution and is double sided (Mason *et al.* 1989). Figure 3.3.1 is a crucial element in the design of experiments and should always be used to determine an appropriate sample size.

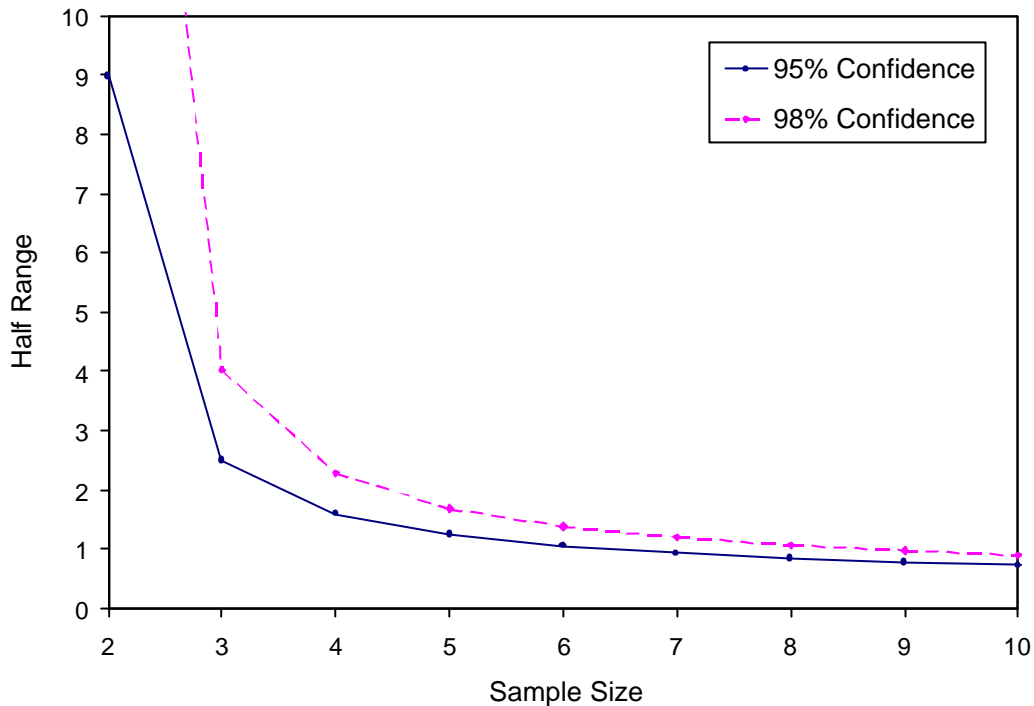


Figure 3.3.1 – Statistical confidence, expressed as a half range (defined as the number of sample standard deviations either side of the sample mean within which the population mean is expected to lie with X% confidence), for various sample sizes

A sample size of 4 (i.e. 4 repetitions of each of the 8 configurations) was chosen by considering Figure 3.3.1 along with the cost and time involved in having large sample sizes.

The specimen designation contains the size of the disbond (25mm or 40mm), the material type used (Glass or Glass Hybrid, see Figure 3.5.1) and the core orientation (Ribbon or Transverse, see Figure 3.5.3).

All specimens were nominally 60mm wide and 320mm long. Disbonds were manufactured into the specimens by inserting a strip of release film (0.026mm thick Teflon film) at the beam centre between the core and the top face-sheet (the side of the sandwich that has only the bag pressing against it, the bottom side is the tool-side and lies on the platen). It has been reported by Ural *et al.* (2003) that there is a significant difference in interfacial fracture toughness between the tool-side and bag-side. This could have been chosen as a parameter to vary in the specimen design but the core orientation (which also affects the fracture toughness) was used instead.

3.4 FOUR-POINT LOADING OF SPECIMENS

The four-point-bend test design was chosen because it applies a controlled compressive load to the disbonded face-sheet. The alternative in-plane compression loading has the potential to load the face-sheets unevenly and tends to introduce global buckling behaviour (Avery and Sankar 2000, Kim *et al.* 1993), which is not the subject of this research. The test rig shown in Figure 3.4.1 was used for all of the sandwich beam tests. Test specimen dimensions were determined in accordance with ASTM C393, which defines specimen geometry limits for flexural testing of sandwich beams.

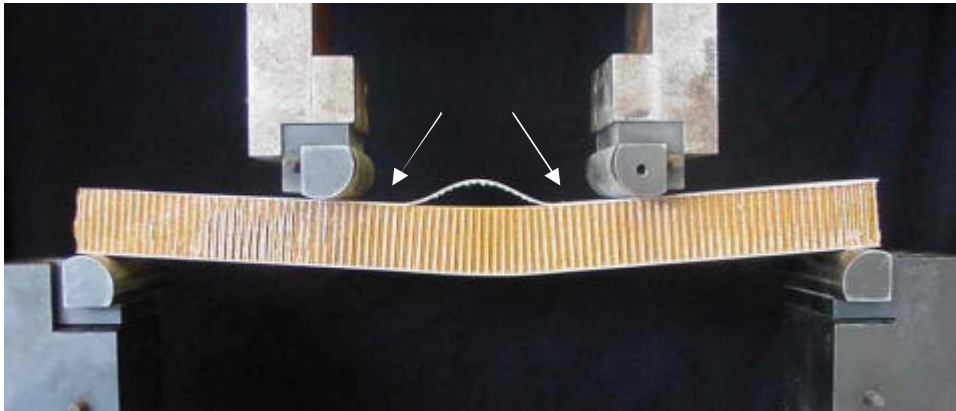


Figure 3.4.1 – Sandwich beam specimen under load in the four-point bending test rig (Arrows indicate the location of the strain gauge and acoustic emission sensor)

A 25 kN load cell and a surface strain gauge were both connected to an Instron 5500R Universal Testing Machine. The acoustic data was recorded separately and is described in the next section. Figure 3.4.2 shows the specimen geometry and the sensor arrangement, where the central load-point span was 110mm, to provide sufficient room for the sensors.

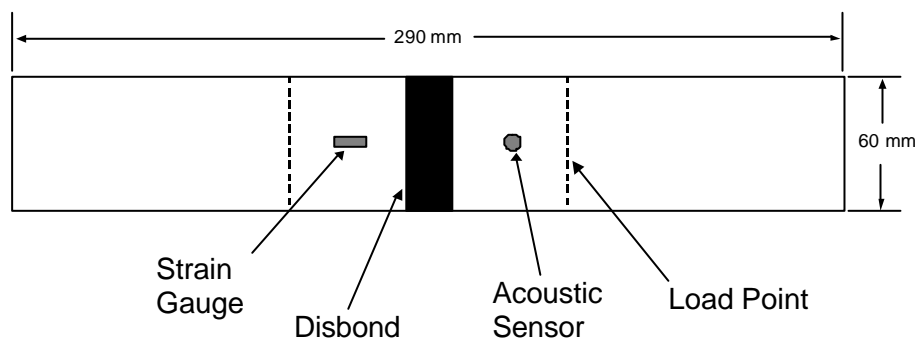


Figure 3.4.2 – Loading geometry (outer span = 290mm, inner load span = 110mm) and arrangement of the strain gauge and accelerometer on the test specimen

Loading was increased at a constant crosshead displacement rate of 4mm/min and to a final displacement of 12mm, by which time all specimens had undergone sufficient disbond growth to cause a significant reduction in structural stiffness.

3.4.1 ACOUSTIC EMISSION MEASUREMENT

To aid in the identification of disbond growth initiation, acoustic emission monitoring was used on all specimens. The acoustic sensor was an accelerometer, mounted opposite the strain gauge (Figure 3.4.1), and its signal was processed by an HP3566A spectrum analyser. The sampling frequency was chosen to be 16 kHz, which allowed frequencies up to 8 kHz to be detected while still allowing for 60 seconds of data capture. The captured frequency range of up to 8 kHz is determined from the Nyquist-Shannon sampling theorem, which states:

“When sampling a signal, the sampling frequency must be greater than twice the bandwidth of the input signal in order to be able to reconstruct the original perfectly from the sampled version.”

This sample rate proved to be sufficient to capture the frequencies associated with disbond growth.

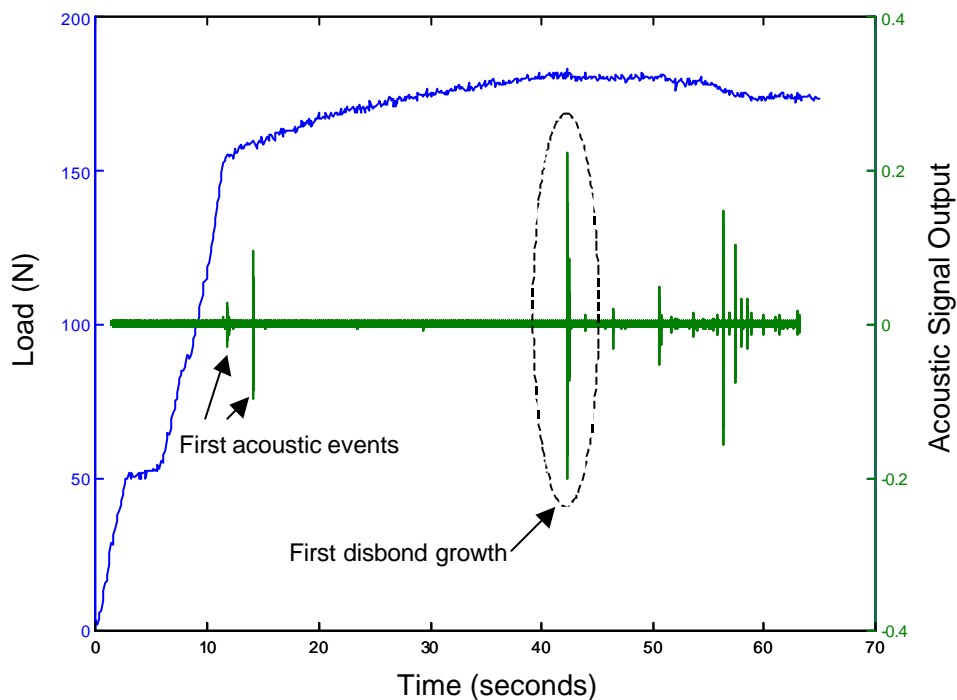


Figure 3.4.3 – Overlaid load and acoustic output profiles (used to determine when disbond growth initiated)

Figure 3.4.3 is an overlay of sample load and acoustic output profiles. It indicates how useful the acoustic output is in identifying growth events. Figure 3.4.3 also shows that there were two possible

acoustic events shortly after buckling. The first of these occurred immediately after buckling and is attributed to separation of the Teflon strip (used to create the disbond) from the core. Most of the test specimens had an acoustic event at this time. The second of these events was less frequently observed and is attributed to fracture through the small region of built-up resin at the disbond tip (i.e. fracture of the resin-rich region that forms around the end of the Teflon strip). This was not considered to be disbond growth because it is crack propagation through a different medium (i.e. not through the cellular core). Considering all of the test data with video recordings of the tests, the initiation of disbond growth was defined to occur at the first of the following events:

- The maximum load being reached
- An observable sudden load drop
- A significant acoustic event and a change in the gradient of the load profile

There were generally less than five significant acoustic events, identified by amplitudes orders of magnitude larger than the average event amplitude.

3.5 MATERIAL PROPERTIES

The sandwich configurations used in testing are typical of secondary structure on commercial aircraft (e.g. trailing edge wing flaps). The core used is a regular aramid-fibre/phenolic-resin honeycomb and the face-sheets are thin fibreglass pre-preg (fibre-weave sheets pre-impregnated with resin). The following sections detail the properties that were determined for specimen constituent materials.

3.5.1 FACE-SHEET PROPERTIES

Table 3.5.1 gives the nominal material properties as supplied by the manufacturer, Hexcel Corporation (see Appendix A for data sheet extract).

Table 3.5.1 – Manufacturer-supplied material properties

Material	Material Designation	In-Plane Moduli	Nominal Thickness
1581 lamina	1581-38"-F155	23.4 GPa	0.26 mm
120 lamina	120-38"-F155	20.7 GPa	0.12 mm

The material designations of the two face-sheets state the type of glass fibre weave, the pre-preg roll width (38") and the resin type (F155 epoxy).

The sandwich models in the following chapters require accurate laminate stiffness values in order to predict the sandwich behaviour accurately. The lamina moduli, as given in Table 3.5.1 are expected to be accurate, but the nominal thickness values need to be determined more accurately, as the laminate stiffness is proportional to the third power of the thickness. In order to treat the laminated facings as homogeneous it is necessary to determine their properties for the method of loading (bending) as accurately as possible.

Each facesheet was made up of several layers of pre-preg material (a fibre weave pre-impregnated with resin), as shown in Figure 3.5.1. The angles shown are all relative to the direction of the pre-preg roll length.

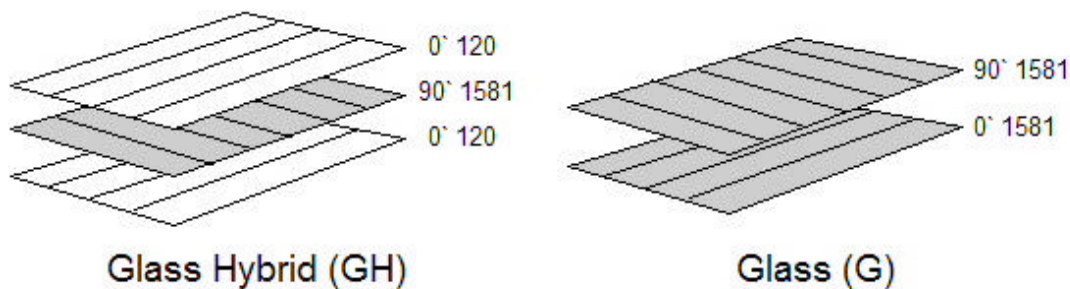


Figure 3.5.1 – Facesheet lay-up sequences and materials

3.5.1.1 EVALUATING THE FACE LAMINATE THICKNESSES

Due to the very dimpled surface of the face laminates it was not possible to measure their thicknesses accurately. Random thickness samples, taken from a single specimen, using a ball-point micrometer had a range of $\pm 20\%$ from the average, which converts to an unacceptable variation in stiffness of approximately $\pm 60\%$. Instead, the thicknesses of both face-sheet types (G and GH) were determined from a series of three-point bend tests. Ural *et al.* (2003) encountered the problem of inaccurate micrometer measurements and also used three-point bend tests to determine specimen thickness. In disbond buckling analysis the face-sheet bending stiffness is a critical parameter and in the buckling models of Chapter Four and Seven it is evaluated from the face-sheet thickness and modulus. Because the present method evaluates the thickness from the bending stiffness, this critical parameter is effectively determined directly from test.

Specimens were manufactured on a honeycomb core with release film to stop adhesion, replicating the actual conditions of the disbonded face regions in the main test specimens. Testing consisted of three sets of 12 specimens, one for the G material and two for the GH material (one set in each

orientation, to check the laminate orthotropy). Test specimens measured 13mm by 55mm and the support span was 32mm, in accordance with ASTM D790-98.

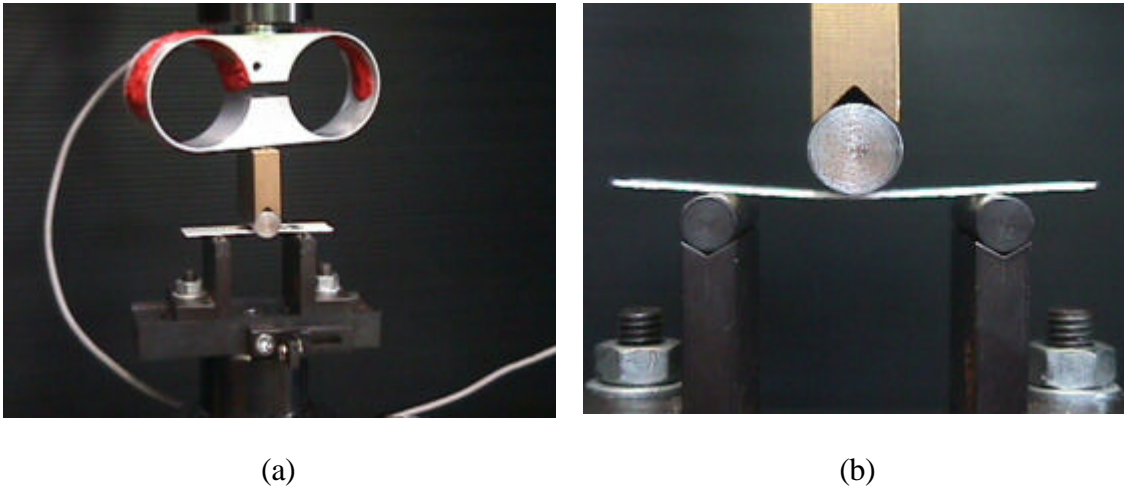


Figure 3.5.2 – The test rig used to evaluate the bending stiffness of the face laminates

The load-displacement measurements were taken between load-point displacements of 0.2mm and 0.5mm, where the load profile is linear and the displacements are small (less than the thickness of the laminates). Using the lamina moduli supplied by the manufacturer in (3.5.1) with the load-displacement relationship for a beam loaded in three-point bending (3.5.2), is sufficient to solve (iteratively for the GH laminate) for the laminate thicknesses (t_L) and moduli (E_L).

$$E_L = \frac{\sum_{m=1}^M E_m t_m}{t_L} \quad (3.5.1)$$

$$\frac{P}{\Delta_b} = \frac{4E_L t_L^3}{L^3} \quad (3.5.2)$$

The length, L , in (3.5.2) is the support span of the test specimen, 32mm. Shear deflections are assumed to be negligible in (3.5.2), so this assumption was tested. The shear factor is expressed as:

$$\frac{\Delta_s}{\Delta_b} = \frac{24D_f}{L^2 S_f} \quad (3.5.3)$$

The bending and shear stiffnesses of the face-sheet defined as:

$$D_f = \frac{E_f t_f^3}{12(1 - \nu_f^2)} \quad (3.5.4)$$

$$S_f = \frac{5}{6} A G_f$$

The shear modulus of the laminate is approximated conservatively as the shear modulus of the neat resin (1.25 GPa). The variable A is the cross-sectional area of the test specimen. These calculations showed the shear factor to be 0.85%, which validates the assumption that shear deflections are negligible.

The resulting laminate properties are given in Table 3.5.2.

Table 3.5.2 – Face laminate properties

Laminate Material	E_0^* (GPa)	E_{90} (GPa)	Thickness
G	23.40	23.40	0.478 mm
GH	22.24	23.23	0.420 mm

** For all specimens the 0° direction is aligned to the transverse core direction*

Even though the fibre weave of both laminae in the GH laminate are specified as being equal harness (i.e. the same number of fibres laying in the 0° and 90° directions), the laminate modulus in the 90° direction was found to be higher than that in the 0° direction.

Because these thickness values are used in models where the critical face-sheet deflections are due to bending, the fact that they were determined directly from bending tests gives higher confidence in the resulting bending stiffnesses (determined from the first of (3.5.4)) than if they had been determined by other means (e.g. measurement by micrometer).

3.5.2 HONEYCOMB CORE PROPERTIES

The type of core used for all of the sandwich specimens was a regular hexagonal Nomex honeycomb (HRH-78-1/8-3.0) with nominal cell size and core thickness of 3.2mm (0.125”) and 26mm (1.024”), respectively. The only core property that was varied among the test specimens was the orientation (see Figure 3.5.3) with respect to the specimen length.

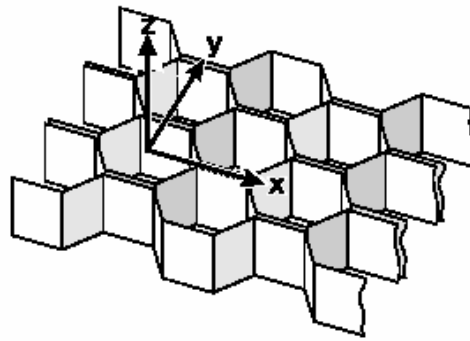


Figure 3.5.3 – Honeycomb core geometry, showing the ribbon (R) and transverse (T) directions as ‘x’ and ‘y’, respectively.

The core orientation was chosen as a variable because the interfacial fracture properties and the in-plane and shear moduli vary with the orientation of the core. The core properties in Table 3.5.3 are from testing performed by Aitken (2000).

Table 3.5.3 – Honeycomb core properties

Core Property	Value from Aitken (2000)
E_x	480 kPa
E_y	330 kPa
E_z	132 MPa
G_{xz}	41 Mpa
G_{yz}	24 Mpa
ν_{zx}	0.3
ν_{xy}	0.49
Thickness	26 mm

3.5.3 A NEW METHOD FOR DETERMINING FRACTURE TOUGHNESS OF THE FACE-CORE INTERFACE

Mode I is the primary fracture mode for buckling driven disbond growth (Whitcomb 1992). The most common test for the critical strain energy release rate (G_c) in Mode I is the double cantilever beam (DCB) test, where the face-sheet is peeled from the core with a transverse load (Ural *et al.* 2003). The test method used here is based on the same principles as the DCB test and is new in that it uses the results of four-point bend tests. Figure 3.5.4 illustrates the loading and reloading profiles of a representative sandwich specimen with a disbond.

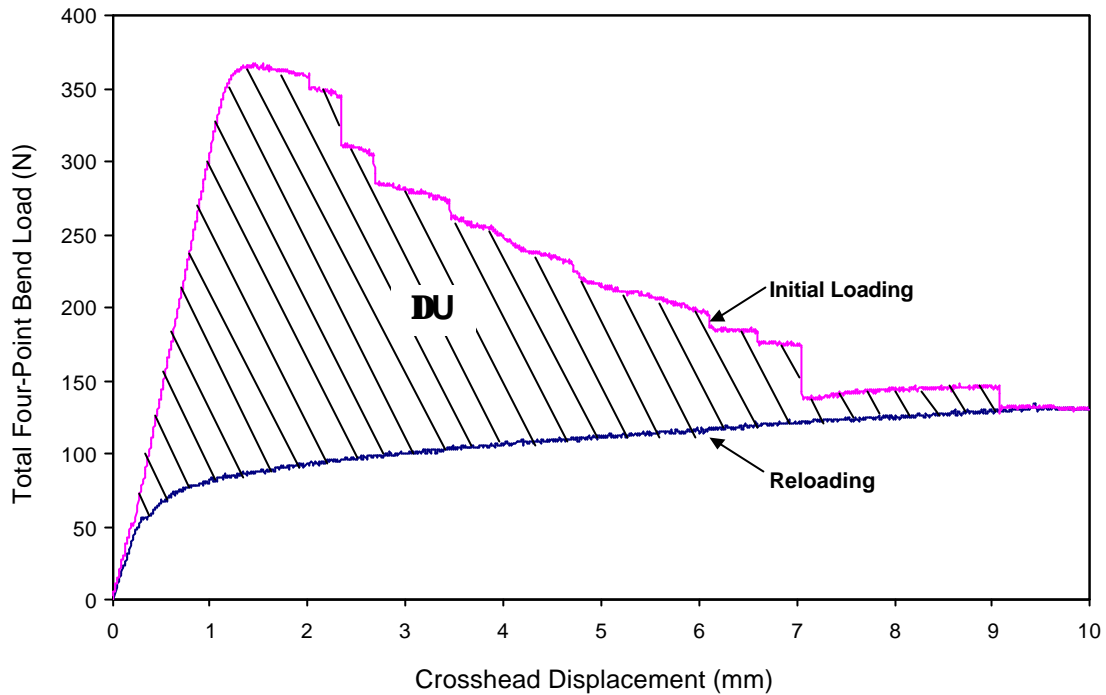


Figure 3.5.4 – Typical specimen loading and reloading profiles used to determine the critical strain energy release rate (G_c)

The area under the initial loading profile is the energy that was put into the beam during loading. The area under the unloading profile is the amount of energy that was recovered. Any difference in these energy values must be unrecoverable energy lost in the loading process. The primary assumption that is made here (as indeed is made in all fracture property test methods) is that the lost energy has gone entirely into creating the new region of disbonding (i.e. into the surface energy of the disbond growth area). This method of extracting fracture properties was proposed after the completion of testing, so the reloading profiles were used instead of the unloading profiles. Several test cases demonstrated that the unloading and reloading profiles were very similar, validating the use of the reloading profiles. The definition of G_c is given as:

$$G_c = \frac{\partial U}{\partial A} \quad (3.5.5)$$

The current method uses a discrete approximation to (3.5.5):

$$G_c = \frac{\Delta U}{\Delta A} \quad (3.5.6)$$

Using (3.5.6) it is only necessary to know the total strain energy lost during the loading process, DU , (see Figure 3.5.4) and the new surface area created by disbond growth (ΔA), in order to determine G_c . The surface area created by disbond growth was determined by measuring the disbond length

after testing for each specimen, using digital vernier callipers, subtracting the initial disbond length and multiplying this by the specimen width. The total strain energy was calculated from the loading and reloading profiles of each specimen, as described above. Thus the equation used to calculate G_c is:

$$G_c = \frac{\Delta U}{W(L_d^e - L_d^o)} \quad (3.5.7)$$

Equation (3.5.7) provides the average critical energy release rate over the entire growth process. The assumptions made in calculating the average value directly in the present method are justified by considering some of the existing methods. In DCB testing, the crack length is monitored as the test progresses in order to evaluate G_c over the entire fracture length. The final value of G_c is then determined from the average value of the results, excluding the initial values and the values for very large crack lengths. The present method may be considered as a direct measurement of the average value in which the initial values and values for large crack lengths cannot be excluded. Test results of Cantwell *et al.* (1999) and Ural *et al.* (2003) indicated that G_c is generally a weak function of disbond length (i.e. G_c remains approximately constant) and is well approximated by the average value (Figures 3.5.5 and 3.5.6). Therefore even with the initial and large crack length values included, the present method provides a comparable final result. One of the main reasons for not measuring the strain energy release rate at regular intervals in the present method is that to do so would require repeated loading and unloading in order to measure the incremental disbond growth. This would have compromised the main test results (i.e. the load-displacement profile) and possibly weakened the face-sheet with each reloading.

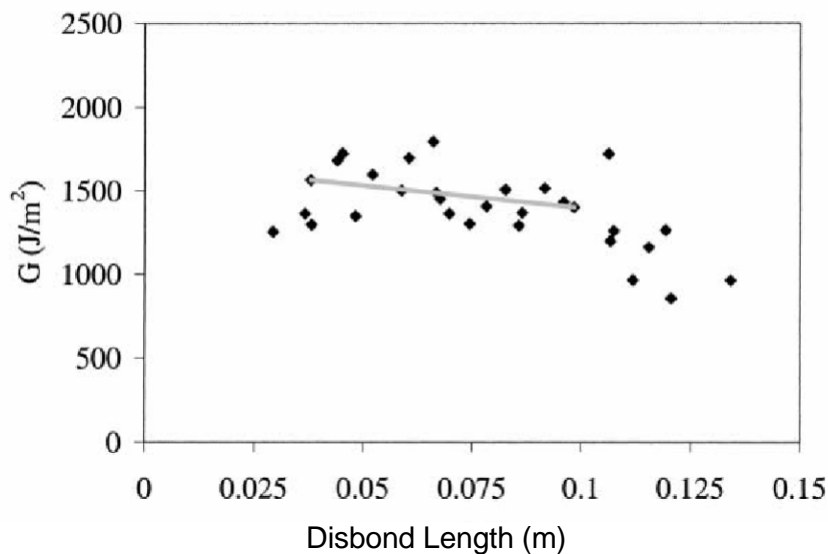


Figure 3.5.5 – Variation of G_c with disbond length (Ural *et al.* 2003)

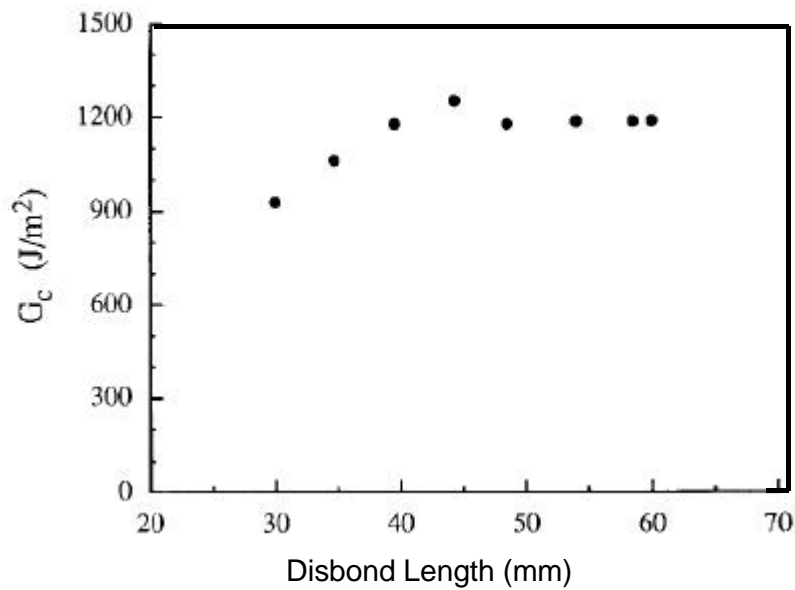


Figure 3.5.6 – Variation of G_c with disbond length (Cantwell et al. 1999)

The advantage of the present method over the DCB test is that the method of peeling the face from the core is exactly as it occurs in reality (i.e. buckling driven). However, the present method does not isolate the fracture modes and cannot exclude initial and large crack length results from the average value. With the type of complicated bi-material interface that a honeycomb-core sandwich has, it is considered particularly beneficial to use the most realistic peel method possible in determining the fracture properties. This is the justification and methodology used to arrive at the fracture properties of each specimen configuration (Table 3.5.4).

Table 3.5.4 – Fracture properties (G_c) for all specimens

Specimen Designation	G_c (J/m ²)	Confidence Range (95%)	COV
25-G-R	349	± 35.5%	22.3%
40-G-R	363	± 36.4%	22.9%
25-G-T	536	± 40.3%	16.2%
40-G-T	676	± 23.1%	14.5%
25-GH-R	240	± 12.5%	7.9%
40-GH-R	268	± 48.5%	30.6%
25-GH-T	373	± 30.0%	18.8%
40-GH-T	376	± 25.0%	15.7%

Table 3.5.4 shows that the fracture properties calculated using the new test method are consistent (given the high degree of scatter associated with fracture properties). The results presented are mean

values of a sample size of four. Scatter is presented in two forms for comparison with existing results. The confidence interval is a statistically based method that accounts for sample size, while the Coefficient of Variance (COV) is a more commonly stated scatter measure. Both of these scatter measures are defined in Appendix G.

Several trends are observed in the fracture results in Table 3.5.4. Firstly, the fracture toughness is higher when the disbond front is moving in the transverse core direction, which is consistent with the results of Avery and Sankar (2000), who suggest that this may be due to the fact that in the transverse direction, growth may be accompanied by delamination of the cell double-walls. The increased flexibility of the cell walls in the transverse direction may also play a part in the higher fracture toughness. However, these explanations are speculation and more detailed analysis was not carried out here.

The thicker, higher modulus G-type face-sheet has the higher fracture toughness. Avery and Sankar (2000) also observed this and suggested that it is likely to be due to the extra resin available to the face-sheet to core bond from the thicker face-sheet.

The average COV value for the fracture results in Table 3.5.4 is 19%. This level of consistency is similar (and better, in some cases) to that obtained from standard fracture tests, such as the TPBS (Cantwell *et al.* 1999), DCB (Ural *et al.* 2003), and ENF tests (Carlsson *et al.* 1991). In the DCB testing of Ural *et al.* (2003) the fracture parameters were quoted with an average COV of $\pm 19\%$, which corresponds exactly to the level of scatter observed in the present results. Cantwell *et al.* (1999) presented fracture results without a standard deviation, however the range (i.e. upper limit minus lower limit) was presented and averages to approximately $\pm 22\%$ from the mean value, which is again the same order of magnitude as the present method.

All of the properties based on the specimens with 40mm disbonds are higher than those for the 25mm disbond specimens (particularly for the G-T configuration), suggesting that fracture resistance increases as the disbond length grows. This represents the variation of G_c with disbond length (refer Figures 3.5.5 and 3.5.6) and it is also likely to be a consequence of other permanent deformation modes that occur during large deflections (e.g. face-sheet matrix cracking). This tends to result in overestimates of G_c towards the end of each test because the method assumes that all dissipated energy goes towards disbond growth. Considering this, the more accurate of all of the fracture values in Table 3.5.4 are those from the 25mm disbond tests, which are taken as the final values (Table 3.5.5).

Table 3.5.5 – Fracture properties for each combination of face material and core orientation

Facing – Core Orientation	G_c
G – T	536 J/m ²
G – R	349 J/m ²
GH – T	373 J/m ²
GH – R	240 J/m ²

3.5.3.1 SUMMARY OF THE DEVELOPED METHOD

The method described above was developed because it is simpler to perform than other fracture tests. This is due to the fact that four-point bend testing is relatively simple, compared with DCB testing, for example. For a DCB test the disbonded face-sheet needs to be mounted with a hinge assembly that can be gripped in a tensile loading arrangement (Ural *et al.* 2003) and if the face-sheet is not sufficiently thick then it needs to be reinforced to avoid excessive deformation and matrix or fibre fracture. The DCB specimen also requires stabilisation so that the specimen remains perpendicular to the loading direction (Ural *et al.* 2003). The other advantage of the present method is that the method of peel is buckling driven, which is representative of the actual disbond growth mechanism for disbonded beams and panels. Finally, it has been shown that the results obtained using the current method are consistent and have a similar level of scatter to the DCB, TPBS and ENF fracture tests.

3.5.3.2 DISCUSSION OF RESULTS

For both face-sheet types G_c is approximately 55% higher in the transverse direction than the ribbon direction. Avery and Sankar (2000) found this difference to be approximately 25% (averaged over a larger range of test configurations), with a range of approximately 0% to 40%.

Another point of interest is that, for the face-sheet epoxy resin, which forms fillets at the interface of the face-sheet and the core cell walls, G_c is 730 J/m², which is generally about twice the sandwich interface values in Table 3.5.5. A similar ratio of neat resin to honeycomb sandwich fracture properties can be seen in the results of Ural *et al.* (2003).

A final point to note is that in all cases the disbond propagated primarily through the core, just below the resin-rich layer of core where the resin fillets occur (see Okada and Kortschot (2002) for more detail on the resin fillet in honeycomb sandwich). Figure 3.5.7 shows the underside of a disbonded face-sheet where the resin-rich layer of core is still bonded to the regions where disbond growth occurred.

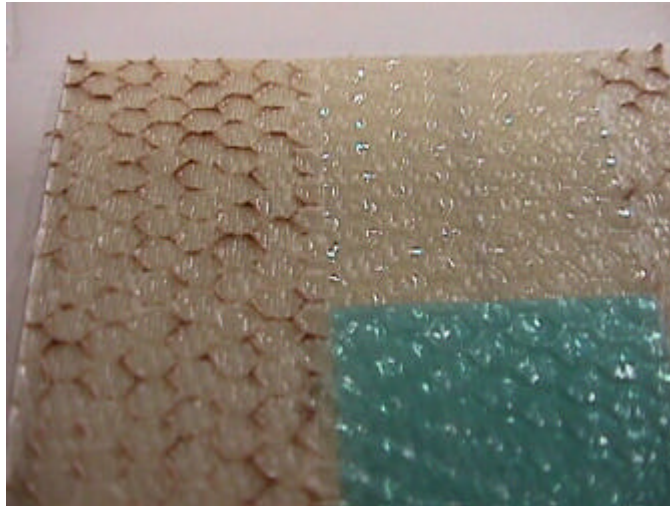


Figure 3.5.7 – Post-testing photograph of the underside of a disbonded face-sheet (with the Teflon release film used to create the disbond shown also)

Cantwell and Davies (1994) performed fracture peel tests of honeycomb core sandwich and also observed this, noting:

“...the crack had not propagated at the skin-core interface, but instead at several tenths of a millimetre away from it within the honeycomb core...”

This result shows that disbond growth resistance is primarily determined by the toughness of the core.

3.6 CONCLUSIONS

The main test results will be presented in the following chapters as comparison to the predictive models of buckling, post-buckling and growth initiation, however there are some general results that can be presented on their own. Firstly, the failure process of sandwich beams with thin faces and containing disbonds has been clearly identified as:

1. Disbond buckling
2. Reduced stiffness post-buckling
3. Initiation of stable disbond growth
4. Gross loss of structural stiffness as the disbond increases in size

Some further general conclusions can be drawn from the four-point loading results:

- There is generally very little load carrying capacity remaining after buckling, so the buckling load is a good approximation of the failure load
- The smallest observed reduction in load carrying capacity (for the 25mm disbond) was 87% based on an undamaged wrinkling stress of 167 MPa Aitken (2000). This indicates criticality of a through-width disbond
- Growth occurred in small regular steps and it was observed that there was a maximum disbond length (at which increased load would not result in disbond growth) which was approximately the same for all specimens (~ 70mm). This is in agreement with the findings of Kardomateas (1990) on post-buckling of delaminated laminate strips.

Some general conclusions can be drawn from the fracture property test results

- The new test method provides very consistent fracture properties, showing all of the general trends identified in DCB testing by Avery and Sankar (2002)
- The fracture toughness is 55% higher in the core transverse direction than the ribbon direction. This is attributed to additional flexibility and delamination of the double walls in the transverse direction, although this was not verified.
- Disbond growth proceeds through the honeycomb core, just below the resin-rich layer of core at the face-core interface. The fracture toughness of the honeycomb core is therefore the weakest link during fracture.

There are two critical points during the failure process that should be modelled to present an overall prediction of failure. Firstly, the buckling load has been identified as a reasonable approximation to

the failure load. The next chapter develops a model to predict buckling and develop a better understanding of the effect of the sandwich beam properties. Secondly, it has been shown that disbond growth dominates the post-buckling behaviour of a sandwich beam. Chapter Five develops a non-linear post-buckling model to investigate disbond growth.

CHAPTER FOUR

Modelling Disbond Buckling in Sandwich Beams

4.1 INTRODUCTION

Chapter Three illustrated that buckling is a critical step in the failure process of a disbonded sandwich beam. It is now necessary to predict the buckling load. Not only will this provide an estimate of the failure load but it is also a critical step in the failure process that needs to be well understood before attempting to model disbond growth.

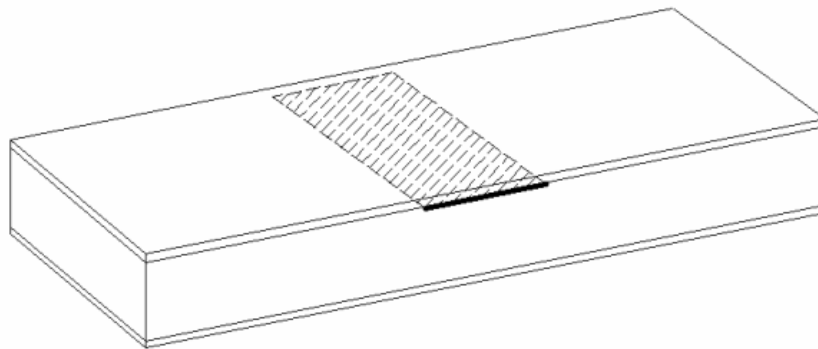


Figure 4.1.1 – Through-width disbond in a sandwich beam

One of the simplest methods of modelling a sandwich beam with a disbond is to treat the face-sheet as an Euler beam supported by a Winkler (discrete spring) foundation. This model is referred to herein as a Winkler beam model. This modelling method assumes that the core can be represented by a series of independent linear springs of constant stiffness. The buckling load of a Winkler beam with a gap in the foundation (representing the disbond) was presented by Hetenyi (1946) as:

$$f_1 = \frac{\mathbf{p}^2 f_2}{1 + \cos\left(\frac{\mathbf{p}}{2}\sqrt{f_2}\right)} \quad (4.1.1)$$

The functions f_1 and f_2 are defined as:

$$f_1 = \sqrt{\frac{kL_d^4}{D_f}} \quad (4.1.2)$$

$$f_2 = \frac{P_{cr}L_d^2}{\mathbf{p}^2 D_f} \quad (4.1.3)$$

This equation can be solved iteratively to find the buckling load for any size disbond in a Winkler beam.

In more recent years authors have solved the same problem using various numerical methods. Vizzini and Lagace (1987) derived the governing equation for a Winkler beam with a disbond and used the Raleigh-Ritz method to solve for the buckling load. Sleight and Wang (1995) compared three methods of solving for the buckling load. Having derived governing equations from an energy analysis, the Raleigh-Ritz method (as used by Vizzini and Lagace (1987)) was compared to a finite difference method. Both of these were then compared to two finite element models, one with core shear stiffness and the other without. The results were the same for the Raleigh-Ritz method, finite difference method and finite element model (without core shear stiffness). The finite element model incorporating core shear resistance and in-plane core modulus yielded buckling loads approximately 20% higher than the other models.

The foundation modulus typically used in a Winkler beam model (as used by all the authors mentioned thus far) is defined for symmetric wrinkling as:

$$k = \frac{E_c}{t_c} \quad (4.1.4)$$

Niu and Talreja (1999) made a modification to the foundation stiffness of the Winkler beam model to incorporate the conditions of plane stress and plane strain within the foundation/core assuming an isotropic core material. They concluded that for an isotropic core in conditions of plane stress (4.1.5) should be used and (4.1.6) should be used in plane strain conditions.

$$k = \frac{E_c}{(1-\mathbf{n}_c^2)t} \quad (4.1.5)$$

$$k = \frac{(1-\mathbf{n}_c)E_c}{(1-2\mathbf{n}_c)(1+\mathbf{n}_c)t} \quad (4.1.6)$$

Niu and Talreja (1999) then found that using (4.1.6) instead of (4.1.4) in the Winkler beam models of Sleight and Wang (1995) increased the buckling loads by approximately 20%, making them

equal to the results of the finite element model with isotropic core (having core shear stiffness). The foundation stiffness values in (4.1.5) and (4.1.6) are useful for cores that may be treated as isotropic (e.g. PVC foam) but they are not applicable to highly orthotropic cores such as honeycomb (Niu and Talreja 1999).

Niu and Talreja (1999) also proposed that the natural wavelength and wrinkling load of a perfect sandwich beam are characteristic properties of the sandwich that can be used to normalise the disbond length and buckling load, respectively, of a disbonded beam. They proposed a characteristic curve for buckling of a disbonded sandwich beam by plotting the load normalised to the wrinkling load (buckling load of a perfectly bonded sandwich beam, P_{cr}) versus the disbond length normalised to the natural wavelength of the sandwich (the wrinkling wavelength, L_{cr}). They had thus identified the wrinkling load and wavelength as characteristic parameters in the disbond buckling problem. They made no attempt to compare the model results to specimen test results, so the accuracy of the models in practice was not determined.

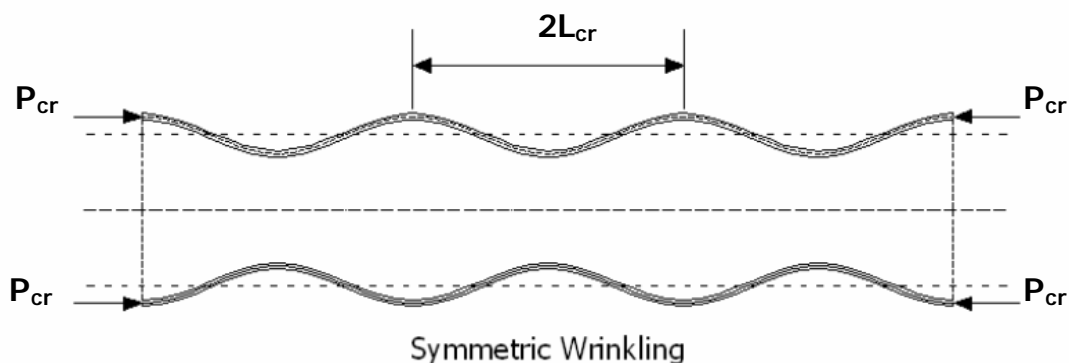


Figure 4.1.2 – Illustration of the wrinkling wavelength and load for a sandwich beam

Cheng *et al.* (1997) also extended on the Winkler beam model by incorporating shear traction at the face-core interface. The governing equations of a Winkler beam were derived to include a fictitious force system that cancels the core support (both transverse and shear) in the disbond region and solved using a Fourier series approximation. The model showed that the effect of core shear stiffness on the buckling load is negligible (increasing by only 8% for a 125-fold increase in the shear stiffness). Ultimately this model only extended on the simple Winkler beam model by including core shear stiffness, which turned out to have negligible effect on the buckling load.

Moving away from the Winkler beam model of sandwich beams, the next group of solutions to the buckling problem considered the interaction of the global and local buckling modes. They all (Gaudenzi *et al.* 1998, Hwu and Hu 1992, Yin *et al.* 1986, Somers *et al.* 1991) model the entire

beam (both faces and the core) with the assumption that the core has infinite out-of-plane stiffness. This assumption provides less accurate local buckling loads but does simplify the analysis of global beam behaviour.

Hwu and Hu (1992) presented elastic buckling and post-buckling analyses of an axially loaded sandwich beam with a through-the-width disbond. The elastic analysis provides an implicit solution for the buckling load and an explicit expression for the energy release rate of the buckled sandwich. They derived the governing equations for a laminated beam using Lagrangian strains (small displacements and moderate rotations) and then applied the equations to pre-defined sections of the disbonded sandwich. The sections were; (1) the fully bonded regions either side of the disbond; (2) the disbonded face-sheet; (3) the core and face-sheet below the disbonded face (Figure 2.1.5). Compatibility was enforced between sections and the governing beam equations were derived, from which the global buckling load of the sandwich was derived.

Avery and Sankar (2000) compared the buckling loads from the model of Hwu and Hu (1992) with failure loads of compression loaded sandwich test specimens with central disbonds. They concluded:

‘In general there is little correlation between the analytical buckling loads and experimental failure loads. Thus the linear buckling load calculated in this way cannot be considered as a conservative estimate of the compressive strength of the sandwich beam.’

Avery and Sankar (2000) did not isolate the load at which buckling occurred and so the model of Hwu and Hu (1992), which predicts buckling, could not be validated from these results.

Yin *et al.* (1986) determined the ultimate axial load carrying capacity of a disbonded beam using a similar method of analysis to Hwu and Hu (1992).

Somers *et al.* (1991) utilised the same sectioning method as Hwu and Hu (1992), again refer to Figure 2.1.5. They developed the stability equation for a general laminate and then used a perturbation method to solve for the general displacement function of each section of the sandwich. Compatibility and equilibrium conditions were then applied and the equations were formed into a matrix. The buckling load was determined by the lowest eigenvalue of this matrix. They also considered post-buckling and performed a growth analysis utilising the J-integral method.

Gaudenzi *et al.* (1998) extended on the model of Hwu and Hu (1992) by using a finite element formulation and including contact effects between the disbonded face and the core.

Frostig and Sokolinsky (1999) added to these models by including a transversely flexible core in a complete sandwich beam model (i.e. including both face-sheets). They argued that the Winkler beam model, which decouples the face-sheets to consider local buckling behaviour, is inaccurate when considering a sandwich beam in pure compression. They modelled the core as a two-dimensional continuum with shear traction at the face-core interface and ultimately showed that the complex buckling modes in a pure compression sandwich beam require this type of model. A polynomial approximation was used for the face-sheet displacements. Details of the model are in Frostig (1992). The model developed by Frostig and Sokolinsky (1999) does not, however, apply to sandwich beams in bending, in which case the face-sheets may be decoupled because there is no possibility of global beam buckling. However, for beams with through-width disbonds, loaded in pure compression this is an accurate modelling philosophy as it includes the complete set of buckling modes.

The above review summarises the complete body of work to date regarding the buckling of disbanded sandwich beams. The conclusion drawn here is that the modelling of Frostig and Sokolinsky (1999) is likely to be the best model to use in a pure compression load case. In the case of a beam in bending there is no global buckling and so it would be more accurate to model the local buckling behaviour alone. Therefore the approach used in this research is a Winkler beam model with a refined foundation stiffness that incorporates the effects of orthotropic core material properties.

4.2 REFINED WINKLER BEAM MODEL

The first step in the analysis of the failure process of a disbonded sandwich beam under compression is the prediction of the buckling load. This is done with an eigenvalue analysis of the governing linear equation of a Winkler beam model (an Euler beam on a Winkler foundation), where symmetry is assumed with respect to the centre of the beam. The main addition to the present buckling model over previous Winkler beam models (Niu and Talreja 1999, Sleight and Wang 1995, Vizzini and Lagace 1987), is a more accurate definition of the foundation stiffness.

4.2.1 ANALYSIS PROCEDURE

A sandwich beam was analysed with a disbond located in the centre of the beam.

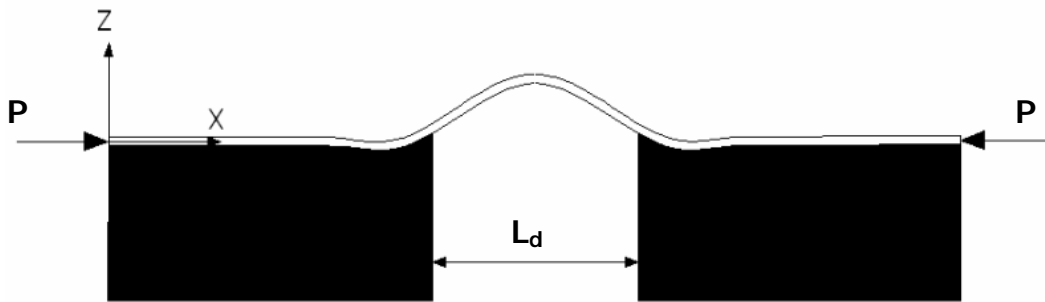


Figure 4.2.1 – A compressively loaded Winkler beam with a central disbond region

The governing equation for an Euler beam under compressive loading on a Winkler foundation is:

$$D_f \frac{d^4 w}{dx^4} + P \frac{d^2 w}{dx^2} + s_z = 0 \quad (4.2.1)$$

The stress is expressed as:

$$s_z = kw \quad (4.2.2)$$

Equation (4.2.1) was discretised to the following form using a central finite differencing scheme:

$$D_f \left(\frac{w_{n+2} - 4w_{n+1} + 6w_n - 4w_{n-1} + w_{n-2}}{\Delta_x^4} \right) + P \left(\frac{w_{n+1} - 2w_n + w_{n-1}}{\Delta_x^2} \right) + kS_n w_n = 0 \quad (4.2.3)$$

In matrix notation this can be represented by:

$$[A]w - P[C]w = 0 \quad (4.2.4)$$

Matrix $[A]$ contains the coefficients in (4.2.3) that do not involve P . Matrix $[C]$ contains the remaining coefficients, with P taken out as a common factor. The disbond is created by reducing the foundation stiffness to zero at every relevant node using the discrete function S_n .

$$S_n = \begin{cases} 0 & \text{in the disbond region} \\ 0.5 & \text{at the disbond edge} \\ 1 & \text{in the bonded region} \end{cases} \quad (4.2.5)$$

The value of 0.5 is used at the disbond edge because at this point only half of the area over which the nodal displacement is averaged has core support. Rewriting (4.2.3) in the familiar eigenvalue form:

$$\left| [C]^{-1}[A] - P[I] \right|_w = 0 \quad (4.2.6)$$

The lowest eigenvalue of the matrix $[C]^{-1}[A]$ is the buckling load. This eigenvalue problem was solved using Arnoldi iteration with implicit restarts, via the function *eigs* in Matlab (version 5.3).

4.2.2 THE MODIFIED FOUNDATION STIFFNESS

The Winkler beam model requires a one-dimensional core stiffness value to approximate a two-dimensional core, as shown in Figure 4.2.2.

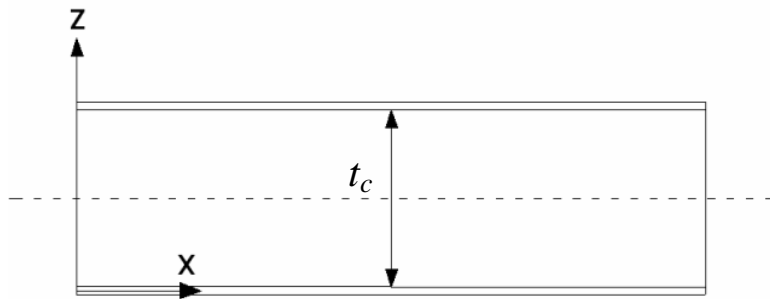


Figure 4.2.2 – Definition of deformed sandwich shape used by previous authors

Vizzini and Lagace (1987), Sleight and Wang (1995) and Cheng *et al.* (1997) all assumed:

$$\mathbf{s}_z = kw_f \quad (4.2.7)$$

The core stress is defined as:

$$\mathbf{s}_z = E_z^c \frac{\partial w_c}{\partial z} \quad (4.2.8)$$

Assuming the core displacement function to decay linearly from the face-sheet displacement, at the face-core interface, to zero at the opposite face, it is defined as:

$$w_c = \frac{w_f}{t_c} z \quad (4.2.9)$$

Differentiating (4.2.9) with respect to z and combining with (4.2.8) and (4.2.7) yields the effective core stiffness term:

$$k = \frac{E_z^c}{t_c} \quad (4.2.10)$$

This definition satisfies two-dimensional equilibrium only when the assumption of a linear core displacement field is satisfied (i.e. for a constant strain through the depth of the core). When the core displacement function is other than (4.2.9), e.g. when there is shear stress in the core, then (4.2.10) will underestimate the core stiffness.

Horrigan (2005) extended on the work of Vonach and Rammerstorfer (2000), developing a foundation stiffness term that accounts for the effects of the in-plane and shear moduli and includes an in-plane strain term at the face-core interface.

The governing equation for a two-dimensional orthotropic material is:

$$\left(\frac{1}{J_z} \right) \frac{\partial^4 \mathbf{f}}{\partial x^4} + \left(\frac{2}{J_{xz}} \right) \frac{\partial^4 \mathbf{f}}{\partial x^2 \partial z^2} + \left(\frac{1}{J_x} \right) \frac{\partial^4 \mathbf{f}}{\partial z^4} = 0 \quad (4.2.11)$$

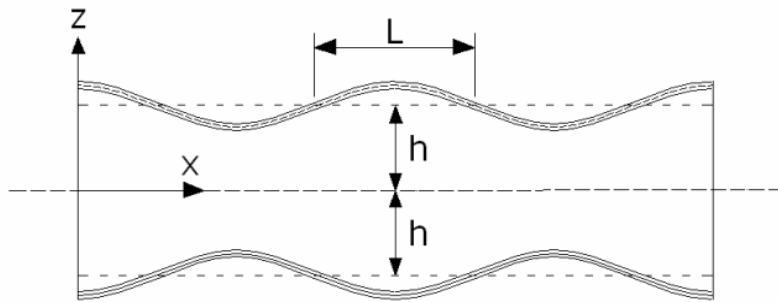


Figure 4.2.3 – Deformed shape and axes of refined core stiffness solution

Both Horrigan (2005) and Vonach and Rammerstorfer (2000) assume plane stress conditions. The following expressions were derived from the general elasticity equations with the assumption of plane strain and they are more appropriate when the face-sheet width is much larger than its thickness (see Appendix E for derivation):

$$J_z = \frac{E_z^c}{1 - \mathbf{n}_{yz}^c \mathbf{n}_{zy}^c} \quad J_x = \frac{E_x^c}{1 - \mathbf{n}_{yx}^c \mathbf{n}_{xy}^c} \quad J_{xz} = \frac{2E_x^c G_{xz}^c}{E_x^c - 4\mathbf{n}_{xz}^c G_{xz}^c} \quad (4.2.12)$$

Vonach and Rammerstorfer (2000) proposed a general stress function in the core region of the form:

$$f(x, z) = C_{amp} \left(\frac{L}{p} \right)^2 \cos \frac{px}{L} [C_1 e^{I_1 z} + C_2 e^{-I_1 z} + C_3 e^{I_2 z} + C_4 e^{-I_2 z}] \quad (4.2.13)$$

This is based on an assumed face-sheet displacement function defined as:

$$w_f(x) = C_{amp} \cos \frac{px}{L} \quad (4.2.14)$$

The core stresses in both the x and z directions are determined from (4.2.13). The core displacement functions are evaluated using Hooke's Law:

$$\begin{aligned} E_z^c \frac{\partial w_c}{\partial z} &= \mathbf{s}_z^c - \mathbf{n}_{zx}^c \mathbf{s}_x^c \\ E_x^c \frac{\partial u_c}{\partial x} &= \mathbf{s}_x^c - \mathbf{n}_{xz}^c \mathbf{s}_z^c \end{aligned} \quad (4.2.15)$$

Enforcing the boundary conditions that the core and face-sheet displacements are equal at the face-core interfaces, and assuming symmetrical face-sheet displacements about the x -axis, (Figure 4.2.3) yields four equations to solve simultaneously for the four constants, C_1 , C_2 , C_3 and C_4 . The constants I_1 and I_2 are defined by Vonach and Rammerstorfer (2000) and are functions of core moduli and face-sheet wavelength. Once the constants are known, the z -direction core stress is determined as:

$$\mathbf{s}_z^c = -C_{amp} \cos \frac{px}{L} [C_1 e^{I_1 h} + C_2 e^{-I_1 h} + C_3 e^{I_2 h} + C_4 e^{-I_2 h}] \quad (4.2.16)$$

Recognising that (4.2.16) is of the form:

$$\mathbf{s}_z^c = k w_f \quad (4.2.17)$$

A refined expression for the effective, one-dimensional core stiffness is obtained:

$$k = -C_1 e^{I_1 t_c} - C_2 e^{-I_1 t_c} - C_3 e^{I_2 t_c} - C_4 e^{-I_2 t_c} \quad (4.2.18)$$

Equation (4.2.18) was derived with the assumption that face-sheet displacements are symmetrical about the centreline of the core (Figure 4.2.3). However, the present Winkler beam model is of a beam in bending, in which the bottom face-sheet is in tension with a displacement function of

negligible amplitude (global bending effects are ignored). To approximate this situation based on the result for symmetrical wrinkling, the thickness variable h (see Figure 4.2.3) was defined as being equal to the total core thickness, t_c . This method approximately defines the beam bending case (in which the top face-sheet has a sinusoidal displacement and the bottom face-sheet displacement is zero) because the displacement of the core mid-plane is zero. Therefore, single-sided face-sheet deformation, as occurs for a disbonded sandwich beam in bending was incorporated approximately by defining $h = t_c$ in (4.2.18). To accurately model the stress state in the core for a beam in bending would require more detailed analysis of the boundary conditions at the bottom face-sheet.

The present solution method was developed by Horrigan (2005) to model wrinkling of perfectly bonded sandwich beams. The displacement function assumed in (4.2.14) is accurate for this scenario when L is equal to the wrinkling wavelength L_{cr} . In the case of buckling of a disbonded sandwich beam, the displacement function differs to this definition (see Figure 4.2.1), so the refined foundation stiffness in (4.2.18) is an approximation. However, the wrinkling wavelength, L_{cr} , is a characteristic length in the disbond buckling problem (Niu and Talreja 1999) so it is reasonable to maintain the assumption that L is equal to L_{cr} . The results of the present buckling model were examined to find that the face-sheet displacement in the core region has a wavelength approximately equal to the wrinkling wavelength. The wrinkling wavelength, L_{cr} , is defined as:

$$L_{cr} = \mathbf{p}^4 \sqrt{\frac{D_f}{k}} \quad (4.2.19)$$

The refined foundation stiffness incorporates all of the orthotropic core properties, while the face-sheet is assumed to be isotropic. The above model derivation has been coded using Matlab (version 5.3) to find the first mode of buckling and the corresponding lowest buckling load. The results of the model are presented in the next section by first completing a non-dimensional analysis and regressing model data to the resulting expression.

4.3 RESULTS AND DISCUSSION

Before presenting the comparison of model results with the experimental results of Chapter Three, a non-dimensional analysis of the problem is presented. The non-dimensional parameters are then regressed to a range of results from the buckling model. This approach provides a method of expressing the model results as a single closed form expression. It also provides insight into the nature of the problem by determining some of the characteristic, non-dimensional problem parameters.

4.3.1 NON-DIMENSIONAL ANALYSIS

Further insight into the nature of the problem was gained by completing a non-dimensional analysis of the problem variables (refer Appendix B for derivation):

$$\Pi_1 = \frac{PL_d^2}{p^2 D_f}, \quad \Pi_2 = \frac{t_c}{t_f}, \quad \Pi_3 = \frac{J_x L_d^3}{D_f}, \quad \Pi_4 = \frac{J_z L_d^3}{D_f}, \quad \Pi_5 = \frac{J_{xz} L_d^3}{D_f} \quad (4.3.1)$$

The Buckingham Π -theorem (White 1994) states that the relationship between the non-dimensional parameters can be expressed as:

$$\Pi_1 = f(\Pi_2, \Pi_3, \Pi_4, \Pi_5) \quad (4.3.2)$$

Using a Padé approximation for Π_2 the assumed functional form is:

$$\Pi_1 = C \left(\frac{c_1}{\Pi_2^3} + \frac{c_2}{\Pi_2^2} + \frac{c_3}{\Pi_2} + c_4 \right) \Pi_3^{x_2} \Pi_4^{x_3} \Pi_5^{x_4} \quad (4.3.3)$$

The constants in (4.3.3) were determined by regression to the buckling model. The model data used for the regression was obtained by independently varying each non-dimensional parameter over a range of 10 values. A least-squares power curve fit provided the three powers (with an R^2 error measure of 0.93) and the constant, C , (which turned out to be unity) in (4.3.3). The variable Π_2 did not fit a simple power law so a Padé approximation was used, with an R^2 value of 0.94. A Padé approximation is an inverse polynomial function. After regression to the model data (4.3.3) becomes:

$$\Pi_1 = \left(1 - \frac{5.82}{\Pi_2^3} + \frac{4.09}{\Pi_2^2} - \frac{0.37}{\Pi_2} \right) \Pi_3^{0.0175} \Pi_4^{0.0876} \Pi_5^{0.0175} \quad (4.3.4)$$

The functional relationship between Π_1 and Π_2 is shown in Figure 4.3.1, holding Π_3 , Π_4 and Π_5 constant, and indicates that there is a value of core thickness at which the buckling load is minimum. For multiple configurations this core thickness was found to be approximately equal to the natural half-wavelength of the fully bonded sandwich face. In Figure 4.3.1 the minimum occurs at 93% of the natural half-wavelength, L_{cr} . A more detailed investigation into the foundation stiffness expression is required to explain why the function minimum occurs where it does and this is left for future research.

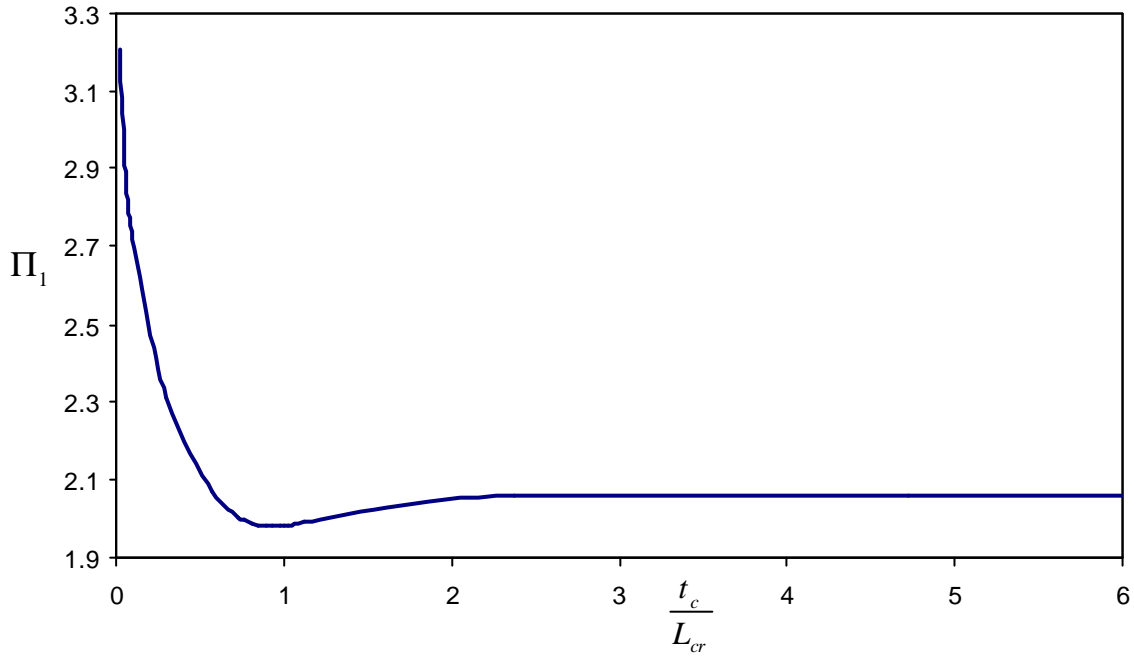


Figure 4.3.1 – Plot of Π_1 versus core thickness normalised with respect to the natural half-wavelength of the face-sheet

It is interesting to observe that above the critical core thickness the buckling load is practically independent of core thickness (The difference between $\Pi_1(1)$ and $\Pi_1(10)$ is less than 3%) and the functional relationship is reasonably replaced by a constant. Under these conditions (4.3.4) becomes:

$$\Pi_1 = \Pi_3^{0.0175} \Pi_4^{0.0876} \Pi_5^{0.0175} \quad (t_c \geq L_{cr}) \quad (4.3.5)$$

Expanding the right-hand side parameters and grouping terms:

$$\frac{PL_d^2}{\mathbf{p}^2 D_f} = \left(J_z \sqrt[3]{J_x J_{xz}} \right)^{0.0876} \left(\frac{L_d^3}{D_f} \right)^{0.1226} \quad (t_c \geq L_{cr}) \quad (4.3.6)$$

To obtain an expression for the buckling load this can be rearranged to the following form

$$P = \left(J_z \sqrt[5]{J_x J_{xz}} \right)^{0.0876} \frac{\mathbf{p}^2 D_f^{0.8774}}{L_d^{1.6322}} \quad (t_c \geq L_{cr}) \quad (4.3.7)$$

4.3.1.1 COMPARISON WITH THE EULER BUCKLING EXPRESSION

The general expression for the Euler buckling load of a beam of length L_d is

$$P_{cr} = C_E \frac{\mathbf{p}^2 D_f}{L_d^2} \quad (4.3.8)$$

The right-hand side of (4.3.6) can be defined as C_E in (4.3.8). It is now apparent that C_E is a function depending on the sandwich configuration. This function can be most clearly expressed through a non-dimensional analysis using the foundation stiffness, k , as a lumped parameter including all of the core stiffness terms. This provides the following non-dimensional parameter to replace Π_2 , Π_3 , Π_4 and Π_5

$$\Pi_k = \frac{L_d}{\mathbf{p}} \sqrt[4]{\frac{k}{D}} = \frac{L_d}{L_{cr}} \quad (4.3.9)$$

Refer to Appendix B for derivation of this parameter.

Vizzini and Lagace (1987) presented a similar model with a scaled version of (4.3.9) as a non-dimensional parameter, however they did not present the correlation for the natural wrinkling wavelength. As in the previous case, the Buckingham Π -theorem defines the relationship between the two non-dimensional parameters Π_1 and Π_k . When expanded, this function is:

$$\frac{PL_d^2}{\mathbf{p}^2 D_f} = f\left(\frac{L_d}{L_{cr}}\right) = C_E \quad (4.3.10)$$

The following Padé approximation for f was regressed to the model data, with an R^2 of 1.00, and is valid for $L_d > L_{cr}$

$$C_E = 4 - \frac{6.88}{\Pi_k} + \frac{6.57}{\Pi_k^2} - \frac{2.68}{\Pi_k^3} \quad (4.3.11)$$

To fit the curve for all L_d would require a considerably more complex functional approximation and wouldn't add much to the practical usefulness of (4.3.11), given that $L_d > L_{cr}$ in most practical disbond situations. Niu and Talreja (1999) presented what they called a master curve which shows this function accurately for values of $L_d < L_{cr}$ by plotting the load normalised to the wrinkling load of a fully-bonded beam. However, the master curve of Niu and Talreja (1999) does not illustrate the

buckling loads for large L_d as usefully as Figure 4.3.2. Note that a linear relationship is assumed for disbond lengths smaller than L_{cr} .

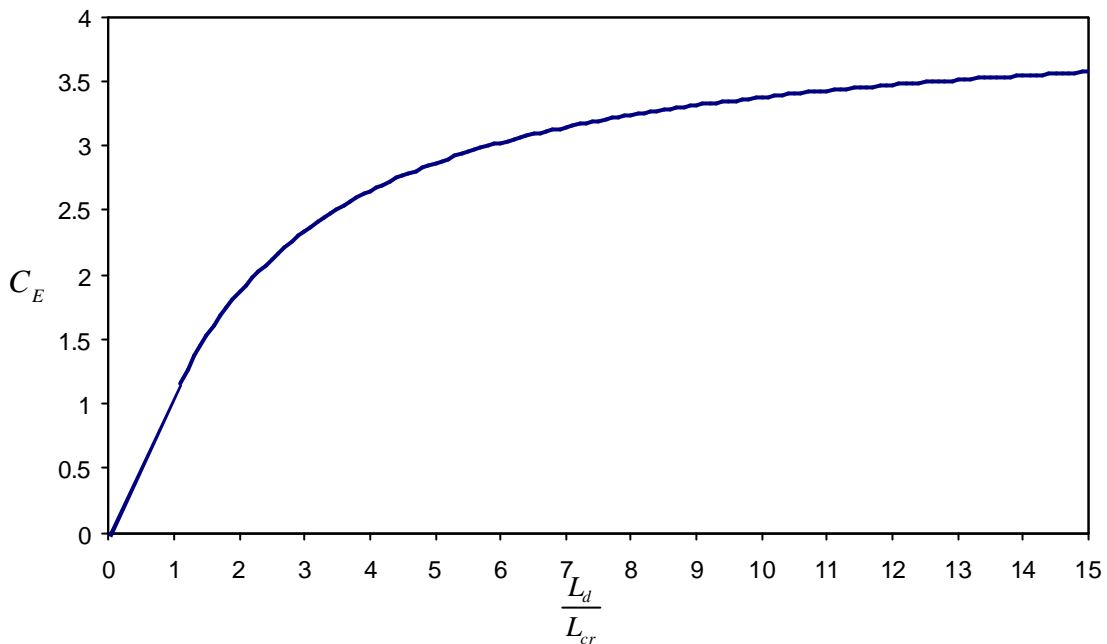


Figure 4.3.2 – Characteristic curve for the Euler buckling load coefficient as a function of the disbond length normalised to the natural half-wavelength

The maximum value of C_E is four, which represents built-in end conditions and occurs when the core stiffness is infinite. Practically this occurs when the core thickness is reduced to zero. An interesting feature of this plot is that when the disbond length equals the natural half-wavelength the disbonded face region behaves as though it had simply supported end conditions. Also, the load at this point corresponds to the wrinkling load of an infinitely long beam with a free-end condition, given by Hetenyi (1946) as:

$$P_{wr} = \sqrt{kD} \quad (4.3.12)$$

This is equal to half the wrinkling load for a beam with either built-in or pinned end conditions. Niu and Talreja (1999) comment on this feature in their discussion of the master curve, but they do not point out that this also corresponds to the Euler buckling load of the disbonded face with simply supported ends.

The function shown in Figure 4.3.2 passes through the origin. Note that this does not mean that the buckling load is zero when $L_d = 0$. Because the Euler equation also has L_d in the denominator, when $L_d = 0$ the buckling load is finite. As expected, as L_d approaches zero, the buckling load approaches the wrinkling load. The master curve of Niu and Talreja (1999) illustrates the buckling behaviour in

this region clearly. Note that the master curve obtained from the present model data is the same as that of Niu and Talreja (1999), but the present definition of foundation stiffness should be used to accurately determine the normalising values, L_{cr} and P_{wr} .

4.3.2 COMPARISON OF MODEL AND EXPERIMENTAL BUCKLING LOADS

Table 4.3.1 summarises the comparison between the experimental buckling loads (P_{exp}) and those predicted by the Winkler beam buckling model (P_{model}). In order to examine the effects of the new foundation stiffness term, the buckling loads obtained using the stiffness term of Sleight and Wang (1995) are also included, labelled P_{sw} . Finally, the load predictions of (4.3.7) (from the non-dimensional regression analysis) are shown and compared to experimental values. All loads are expressed per unit beam width and differences are given, to the immediate right of the model results to which they refer, as a percentage variation from the experimental values. Difference averages and standard deviations are given for each prediction set.

Table 4.3.1 – Comparison of buckling load results from specimen testing and the present buckling model

Specimen Designation *	P_{exp} (N/m)	P_{model} (N/m)	Difference	P_{sw} (N/m)	Difference	Eq. 4.3.7 (N/m)	Difference
25-G-T	9996	9848	-1.5 %	8725	- 12.7 %	9253	-7.4 %
25-G-R	9791	10082	3.0 %	8725	-10.9 %	9438	-3.6 %
25-GH-T	6526	6713	2.9 %	5901	-9.6 %	6280	-3.8 %
25-GH-R	7219	7127	-1.3 %	6134	-15.0 %	6655	-7.8 %
40-G-T	4383	4454	1.6 %	4103	-6.4 %	4296	-2.0 %
40-G-R	4317	4515	4.6 %	4103	-5.0 %	4382	1.5 %
40-GH-T	2867	2970	3.6 %	2728	-4.8 %	2916	1.7 %
40-GH-R	3124	3136	0.4 %	2840	-9.1 %	3090	-1.1 %
		Average	1.7 %		9.2 %		-2.8 %
		Std dev	2.3 %		3.7 %		3.6 %

* See Chapter Three for an explanation of the specimen designation

Use of the foundation stiffness term of Sleight and Wang (1995) consistently under-predicted the experimental buckling load by an average of 9.2%. Niu and Talreja (1999) proposed the following foundation stiffness term to incorporate the assumption of plane strain conditions in an isotropic core:

$$k = \frac{E_c(1 - \nu_c)}{t_c(1 - 2\nu_c)(1 + \nu_c)} \tag{4.3.13}$$

They found this term to reduce the difference, relative to a plane strain finite element model, from 15% to 3% for an isotropic core. However, (4.3.13) is not applicable to honeycomb material (Niu and Talreja 1999) and it also fails to consider stress equilibrium within the core. The present definition of k is based on the solution of a two-dimensional stress function in the core region and provides an accurate prediction of disbond buckling, with an average difference of only 1.7% from specimen test results. This result demonstrates that, when an appropriate foundation stiffness is used, sandwich structure can be accurately modelled as a Winkler beam. The characteristic curve (Figure 4.3.2) can be confidently used when considering disbond buckling in sandwich beams.

4.4 CONCLUSIONS

A foundation stiffness term, based on a two-dimensional stress analysis of the core, was used in a Winkler beam model to predict disbond buckling to within 1.7% of experimental values. It was concluded that this foundation stiffness model is necessary when considering disbond buckling in a sandwich beam with an orthotropic core (such as honeycomb). It has also been shown that the simple foundation stiffness term used by many authors in the past (Kim *et al.* 1993, Niu and Talreja 1999, Sleight and Wang 1995, Vizzini and Lagace 1987) has 9.2% average variation from experimental results. Two non-dimensional regression analyses were done to show the influence of the constituent material properties and geometries on the buckling load. The following semi-empirical expression is valid for core thicknesses larger than the natural wavelength of the fully-bonded sandwich face and has an average variation from experimental results of 2.8%:

$$P = \left(J_z \sqrt[5]{J_x J_{xz}} \right)^{0.0876} \frac{P^2 D_f^{0.8774}}{L_d^{1.6322}} \quad (t_c \geq L_{cr})$$

The following conclusions were drawn from the non-dimensional analysis:

1. There is a critical core thickness ($t_c = L_{cr}$) at which the buckling load is minimum. Above this value the buckling load is practically independent of core thickness.
2. A characteristic buckling-curve was presented, with the Euler buckling coefficient C_E plotted against L_d/L_{cr} (disbond length normalised by the natural wrinkling wavelength of the face). It was found that, when $L_d = L_{cr}$, the buckling load is equal to the Euler buckling load of the disbonded face region with simply supported end conditions (i.e. $C_E = 1$). Also at this point the buckling load equals the wrinkling load for a face with at least one free-end condition.

Not only does the present analysis provide accurate buckling loads, it has provided insight into the fundamental problem of disbond buckling. The natural wavelength has been identified as a characteristic length, not only of the disbond but also of the core thickness.

Having accurately predicted the buckling load the remaining critical point in the failure process is the initiation of disbond growth. The next chapter describes the development of a non-linear post-buckling model to predict growth behaviour. The model will consider both growth initiation and subsequent steady growth.

CHAPTER FIVE

Modelling Disbond Growth in Sandwich Beams

5.1 INTRODUCTION

Given an accurate prediction of buckling, the next important analysis is that of post-buckling and the growth behaviour leading to failure of the sandwich structure. Only two published studies (Sankar and Narayanan 2001 and Frostig and Thomsen 2004) were found that model the post-buckling behaviour of a sandwich panel with a disbond where the transverse stiffness of the core is considered to be finite (the distinct difference between modelling sandwich structure and solid laminate structure).

Sankar and Narayanan (2001) found that a linear buckling analysis is insufficient to predict failure of a disbonded sandwich beam in pure compression. They developed a non-linear finite element model of disbonded sandwich beams to compare with the experimental results of Avery and Sankar (2000). The model they developed was two-dimensional (modelling a sandwich beam with a through-width disbond) and used bi-quadratic plane strain elements. The buckling loads and the maximum load attained in post-buckling were compared to the experimental failure loads. The post-buckling analysis did not include a growth analysis because the experiments of Avery and Sankar (2000) showed little or no growth of the disbonds before failure. Also, when the strain energy release rate was calculated in the finite element model it was shown to be below the critical value (required for fracture). The maximum load attained in the post-buckling analysis corresponded to the experimentally determined compressive failure load in 50% of the specimens. These were typically the specimens that contained long disbonds (1.5 or 2.0 inches). As the load was increased these specimens became unstable, and the stresses and energy release rate at the crack-tip increased rapidly, causing catastrophic failure. In the remaining 50% of the specimens (those with short disbonds, 0.5 to 1.0 inches) failure occurred before the maximum load predicted by the post-buckling analysis. The stress analysis results indicated that in these specimens the compressive stress in the core exceeded the compressive strength, indicating that core failure could have

triggered the specimen failure. This analysis was limited to a comparison with a prior set of test results and there were no generalised conclusions made.

Frostig and Thomsen (2004) developed a non-linear model of a sandwich beam containing an arbitrarily located disbond. The loading considered was a transverse point load applied in the disbonded face-sheet region. The model assumes a transversely flexible core and models the entire beam (both face-sheets) so that the overall beam behaviour can be considered for a number of loading scenarios. This analysis is based on the High-Order Sandwich Panel Theory (Reddy 2004) and incorporates contact conditions. When the load is not applied directly to the disbonded region it is found that contact is minimal. The model identifies high transverse stresses at the disbond tip but does not incorporate a growth criterion to determine when fracture occurs.

There are several papers that model the post-buckling behaviour of a laminated beam with a through-the-width delamination (Gaudenzi *et al.* 2001, Kyoung and Kim 1995, Yin 1988, Yin *et al.* 1986). There are also those that model the post-buckling behaviour of laminated plates with embedded (circular or elliptical) disbonds (Klug *et al.* 1996, Pradhan and Tay 1998, Riccio *et al.* 2000, Rinderknecht and Kroplin 1997, Whitcomb 1992; Whitcomb 1989). Some of these papers also contain analysis of delamination growth, but none of them can be used to model sandwich structure where the core has a finite transverse stiffness.

Kim and Dharan (1992) and Kim *et al.* (1993) developed a linear model of a Winkler beam (Euler beam on a Winkler foundation) with a disbond and found an expression for the energy release rate at the crack tip. Kim *et al.* (1993) performed an experimental study on a set of sandwich beams to compare fracture loads to those predicted by their model. The model over-predicted the critical fracture load by approximately 150%. The analysis was primarily limited by the assumption of linearity. Most of the growth models in the literature (Klug *et al.* 1996, Krueger and O'Brien 2000, Pradhan and Tay 1998, Riccio *et al.* 2001, Riccio *et al.* 2000, Thomson and Scott 2000, Whitcomb 1992) evaluate delamination growth in solid laminates using linear elastic fracture mechanics (LEFM) by way of the virtual crack closure technique. This technique is preferred due to its relative ease of implementation and computational efficiency.

The above review highlights the fact that the published literature does not contain any non-linear, post-buckling models that consider growth of disbonds in sandwich beams.

The present study provides such a model by utilising the modified Winkler beam model described in the previous Chapter. The Winkler beam model was modified to account for large displacements and rotations in the disbond region and the virtual crack closure technique was utilised to calculate

the strain energy release rate at the disbond tip and predict disbond growth initiation. Results of the experimental study described in Chapter Three were then used as to compare with the model predictions.

5.2 LARGE DISPLACEMENTS OF A REFINED WINKLER BEAM

5.2.1 POST-BUCKLING MODEL

This section describes the non-linear post-buckling model, in which the buckling load and mode shape, from the buckling model of Chapter Four, were used as initial conditions. The post-buckling analysis is described first and the results validated, then in Section 5.2.3 the fracture criterion is described and added, to complete the model.

5.2.1.1 GOVERNING EQUATIONS

Symmetry was assumed in post-buckling and the resulting half-beam was divided into two regions. One region, the area of perfect bonding, was modelled as a Winkler beam with the assumption of small rotations. The other region, the disbonded region of the beam, was modelled as a beam with large rotations and no foundation. The assumption of small rotations within the bonded region simplified the analysis considerably and subsequent testing of the model has shown that the average and maximum errors introduced by this assumption are 0.009% and 3.5%, respectively. The maximum error occurs only at the disbond tip node, where the maximum rotation is typically 15° (for a sample test specimen at the point of disbond growth initiation).

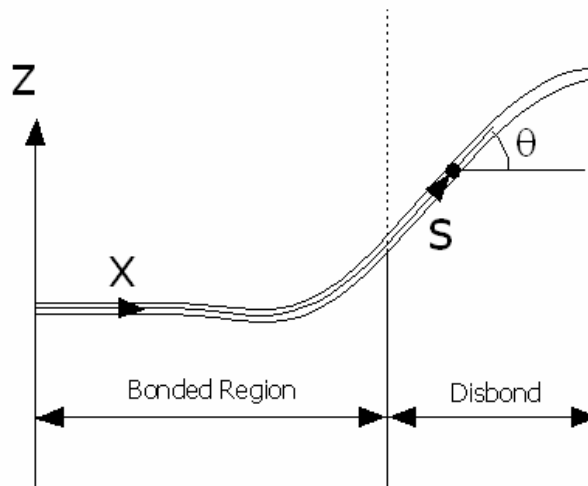


Figure 5.2.1- Lagrangian formulation for the post-buckling Winkler beam model

Formulating the problem using Lagrangian coordinates allows the exact curvature expression (5.2.1), which is not restricted to small rotations, to be used in place of the typical approximation (5.2.2).

$$\mathbf{k}_{exact} = \frac{d\mathbf{q}}{ds} \quad (5.2.1)$$

$$\mathbf{k}_{approx} = \frac{d^2w}{dx^2} \quad (5.2.2)$$

In the Lagrangian coordinate system any point on the beam has a rotational variable \mathbf{q} and a variable s , which represents the distance along the beam.

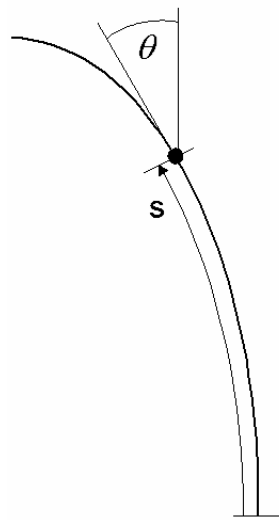


Figure 5.2.2 – Lagrangian co-ordinate system used for the post-buckling model

The governing equations for the two beam regions are derived separately and for the region with a Winkler foundation the governing equation, assuming small rotations, is:

$$D_f \frac{d^4\mathbf{q}}{ds^4} + P \frac{d^2\mathbf{q}}{ds^2} + k \sin \mathbf{q} = 0 \quad (5.2.3)$$

Timoshenko (1936) derived the general equation for large rotations of an Euler beam in pure compression (5.2.4) and this is the expression used to model the disbonded face-sheet region.

$$D_f \frac{d^2\mathbf{q}}{ds^2} + P \sin \mathbf{q} = 0 \quad (5.2.4)$$

A second order finite differencing scheme was used to discretise (5.2.3) and (5.2.4), resulting in (5.2.5) for the bonded region and (5.2.6) for the disbonded region.

$$\frac{D_f}{\Delta_s^4} (\mathbf{q}_{n-2} - 4\mathbf{q}_{n-1} + 6\mathbf{q}_n - 4\mathbf{q}_{n+1} + \mathbf{q}_{n+2}) + \frac{P}{\Delta_s^2} (\mathbf{q}_{n-1} - 2\mathbf{q}_n + \mathbf{q}_{n+1}) + k \sin \mathbf{q}_n = 0 \quad (5.2.5)$$

$$\frac{D_f}{\Delta_s^2} (\mathbf{q}_{n-1} - 2\mathbf{q}_n + \mathbf{q}_{n+1}) + P \sin \mathbf{q}_n = 0 \quad (5.2.6)$$

The Newton-Raphson procedure was used to solve (5.2.5) and (5.2.6), where the initial guess for the displacement function was the linear buckling shape, scaled to a prescribed height before being converted to Lagrangian coordinates by a central finite differencing scheme. The buckling load was used as the initial load estimate. Using a nodal rotation variable as the constant value in the problem, the Newton-Raphson method solves for the remaining variables and the load. Due to the low post-buckling stiffness associated with the problem, this was found to be a much more stable process than using constant load increments and solving for the nodal rotations.

5.2.2 VALIDATION PROCESS

The post-buckling model was verified by the satisfaction of two criteria. Firstly, that the post-buckling load converged to within 0.15% of the linear buckling load when displacements were very small. Secondly, the model was degenerated to a column with built-in ends by making the disbond length equal to the beam length. Timoshenko (1936) presented an exact solution to this problem and Figure 5.2.3 shows that the present model corresponded exactly to this result.

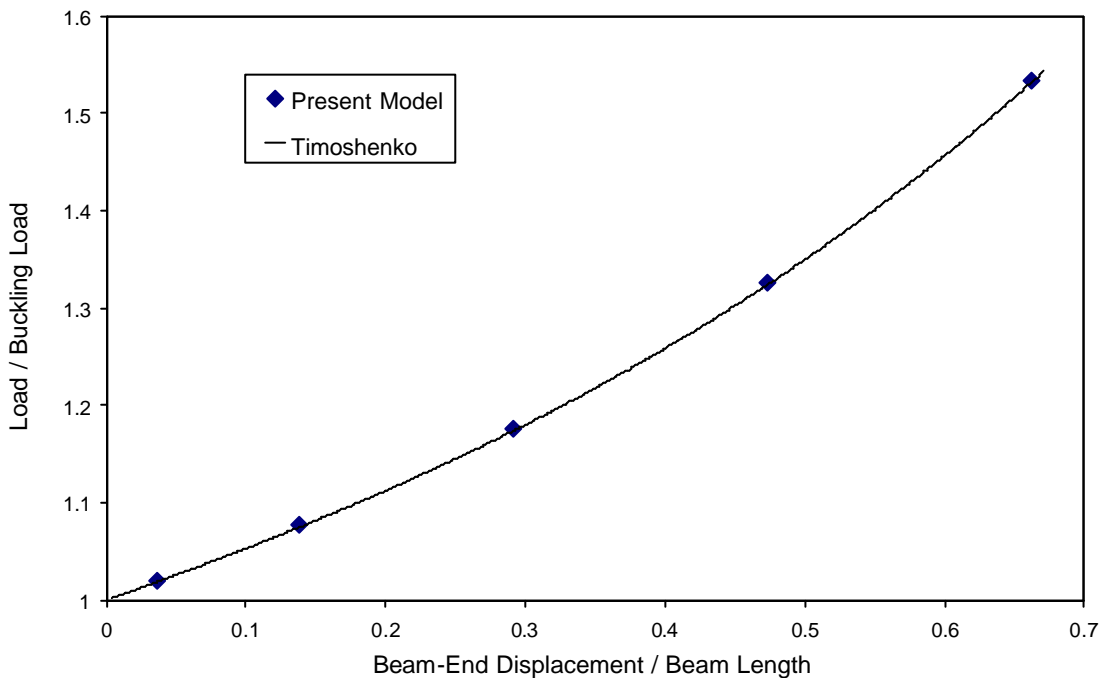


Figure 5.2.3 – Post-buckling behaviour of an end loaded column with built-in ends (Comparison between the present model and the solution presented by Timoshenko (1936))

Figure 5.2.4 illustrates the deformed column shapes for each of the five data points in Figure 5.2.3. The beam-end displacement used in Figure 5.2.3 is the vertical displacement of the end of the column/beam.

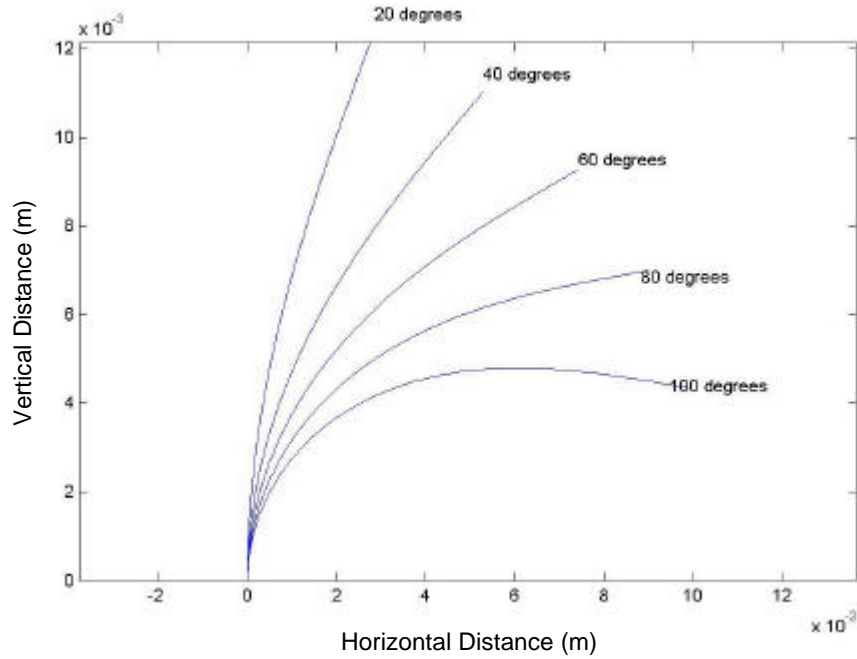


Figure 5.2.4 – Range of large deflections over which the non-linear beam model is verified by comparison to an exact solution

These two criteria were considered sufficient to verify the numerical technique and validate the model.

5.2.3 DISBOND GROWTH CRITERION

Thus far the model predicts the post-buckling behaviour of a disbonded sandwich beam. This section describes the addition of a fracture criterion, used to predict disbond growth initiation.

The growth criterion used in this model was the strain energy release rate, G . The virtual crack closure technique (VCCT) (Raju 1987) was used to determine this property from the post-buckling displacements.

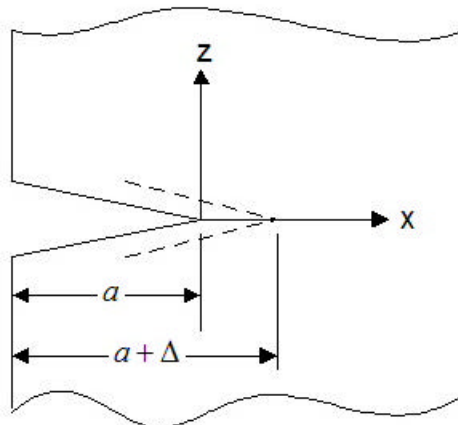


Figure 5.2.5 – Notation used in the general Virtual Crack Closure technique derivation

Referring to Figure 5.2.5, the Mode I and Mode II strain energy release rates are obtained by calculating the work required to close the crack from $(a + \Delta)$ to (a)

$$G_I = \lim_{\Delta \rightarrow 0} \frac{1}{2\Delta} \int_0^{\Delta} \mathbf{s}_z(x,0) \cdot w(x-\Delta,0) dx$$

$$G_{II} = \lim_{\Delta \rightarrow 0} \frac{1}{2\Delta} \int_0^{\Delta} \mathbf{s}_{xz}(x,0) \cdot u(x-\Delta,0) dx$$
(5.2.7)

The Mode III contribution to the total energy release rate cannot be incorporated into a two-dimensional model and it is typically negligible in practice (Whitcomb 1989). For the present model, into which the criterion was implemented, the Mode II contribution is irrelevant, as the model is one-dimensional and assumes no shear stresses at the face-core interface. This assumption was shown to have very little effect in the Winkler beam model (Cheng *et al.* 1997). Hence it is only the Mode I component that can be translated into a form useful for input into the model.

5.2.3.1 IMPLEMENTATION INTO A WINKLER BEAM MODEL

This section describes the method used to implement the numerical evaluation of G into a Winkler beam model.

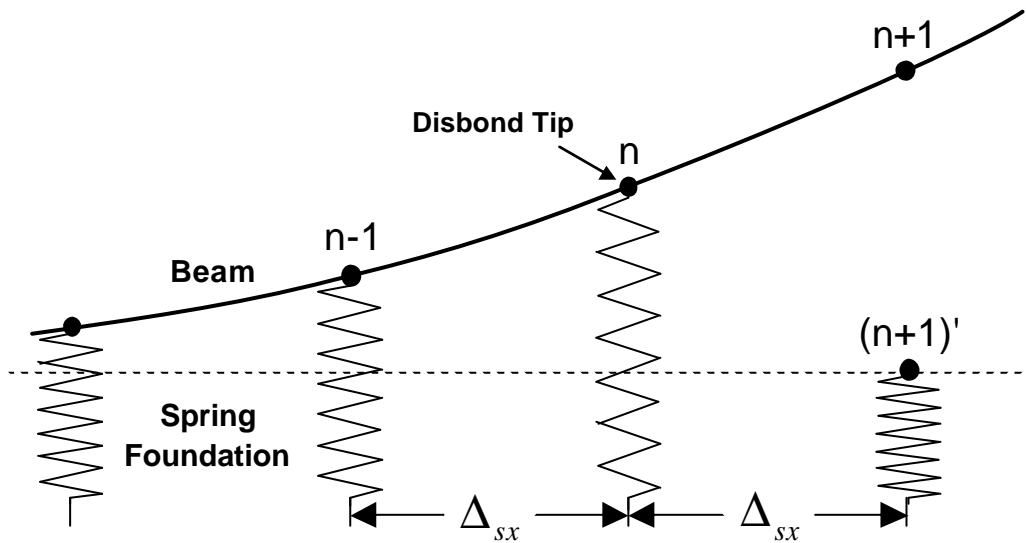


Figure 5.2.6 – The displacements in the disbond region are assumed to be at the undeformed reference state (dotted line) for the purpose of evaluating the strain energy release rate at node n

The critical piece of information lacking in this problem is the displacement of the core material at all disbonded nodes. The assumption made is that the displacement of all such nodes (i.e. $(n+1)'$ in Figure 5.2.6) is zero. This assumption is consistent with the one-dimensional model formulation. Also, the face-sheet displacement is assumed to vary linearly between the nodes. With these assumptions used in (5.2.7) the Mode I strain energy release rate is defined as:

$$G_I = \frac{k}{2} \left(\frac{w_{n+1} w_n}{3} + \frac{w_{n+1} w_{n-1}}{6} + \frac{w_n^2}{6} + \frac{w_n w_{n-1}}{3} \right) \quad (5.2.8)$$

See Appendix C for the complete derivation of (5.2.8). This is the expression used to calculate the total energy release rate in the post-buckling model.

The buckling model in Chapter Four was presented by developing a non-dimensional regression analysis. This proved to be a very useful and resulted in the characteristic disbond buckling curve. The present post-buckling model is complete with a disbond growth criterion and the next section presents the results in the same manner as Chapter Four.

5.3 THE CHARACTERISTIC DISBOND GROWTH CURVE

The strain energy release rate is the model output that provides the ability to predict the initiation of disbond growth. This is a critical point in the failure process of a disbonded sandwich beam because it represents an irreversible change to the structure. A non-dimensional analysis using the parameters defined in (5.3.1) provides insight into the problem of disbond growth (See Appendix B for derivation).

$$\Pi_1 = \frac{G}{P} \quad , \quad \Pi_2 = \frac{L_d}{p} \sqrt{\frac{k}{D}} = \frac{L_d}{L_{cr}} \quad , \quad \Pi_3 = \frac{\Delta}{L_d} \quad (5.3.1)$$

These represent all of the parameters required to describe the model. Utilising the Buckingham Π -theorem (White 1994):

$$\Pi_1 = f(\Pi_2, \Pi_3) \quad (5.3.2)$$

The first observation was that the relationship between Π_1 and Π_3 is linear. The reason for this linear relationship was considered first. A linear relationship between Π_1 and Π_3 means that for any disbonded beam specimen:

$$\frac{P\Delta}{G} = \text{constant} \quad (5.3.3)$$

The variables on the left-hand side of (5.3.3) are the only parameters that vary during the non-linear loading process. The remaining parameters are material properties and disbond length. One of the features of the post-buckling model results was that the post-buckling stiffness was very low. In fact the load, post-buckling, was almost constant (Figure 5.3.1). This is in agreement with the experimental results of Chapter Three.

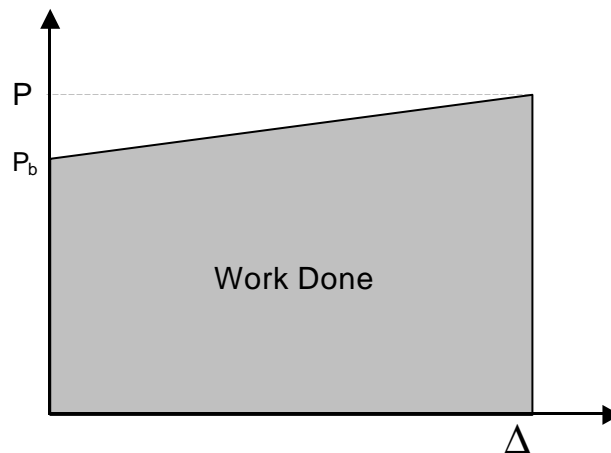


Figure 5.3.1 – Load-displacement profile predicted by the post-buckling model

Considering Figure 5.3.1 alongside (5.3.3) it is apparent that $P\Delta$ is a reasonable approximation to the work input to the system, W . Considering a range of specimen configurations, it was found that $P\Delta$ over-predicts the actual integrated value of energy input to the system by an average of only 0.6%. Therefore, (5.3.3) may be rewritten as:

$$\frac{W}{G} = \text{constant} \quad (5.3.4)$$

All of the work input to the beam, W , is stored as strain energy. Because the model does not incorporate in-plane strain terms, the strain energy is due purely to bending of the face-sheet and does not include in-plane (membrane) strain. Strain energy release rate is determined by the amount of strain energy that is released upon an increment of disbond growth. The linear relationship in (5.3.4) implies that the proportion of the total stored strain energy that is released during disbond growth is independent of the post-buckled shape of the disbond (i.e. doubling the fracture toughness will double the work input required to initiate disbond growth). The constant in the relationship is dependant on the geometry and material properties of the sandwich beam and can be determined from the disbond growth model. To consider the constant in (5.3.4) in more detail, (5.3.2) is rewritten incorporating the definitions in (5.3.1) and replacing $P\Delta$ with W :

$$\frac{W}{GL_d} = f\left(\frac{L_d}{L_{cr}}\right) \quad (5.3.5)$$

The disbond length, L_d , is put on the left-hand side of (5.3.5) to simplify the function f in the regression analysis to follow.

Defining the values of G and W at fracture as G_c and W_c , it is possible to rewrite (5.3.5) at the initiation of disbond growth as:

$$\frac{W_c}{G_c L_d} = f\left(\frac{L_d}{L_{cr}}\right) \quad (5.3.6)$$

W_c is the work input required to initiate disbond growth. The denominator on the left-hand side of (5.3.6) has units of energy (given that G_c is per unit beam depth) and will be considered in more detail. The definition of G_c was given in Chapter Three as:

$$G_c = \frac{\partial U}{\partial A} \quad (5.3.7)$$

Therefore the surface energy of the disbond can be determined by integration of (5.3.7) over the entire disbond area:

$$U_s = \int_0^A G_c dA \quad (5.3.8)$$

Assuming that G_c is invariant with disbond area (which was shown to be a valid assumption in Section 3.4) the surface energy is defined as:

$$U_s = G_c A \quad (5.3.9)$$

For the present model the beam is unit depth, therefore (5.3.9) can be rewritten:

$$U_s = G_c L_d \quad (5.3.10)$$

Equation (5.3.10) represents the energy required to create a disbond of length L_d .

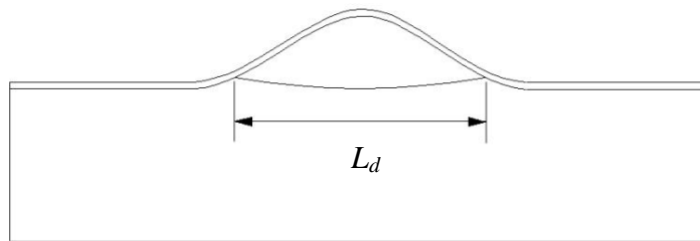


Figure 5.3.2 – Disbond in a sandwich beam

It is now apparent that (5.3.6) defines the ratio of the work input required for disbond growth, to the surface energy of the disbond. All that is required to determine the amount of work input to initiate disbond growth is knowledge of the function, f , in (5.3.6).

The function, f , was determined by regressing (5.3.6) to the post-buckling model. The data used in the regression analysis was obtained from the model by independantly varying k , D_f and L_d (the main problem parameters). Ten values of each parameter were used to obtain a total of 30 model results. Table 5.3.1 defines the ranges over which each parameter was varied. These ranges correspond to variation of L_d/L_{cr} between 0.5 and 11.

Table 5.3.1 – Parameters ranges used in the regression analysis

Variable	Minimum Value	Maximum Value
D_f	0.114 Nm ²	2.289 Nm ²
k	4.43×10^9 N/m ²	6.85×10^{10} N/m ²
L_d	3 mm	60 mm

A Padé function was fitted to the model data using the least-squares method, resulting in the following expression with an R^2 of 0.98:

$$\frac{W_c}{G_c L_d} = 0.24 \left(\frac{L_d}{L_{cr}} \right)^{-2} + 0.38 \left(\frac{L_d}{L_{cr}} \right)^{-1} + 0.51 \quad (5.3.11)$$

Equation (5.3.11) is a characteristic expression for growth initiation of a through-width disbond in a sandwich beam. The values in Table 5.3.1 cover a spectrum of typical sandwich configurations with thin faces (i.e. less than 1.2mm). However, because (5.3.11) is derived from a non-dimensional analysis, it is generally applicable (i.e. applicable beyond the range of values in Table 5.3.1). It was observed that, as the face thickness increases, L_{cr} becomes very large, which in turn makes L_d / L_{cr} small. The lower limit of applicability of (5.3.11) is $L_d / L_{cr} = 0.5$. At this relative disbond size, the buckling load is 78% of the wrinkling load. At a load equal to 78% of the wrinkling load, other failure mechanisms such as core shear and face-sheet fracture are likely to be more critical to the failure load than disbond growth. Therefore, in reality, this is a reasonable limit to the applicability of (5.3.11).

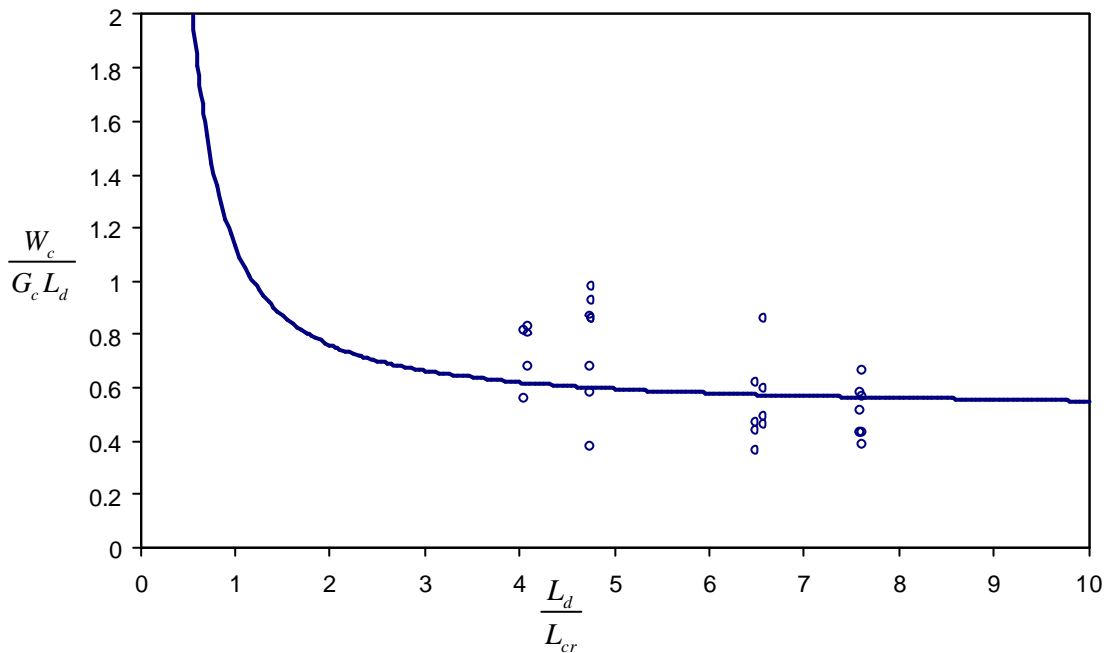


Figure 5.3.3 – The characteristic disbond growth curve

The characteristic curve (Figure 5.3.3) shows clearly that the relative amount of work required to initiate disbond growth increases as the relative size of the disbond decreases. Also, the energy ratio is undefined when the disbond length is zero and is approximately constant for relative disbond lengths above five (there is an asymptote at an energy ratio of 0.51).

The most important concepts from this analysis are:

1. The ratio of work input to strain energy release rate is a constant for any given beam

2. The work input required to initiate disbond growth can be scaled to the work input that was required to create the disbond in the first place (i.e. the surface energy of the disbond). This ratio is then dependent only on the relative size of the disbond (for which the wrinkling wavelength is a characteristic size)
3. There is a characteristic curve for disbond growth of a sandwich beam (Figure 5.3.3), providing a simple means with which to evaluate disbond criticality.

The energy expressions that arise out of this non-dimensional analysis are potentially very useful in practice because they imply that the method of applying load to the structure may not be as important as the actual amount of work done. It should be emphasised again that the work done in the present post-buckling model goes purely into bending strain energy (i.e. membrane strain energy is not considered). The applicability of the characteristic growth curve to other beam loading methods is limited to those in which the entire disbond region is located in a constant compression load, as obtained in the centre section of a four-point bending configuration. For example, it applies exactly to a cantilever beam with an end moment applied because the bending moment, and consequently the face-sheet compression load, is constant along the full length of the beam. It also applies to a sandwich beam in pure compression provided that the bending stiffness of the sandwich is significantly higher than the bending stiffness of the face-sheet. This requirement stems from the fact that the present model decouples the face-sheets and neglects the overall curvature of the sandwich beam. This is the equivalent of assuming that the bending stiffness of the sandwich beam is infinitely large, hence the requirement that it is large. The characteristic curve does not apply to a three-point bending configuration because in this case the bending moment and therefore the face-sheet compressive load vary linearly along the beam. It may still provide a reasonable approximation in this case if the disbond is small relative to the beam length.

5.3.1 COMPARING THE CHARACTERISTIC CURVE TO TEST RESULTS

The specimen tests are described in Chapter Three. The tests were done using four-point loading and the model is of a beam in pure compression. This difference could be complicated but, as previously stated, a particularly useful feature of the characteristic curve is that work input is required, instead of the in-plane load and end shortening of the beam (which would be very difficult to extract from four-point-bend test results).

The characteristic curve is defined by two ratios (see Figure 5.3.3) where W_c is the total work input required to initiate disbond growth and $G_c L_d$ is the surface energy of the disbond. The work done up to the point of growth initiation, W_c , was obtained from the test results of Chapter Three by

measuring the area under each load-displacement profile until the first growth event, as illustrated by the shaded area in Figure 5.3.4.

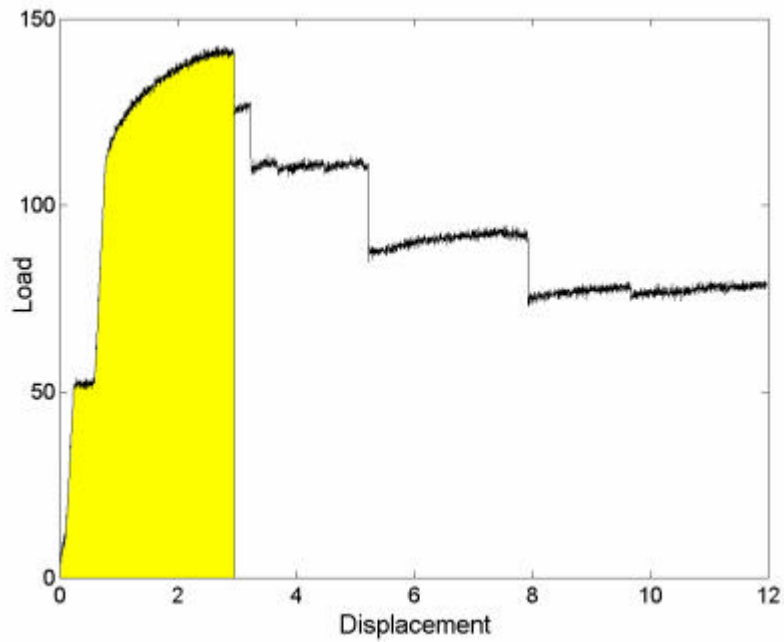


Figure 5.3.4 – Load-displacement profile of a sample test specimen (shaded area indicates work done up to the point of growth initiation)

Using the known fracture properties for all tests and the known disbond lengths, $G_c L_d$ was calculated. The values obtained in this manner, from all 32 specimen test results (having 8 different configurations), are plotted on the characteristic curve in Figure 5.3.5.

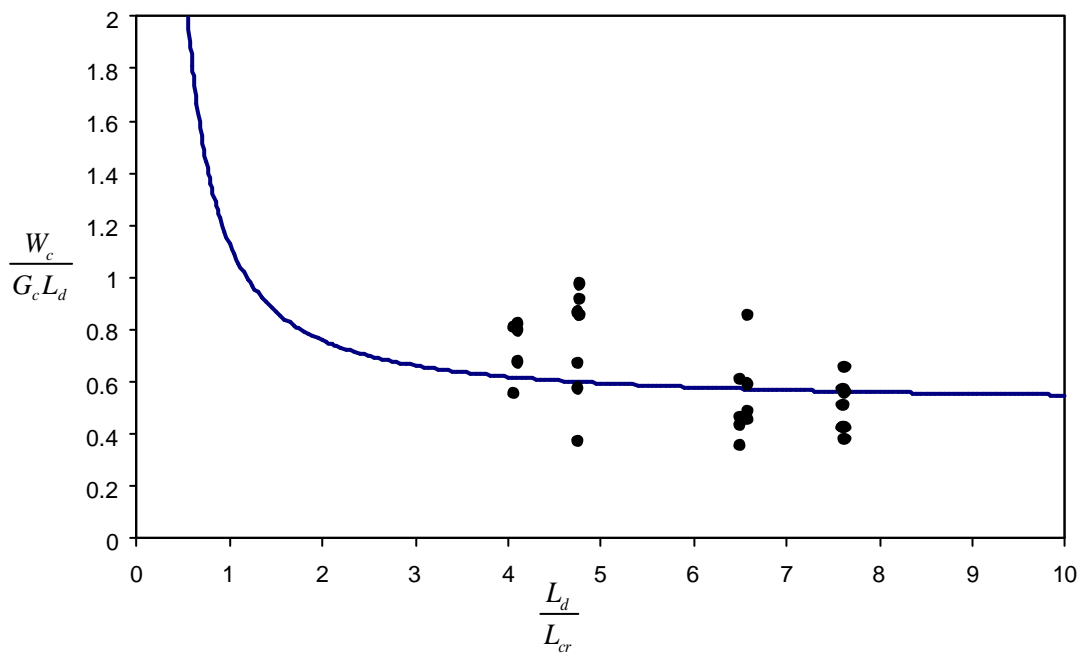


Figure 5.3.5 – Characteristic curve with model results included

The average difference between the specimen test values and the characteristic curve, as defined in (5.3.11), is 3.3% (with a standard deviation of 27.8%). The scatter observed is typical of experimental fracture measurements and is within reasonable limits considering that the scatter in G_c values is 19% (refer Section 3.5.3). The close agreement with specimen test results, particularly for fracture test results, validates the use of the characteristic curve as an assessment tool for disbanded sandwich.

Now that the characteristic disbond growth curve has been validated as a simple and effective means of predicting growth initiation, its application to continued disbond growth should be considered.

5.3.2 ANALYSIS OF CONTINUED DISBOND GROWTH

Having developed and tested the characteristic disbond growth curve, it is used in an analysis of continuing disbond growth, which begins at the initiation of growth and uses the characteristic curve to predict the load-displacement profile post-growth-initiation. The assumption was made that disbond growth occurs as a series of infinitely small increments and that the post-buckling stiffness is negligible.

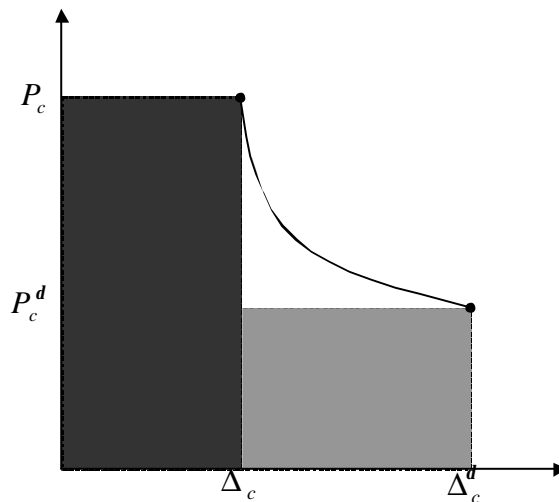


Figure 5.3.6 – The load-displacement profile for continuous disbond growth (shaded areas represent the strain energy stored in the beam at each point)

The load and displacement at growth initiation are defined as P_c and Δ_c . Recalling that the post-buckling stiffness is negligible, the work input required for disbond growth is defined as:

$$W_c = P_c \Delta_c \tag{5.3.12}$$

Rewriting (5.3.11) to incorporate (5.3.12) yields:

$$P_c = \frac{G_c L_d}{\Delta_c} \left(0.24 \left(\frac{L_d}{L_{cr}} \right)^{-2} + 0.38 \left(\frac{L_d}{L_{cr}} \right)^{-1} + 0.51 \right) \quad (5.3.13)$$

Equation (5.3.13) defines the load at any point on the load-displacement profile. However, it currently contains three unknowns that vary during the growth process; the load, the displacement and the disbond length. In order to predict the load displacement profile as growth continues steadily it is necessary to relate either the load or the displacement to the disbond length. With the assumption of negligible post-buckling stiffness, it is reasonable to assume that the post-buckling load is constant and equal to the buckling load. From Chapter Four the relationship between buckling load and disbond length is known as:

$$P_{cr} = \frac{P^2 D_f}{L_d^2} \left(4 - 6.88 \left(\frac{L_d}{L_{cr}} \right)^{-1} + 6.57 \left(\frac{L_d}{L_{cr}} \right)^{-2} - 2.68 \left(\frac{L_d}{L_{cr}} \right)^{-3} \right) \quad (5.3.14)$$

Letting P_{cr} equal P_c , combining (5.3.13) and (5.3.14) and rearranging for the displacement yields:

$$\Delta_c = \frac{G_c L_d^3}{P^2 D_f} \frac{\left(0.24 \left(\frac{L_d}{L_{cr}} \right)^{-2} + 0.38 \left(\frac{L_d}{L_{cr}} \right)^{-1} + 0.51 \right)}{\left(4 - 6.88 \left(\frac{L_d}{L_{cr}} \right)^{-1} + 6.57 \left(\frac{L_d}{L_{cr}} \right)^{-2} - 2.68 \left(\frac{L_d}{L_{cr}} \right)^{-3} \right)} \quad (5.3.15)$$

Using both (5.3.14) and (5.3.15) for a range of disbond sizes provides the load-displacement profile for a particular specimen configuration. The profile is compared to an actual specimen profile in Figure 5.3.7, showing that the general form of the growth profile is well predicted.

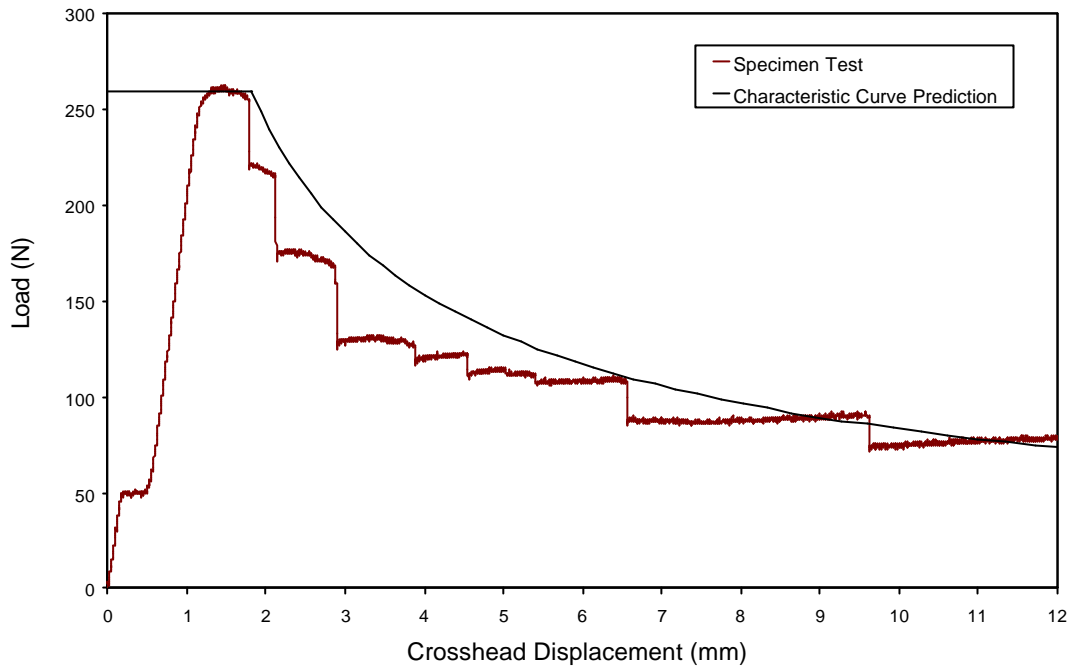


Figure 5.3.7 – Comparison of predicted growth profile with a specimen test profile

One obvious difference between the actual and predicted load profiles is that the specimen test exhibited discrete disbond growth, where the predicted profile assumes steady growth. Growth in the test specimens (refer Chapter Three) typically occurred in step increments approximately equal to the length of the cellular core, although this was not explicitly measured during loading of the test specimens. The analysis was rerun incorporating the assumption that growth occurs in discrete increments equal to the diameter of a circle inscribed in the core cells (nominally 3.2mm for the specimens used in Chapter Three testing).

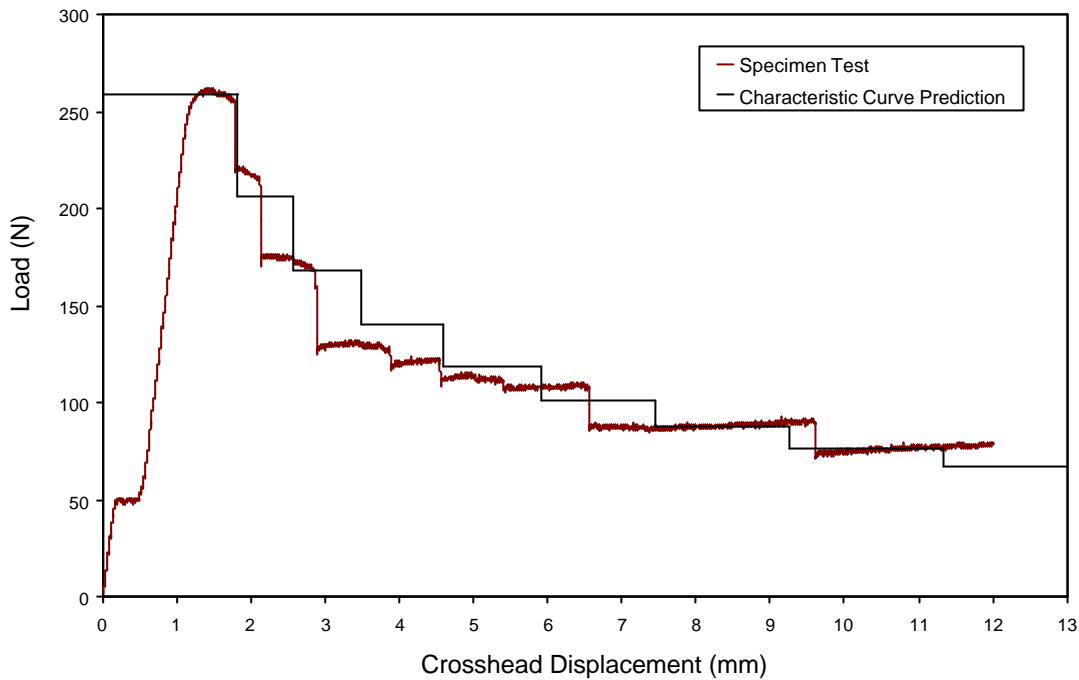


Figure 5.3.8 – Comparison to specimen test results of the predicted growth profile, incorporating discrete growth increments equal to the cell diameter

The comparison in Figure 5.3.8 shows that the analysis closely predicts all of the following elements of disbond growth behaviour:

- Buckling load
- Overall load-displacement profile
- Load reduction at each growth increment
- Displacement between growth increments

This result also verifies the assumption that growth occurs in increments approximately equal to the size of the honeycomb core cells.

A further test of the accuracy of the predicted growth curve was performed by predicting the final length of the disbond. The disbond length was measured after testing for all of the test specimens in Chapter Three. Using the final loads, and corresponding displacements, of the specimen tests in (5.3.13) it is possible to solve iteratively for the disbond length. This was performed for all of the specimen configurations as a means of predicting the actual final disbond length. Table 5.3.2 shows the comparison of the measured disbond lengths at the end of testing, L_{test} , with the lengths predicted by (5.3.13), L_{pred} .

Table 5.3.2 – Comparison between actual and predicted final disbond lengths

Specimen Group	Original Length	L_{test} (mm)	L_{pred} (mm)	Difference
40-G-T	40 mm	56	66	17.8 %
25-G-T	25 mm	56	63	12.9 %
25-G-R	25 mm	77	74	-4.2 %
40-GH-T	40 mm	62	64	3.6 %
25-GH-T	25 mm	57	66	15.4 %
25-GH-R	25 mm	70	83	19.5 %
40-G-R	40 mm	68	70	2.3 %
40-GH-R	40 mm	70	81	15.9 %
			<i>Average</i>	<i>10.4 %</i>
			<i>Std Dev</i>	<i>8.6 %</i>

Table 5.3.2 shows that there is good correlation between actual and predicted disbond lengths using the method described. The characteristic growth curve can therefore be used to predict not only the initiation of growth but also the structural response during growth up to any load.

5.4 CONCLUSIONS

The post-buckling behaviour of a sandwich beam with a disbond was modelled using a Winkler beam with a foundation gap, modified to incorporate large displacements within the disbond region. A modified version of the virtual crack closure technique was developed to measure the strain energy release rate at the disbond boundary. The Newton-Raphson procedure was used to solve the governing non-linear equations in Lagrangian coordinates and a non-dimensional analysis, regressed to the post-buckling model data identified a characteristic disbond growth curve. The characteristic curve implies that knowledge of the fracture toughness, geometry and material properties of a sandwich beam are sufficient to predict the work input required to initiate disbond growth. Also, a linear relationship was observed between the strain energy release rate at the disbond tip and the work done by the applied load.

The results of beam specimen tests were compared with predictions of the characteristic growth curve with an average difference of -0.5% (with a standard deviation of 20.7%).

The characteristic curve not only provides accurate predictions of growth initiation, it also accurately predicts the structural response during growth. The load-displacement profile was closely predicted assuming discrete growth increments equal to the nominal diameter of the cellular core. The predictive capability was further verified by comparing predicted final disbond lengths to those measured from the test specimens with an average difference of 10.4% (standard deviation of 8.6%). Therefore the characteristic disbond growth curve, along with the buckling analysis of Chapter Four, provides a complete and accurate description of the failure process of a disbonded sandwich beam. The analysis has also led to the discovery that the characteristic parameters of disbond growth can be described in terms of energy expressions; the surface energy of the disbond and the work required to initiate growth.

Having identified, through specimen testing, and successfully modelled the behaviour of disbonded sandwich beams, the subject of disbonds embedded in sandwich panels will now be addressed. This is the subject of the next three Chapters.

CHAPTER SIX

Testing of Disbonded Sandwich Panel Specimens

6.1 INTRODUCTION

The previous chapters have described the testing and modelling of sandwich beams with compressively loaded through-width disbonds and provided insights into the failure process. A more common real-world disbond situation is one in which the disbond is embedded locally within a sandwich structure. While there are many papers on the failure of embedded delaminations in solid laminates, only three relevant experimental studies were found regarding the response of sandwich structure to an embedded disbond.

Han *et al.* (2002) tested a sandwich panel in pure compression, having an initial rectangular disbond (307×457 mm) located at the interface of the core and face-sheet. The edges of the disbond were 95 mm from stiffeners (oriented parallel to the loading direction) attached externally to the face-sheet. The disbond was observed to buckle and growth was described as:

“initially stable, but it became unstable and very fast propagation was observed. The fast crack propagation was retarded when the crack front reached the stiffener”

The experiment was displacement controlled and the results were used to validate a sandwich model (reviewed at the beginning of Chapter Eight). Only one specimen was tested in this study, primarily to determine the accuracy of a finite element model of the specimen. There were no substantial insights into the parameters governing the failure process from this single test, nor could there be, due to the lack of statistical significance of a single test. The most notable aspect of the experiment is that disbond growth was observed to be predominantly unstable.

Hansen (1998) performed tests using rectangular disbonds in a honeycomb core sandwich panel to investigate buckling and failure loads due to pure-compression loading. Two types of specimen were used, varying only in face-sheet thickness. The face-sheet thicknesses were 1.028mm and 2.056mm and were referred to as ‘thin’ and ‘thick’ specimens respectively. Each specimen

contained four 15×35 mm disbonds, each one located approximately 20 mm from an edge (with two disbonds on either side of the panel). The panels were 300mm long in the loaded direction and 200mm wide, having 15mm thick honeycomb core. Strain gauges were placed on the face-sheets over each of the disbonded regions and a fifth was located away from any disbond region. The strain outputs were used to determine when buckling occurred. For the thin specimens, failure occurred through disbond buckling and growth across the panel width at loads approximately 40% lower than undamaged failure load. For the thick specimens, disbond growth was not observed and failure occurred shortly after disbond buckling. Hansen observed that; “Apparently, upon reaching the debond buckling load, the buckled debond acts as an imperfection”. This triggered a core-shearing type of buckling mode in the sandwich at approximately 80% of the undamaged failure load. Hansen concludes that failure is initiated in both cases by disbond buckling, which is determined to be “a key parameter in assessing the structural integrity of a sandwich component in compression”.

Falk (1994) performed a unique series of tests on sandwich panels with circular embedded disbonds. He developed a rig to load the panels with a uniform pressure load and clamped edges. Because the disbond region had a pressure load applied in this test, the residual strengths obtained were higher than those observed in the pure compression tests of Han *et al.* (2002) and Hansen (1998).

Of the studies that investigated delamination in solid laminates there is one that considered delamination within a sandwich face-sheet and is worth mentioning. Kassapoglou (1988) conducted 12 experiments on honeycomb sandwich in pure compression. Each of the tests contained a central elliptical delamination created by inserting Teflon pieces in one face-sheet at the ply interface next to the face-core interface. While this is not disbond damage, the failure process may provide qualitatively relevant insights. Four different configurations were tested with three tests per configuration. Two delamination sizes were used; large (57.2×50.8 mm) and small (25.4×19.1 mm). The small delamination did not affect specimen failure, which was by column buckling. The specimens with large delaminations failed at loads up to 30% lower than the specimens with small delaminations. Delamination growth was rapid, with no stable growth observed, meaning that the failure load and the load at which growth initiated were virtually identical.

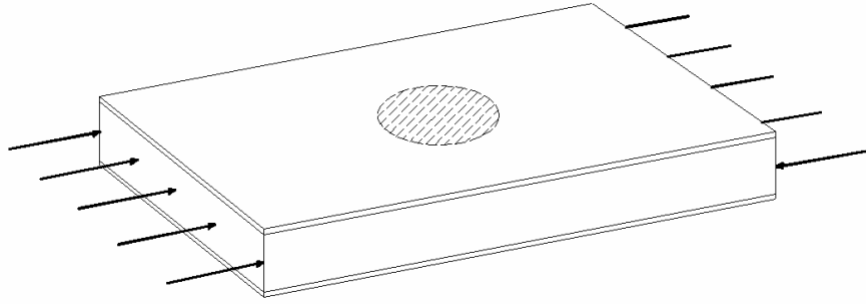


Figure 6.1.1 – Pure compression loading of a disbonded sandwich panel

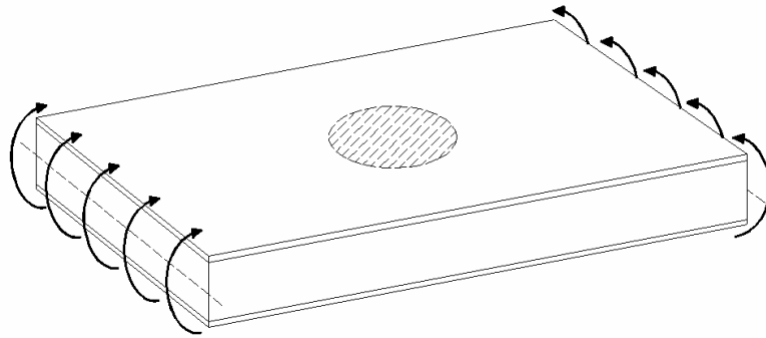


Figure 6.1.2 – Bending of a disbonded sandwich panel

One of the features observed in pure-compression load tests is that global buckling and disbond buckling are inextricably linked. They either occur as one instability mode or local buckling is a trigger for global buckling. In any case, they cannot be separated (Frostig and Sokolinsky 1999). Because the buckling load is proportional to the inverse square of the panel length, in the direction of loading, this length is a critical parameter in the failure process. This literally adds another dimension to the analysis and requires considerably more testing to determine the relationships between all of the material and geometric parameters involved in failure. These relationships must be known when the disbond buckling load is a significant fraction of the panel buckling load. However, when considering a thick sandwich panel (relative to its length), for which panel buckling is orders of magnitude larger than the wrinkling load, then at some point it is reasonable to decouple the face-sheets and consider the localised behaviour of the disbond without considering the global panel behaviour (in the limit case, disbond buckling still occurs in an infinitely thick sandwich panel). The range of panel dimensions for which this decoupling is reasonable is not the subject of this research and could not be determined from a review of the literature. It is stated only for consideration and to illustrate that bend testing, in which panel buckling does not occur, can not only model the behaviour of panels in bending but also of a range of pure-compression panels. The reverse is not true of pure-compression testing. Because sandwich panels are utilised primarily for the excellent bending stiffness-to-weight ratios that they provide, they are usually in situations

where they are subject to bending loads (e.g. control surfaces on commercial aircraft). This chapter describes testing (to failure) of sandwich panels containing circular disbonds in a four-point bend arrangement, so as to provide a pure bending moment to the disbond region and apply a compressive load to the disbonded face-sheet. This leads on to the next two chapters, which develop models to predict the failure process observed in the specimen test results.

6.2 SPECIMEN MANUFACTURE

A total of 24 specimens were manufactured, by the process described in Chapter Three (refer also to Appendix A), with centrally located circular disbonds of various diameters (25mm, 50mm and 75mm). All of the panels were loaded in four-point bending such that the disbonded face was in compression without any shear loading. Loading was continued until gross loss of structural stiffness occurred, as for the beam specimens of Chapter Three.

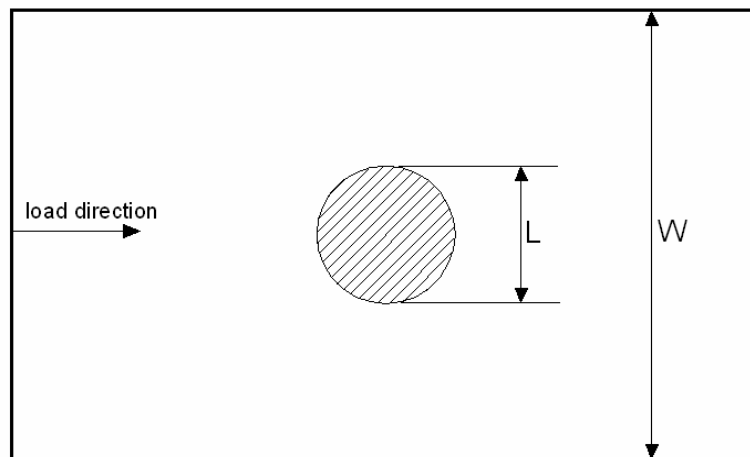


Figure 6.2.1 – Plan view of general panel specimen dimensions

The methodology behind the test design is similar to that used for the beam specimens of Chapter Three, with the main exception being that the test plan was half-factorial (Table 6.2.1), rather than full factorial. One of the variables in the test plan was the ratio of panel width to disbond diameter, R , defined as W/L (refer Figure 6.2.1). A full test plan for three variables (disbond diameter, face-sheet stiffness and disbond ratio, R) having 3, 2 and 2 variations on each, respectively, would require 12 different configurations. There are four repetitions of each configuration, which would result in 48 tests. Therefore, in order to optimise resources, and recognising that the ratio R may have negligible effect on the results, a semi-factorial test plan was developed.

Table 6.2.1 – Half-factorial test plan for panel specimens

Specimen Designation *	Disbond Diameter (L)	Face Material	Disbond Ratio (R)
25-G-100	25mm	Glass	4
25-GH-50	25mm	Glass Hybrid	2
50-G-100	50mm	Glass	2
50-GH-200	50mm	Glass Hybrid	4
75-G-300	75mm	Glass	4
75-GH-150	75mm	Glass Hybrid	2

* Represents the three variables, where the last is panel width (Table 6.3.1)

A semi factorial test plan can be designed in several ways. The chosen design (Table 6.2.1) allows the maximum coverage of all parameters with only half the number of tests of a full-factorial plan. It also happens that if one of the chosen parameters has a negligible effect (as suspected for the ratio R) then the tests form a full-factorial plan in the remaining two parameters. As for the beam test specimens, four repetitions of each test were done to obtain statistically significant results and all quoted values are the average of the four tests. All of the material designations and properties can be found in Chapter Three. In all cases the core was oriented such that the ribbon direction was parallel to the panel width direction.

6.3 FOUR-POINT LOADING OF PANEL SPECIMENS

All specimens were loaded in an Instron Universal Testing Machine with a 25kN load cell in a four-point bending rig with the arrangement as shown in Figure 6.3.1.

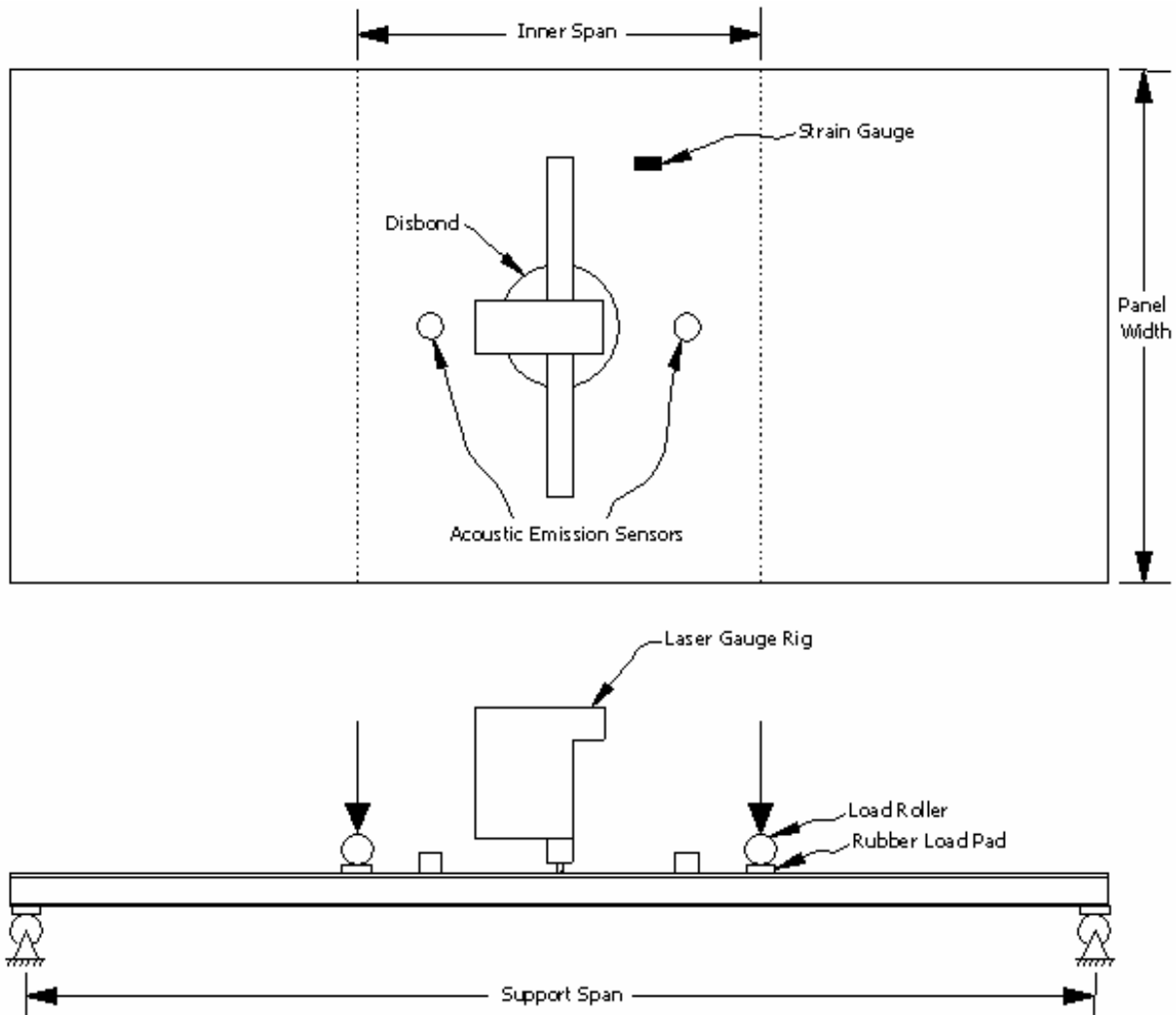


Figure 6.3.1 – Specimen layout (top surface shown). The Acoustic Emission sensors are located halfway between the load application line and the disbond edge.

The panel width was one of the variable parameters and the inner span was always approximately one third of the support span. Table 6.3.1 is a summary of the panel lengths and widths for each configuration (using the designations defined in Table 6.2.1).

Table 6.3.1 – Dimensions of each specimen configuration

Specimen Designation	Inner Span (mm)	Support Span (mm)	Panel Width (mm)
25-G-100	180	475	100
25-GH-50	180	475	50
50-G-100	180	475	100
50-GH-200	180	550	200
75-G-300	220	660	300
75-GH-150	180	475	150

Testing was done with a low, constant crosshead displacement rate of 3 mm/minute until the disbond grew through the full width of the panel, causing gross loss of structural stiffness and defining failure. The displacement rate was chosen to be a low value to minimise any rate effects (i.e. quasi-static loading).

6.3.1 BUCKLING AND FAILURE LOAD RESULTS

In all cases the load-point displacements at failure were less than 50% of the specimen thickness and less than 3% of the panel length. The most fundamental results are the buckling and failure loads for each of the six configurations. Disbond growth behaviour is presented at the end of the Chapter after the method of measurement.

Table 6.3.2 presents the mean of the four tests of each configuration along with the 95% confidence range (see Appendix G for definition).

Table 6.3.2 – Buckling and failure load result averages for each configuration

Configuration	Buckling Load (N/m)	Confidence Range (95%)	Failure Load (N/m)	Confidence Range (95%)	Buckling / Failure
25-G-100	24900	± 3.6 %	54333	± 6.4 %	45.8 %
50-G-100	7832	± 7.4 %	40092	± 5.0 %	19.5 %
75-G-300	3385	± 20.9 %	33975	± 10.0 %	10.0 %
25-GH-50	17144	± 8.1 %	38438	± 7.6 %	44.6 %
50-GH-200	4849	± 13.6 %	27992	± 10.6 %	17.3 %
75-GH-150	1894	± 19.7 %	25245	± 6.2 %	7.5 %

For the sandwich configuration types shown it is reasonable to assume that failure of an undamaged specimen might occur due to wrinkling (Aitken 2000). Aitken (2000) experimentally determined the

wrinkling failure load for the G-type face-sheet configurations to be 167MPa. This corresponds to a failure load of approximately 80,000 N/m for the G-type face-sheet and 70,000 N/m for the GH-type face-sheets. Table 6.3.3 shows the reduction in load carrying capacity (based on these failure loads) for each configuration.

Table 6.3.3 – Average reduction in load carrying capacity for each specimen

Configuration	Reduction of Undamaged Failure Load
25-G-100	32 %
50-G-100	50 %
75-G-300	57 %
25-GH-50	45 %
50-GH-200	60 %
75-GH-150	64 %

Figure 6.3.2 shows the variation of both buckling and failure loads with disbond diameter. The loads are expressed as a fraction of the wrinkling load.

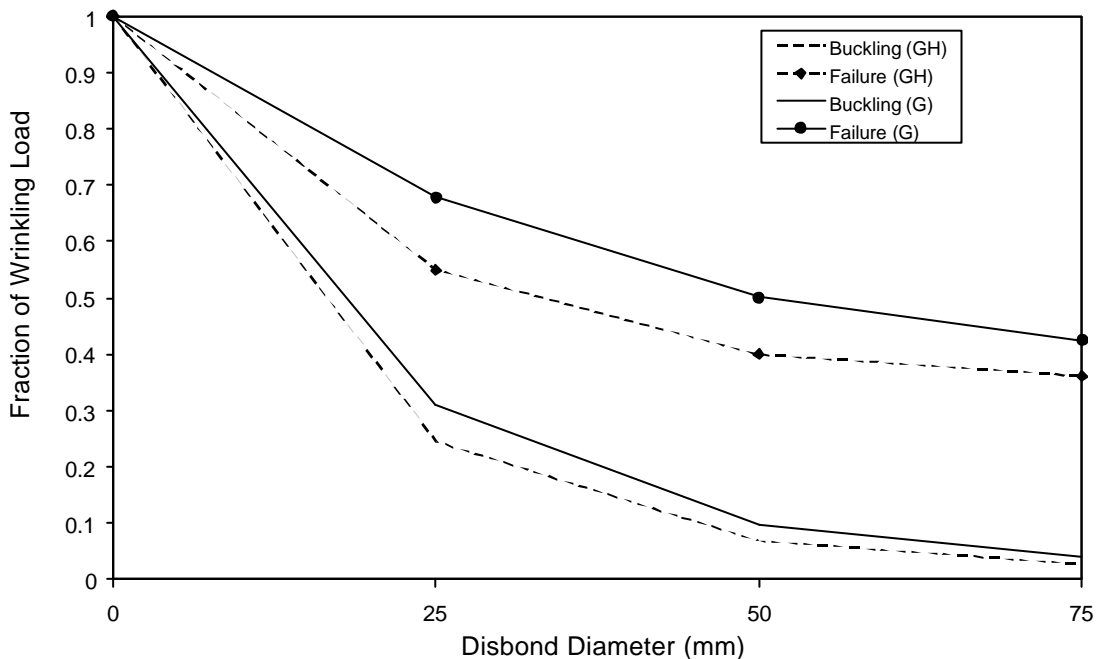


Figure 6.3.2 – Buckling and failure loads versus disbond diameter for all of the test specimens

One of the most important aspects of Figure 6.3.2 is that the dependency on disbond size is considerably less for the failure load than the buckling load. This is illustrated by assuming the load

curves in Figure 6.3.2 (excluding the undamaged failure load point) to fit a power function of the type:

$$P = CL^z \quad (6.3.1)$$

Fitting (6.3.1) to each load curve using a least squares curve fit resulted in the following powers (z) shown in Table 6.3.4 for each curve (the constant C is simply a scaling value and is not of interest at present).

Table 6.3.4 – Power coefficients of buckling and failure curves

Configuration	z
Buckling – GH	-1.99
Buckling – G	-1.80
Failure – GH	-0.39
Failure – G	-0.43

If damage tolerance is expressed in terms of the power law defined in (6.3.3), then a perfectly tolerant material (i.e. any amount of damage does not reduce the failure strength) has a z -value of zero. Therefore, the closer the z -value is to zero, for a failure load curve, the more tolerant the structure is to damage. The results clearly indicate that the failure load is significantly less dependent on disbond size than the buckling load. Also, the fact that there is significant load carrying capacity remaining after buckling, which causes the lower z values for the failure curves, is a good result in terms of damage tolerance. Table 6.3.4 also shows that the buckling load is approximately proportional to the inverse square of the disbond diameter, which is a typical result for buckling.

6.4 LASER GAUGING TO MEASURE BUCKLE HEIGHT

Buckling of through-width disbonds was easily identified in Chapter Three through a change in the overall structural stiffness, which occurs because the post-buckling stiffness is considerably smaller than the pre-buckling stiffness. For sandwich panels with embedded disbonds the difference between the pre and post-buckling structural stiffness was found, in preliminary testing, to be negligible (particularly for a small disbond in a wide panel). It is therefore not possible to determine accurately the occurrence of buckling from the load profile. By definition disbond buckling is defined as the point at which the disbonded region deflects out-of-plane (i.e. either inward or outward from the core). To capture this event for the panel specimens, a laser displacement gauge (L-GAGE model LG10A65PU) was mounted in a bracket (Figure 6.4.1), which enabled the measurement of the displacement of the centre of the disbond relative to its original position. As well as determining the onset of buckling, this also provided a complete record of the disbond height throughout the loading process.



Figure 6.4.1 – The laser gauge mounting rig used on all panel specimens

A mounting rig was purpose built to hold the laser gauge directly above the centre of a circular disbond and to allow it to translate in the out-of-plane direction as the panel was loaded. The rig was supported by two pins located on a line perpendicular to the length of the beam, enabling the measurement of the relative ‘height’ of the buckled disbond. To allow the rig to translate smoothly

and stay permanently in contact with the specimen, a linear bearing assembly was used. The laser gauge mounting rig had a 5mm diameter steel bar fixed in an axis parallel to the laser beam. A 5mm diameter linear roller bearing was mounted in an aluminium housing and attached to the loading unit. The bearing assembly was realigned prior to each test to ensure that the laser gauge was free to slide vertically, maintaining contact with the specimen at all times. The distance between the pins was adjustable to accommodate the different specimen widths. The only specimen that this rig could not be used for was the 50mm wide panel. In this case the laser gauge was rigidly mounted to the loading assembly. While this did not provide information about the buckle height, buckling could still be identified by a gradient change in the laser gauge output.

The mass of the laser displacement gauge was approximately 0.8 kg, which is a negligible addition to the loading of the panel. The strain gauges were always zeroed before the laser gauge rig was mounted on top of the panel to ensure that the weight of the rig was included in the total applied load.

A typical plot of buckle height (laser gauge output) versus face-sheet load (from the strain gauge) illustrates the usefulness of the laser gauge in determining the location of buckling. In some cases the buckle height increased more gradually at the buckling event than the sample shown in Figure 6.4.2.

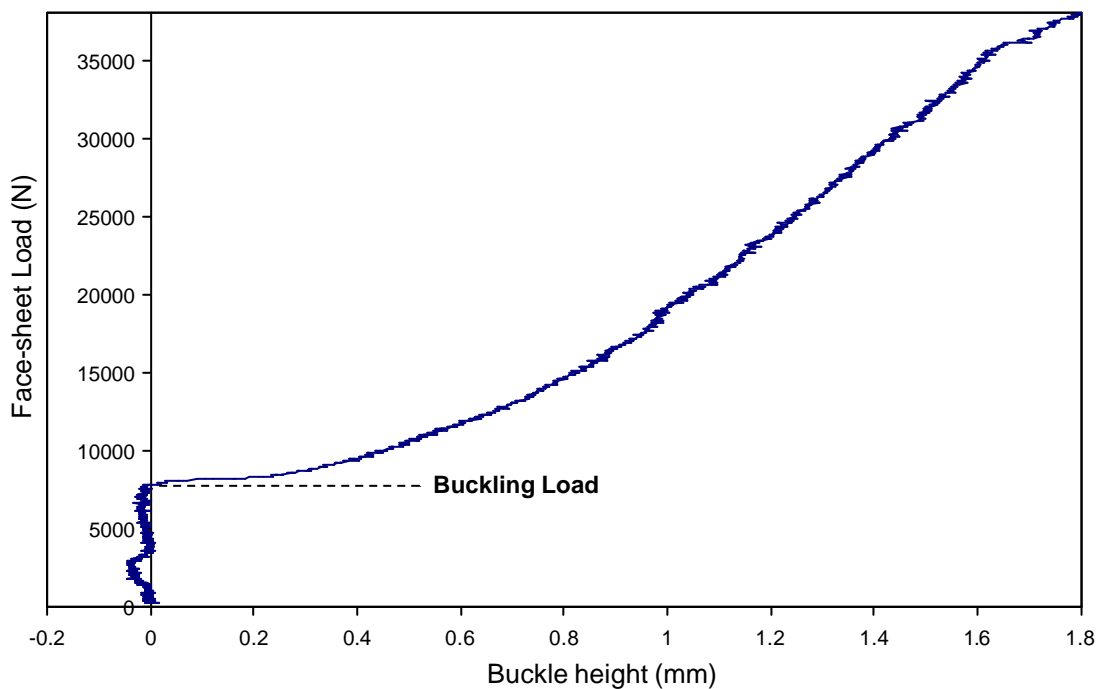


Figure 6.4.2 – Typical plot of face-sheet load versus buckled disbond height

Using a least-squares curve fit to the post-buckling profiles (i.e. beginning at the buckling load) for loads up to 70% of the failure load showed that all of the specimen profiles could be approximated by a function of the form:

$$P = C_1 h^2 + C_2 h + C_3 \quad (6.4.1)$$

The R^2 error values for these approximations were at least 0.99. For all four of the specimens with 25mm diameter disbonds and G-type face-sheets, ‘snap’ buckling occurred. Snap buckling refers to the action of the disbond buckling towards the core and at some point ‘snapping’ through its original position to form a typical (away from the core) buckle. A typical plot of buckled disbond height versus face-sheet load for one of these specimens is shown in Figure 6.4.3. This figure also illustrates a typical level of scatter, or disturbance, observed in the laser gauge output. The laser gauge output also records minor events, such as slip-stick behaviour of the laser gauge rig bearing assembly, that show up as premature out-of-plane displacements. These were typically small events, such as the example highlighted in Figure 6.4.3, and could not be confused with buckling.

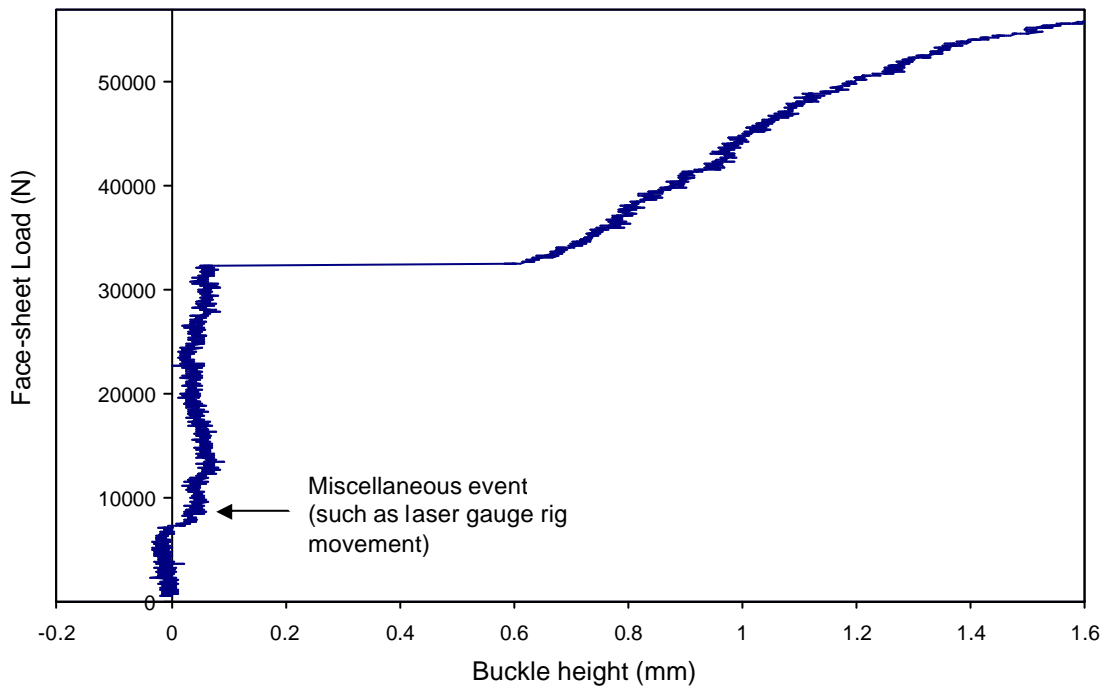


Figure 6.4.3 – Typical plot of buckled disbond height in the case of ‘snap’ buckling

In this instance the buckling load was determined by extrapolating the disbond height profile back to zero assuming the generic profile defined by (6.4.1). This overlay function is shown for the same sample as shown in Figure 6.4.3. This extrapolation method was not required for the specimens with GH-type face-sheets and 25mm disbonds because snap buckling did not occur.

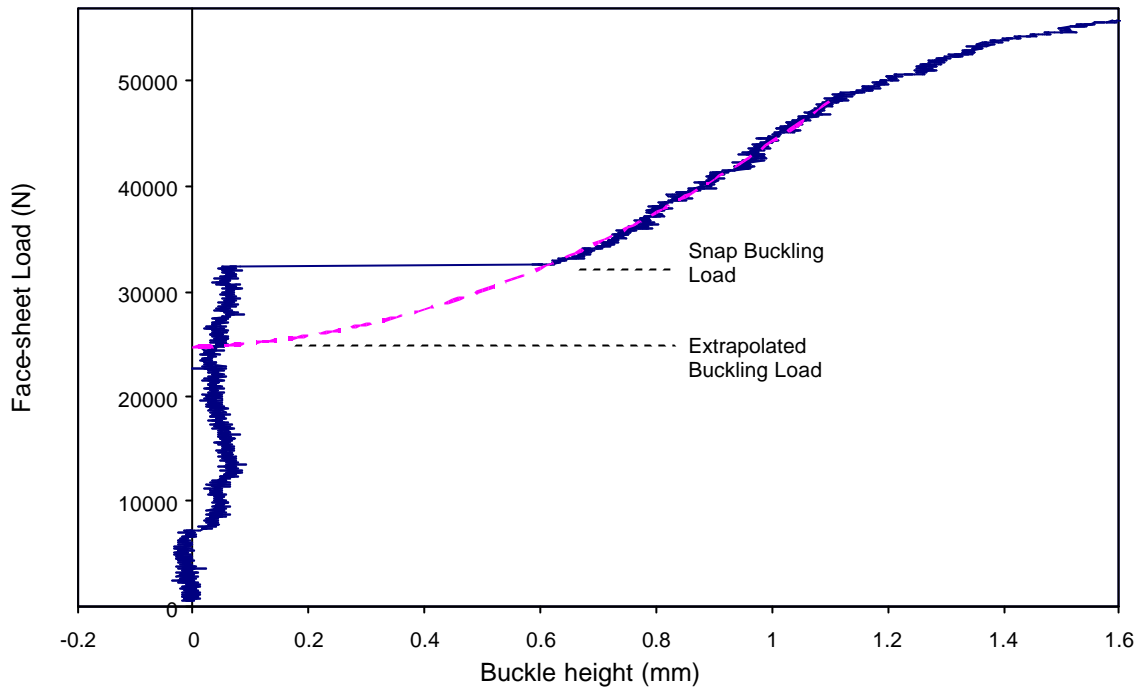


Figure 6.4.4 – Plot of buckled disbond height with the parabolic post-buckling function overlaid to find the approximate buckling load

When snap buckling occurred it did so because the panel deflections were relatively large at the buckling load and the disbonded face-sheet was already relatively concave (having curvature towards the core). The loads at snap buckling were, on average, 40% higher than the extrapolated buckling loads.

6.5 ACOUSTIC EMISSION MONITORING TO IDENTIFY DISBOND GROWTH EVENTS

Disbond growth is particularly difficult to monitor when the disbond is embedded because, unlike the beam specimens, there is no visual access to the growth front. This is a common problem when monitoring the failure process of sandwich beams, damaged or undamaged. The failure often initiates in the core and is not visible or easily monitored. Burman (1998) encountered this problem when investigating fatigue failure of foam-core sandwich beams, where shear failure initiates in the centre of the core and used Acoustic Emission (AE) monitoring to isolate the location and time of initiation of core failure. Monitoring the growth of an embedded disbond poses the same problems and because it is also a fracture process AE is ideally suited.

The acoustic emission monitoring of the beam specimens in Chapter Three utilised a non-specialised, low sample rate (16 kHz) assemblage of equipment, which proved to be useful in conjunction with other methods of determining the initiation of growth but was not accurate enough to specifically define growth initiation on its own. Preliminary testing of embedded disbonds in sandwich panels showed that there is no accurately quantifiable change in the specimen stiffness after buckling or during growth. The only feedback indicating that disbond growth was occurring was the visible increase in the size of the buckled face-sheet region and the audible fracturing of the face-core interface. Monitoring the visible increase in the buckled disbond region would require continuous high-resolution surface scanning and such equipment was not available. Monitoring the acoustic emission is much simpler. The AE system utilised here is described in Appendix A.

6.5.1 ANALYSIS OF ACOUSTIC EMISSION DATA

The raw AE data for each test consisted of up to 3000 acoustic events sampled at 5 MHz, some of which were stored as transient files, which contain the full waveform of the acoustic event. For the remainder of the acoustic events, some general features are recorded by the acquisition system; rise time, duration, counts, amplitude and energy. Figure 6.5.1 is a sample transient file with these features indicated.

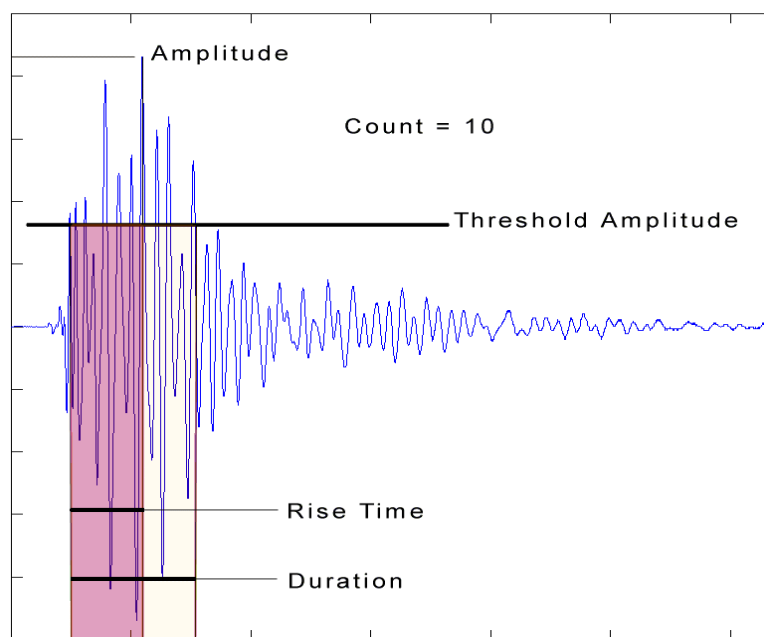


Figure 6.5.1 – Acoustic profile features recorded for every acoustic event

The issue of which acoustic features to use, and how to use them to identify disbond growth, is the subject of the next four sections.

6.5.1.1 CUMULATIVE ACOUSTIC EVENT COUNT

The AE data was recorded primarily to identify the initiation of disbond growth. Prior to testing it was assumed that the amount of acoustic activity would increase significantly when the disbond began to grow. The test results proved this to be generally true, however there were often individual disbond growth events that occurred well before failure. Figure 6.5.2 shows a typical plot of the cumulative acoustic event count during one test.

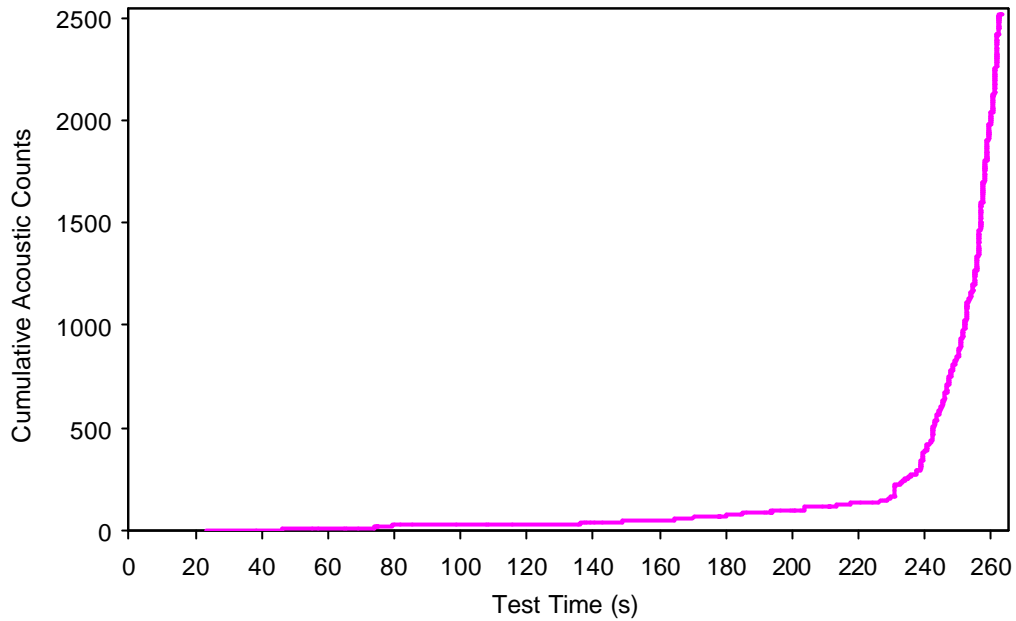


Figure 6.5.2 – Typical plot of cumulative acoustic event count during a test

Just prior to failure there is a rapid change in gradient of Figure 6.5.2. This was observed in all test cases and is likely to indicate the initiation of disbond growth (it almost certainly indicates the initiation of steady and continued growth). However, to accurately identify the first disbond growth event, an analysis of the individual acoustic events was required. Firstly though, the following general observations were made regarding the growth of disbonds in the test specimens:

1. Disbond growth occurred in small discrete fracture events at the two points on the disbond boundary that intersect a line running across the panel width through the centre of the disbond. This behaviour was observed by all authors studying embedded delaminations in solid laminates (Gaudenzi *et al.* 2001, Klug *et al.* 1996, Nilsson *et al.* 2001, Pradhan and Tay 1998, Riccio *et al.* 2001, Rinderknecht and Kroplin 1997, Tafreshi and Oswald 2003, Whitcomb 1992).
2. There were very few (approximately 1 to 5) discrete growth events before failure
3. Failure occurred when disbond growth became unstable and the disbond propagated through the entire panel width (extending in the bading direction also). The face-sheet remained intact (i.e. did not fracture) in all cases and failure was defined as a gross loss of structural stiffness.

6.5.1.2 TIME DOMAIN ANALYSIS

The analysis of acoustic events in order to identify particular damage types is a developing field of study. In the specific area of fibre fracture in composite materials, Pappas *et al.* (2004) presented a

thorough review of the literature. They also examine several methods of correlating acoustic signals with fibre fracture for a range of different fibres. The first of these methods was in the time domain, where they proposed a set of characteristic parameters, two of which are relevant to the results of this study (refer to Figure 6.5.1):

$$AvF = \frac{(\text{counts} - 1)}{\text{duration}} \quad (6.5.1)$$

$$THA = \frac{\text{threshold amplitude}}{\text{maximum amplitude}}$$

Pappas *et al.* (2004) only extracted acoustic signals for which $THA < 0.8$ and, for the range of fibres tested, the values of AvF (average frequency) that were found are given in Table 6.5.1.

Table 6.5.1 – Fibre fracture frequencies (Pappas *et al.* 2004)

Fibre	AvF (kHz)
Nextel 312	250
Nextel 720	320
Hi Nicalon	285
Carbon M40-B	280
Spectra PE-40	290
S-Glass	240
Kevlar 29	325

Utilising the definitions in (6.5.1) and by inspection of the AE data for all specimen tests, acoustic events corresponding to disbond growth events were identified by the following two criteria:

$$40\text{kHz} < AvF < 70\text{kHz} \quad (6.5.2)$$

$$THA < 0.7$$

This conclusion was based on the following facts:

1. Four of the 24 specimens displayed snap buckling of the disbonded face and a simultaneous small increment of disbond growth. All of the acoustic event/s recorded at the time of this disbond growth satisfied (6.5.2)
2. Of the events satisfying (6.5.2) none occurred before buckling. Given that there is no disbond growth before buckling, this is a necessary observation to validate (6.5.2).
3. It was observed during loading of the test specimens that there were one or two audible events accompanied by visible disbond growth. The audibility of these events indicated that

they would show up as the highest-energy events in the AE data. The highest-energy acoustic event in each of the tests had an AvF value of less than 70 kHz in 21 out of the 24 tests (and in the remaining 3 cases there was an event with AvF less than 70 kHz within 0.4 seconds of the highest energy event). In 19 out of the 24 tests the highest energy event had an AvF of less than 60 kHz. The actual distribution is shown in Figure 6.5.3.

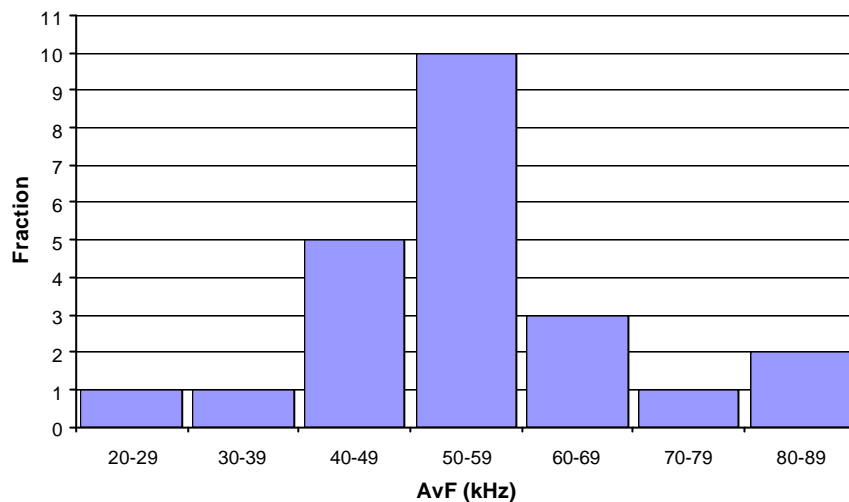


Figure 6.5.3 – Distribution of AvF values for the highest-energy events in each specimen test

4. Considering only those events for which $THA < 0.7$
 - a. AvF was less than 40 kHz for approximately 0.2% of all events (and for 14 of the 24 tests there were no values lower than 40 kHz)
 - b. The average value of AvF was 77 kHz
 - c. The average value of AvF for all events occurring before the first disbond growth event (6.5.2) was approximately 100 kHz (for 5 out of the 24 tests the first event was one for which $AvF < 70$ kHz)
5. In all of the tests a step increase in the cumulative number of acoustic counts corresponded to the occurrence of an event satisfying the criteria in (6.5.2)

Further investigation into the events satisfying (6.5.2) was performed using a frequency analysis of the recorded transient signals and is described in the next section.

6.5.1.3 FREQUENCY CONTENT OF THE ACOUSTIC EVENTS

The frequency content of acoustic events can be analysed to isolate frequencies specific to particular damage events (Giordano *et al.* 1998, Haselbach and Lauke 2003, Pappas *et al.* 2004). This analysis was first done in 1971 using a fast Fourier transform (FFT) of the transient waveform and since then many authors have used FFT analysis to identify damage in composite materials (Pappas *et al.* 2004).

Due to the large number of transient files obtained from each test (typically about 800) and the work involved in analysing each transient, it was not practical to analyse every one (a total of approximately 20,000 files). The desired result from this analysis was the identification of frequencies specific to disbond growth so that transients with these frequencies could be linked to growth events. Considering this aim and the restriction on the number of transients that can be analysed, it was proposed that transients from the following identifiable stages of the test be used:

1. Pre-buckling
2. Immediately after buckling
3. Between buckling and possible growth initiation
4. Possible growth initiation
5. Growth

Zone 2 is separated from zone 3 because the acoustic response of the beam specimens in Chapter Three indicated that there might often be an acoustic event immediately after buckling, due to an initial separation of the Teflon, used to create the disbond, and the core. Figure 6.5.4 shows an example of how these zones were defined in terms of the cumulative hit count (from Figure 6.5.2). Note that the definition of zone boundaries was partly subjective but that they also varied between specimens due to configuration differences.

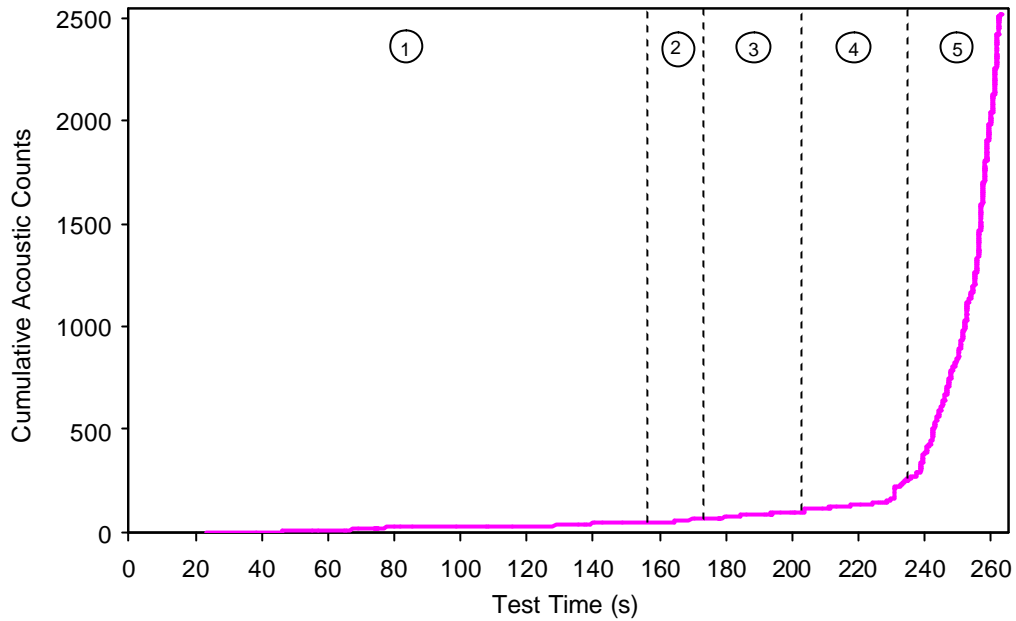


Figure 6.5.4 – Location of the zones from which transient files were taken

Totals of 11, 5, 9, 80 and 17 transients were taken from zones 1, 2, 3, 4 and 5, respectively, and the frequency content of each was analysed. The fast Fourier transform function in Matlab, *fft.m* (Matlab v5.3 help files) was used to create a frequency versus power plot for each transient waveform.

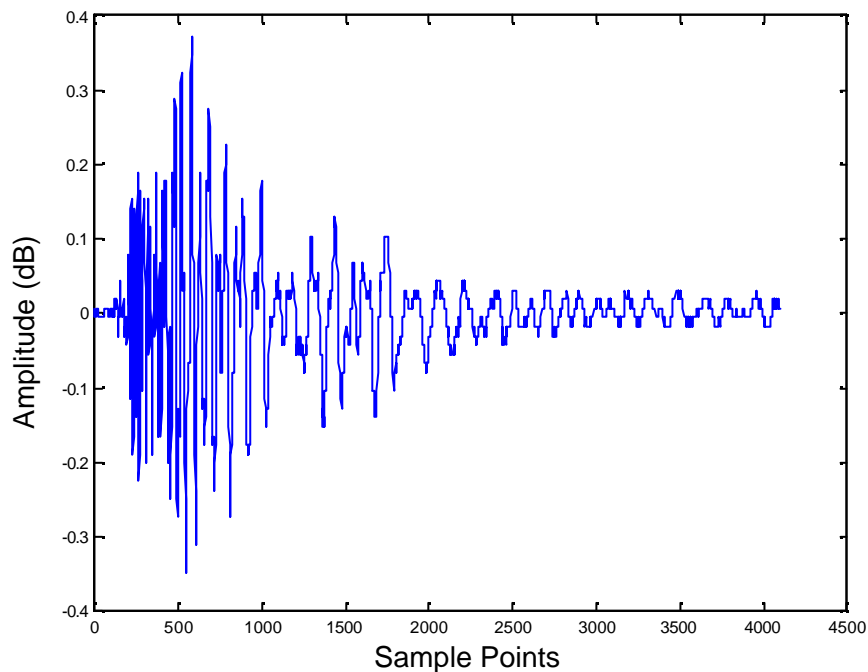


Figure 6.5.5 – Sample waveform of a zone four transient files

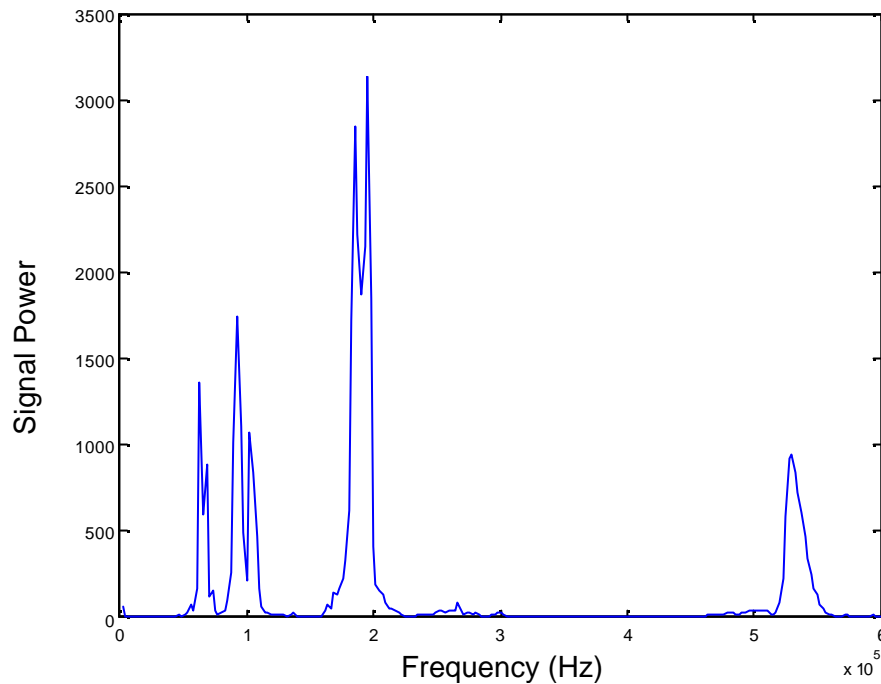


Figure 6.5.6 – Sample FFT of a zone four transient

A function was written in Matlab to isolate the top eleven frequency peaks from each of these plots and this data was used in a pivot table in Microsoft Excel. The dominant frequencies were isolated and frequencies lying within ± 3 kHz were included in the total number of occurrences of the dominant frequency. The values in Table 6.5.2 are the dominant frequencies in descending order of the number of occurrences of each frequency.

Table 6.5.2 – Dominant frequencies ordered from most to least common

Frequencies in ALL zones (kHz)
195
186
168
90
66
161
134
308
105
259

By far the most dominant frequencies (in terms of their power in the signal) in all transient files were 195 kHz and 186 kHz and it is therefore likely that these are the propagation frequencies (sonic transmission velocity) of the face-sheet.

Pappas *et al.* (2004) identified the propagation and fracture frequencies for a variety of fibre types by using ultrasonic testing in conjunction with AE monitoring. The values determined by Pappas *et al.* (2004) for S-Glass and Kevlar[®]-29 are given in Table 6.5.3.

Table 6.5.3 – Propagation and damage frequencies identified by Pappas et al. for fibre types similar to those in the present sandwich constituent materials

Fibre Type	Propagation Frequencies (kHz)	Fracture Frequencies (kHz)
S-Glass	136, 176, 360	59, 115, 223
Kevlar-29	229, 352	31, 196

Considering the fact that the fibres in the face-sheet have a similar modulus and density to S-Glass and the fibres in the Nomex[®] core are likewise similar to the Kevlar[®]-29, these frequencies may be compared to those in Table 6.5.2.

Table 6.5.4 – Comparison of fibre propagation and damage frequencies

S-Glass and Kevlar[®] 29 Frequencies [Pappas et al.]	Similar frequencies in Table 6.5.2
59 kHz *	66 kHz
115 kHz *	105 kHz
136 kHz	134 kHz
176 kHz	168, 186 kHz
196 kHz *	195 kHz

** These values represent the fibre fracture frequencies observed by Pappas et al. (2004)*

The result shows that at least some of the dominant frequencies observed in testing correspond approximately to identified propagation and fracture frequencies of similar fibres.

An attempt was made to isolate frequencies occurring exclusively in some zones and not in others but it was found that the number of transient files analysed was too small to do this with a reasonable level of statistical significance. For example, the frequencies of the post-buckling zones (2, 3, 4 and 5) were analysed and it was found that the peaks: 247 kHz, 61 kHz, 320 kHz and 522 kHz occurred exclusively in these zones. However, a simple statistical analysis showed that for the small number of total occurrences of these frequencies there was approximately a 34% chance that they would not occur in zone one anyway. In order to reduce this probability to 1%, for example, there would have to be four times as many transient samples taken.

The same statistical analysis was performed using only the transient files satisfying the growth criteria in (6.5.2) to identify any frequency peaks specifically associated with these transients. This resulted in a group of 220 frequency peaks out of the total of 1342. The analysis considered the number of occurrences of each frequency in the disbond growth sample versus the expected number of occurrences of a random sample of 220 from the 1342 total. It was assumed that the number of occurrences of each frequency would follow a binomial distribution and the probability of observing the disbond sample count for each frequency was calculated. For example, the 90 kHz peak occurred 26 times (1.9%) in the 1342 population and 6 times (2.7%) in the disbond growth sample. The mean and standard deviation of a random sample of 220 from the population are given by:

$$s_s = n_s p = 220 \times 1.9\% = 4.26$$

$$s = \sqrt{n_s p(1-p)} = 2.04$$

Given this sample distribution, the probability of the sample having exactly 6 occurrences of the 90 kHz frequency peak is given by:

$$P(X = 6) = \binom{220}{6} 0.019^6 (1 - 0.019)^{220-6} = 12\%$$

This value is determined from the probability mass function (PMF). The cumulative density function (CDF) gives the probability of 6 or more occurrences of this frequency (equal to 26% for this example). Figure 6.5.7 shows sample binomial distributions with a mean of four and variance of two and illustrates the meaning of the PMF and CDF values. Note that the cumulative density function (CDF) is not shown, rather the method of determining it is illustrated with the use of the PMF.

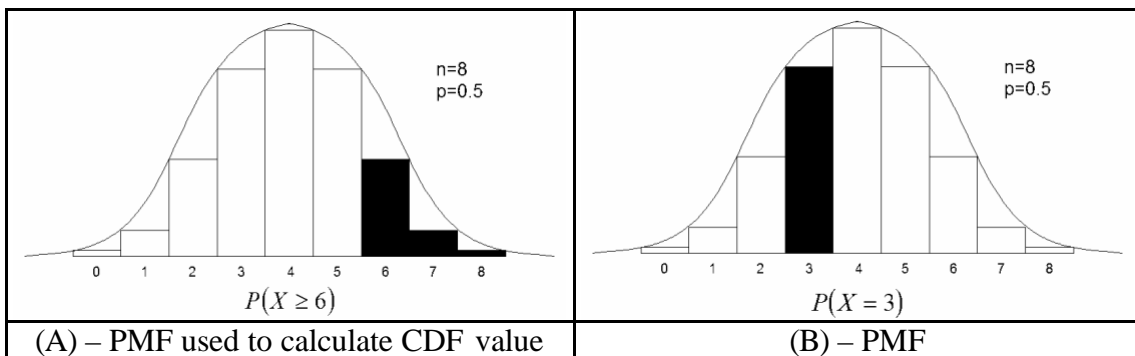


Figure 6.5.7 – Examples of binomial distribution curves for different probabilities

The minimum CDF value (out of $P(X \leq S_s)$ and $P(X \geq S_s)$) is given in the right-most column of Table 6.5.5, where only frequency peaks with a CDF value of less than 10% are shown.

Table 6.5.5 – Probabilities of the disbond growth frequency occurrences being random

Frequency Group	S_s	S_p	PMF $P(X=S_s)$	CDF value
78 kHz	0.91 %	0.22 %	7.4 %	8.8 %
85 kHz	1.36 %	0.45 %	5.9 %	7.7 %
88 kHz	2.27 %	0.97 %	4.3 %	6.4 %
98 kHz	2.73 %	1.04 %	2.0 %	2.9 %
234 kHz	0.91 %	0.22 %	7.4 %	8.8 %
249 kHz	1.36 %	0.30 %	2.4 %	2.9 %

The two frequencies that stand out in Table 6.5.5 are 98 kHz and 249 kHz. There is only a 2.0% chance that the observed number of 98 kHz peaks would occur randomly and only a 0.9% chance of randomly observing more than this number of occurrences. These probabilities are similar for the 249 kHz peaks. It is concluded that these frequency peaks occur more often in acoustic events associated with disbond growth and therefore that they are likely to be characteristic frequencies of core fracture (due to the observation in Chapter Three that the disbond propagates through the core). The fact that these frequencies do not occur exclusively in disbond growth events is not unexpected. Stresses throughout the core may cause core fibres and matrix to fracture in very localised regions at any time during loading.

6.5.1.4 CONCLUSIONS

A criterion for identifying disbond growth was established and is defined as an acoustic event satisfying the following two criteria:

$$40 \text{ kHz} < A_v F < 70 \text{ kHz}$$

$$THA < 0.7$$

The frequency analysis ultimately proved to be unable to isolate a disbond growth event. It did, however, identify the dominant frequencies in all cases, which were 195 kHz and 186 kHz and these are assumed to be the propagation frequencies of the face-sheet. The frequencies 98 kHz and 249 kHz occur more often in acoustic events that satisfy the criteria for disbond growth (above) and as such they are likely to be characteristic of core fracture. A similar frequency analysis of a larger sample size may have been able to identify, with statistical significance, frequencies associated with disbond growth.

Based on the criteria discussed above, the disbond growth initiation loads were determined (Table 6.5.6).

Table 6.5.6 – Loads for buckling, growth initiation and failure events for all specimens

Specimen Designation	Buckling Load (N/m)		Growth Initiation Load (N/m)		Failure Load (N/m)	
	Mean	Conf. Range	Mean	Conf. Range	Mean	Conf. Range
25-G	24900	± 3.6%	42722	± 19.8%	54333	± 6.4%
25-GH	17144	± 8.1%	26756	± 25.4%	38438	± 7.6%
50-G	7832	± 7.4%	28000	± 25.4%	40092	± 5.0%
50-GH	4849	± 13.6%	14242	± 62.8%	27992	± 10.6%
75-G	3385	± 20.9%	21313	± 13.2%	33975	± 10.0%
75-GH	1894	± 19.7%	14727	± 18.7%	25245	± 6.2%

The confidence range in Table 6.5.6 is the range within which the population mean is expected to lie 95% of the time.

Table 6.5.7 – Fraction of post-buckling load at which growth initiates

Specimen Designation	Growth Ratio
25-G	61%
25-GH	45%
50-G	63%
50-GH	41%
75-G	59%
75-GH	55%

The growth ratio is defined as:

$$GrowthRatio = \frac{N_{grow} - N_{cr}}{N_{ult} - N_{cr}}$$

This is the fraction of the post-buckling load at which disbond growth initiated. Note that for the specimens with G-type face-sheets the growth ratio range is 59% to 63% and for specimens with GH-type face-sheets the range is 41% to 55%. However, given the large spread of growth initiation values it would not be reasonable to predict the failure load by using these ratios along with a known growth initiation load. They do, however, provide some insight into the failure process.

These results are plotted in Figure 6.5.8 and Figure 6.5.9, where the failure for a panel with no disbond is included. Failure is assumed to be due to wrinkling in this case and the wrinkling loads experimentally determined by Aitken (2000) are used (see Section 6.3.1).

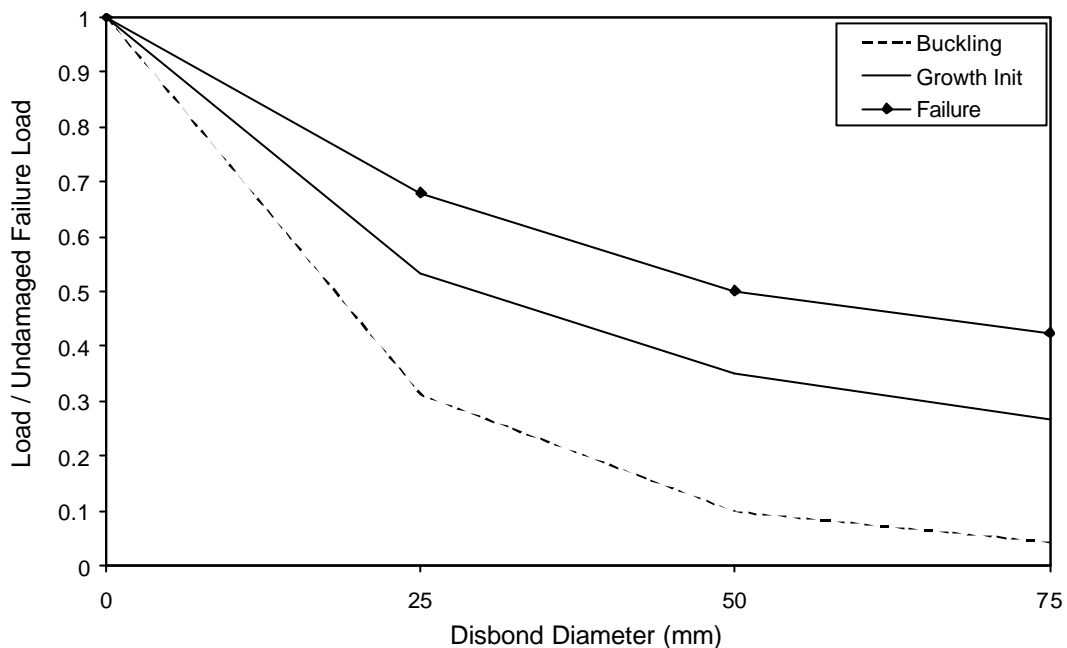


Figure 6.5.8 – Buckling, growth initiation and failure loads with G-type face-sheets

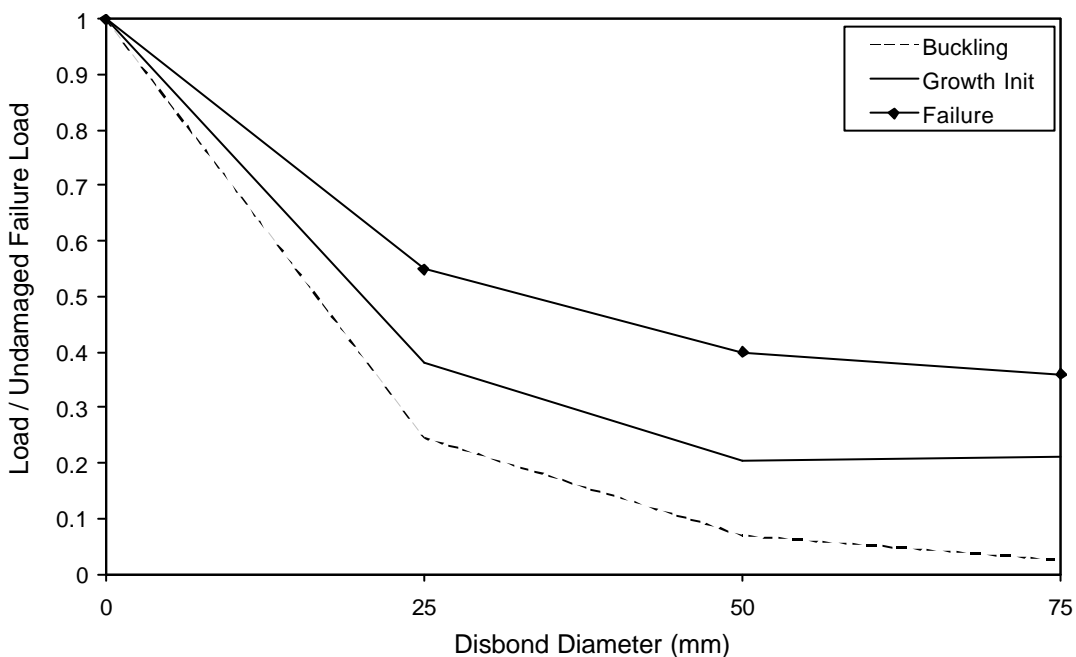


Figure 6.5.9 – Buckling, growth initiation and failure loads with GH-type face-sheets

Observation of the tests as they progressed indicated that disbond growth initiated very shortly before failure. The AE results indicate that the first growth increments occurred well before failure, at approximately 50% of the post-buckling load. This discrepancy is considered to be due to the sensitivity of the AE monitoring equipment and the fact that it would pick up increments of growth that were not audible and did not result in a visible increase in disbond size.

6.6 CONCLUSIONS

The following points summarise the findings of the specimen testing described in this chapter:

- Of the literature reviewed there is a significant lack of experimental studies into the behaviour of sandwich panels containing embedded disbonds
- The failure processes of the tested specimens can be generally described as; disbond buckling; continued loading where the stiffness of the structure remains virtually the same as in pre-buckling; several discrete growth increments followed soon after by unstable disbond growth to the edges of the panel. Failure is defined as a gross loss of structural stiffness.
- The maximum observed reduction in load carrying capacity was 64%, due to the presence of a 75mm diameter disbond. The minimum reduction was 32%, for a 25mm diameter disbond
- Acoustic emission monitoring was successfully used to determine the initiation of disbond growth. This proved to be a difficult task, involving considerable analysis of a large amount of data but no better method was determined.
- The AE results offered generalised results regarding the specific frequencies associated with disbond growth for the combination of core and face-sheet used.
- Observation of the tests indicated that disbond growth initiated very shortly before failure. The AE monitoring indicated that the first increments of growth were in fact very small and occurred at approximately 50% of the post-buckling load.
- The growth initiation loads displayed a high degree of scatter (up to $\pm 63\%$). This indicates that these first growth increments are very sensitive and quite small. The fact that they were not visually detectable during testing indicates that they involved growth over a distance smaller than (or possibly equal to) one cell diameter (3.2mm).
- The failure load is much less sensitive to disbond size than the buckling load. This was illustrated by fitting a power function to the load curves. The failure load was found to be proportional to the disbond diameter raised to the power of approximately -0.4 . This power is an indication of the damage tolerance of the tested panels (considering that a power of zero represents a perfectly damage tolerant structure). The buckling load was found to be inversely proportional to the disbond diameter squared, as it is for Euler buckling of a column.

CHAPTER SEVEN

Modelling Disbond Buckling in Sandwich Panels

7.1 INTRODUCTION

The study of sandwich beams, described in Chapters Three through Five, considered a relatively simple physical example of disbonding. A more realistic situation is a sandwich panel with an embedded circular or elliptical disbond, as described in Chapter Six. The beam study provided valuable insight into the problem of disbonding. Not only did it identify several characteristic expressions defining buckling and growth of disbonds, it also verified that a Winkler beam is an accurate method of modelling localised compression behaviour of sandwich structure. The study of sandwich panels with embedded disbonds will follow the same approach developed in the beam study; a linear buckling analysis followed by a non-linear post-buckling analysis. Although the specimen test results from Chapter Six indicated that the load carrying capacity far exceeds the buckling load, a complete non-linear post-buckling analysis requires an accurate prediction of buckling load and mode shape. Therefore this chapter develops and validates a linear buckling analysis, following a review of the existing relevant literature.

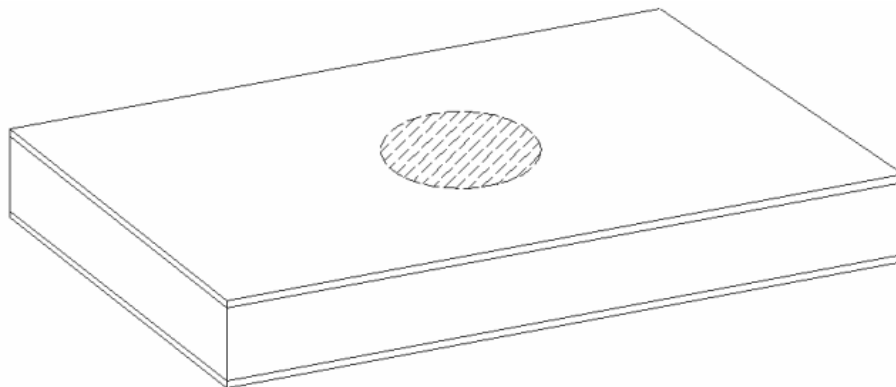


Figure 7.1.1 – Embedded face-core disbond in a sandwich panel

7.1.1 LITERATURE REVIEW

Very few authors have extended upon the through-width disbond model to investigate embedded disbonds.

Hansen (1998) described a finite element model using shell elements to model the face-sheet and solid elements to model the core. He concluded that this model is “expensive”, in terms of computational time, and that the structure is equally well modelled as a plate on an elastic foundation for the majority of practical cases and the differences in the models are small in any case. He also demonstrated that the assumption of clamped boundary conditions (at the disbond boundaries), which is appropriate for delaminations in laminated composites, is a very crude assumption when considering sandwich structures, where the core modulus is typically orders of magnitude lower than the face-sheet modulus. From the results of two specimen tests Hansen concluded that the buckling load of a disbonded region is “a key parameter in assessing the structural integrity of a sandwich component in compression”.

Lin *et al.* (1996) developed a Winkler plate model (a plate on an elastic foundation) to predict disbond buckling loads. The model incorporated core shear stiffness, which was subsequently found to have a negligible effect on the buckling load. The method was the two-dimensional equivalent of the one-dimensional Winkler beam model of Cheng *et al.* (1997). This model was not compared with specimen test results so its accuracy could not be commented on.

This Chapter presents a model of a plate on a Winkler foundation (herein referred to as a Winkler plate) use to predict disbond buckling. The model extends on that of Cheng *et al.* (1997) by including the refined core stiffness term. This Chapter also describes a non-dimensional regression analysis that was used to obtain insights into the buckling of embedded disbonds. The effects of disbond shape and proximity to a panel edge were investigated and are described at the end of this chapter.

7.2 A WINKLER PLATE MODEL

7.2.1 PANEL BUCKLING

The first step in the analysis of the failure process of a disbonded sandwich panel under compression is prediction of the buckling load. This was done with an eigenvalue analysis of the governing linear equations of a Winkler plate. The effects of core shear are neglected as their effect on the buckling load is negligible (Lin *et al.* 1996).

7.2.1.1 SOLUTION PROCEDURE

The governing equation of an orthotropic plate in the x - y plane, under uniaxial x -direction compressive loading, on an elastic foundation is given in terms of z -direction displacement functions by (Reddy 2004):

$$D_{11} \frac{\partial^4 w}{\partial x^4} + 2(D_{12} + 2D_{66}) \frac{\partial^4 w}{\partial x^2 \partial y^2} + D_{22} \frac{\partial^4 w}{\partial y^4} + N_x \frac{\partial^2 w}{\partial x^2} + kw = 0 \quad (7.2.1)$$

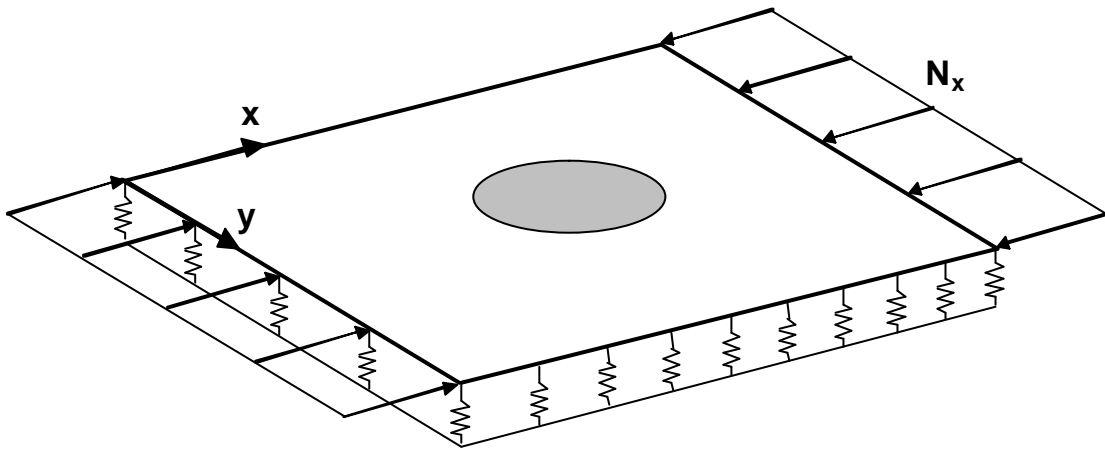


Figure 7.2.1 – Winkler plate in uni-axial compression

Equation (7.2.1) was discretised using a central finite differencing scheme. In matrix notation this can be represented by:

$$[A]\underline{w} - N_x [C]\underline{w} = 0 \quad (7.2.2)$$

Matrix $[A]$ contains the coefficients in (7.2.1) that do not involve N_x . Matrix $[C]$ contains the remaining coefficients, with N_x taken out as a common factor. Rewriting (7.2.2) in the familiar eigenvalue form:

$$\left| [C]^{-1}[A] - N_x[I] \right|_{\underline{w}} = 0 \quad (7.2.3)$$

The lowest eigenvalue of the matrix $[C]^{-1}[A]$ is the buckling load. This eigenvalue problem was solved using Arnoldi iteration with implicit restarts, via the function *eigs* in Matlab (Version 5.3). Note that this is the same solution procedure used to solve the beam-buckling model presented in Chapter Four.

7.2.1.2 INCORPORATING AN EMBEDDED DISBOND

The disbond is introduced by reducing the foundation stiffness to zero at every node in the disbonded region, using the function $S(x,y)$.

$$S(x,y) = \begin{cases} 0 & \text{in the disbond region} \\ \mathbf{a} & \text{at the disbond boundary} \\ 1 & \text{in the bonded region} \end{cases} \quad 0 < \mathbf{a} < 1 \quad (7.2.4)$$

The value of \mathbf{a} represents the fraction of the area represented by a node that contains core support. The simplest example is a node that lies exactly on the boundary of the disbond, for which \mathbf{a} is equal to 0.5 because only half of the area around the node is bonded. See Appendix D for a complete description of the method of determining \mathbf{a} .

This method can be adapted to suit any disbond shape. It also allows for the possibility of modelling a damaged core region (where the modulus is a known fraction, f_E , of the undamaged core) by using f_E instead of zero in $S(x,y)$. The same approach could be used to incorporate a variable face-sheet thickness (e.g. to model the effect of a tapered patch repair). This makes the present modelling method extremely useful for considering the effects of a variety of discontinuities on the buckling behaviour.

7.2.1.3 FOUNDATION STIFFNESS TERM

The refined foundation stiffness term described in Chapter Four is equally as accurate in a panel model as it is in a beam model. The rest of this section explains why this is so, justifying the use of the unmodified stiffness term in the Winkler plate model.

The refined foundation stiffness was derived by Horrigan (2005), who extended on the analysis of Vonach and Rammerstorfer (2000), by modelling the finite thickness of a sandwich core. The core was assumed to be in a state of plane stress. The analysis was further extended, as part of the present work, to incorporate plane strain conditions in the core (see Appendix E). The refined foundation

stiffness has so far only been used in a two-dimensional Winkler beam analysis. Before using it in a three-dimensional Winkler plate analysis, the accuracy of doing so must be assessed. Vonach and Rammerstorfer (2000) set out to determine this dimensionality problem for the case of sandwich panel wrinkling. They developed a three-dimensional finite element model of a sandwich panel, modelling the core with solid elements and the face-sheet (only one was modelled and the core was treated as being infinitely thick) with shell elements. The model verified that the two-dimensional foundation stiffness is applicable for general three-dimensional (plate) face-sheet displacements.

That the refined Winkler beam foundation stiffness applies equally to a Winkler plate model can also be shown for the typical definition of foundation stiffness:

$$k = \frac{E_c}{t_c} \quad (7.2.5)$$

Equation (7.2.5) is derived in Chapter Four assuming a constant face-sheet displacement, w^* . However it is evident by observation of (4.2.9) that (7.2.5) is valid for any general face-sheet displacement function, $w(x,y)$, because the differentiation of (4.2.9) is with respect to z only. This approach assumes a linear core displacement function.

Zenkert (1997) developed an expression for the effective core stiffness of a sandwich panel with a general bi-directional sinusoidal face-sheet displacement:

$$w_f = W \sin \frac{\mathbf{p}x}{L_x} \sin \frac{\mathbf{p}y}{L_y} \quad (7.2.6)$$

He assumed an exponential decay displacement function in an infinitely thick core. Zenkert (1997) noted that the exponential displacement decay was sufficiently rapid for the assumption of an infinitely thick core to be reasonable. The following illustration summarises the three approaches described, including the assumed core and face-sheet displacements for each. The core displacement function for method three is shown with the assumption that the bottom face-sheet has zero displacement, whereas in the actual derivation the core displacement is symmetric about the core mid-plane.

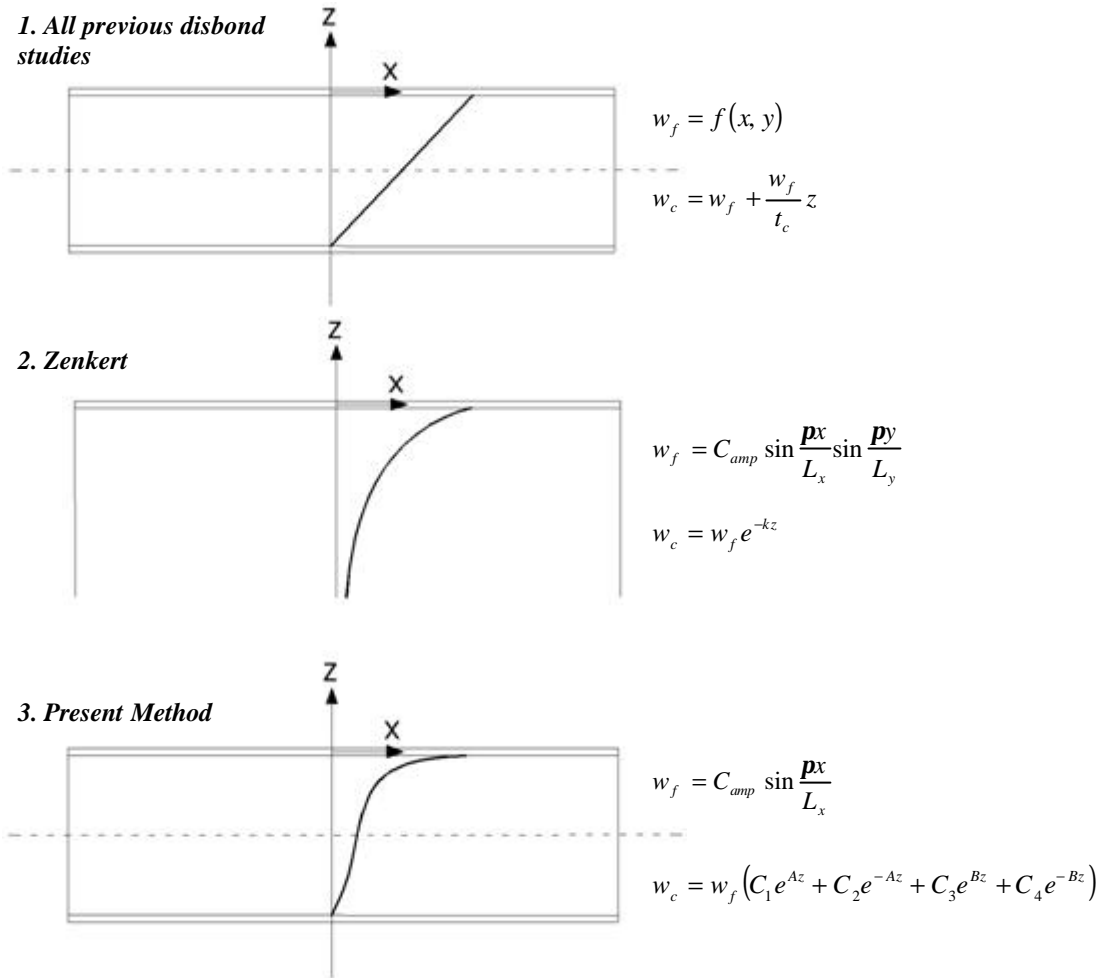


Table 7.2.1 shows the stiffness definitions obtained from each of the three methods described.

Table 7.2.1 – Foundation stiffness definitions from three methods

Method	Foundation Stiffness	Reference Value [#]
1	$k = \frac{E_z^c}{t_c}$	5.1×10^9
2	$k = \sqrt[3]{\frac{(E_z^c G_{xz}^c)^2}{D_f}} \quad (L_x = L_y)$	5.0×10^{10}
	$k = \sqrt[3]{\frac{(E_z^c G_{xz}^c)^2}{2D_f}} \quad (L_y = \infty)$	4.0×10^{10}
3	Based on the solution to Airy's stress function for a plane strain orthotropic material (See Chapter Four)	1.7×10^{10}

[#] Based on the sandwich panels used in Chapter Three testing

Method 1 is valid for any general face-sheet displacement. The solution to method 2 depends on the ratio of L_x to L_y (the orthogonal face-sheet wavelengths). Assuming them to be equal (i.e. biaxial sinusoidal face-sheet displacement) results in a stiffness term approximately 25% higher than the uniaxial sinusoidal face-sheet displacement result. Method 3 does not have a closed form solution and has been shown to apply for a general three-dimensional face-sheet displacement (Vonach and Rammerstorfer 2000).

Typical values determined from each method are given for comparison in Table 7.2.1. Another method of determining effective stiffness values is to consider the familiar wrinkling load equation proposed by Hoff and Mautner (cited in Zenkert 1997):

$$\begin{aligned} \mathbf{s} &= 0.5 \sqrt[3]{E_z^c G_{xz}^c E_f} \\ \Rightarrow P &= 1.145 \sqrt[3]{E_z^c G_{xz}^c D_f} \end{aligned} \quad (7.2.7)$$

Comparing this to the general expression for wrinkling load of a beam on a Winkler foundation (Niu and Talreja 1999):

$$P = 2 \sqrt{k D_f} \quad (7.2.8)$$

Equating (7.2.7) and (7.2.8) results in the following effective foundation stiffness:

$$k = 0.328 \sqrt[3]{\frac{(E_z^c G_{xz}^c)^2}{D_f}} \quad (7.2.9)$$

As expected this is of the same form as method 2 (Zenkert 1997) above. For comparison, the stiffness obtained from (7.2.9) for the same material properties as used in Table 7.2.1 is 1.64×10^{10} , which is similar to the stiffness obtained through the present method. It is apparent that the assumed displacement functions of methods 1 and 2 significantly affect the effective stiffness. Method 3 (the present method) provides an accurate result that is applicable to both Winkler beam (two-dimensional) and Winkler plate (three-dimensional) models.

7.3 COMPARISON WITH SPECIMEN TEST RESULTS

The buckling load results from the specimen testing described in Chapter Six were used as a comparison to the present buckling model (Table 7.3.1). All input material properties to the model are given in Tables 3.5.2 and 3.5.3 (Chapter Three).

Table 7.3.1 – Comparison of Experimental and Model Buckling Loads

Specimen Designation	N_{cr} (testing)	N_{cr} (model)	Difference	Exp. Conf. Range[#]
25-G-100	24900*	23895	-4.0 %	± 3.6%
25-GH-50	17144	16564	-3.4 %	± 8.1%
50-G-100	7832	7242	-7.5 %	± 7.4%
50-GH-200	4849	4864	0.3 %	± 13.6%
75-G-300	3385	3448	1.9 %	± 25.1%
75-GH-150	1700	2298	35.2 %	± 25.1%
		<i>Mean</i>	3.7 %	
		<i>Std. Dev.</i>	15.8 %	

**Snap buckling occurred for all specimens so this value was extrapolated using the laser gauge results*

Experimental confidence range (refer Chapter Six)

Table 7.3.1 shows close agreement between the experimental and model results. The 35% difference apparent in the last test specimen should be considered alongside the confidence range of the experimental results (refer to Table 7.5.6 in the previous chapter). Ignoring this single large difference reduces the average difference to -2.6% with a standard deviation of 3.7%. The effects of the various ratios of panel width to disbond diameter appear to have had little or no effect on the experimental buckling loads (this result is explained in the next section).

7.4 NON-DIMENSIONAL ANALYSIS

In Chapters Four and Five a non-dimensional analysis was considered for each problem and the relationship between the dimensionless parameters was determined by regression to data from the respective models. In each case this provided characteristic curves that concisely expressed the model behaviour and proved to be useful tools. The same approach is applied here as a method of presenting the buckling load results for the Winkler plate model.

For the non-dimensional analysis the following dimensionless parameters are used (derivation in Appendix B):

$$\Pi_N = \frac{N_x L_d^2}{4p^2 D_{11}}, \quad \Pi_k = \frac{L_d}{p} \sqrt[4]{\frac{k}{D_{11}}}, \quad \Pi_D = \frac{D_{22}}{D_{11}}, \quad \Pi_G = \frac{D_{12} + 2D_{66}}{D_{11}} \quad (7.4.1)$$

For the initial analysis the face-sheet was assumed to be isotropic, which was enforced by the following definitions:

$$D_{11} = D_{22} = D_f \quad \text{and} \quad G_{xy}^f = \frac{E_x^f}{2 + 2\nu_f} \quad (7.4.2)$$

The result of (7.4.2) is that Π_D and Π_G are unity. The Buckingham Π -theorem (White 1994) implies that the relationship between the remaining non-dimensional parameters can be expressed as:

$$\Pi_N = f(\Pi_k) \quad (7.4.3)$$

Assuming a function of the form:

$$\Pi_N = \frac{c_1}{\Pi_k^3} + \frac{c_2}{\Pi_k^2} + \frac{c_3}{\Pi_k} + c_4 \quad (7.4.4)$$

The constants in (7.4.4) were determined by regression to buckling model data, which was obtained by independently varying each of the variables, D_f , k and L , over a range of 10 values. A least-squares power curve fit then provided the four constants, with an R^2 of 1:

$$\Pi_N = 2.74 - \frac{0.63}{\Pi_k^3} + \frac{2.86}{\Pi_k^2} - \frac{4.50}{\Pi_k} \quad (7.4.5)$$

Equation (7.4.5) is a characteristic expression for embedded disbond buckling in a sandwich panel and is comparable to the characteristic beam buckling expression. Note that the general expression for the Euler buckling load of a square plate of side-length b can be expressed as:

$$N_{cr} = C_{PE} \frac{4p^2 D_f}{b^2} \tag{7.4.6}$$

The value of C_{PE} for a square plate with all edges simply-supported is 1, and for a square plate with all edges built-in C_{PE} is 2.68. Π_N represents the actual value of C_{PE} for a square embedded disbond in a sandwich plate and its value will lie somewhere between zero and 2.68. This function is defined by the characteristic panel curve (Figure 7.4.1). This is a similar result to the characteristic Winkler beam buckling curve (Chapter Four).

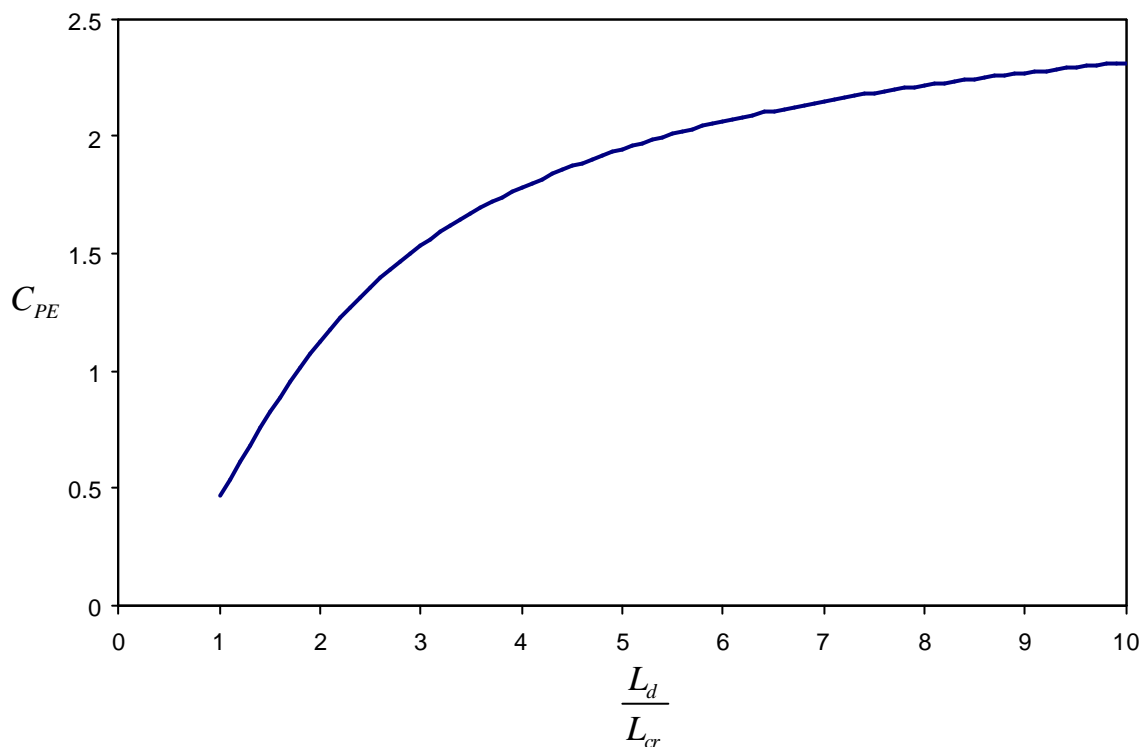


Figure 7.4.1 – Characteristic buckling curve for a sandwich panel with an embedded circular disbond of diameter L_d

For the Winkler beam it was found that the simply supported disbond edge condition corresponded to a relative disbond length of 1. From Figure 7.4.1 it is apparent that, in the Winkler plate model this occurs when the relative disbond diameter is two. This means that when the disbond diameter is equal to the wrinkling wavelength then the circular disbond behaves as though it had simply supported edge conditions. In form Figure 7.4.1 is very similar to the characteristic curve for a Winkler beam.

Another type of characteristic buckling curve, proposed by Niu and Talreja (1999), uses the wrinkling load of undamaged sandwich to normalise the buckling load. The wrinkling load for an infinitely long and wide panel (with either built-in or simply supported end conditions) is given as:

$$P_{wr} = 2\sqrt{kD_f} \quad (7.4.7)$$

Niu and Talreja (1999) utilised this term for normalising results from a Winkler beam model. In the present analysis the same term is used to normalise the Winkler plate model. The curve in Figure 7.4.2 is obtained.

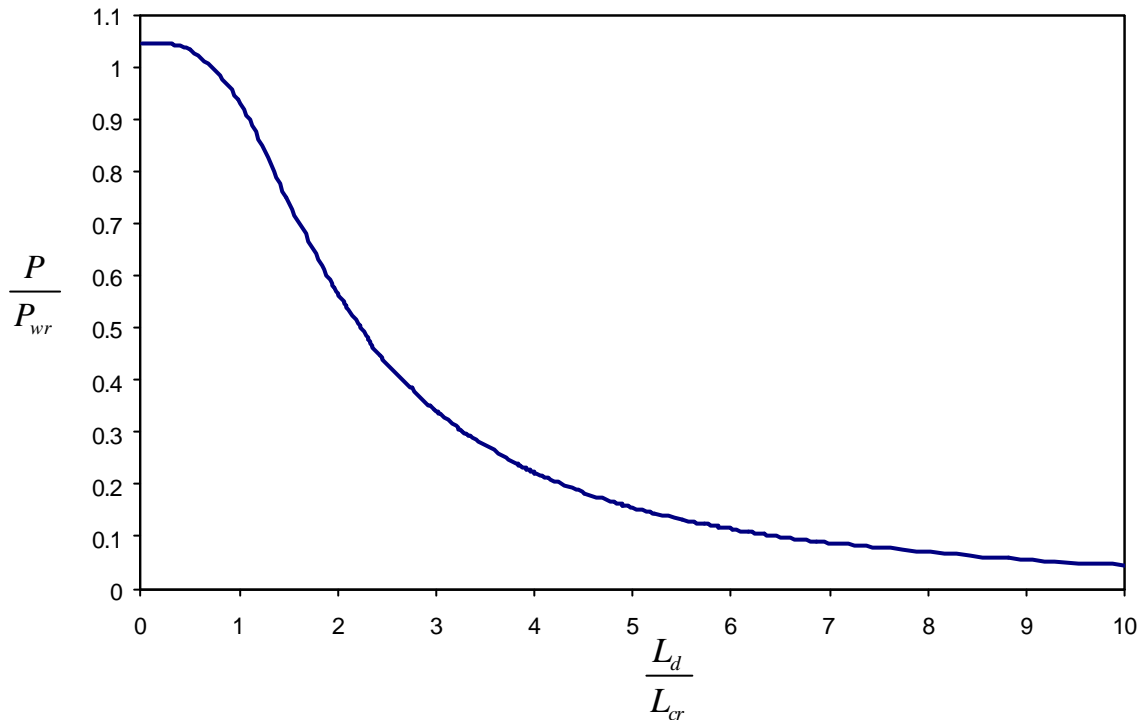


Figure 7.4.2 – Master buckling curve for an embedded disbond in a sandwich panel

A first point to note is that the load exceeds the wrinkling load for a zero length disbond. This was also observed by Niu and Talreja (1999). In the present case it is due to plane strain effects in the panel model that are not incorporated in to the wrinkling load definition. Comparison to the master curve presented by Niu and Talreja (1999) shows that the panel curve in Figure 7.4.2 is of the same form as that for a beam with a through-width disbond. In fact Figure 7.4.2 is identical to the master curve presented by Niu and Talreja (1999) for a Winkler beam if the disbond radius is used as the characteristic disbond length instead of the disbond diameter. However, in order to more accurately obtain the wrinkling wavelength and load for normalising, the refined foundation stiffness used in the present model should be used (particularly for sandwich panels with honeycomb core).

7.4.1 EFFECTS OF AN ORTHOTROPIC FACE MATERIAL

Frequently the facing of a sandwich structure is an orthotropic laminate of fibre composite materials. To consider the effects of orthotropy the constraints defined in (7.4.2) are relaxed and all of the non-dimensional parameters, (7.4.1), are considered. The last two of these parameters are unity for the isotropic case, which is how they were ignored in the previous analysis. As before, the functional relationship between these parameters is given by the Buckingham Π -theorem (White 1994) as:

$$\Pi_N = f(\Pi_k, \Pi_D, \Pi_G) \quad (7.4.8)$$

Regressing (7.4.8) to model data yielded (7.4.9) with an R^2 of 0.97.

$$\Pi_N = \left(2.74 - \frac{0.08}{\Pi_k^3} + \frac{0.71}{\Pi_k^2} - \frac{2.25}{\Pi_k} \right) (\Pi_D)^{0.38} (\Pi_G)^{0.17} \quad (7.4.9)$$

The additional parameters are effectively scaling parameters to the isotropic characteristic curve. For example, if Π_D is equal to $\frac{1}{2}$ then the characteristic curve is scaled to 77% of the isotropic curve, or if Π_G is equal to $\frac{1}{2}$ then the characteristic curve is scaled to 89% of the isotropic curve. Figure 7.4.3 shows the isotropic characteristic curve along with two curves of varying orthotropy.

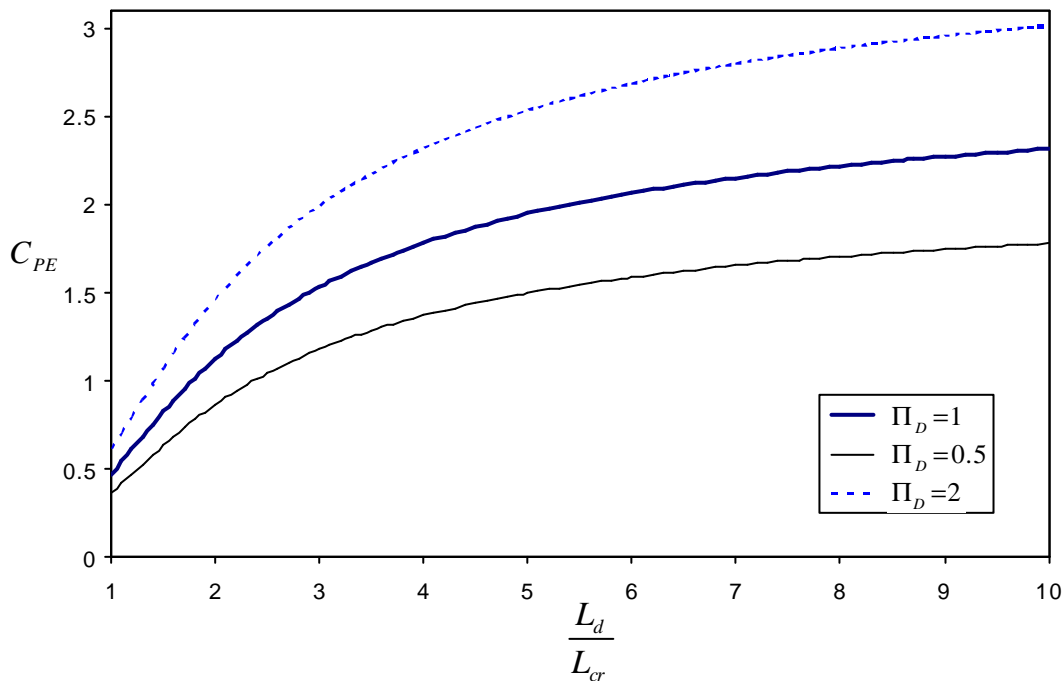


Figure 7.4.3 – Characteristic curves for three different orthotropy ratios

A typical carbon/epoxy laminate may have an orthotropy ratio of 12 and Figure 7.4.3 shows even that for an orthotropy ratio of 2 the buckling load is affected to the order of 20%. Therefore face-sheet orthotropy must always be modelled when applicable, as it has significant influence on buckling load.

7.5 EDGE EFFECTS AND DISBOND SHAPE EFFECTS

The model is capable of including any number of circular or rectangular disbonds located anywhere in a sandwich panel. It is also capable of modelling any number of arbitrarily shaped disbonds, although this feature was not utilised in this research. In practice, the shape of a disbond is approximated by a simple geometrical shape. For example, the Boeing structural repair manual (SRM) for the 767-300 aircraft defines the size of a disbond by the diameter of the smallest circle required to completely encompass it. It is therefore practically relevant, in terms of providing conservative buckling load results, to consider a circular disbond as this model does. However, it is useful to gauge the approximate effect of the assumed disbond shape. The two considerations of this section are the effects of disbond proximity to a restrained edge and disbond shape.

7.5.1 PROXIMITY TO A RESTRAINED EDGE

The edge effects were considered by varying the ratio, R , of panel width, L , to disbond diameter, L_d , for a circular disbond located centrally in a panel. Five specimen configurations were considered. All configurations had built-in conditions at the panel boundaries. Table 7.5.1 identifies each configuration. Notice that the configuration is defined purely by the ratio of disbond length to natural wavelength.

Table 7.5.1 – Configurations used to examine edge effects

Configuration	L_d / L_α
C1	3.6
C2	4.2
C3	5.0
C4	7.1
C5	10.7

Figure 7.5.1 illustrates the effect of varying R for each configuration. The loads, N , were normalised to the loads for very large R -values, N_{inf} . This provides a simple means of comparing the results on one plot.

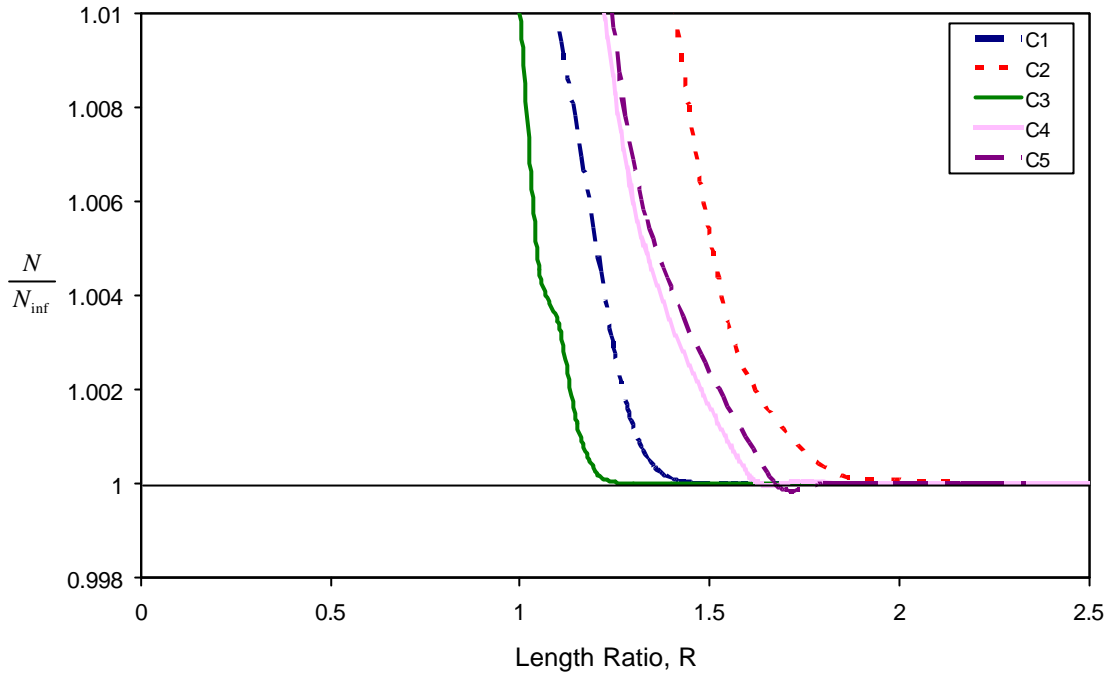


Figure 7.5.1 – Edge effects for each of the five configurations

For the tested configurations the critical ratio of R (the value at which the edge proximity affects the buckling load) varies between 1.25 and 2.1. Knowing that the natural wavelength is a characteristic value for sandwich buckling problems (Chapter Four), the ratio R_L was defined as:

$$R_L = \frac{L}{L_d + 4L_{cr}} \tag{7.5.1}$$

This is the ratio of the panel width to the disbond diameter plus four times the natural wavelength, L_{cr} , defined as:

$$L_{cr} = \mathbf{P}^4 \sqrt{\frac{D_f}{k}} \tag{7.5.2}$$

Figure 7.5.2 shows the effect of defining the ratio this way.

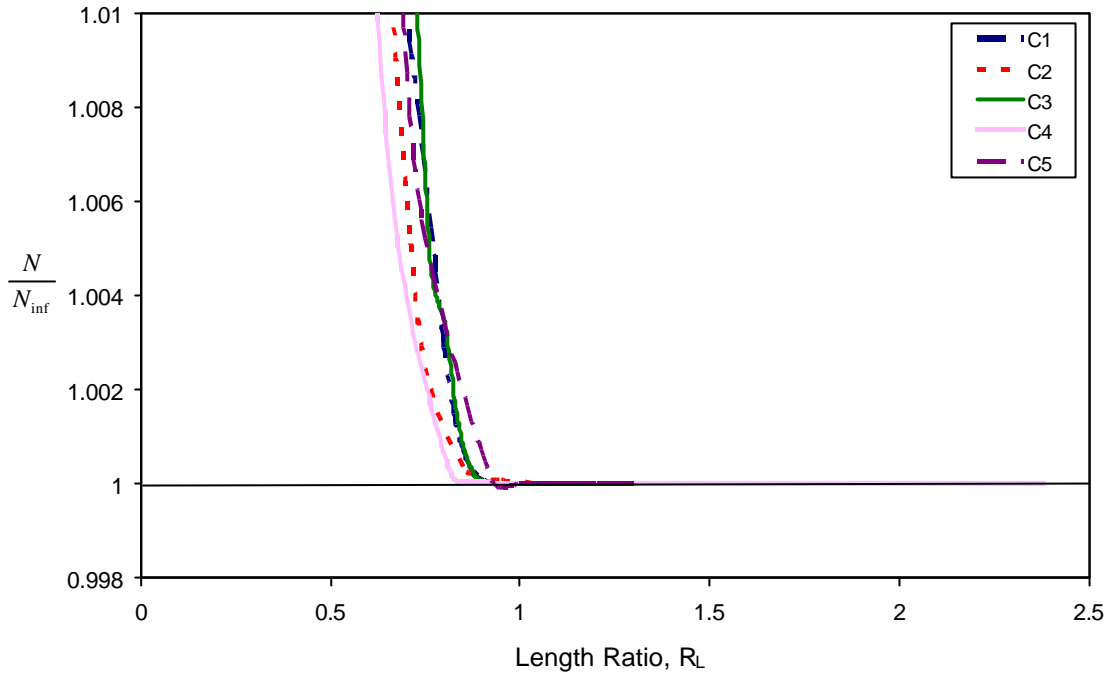


Figure 7.5.2 – Edge effect comparison with the modified width ratio

Figure 7.5.3 demonstrates the main finding of the edge effects analysis; that the natural wavelength is a characteristic value in relation to edge effects and that edge effects are negligible if the distance between the disbond edge and the panel edge is greater than twice the natural half-wavelength, L_{cr} .

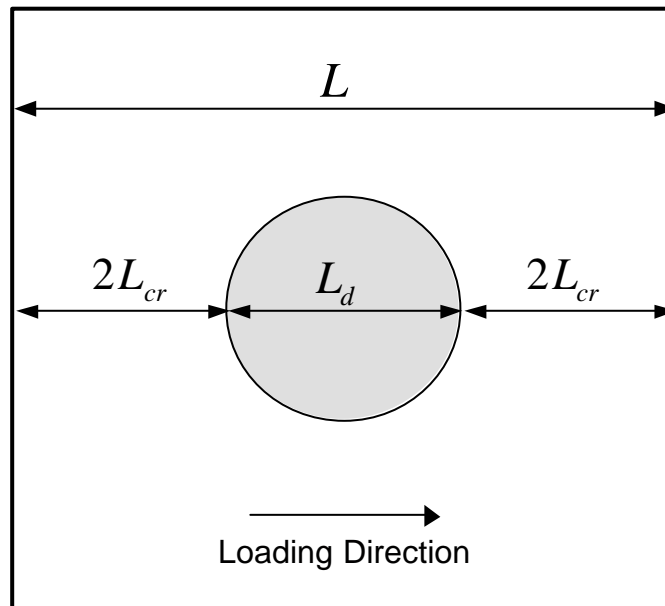


Figure 7.5.3 – An illustration of the minimum required panel size, to avoid edge effects.

The reason for this critical distance from the edge is that this is the distance over which the face displacement decays to approximately zero (which is enforced at the panel edges). Figure 7.5.3

specifies the loading direction because this was found to be the critical direction. The panel width in the transverse-to-loading direction could be reduced slightly before edge proximity affected the buckling load. This effect is apparent by observation of Figure 7.5.4.

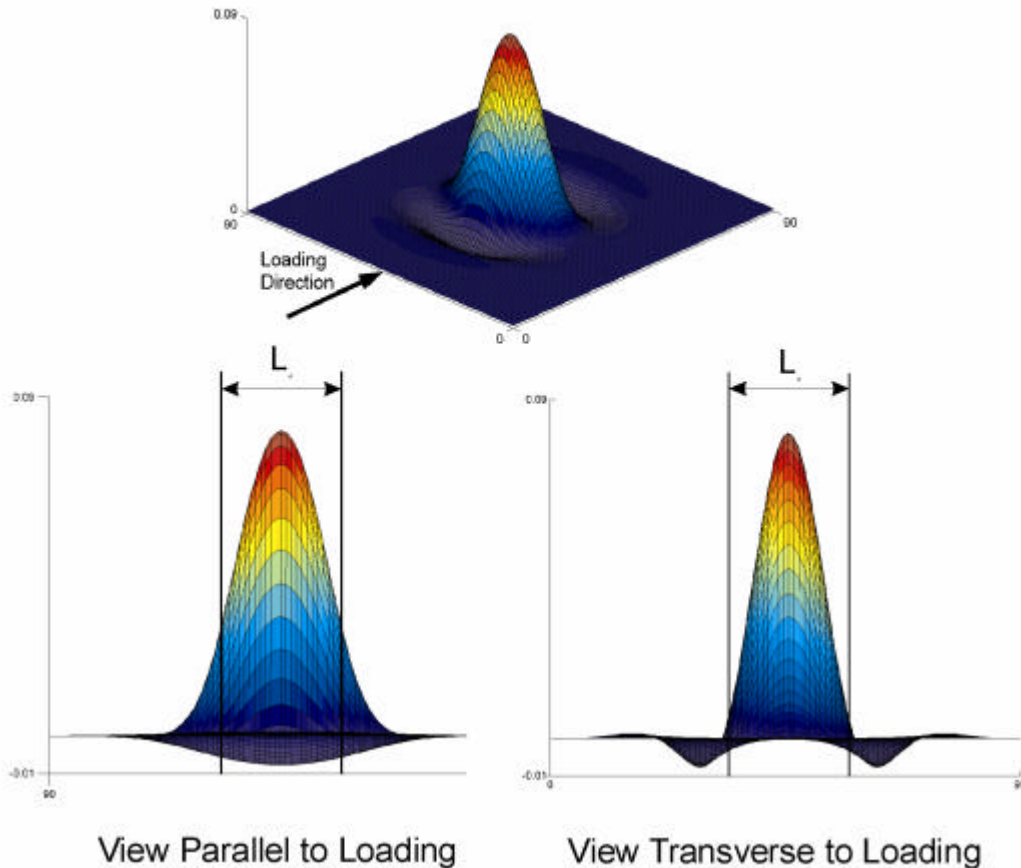


Figure 7.5.4 – Illustration of the reason for the varying edge effects in the parallel and transverse directions

It is also apparent from Figure 7.5.4 (view parallel to loading) that there is considerable tensile stress at the edges of the disbond, which will tend to induce fracture and disbond growth in the y -direction (transverse to the load), as was observed in the specimen test results of Chapter Six. This growth behaviour is the subject of Chapter Eight.

7.5.1.1 INTERACTION EFFECTS BETWEEN MULTIPLE DISBONDS

The previous analysis can be simply extended to provide an analysis of the minimum distance required between disbonds before there is significant interaction between them. Figure 7.5.5 can be modified to illustrate this principle.

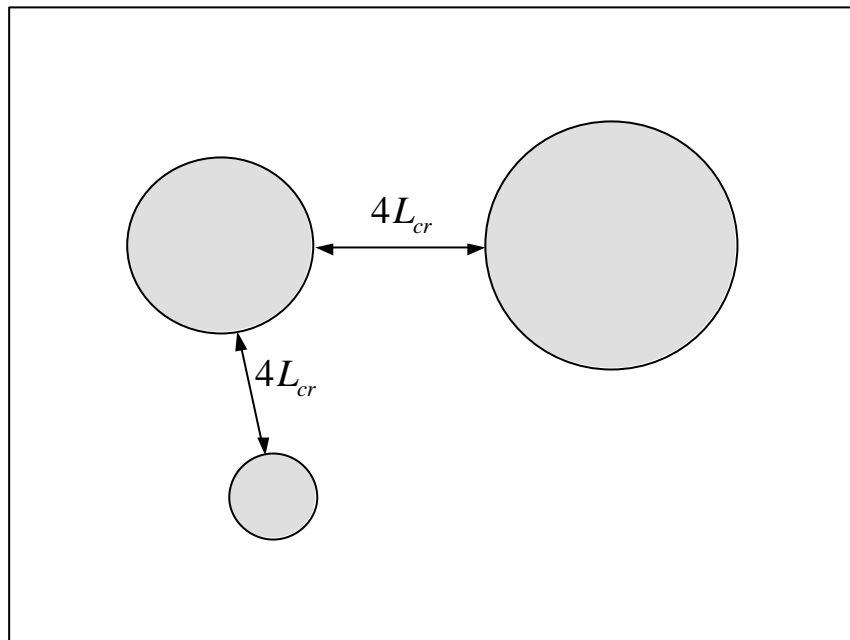


Figure 7.5.5 – Minimum separation required for disbonds to act independently (extension of the edge effects analysis to the interaction of multiple disbonds)

Notice in Figure 7.5.5 that, because the natural wavelength is unaffected by disbond size, the distance between each disbond is constant for the one panel. The first disbond to buckle will be the largest one and its buckling load will be unaffected by the presence of the other two disbonds as long as they are at least as far away as shown in Figure 7.5.5. A more complete analysis of the interaction effects that occur when the disbonds are closer than this is possible with the present model but has not been considered here.

7.5.2 DISBOND SHAPE

Considering disbond shape is an important practical aspect of predicting disbond buckling because in reality a disbond is very rarely exactly circular. The sensitivity of the buckling load to the assumed disbond shape will first be considered by comparing the buckling loads of circular and square disbonds. Table 7.5.2 shows that the buckling load of a circular disbond is 8.6% higher, on average, than an equivalent square disbond (where the side length of the square is equal to the diameter of the circle). It was found that if the dimensions were set such that the area of the circle and square were the same then the buckling load of the square was considerably higher than that of the circle. This highlights that the most critical dimension in approximating a disbond shape is the length in the loading direction. For both of these shapes the aspect ratio is unity.

Table 7.5.2 – Comparison between Circular and Square Disbonds

$\frac{L_d}{L_{cr}}$	$\frac{N_{cr}L_d^2}{4p^2D_f} \Big _{\text{SQUARE}}$	$\frac{N_{cr}L_d^2}{4p^2D_f} \Big _{\text{CIRCLE}}$	Difference
2	1.026	1.108	7.9 %
3	1.360	1.510	11.0 %
4	1.627	1.764	8.4 %
5	1.785	1.932	8.2 %
6	1.898	2.051	8.1 %
7	1.984	2.141	7.9 %
8	2.044	2.216	8.4 %
9	2.089	2.270	8.7 %
11	2.168	2.355	8.6 %
14	2.243	2.439	8.7 %
		<i>Average</i>	8.6 %

The effect of varying the aspect ratio of a rectangular disbond (for which L_d/L_{cr} is equal to six) is illustrated in Figure 7.5.6. As expected, this profile is of the general form for buckling of a plate.

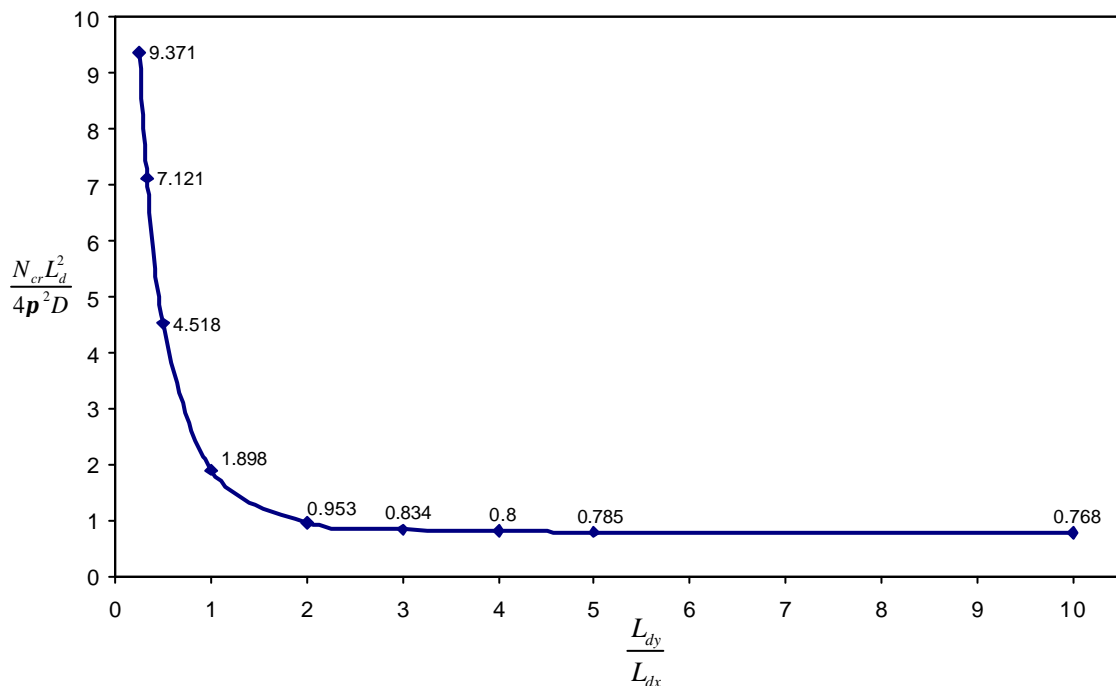


Figure 7.5.6 – Effect of disbond aspect ratio on the buckling load

It is useful to relate these findings back to the practical case of having to approximate several disbonds in close proximity (distance of less than $4L_{cr}$ between edges) as one large disbond. If the

loading situation is multi-axial or the loading direction is unknown then the safest approximation is a circle (which has an aspect ratio of unity in all directions) that encompasses all of the critical proximity disbonds. However, this may be a particularly over-conservative estimate in some cases and if the loading direction is known then a rectangle oriented so as to have sides parallel to the loading direction should be used. The aspect ratio should be set so that the rectangle encompasses all of the critical proximity disbonds. To illustrate the effect that this could have on the predicted buckling load, consider a disbond or group of disbonds (in a sandwich panel as used in the experiments of Chapter Six) that are grouped according to the rectangle method where the aspect ratio is two. The buckling load obtained from this scenario is 120% higher than the buckling load obtained using the circular grouping method. If the aspect ratio is three then this difference in buckling load increases to 250%. Therefore, the rectangular grouping method should be used wherever possible (when the loading direction is known) to avoid this kind of significant buckling load under-prediction. Given that disbond buckling is the first step in the failure process of disbanded sandwich panels, these results highlight the importance of accurately identifying the aspect ratio of the disbond.

7.6 CONCLUSIONS

A Winkler plate model was utilised to model the buckling behaviour of an embedded disbond in a sandwich plate. The characteristic buckling curve proved to be similar in form to that of a sandwich beam (Chapter Four). This type of buckling model is very accurate. Comparison with specimen test results showed that the average difference in buckling loads was only -2.6% (excluding one result, see Section 7.3) with standard deviation of 3.7%.

The following conclusions were drawn from the non-dimensional analysis and the disbond shape and edge effects analyses:

- The natural wavelength is a characteristic parameter not only of the buckling load but also in the edge effects analysis
- The characteristic buckling load curve of an embedded disbond is of the same form as that of a through-width disbond
- Face-sheet orthotropy significantly affects buckling load results and must always be modelled where applicable
- The edge effects analysis identified the critical edge proximity of a disbond (i.e. the proximity at which the buckling load begins to be affected) and this distance was found to be twice the natural wavelength of the sandwich panel
- The critical interaction proximity of multiple disbonds in a single panel has been extrapolated from the edge effects analysis and is equal to four times the natural wavelength
- The disbond shape analysis showed that the circle method of approximating a disbond or group of disbonds should only be used when the loading direction is unknown. To avoid underestimating the remaining strength of a disbonded panel the rectangular grouping/sizing method (described in Section 6.2) should be used whenever possible.

The model developed in this chapter accurately predicts disbond buckling. The non-dimensional analysis helped to determine the characteristic buckling curve and provided an efficient and insightful method of presenting the model results. The next phase of modelling aims to predict the initiation and propagation of a disbond. The analysis is non-linear and includes not only prediction of the initiation of disbond growth but also a re-meshing procedure that iteratively grows the disbond in size until it reaches the panel edges. Together with the buckling results presented in this chapter, this will provide a complete failure analysis of embedded disbonds in compression sandwich panels.

CHAPTER EIGHT

Modelling Disbond Growth in Sandwich Panels

8.1 INTRODUCTION

The specimen test results of Chapter Six indicated that the load carrying capacity of a sandwich panel with an embedded disbond can be several times larger than the buckling load. This is in contrast to the sandwich beam results of Chapter Three, for which the buckling load was a reasonable estimate of the failure load. Modelling post-buckling is therefore critical to obtaining a realistic estimate of sandwich panel failure. It was also observed in Chapter Six that failure was initiated by rapid, unstable disbond growth, propagating the disbond through the entire width of the panel. Therefore disbond growth must also be considered in a post-buckling analysis. This Chapter describes a non-linear Winkler plate model including the disbond growth criteria developed in Chapter Five. The aim of this model is to predict the post-buckling behaviour with particular focus on predicting disbond growth.

8.2 LITERATURE REVIEW

The only model in the reviewed literature that considered post-buckling and growth of an embedded disbond in a sandwich panel was developed by Han *et al.* (2002). They developed a finite element model in which the core was modelled as an orthotropic solid and the face-sheets were modelled as isotropic plates. The primary aim of the study was to verify the use of a cohesive zone model for predicting disbond growth. A model of a Double Cantilever Beam (DCB) specimen was developed, using a cohesive zone model, and tested against DCB specimen tests. It was found to be accurate in predicting the onset and propagation of crack growth between the face-sheet and core. The two inputs to the cohesive zone model are fracture stress and strain energy release rate. A sensitivity analysis found the model to be very sensitive to strain energy release rate and very insensitive to fracture stress. Han *et al.* (2002) concluded from this that a fracture mechanics approach is much more accurate than a strength-based approach to disbond growth analysis. A single compression test

of a sandwich panel with a large disbond ($305 \times 457\text{mm}$) was conducted. The panel had stringers parallel to the loading direction and disbond growth was observed to be largely unstable, propagating transverse to loading, until it was arrested by the stringers. This is the same type of growth behaviour observed in Chapter Six. The test geometry was modelled and the load at which growth became unstable was found to be 9% lower than the experimental value. From the present literature review, this is the only model of disbond growth in sandwich structure that considered the transverse flexibility of the core.

Hansen (1998) developed a finite element model of sandwich with an embedded disbond to predict buckling and post-buckling behaviour. The model was similar to that of Han *et al.* (2002), modelling the orthotropic core as a solid and the isotropic face-sheets as plates, except that it did not include a growth analysis. The finite element models were found to be very computationally expensive and a one-dimensional Winkler beam buckling model (similar to those reviewed in Chapter Four) was developed to provide a more efficient solution procedure. Hansen (1998) noted that the assumption (made by many authors) of a transversely incompressible core (i.e. infinitely stiff out-of-plane) is crude and provides a poor approximation to the actual disbond behaviour.

Chen and Bai (2002) developed a model of sandwich structure containing an embedded disbond with the aim of identifying failure responses. A sandwich finite element was developed and used in a plate model of sandwich structure with a circular or elliptical disbond. As with many other models of sandwich structure, the core was treated as being infinitely stiff out-of-plane. The model incorporated a face-sheet damage model to consider stiffness degradation due to matrix cracking as well as a contact algorithm in the disbond region. The effect of including a contact analysis was examined and found to be crucial in obtaining accurate results. For the face material strengths that were considered, the effect of incorporating a damage model was to reduce the buckling and post-buckling loads by up to 20%. This indicates that face-sheet damage effects may be a very important consideration, particularly for materials exhibiting brittle fracture, such as composite laminates. However, there was no comparison to experimental results made, so the results were not verified. This model did not consider disbond growth.

Kassapoglou (1988) developed a nonlinear model to consider buckling and post-buckling of elliptical delaminations within a sandwich face-sheet under compressive loading. The model used a series solution approach in conjunction with the perturbation technique to solve the laminated plate equations with von Karman strains. A strength-based growth criterion was used to predict the initiation of delamination growth. The model results were compared with four tests of honeycomb

sandwich in pure compression, with elliptical delaminations located centrally in the panel and one ply from the core (in a five ply face-sheet). In the comparison the difference between failure loads was 13%. Based on experimental observations it was noted that delamination growth occurred only after buckling of the delaminated region.

8.2.1 LAMINATED PLATES CONTAINING DELAMINATIONS

There are a number of papers that have considered delamination buckling and growth in solid laminates (Pradhan and Tay 1998, Rinderknecht and Kroplin 1997, Krueger and O'Brien 2000). The main distinction between these models and disbond models is the transverse stiffness of the core, where delamination models almost always assume clamped edge conditions at the delamination boundary. These models are reviewed here because they can provide informative, qualitative results. It has been observed during the review that the models that do grow the disbond are generally good predictors of the growth path but poor predictors of the growth loads. In other words, the results are only qualitatively useful even for the delaminations that they are modelling. This observation illustrates the difficulties encountered when modelling a fracture process.

Thomson and Scott (2000) developed a model for predicting the effect of delaminations in a post-buckled, stiffened laminate structure. Their emphasis was to determine if delamination growth would occur under given loading conditions. A finite element model was developed to model a section of a panel having a central delamination and three rows of stiffeners. The panel was loaded in shear by using a tensile load applied diagonally. The model accurately predicted the buckling loads for three sizes of delamination, 25mm, 50mm and 75mm. Thomson and Scott (2000) then determined the Strain Energy Release Rate (SERR) distribution around the delamination circumference for a variety of loads. Experiments used to validate the models indicated that the buckling mode shapes and loads were accurately predicted but the SERR distribution was not. Using the model, the SERR at the experimental fracture initiation load was predicted to be 380 Jm^{-2} . This compared poorly with the critical SERR of the material, which was 150 Jm^{-2} . Even though the panel specimens were loaded in shear, it was determined that Mode I fracture was the critical fracture mode. This is further evidence that fracture is primarily driven by Mode I fracture and explains why growth occurs only after buckling.

Klug *et al.* (1996) developed a computationally efficient model of an embedded delamination in a composite plate using plate elements to predict delamination buckling and growth. The virtual crack closure method was used to predict fracture. The SERR results at the delamination front were compared to 3D modelling results with reasonable accuracy to validate the plate model.

Whitcomb (1989) developed a non-linear finite element model including an embedded delamination, similar to that of Thomson and Scott (2000). The virtual crack closure technique was used with quadratic finite elements to predict fracture. It was concluded that there is generally a large gradient in the SERR along the delamination front and it is dependant on delamination shape and applied strain. It was also found that Mode III fracture was negligible for all cases tested.

8.2.2 LITERATURE REVIEW CONCLUSIONS

Of the papers that have modelled disbonded sandwich structure, many have aimed to develop methods more computationally efficient than the finite element method (Hansen 1998). The value of the finite element method and software packages that implement it is largely in their ability to model a wide range of problems. As a consequence there are often tailored procedures that provide a more efficient solution to specific problems. The review indicated a need for a computationally efficient model of post-buckling and growth behaviour of general disbonds in compressively loaded sandwich structure. The efficiency of the Winkler-type models is the reason for their usage in the present research.

The Winkler plate model was used successfully in Chapter Seven in a linear buckling analysis. The same model is extended in this Chapter by relaxing the assumption of small displacements and incorporating moderate rotations and displacements as observed in the specimen testing reported in Chapter Six. Disbond growth is modelled using the virtual crack closure technique, which was successfully employed in the non-linear beam model of Chapter Five and is an efficient numerical method. Because contact analysis is crucial in obtaining accurate post-buckling results (Chen and Bai 2002), a contact algorithm was incorporated in the model.

8.3 NON-LINEAR WINKLER PLATE MODEL

The Winkler plate model of Chapter Seven was modified to incorporate moderate plate rotations (defined by Reddy (2004) as rotations less than 15 degrees) and a criterion for disbond growth. The deflections observed in specimen test results supported the assumption of moderate rotations. The face-sheet was treated as an orthotropic solid.

8.3.1 GOVERNING EQUATIONS

The governing equations for a Winkler plate are based on classical plate theory (neglecting shearing deflections) and incorporate a Winkler foundation (Reddy 2004):

$$\begin{aligned} \frac{\partial N_{xx}}{\partial x} + \frac{\partial N_{xy}}{\partial y} &= 0 \\ \frac{\partial N_{yy}}{\partial y} + \frac{\partial N_{xy}}{\partial x} &= 0 \\ \frac{\partial^2 M_{xx}}{\partial x^2} + 2\frac{\partial^2 M_{xy}}{\partial x\partial y} + \frac{\partial^2 M_{yy}}{\partial y^2} + \frac{\partial}{\partial x} \left(N_{xx} \frac{\partial w_0}{\partial x} + N_{xy} \frac{\partial w_0}{\partial y} \right) + \frac{\partial}{\partial y} \left(N_{xy} \frac{\partial w_0}{\partial x} + N_{yy} \frac{\partial w_0}{\partial y} \right) + kw_0 &= 0 \end{aligned} \quad (8.3.1)$$

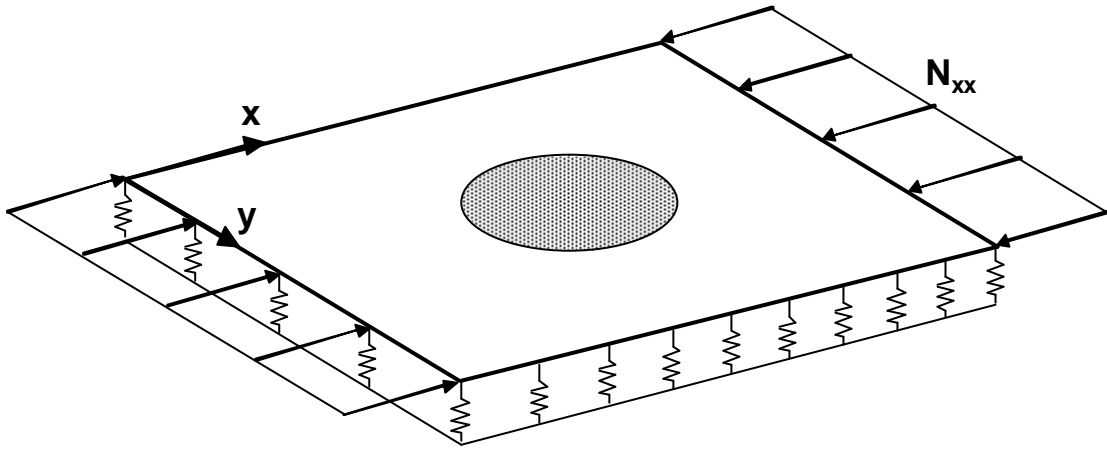


Figure 8.3.1 – Winkler plate in uni-axial compression

The assumptions of small in-plane strains and moderate rotations (i.e. rotations large enough to consider their effect on the in-plane strain but small enough to maintain an approximate definition of curvature) were used, giving the following strain definitions:

$$\begin{aligned}
 \mathbf{e}_{xx} &= \frac{\partial u_0}{\partial x} + \frac{1}{2} \left(\frac{\partial w_0}{\partial x} \right)^2 \\
 \mathbf{e}_{yy} &= \frac{\partial v_0}{\partial y} + \frac{1}{2} \left(\frac{\partial w_0}{\partial y} \right)^2 \\
 \mathbf{e}_{xy} &= \frac{\partial u_0}{\partial y} + \frac{\partial v_0}{\partial x} + \frac{\partial w_0}{\partial x} \frac{\partial w_0}{\partial y}
 \end{aligned} \tag{8.3.2}$$

The strain definitions account for the in-plane strain caused by the displacement gradients but ignore the second order in-plane strain terms. Utilising the force and moment definitions, the governing equations were written in terms of displacements, u , v and w (Appendix F). These equations were discretised using a central finite differencing scheme, dividing the plate into m nodes in the y -direction and n nodes in the x -direction, resulting in three non-linear equations for N ($n \times m$) discrete nodes. These equations were then written as a single matrix equation:

$$[F]d = 0 \tag{8.3.3}$$

The displacement vector in (8.3.3) is defined as:

$$d = \begin{bmatrix} u_{11} \\ v_{11} \\ w_{11} \\ \vdots \\ u_{mn} \\ v_{mn} \\ w_{mn} \end{bmatrix} \tag{8.3.4}$$

8.3.2 BOUNDARY CONDITIONS

The boundary conditions used on each edge of the plate were as follows:

- On the loaded edge there was a prescribed load ($N_{xx} = N$) and on the opposite edge the x -displacements were restrained ($u = 0$).
- At the corner defined by $x = y = 0$ all in-plane displacements were restrained ($u = v = 0$).
- At all boundaries the condition of zero shear force (N_{xy}) and zero out-of-plane displacement (w) were enforced.
- Built-in conditions were defined by setting the gradient of the out-of-plane displacements normal to the boundary as zero.

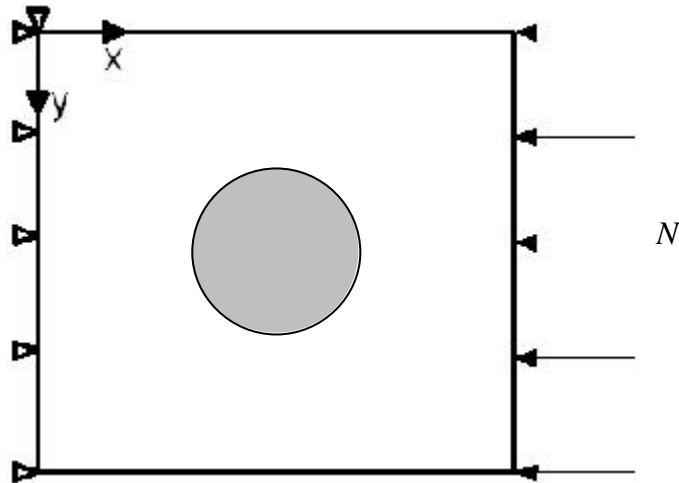


Figure 8.3.2 – Boundary conditions applied to the Winkler plate model

The boundary conditions were satisfied by creating a mesh having two rows of nodes external to the plate, i.e. outside the geometric boundary. The displacements, u , v and w , of these nodes were specified, based on the internal nodal displacements, with values required to satisfy the boundary conditions. This method makes it a relatively simple matter to change the boundary conditions. The other method of implementing these conditions would be to modify the governing equations for each of the boundary nodes, which would be more labour intensive and would also make boundary condition changes very difficult. The method used was found to work very well.

8.3.3 NON-LINEAR SOLUTION PROCEDURE

The Newton-Raphson procedure is one of the few non-linear procedures that can be extended into multiple dimensions, and of the few it is the simplest to implement, which is why it was used to solve the current set of non-linear equations. The Newton-Raphson procedure assumes that the function is close to linear in the region of the root. For most functions this is a good assumption in only a small region close to the root, hence the initial guess is very important and if it is not close enough to the root, the iterative solution may not converge. Also, in the present method it is necessary that the function is differentiable with respect to all of its variables. If this were not possible the Secant method could be used to evaluate the derivatives numerically (Dennis and Schnabel 1996). Appendix F contains a description of the Newton-Raphson method as used in the present non-linear plate model. Full Newton-Raphson was used, i.e. the Jacobian (tangent stiffness matrix) was determined for each iteration, as opposed to modified NR which determines the Jacobian only once per load increment.

8.3.3.1 LINE SEARCHES AND BACKTRACKING

Line searches and backtracking were used to improve the convergence of the Newton-Raphson method. A line search algorithm was used to avoid divergence of the solution. The method is described in Appendix F.

8.3.3.2 LOAD REDUCTION

A load reduction algorithm was used when the number of iterations required for convergence exceeded the prescribed maximum, which was 15 by default. This feature aids convergence and also allows the load to reduce as disbond growth occurs. The load reduction factor was typically set at 30% of the input load increment.

8.3.3.3 CONTACT CONDITIONS

Several studies (most recently that of Chen and Bai (2002)) have determined that it is critical to model the face to core contact in the disbonded region. This is enforced in the present model by monitoring the out-of-plane displacements in the disbond region and inserting core support at nodes that have a negative displacement. This was shown to be an accurate and consistent method of enforcing contact as the spring stiffnesses used at contact nodes have the exact stiffness of the core. Typically in a contact problem there are two distinct bodies and contact is approximately enforced by inserting very stiff springs between the surfaces when they overlap (Lusas Theory Manual v13.5).

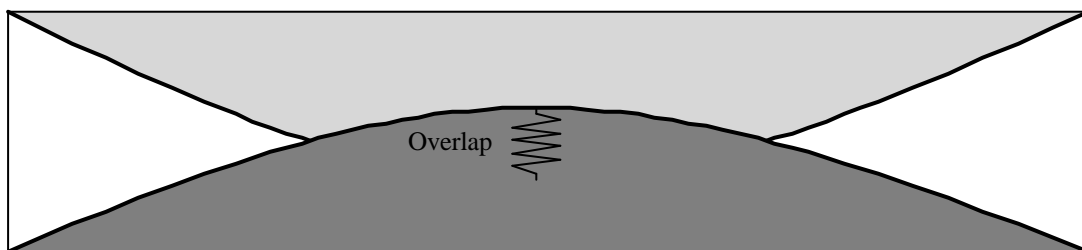


Figure 8.3.3 – A typical method of enforcing contact between two bodies

This type of method allows an overlap proportional to the spring stiffness and to avoid numerical error it requires that the spring stiffness is not too large. The method used here does not suffer from this problem because when contact occurs the condition is identical to that of a fully bonded region.

The contact method was tested by applying a positive pressure load to the entire surface of a disbonded panel model. The resulting out-of-plane deflections were constant and all in-plane deflections were zero, verifying the contact method.

8.3.3.4 SOLUTION METHOD

The initial guess for displacements is crucial in this type of problem to ensure convergence to a non-trivial solution. Initially, the buckling mode shape was scaled to a prescribed maximum buckle height for the initial guess to the out-of-plane displacements (w). The in-plane displacements were approximated by the flat plate displacements (i.e. assuming $w(x,y) = 0$) for the given compression load. Using this method the displacements typically converged to those of a flat plate, because the initial buckle height was necessarily small. It proved difficult to obtain convergence to a non-trivial solution for loads near the buckling load (see Appendix F for convergence criteria), therefore this method was abandoned and instead a small vacuum pressure load was applied to the surface of the plate to initiate a stable out-of-plane displacement, having an amplitude less than 2% of the face-sheet thickness. Using this method, a stable, non-trivial solution could be obtained for any in-plane compression load. In practice the buckling load was used as the initial compressive load and the load increments were entered as a percentage of the buckling load (generally 2-5%). The pressure load was removed after 10 load increments, when the solution was stable and would no longer converge to the flat-plate solution. This was typically at load levels 10-30% higher than the buckling load and in all cases this was well before fracture initiation, so the growth initiation loads were unaffected.

8.3.3.5 MODELLING DISBOND GROWTH INITIATION

The strain energy release rate as defined in Chapter Five was again used to predict the initiation of disbond growth. The definition in Chapter Five was implemented for the three-dimensional case exactly as it was for the two-dimensional model (refer Appendix C for derivation):

$$G_I = \frac{k}{2} \left(\frac{w_{n+1}w_n}{3} + \frac{w_{n+1}w_{n-1}}{6} + \frac{w_n^2}{6} + \frac{w_n w_{n-1}}{3} \right) \quad (8.3.5)$$

Equation (8.3.5) is based on the assumption that the face-sheet bending is cylindrical in the local region in which the strain energy release rate is evaluated. This assumption was motivated by noting that this region is typically very small compared to the radius of the disbond.

The strain energy release rate was calculated at one of the points of intersection of the disbond boundary and a line perpendicular to loading passing through the disbond centre (Figure 8.3.4). Based on present and reviewed specimen test results this was found to be the location at which disbond growth initiates when subject to uni-axial compression loading. In the specimen testing described in Chapter Six, disbond growth was observed to proceed perpendicular to the loading

direction and therefore this was considered to be the only location along the boundary at which the strain energy release rate needed to be calculated. That disbond growth proceeds in this direction was also observed by Han *et al.* (2002), Hansen (1998), Whitcomb (1992) and Kassapoglou (1988). Furthermore, all of the testing of disbanded solid laminates reviewed in Chapter Two displayed the same growth directional behaviour.

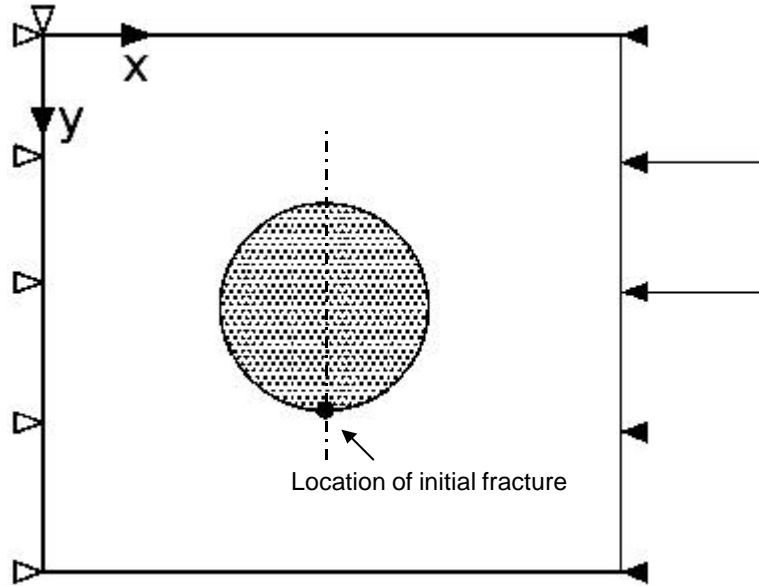


Figure 8.3.4 – Location at which fracture criterion was measured

8.3.3.6 MODELLING DISBOND PROPAGATION

Damage progression analysis was incorporated into the present model by switching to a strength based growth criterion when the critical strain energy release rate was obtained at the disbond boundary. At disbond growth initiation the stress at the fractured node was recorded and defined as the tensile fracture stress of the core, S_{fr} . From then onwards in the solution any node with an out-of-plane stress greater than this value was released, i.e. core support was removed. In this way the disbond could propagate until it reached the edges of the panel. This method was used because it is considerably simpler to implement than to continue a fracture mechanics growth criterion once the disbond shape has become irregular.

The core support definition, as used in Chapter Seven and referring to Appendix D for the derivation of \mathbf{a} , is now subject to two conditions, (8.3.7), for contact and fracture.

$$S(x, y) = \begin{cases} 0 & \text{in the disbond region} \\ \mathbf{a} & \text{at the disbond boundary} \\ 1 & \text{in the bonded region} \end{cases} \quad 0 < \mathbf{a} < 1 \quad (8.3.6)$$

Conditions:

$$\begin{aligned} \text{Contact :} \quad & S(x, y) = 1 \quad \text{if } w(x, y) < 0 \\ \text{Fracture :} \quad & S(x, y) = 0 \quad \text{if } \mathbf{s}(x, y) > \mathbf{s}_{fr} \end{aligned} \quad (8.3.7)$$

8.3.3.7 SUMMARY OF THE NON-LINEAR CONTROLS

Table 8.3.1 shows the non-linear controls available for each solution, along with their default values.

Table 8.3.1 – Non-linear controls used in the present model

Program Variable	Description	Default Value
RMSRES	Convergence limit for the RMS residual	10^{-8}
L2DISP	Convergence limit for the incremental displacement L2-norm	10^{-6}
MAXIT	Maximum number of iterations before load reduction	15
CNTCT	Variable defining whether or not to implement contact conditions	Yes
NINCR	Number of load increments	100
DP	Load increment as a fraction of the initial load	0.04
ALPHA	Line searches – convergence limit	10^{-4}
LMIN	Line searches – minimum line search parameter in any backtracking step	0.05
LAMMIN	Line searches – minimum step reduction factor	10^{-4}
PINCR	Number of iterations after which the vacuum pressure is removed	10

8.3.4 VALIDATION PROCESS

8.3.4.1 PRESSURE LOADING

Several simple test cases were considered for the purpose of validating the accuracy of the model. Firstly, pressure loading was considered. The exact solution for a circular plate with built-in edges gives the maximum deflection (at the centre of the plate) as:

$$w_{\max} = \frac{pR^4}{64D_f} \quad (8.3.8)$$

However this assumes small deflections with respect to the thickness of the plate. A better approximate solution was presented by Timoshenko (1936) and is expressed as:

$$\frac{w_{\max}}{t_f} + A \left(\frac{w_{\max}}{t_f} \right)^3 = B \frac{P}{E_f} \left(\frac{R}{t_f} \right)^4 \quad (8.3.9)$$

The constants A and B depend on the boundary conditions and for built-in edges, where the edges are free to move in-plane, the values are $A = 0.146$ and $B = 0.171$ (Timoshenko 1936). The result of (8.3.9) will be the same as that of (8.3.8) for small displacements.

The condition of built-in edges was approximated in the model by using a flexible face ($E_f = 20.4\text{GPa}$, $\nu_f = 0.3$ and $t_f = 0.1\text{mm}$), very stiff core ($k = 10^{20} \text{Nm}^{-3}$) and a 50mm diameter disbond region. The mesh size used in this study was 45×45 nodes and the square plate edge length was 65mm. Table 8.3.2 shows the comparison between the two analytical expressions and the model results.

Table 8.3.2 – Comparison of circular plate displacements due to pressure loading

Pressure (Pa)	Present Model w_{\max} (mm)	Eqn. (8.3.9) w_{\max} (mm)	Eqn. (8.3.8) w_{\max} (mm)
3	0.0104	0.0098	0.0098
5	0.0173	0.0163	0.0163
10	0.0337	0.0323	0.0327
35	0.0920	0.1000	0.1144
100	0.1846	0.2038	0.3267
1000	0.4986	0.5700	3.2672

The model results compare well to (8.3.9) and it is also evident that membrane effects become significant as the maximum deflection becomes larger relative to the plate thickness. Timoshenko (1936) states that the membrane effects become considerable once the maximum plate deflection exceeds 40% of the plate thickness and this is borne out by Table 8.3.2. One specific point of difference between this model and (8.3.9) is the boundary conditions. The solution of Timoshenko (1936), (8.3.9), assumes built-in edges that are free to translate in-plane. In the model the condition of in-plane translational freedom is not exactly satisfied because the circular disbond lies within a square plate, which gives it additional stiffness in-plane. This could explain why the displacements at larger pressure loads are smaller than those of (8.3.9). The results from (8.3.9) are approximate and this comparison was meant only to provide reference to a previous solution.

8.3.4.2 IN-PLANE LOADING

The simple cases of applying uniaxial compression and tension loads were tested and the displacement results compared with simple plate theory. The maximum deflections of a plate in the x and y directions are given respectively as:

$$u(L_x, y) = \frac{L_x N_x}{E_f t_f} \quad (8.3.10)$$

$$v(x, L_y) = \frac{n_{xy} L_x N_x}{E_f t_f} \quad (8.3.11)$$

In both the tensile and compressive load cases the model results showed uniform stress and strain fields. This verified that the boundary conditions were defined and implemented accurately. Also in both load cases, the maximum displacements in the x and y directions corresponded exactly to (8.3.10) and (8.3.11), respectively.

8.3.5 CONVERGENCE STUDY

8.3.5.1 MESH DENSITY

One of the most basic checks that should be done for any discretised numerical model is a check that the solution is reasonably converged towards the exact solution, i.e. the solution for an infinitely fine mesh. In performing this check four mesh densities were used, 21×21 , 29×29 , 35×35 and 41×41 nodes and the load versus maximum displacement and load versus strain energy release rate, G , plots were compared for both cases.

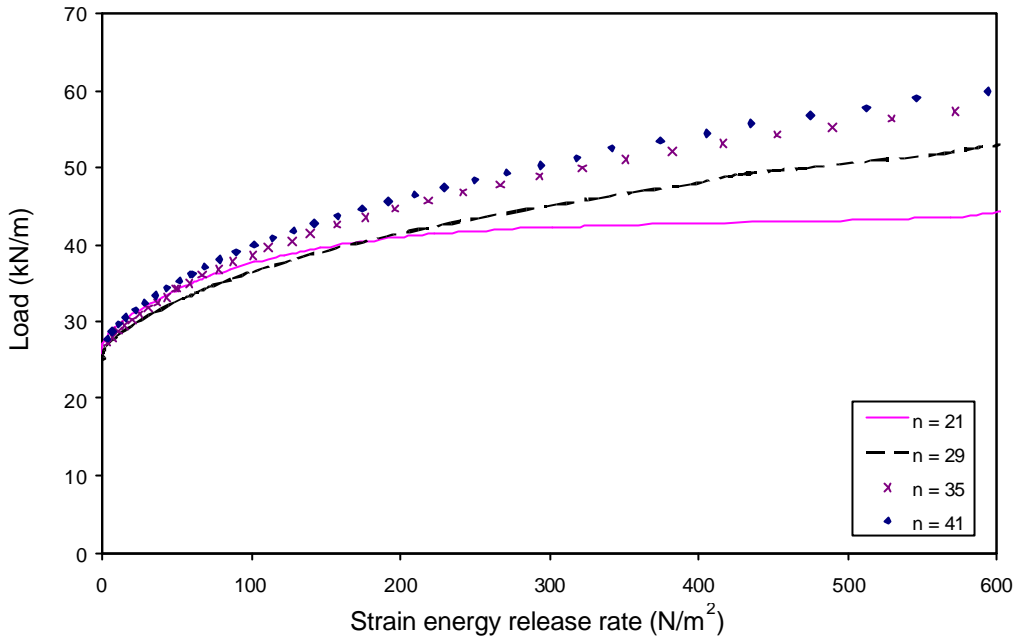


Figure 8.3.5 – Load versus strain energy release rate for various mesh densities

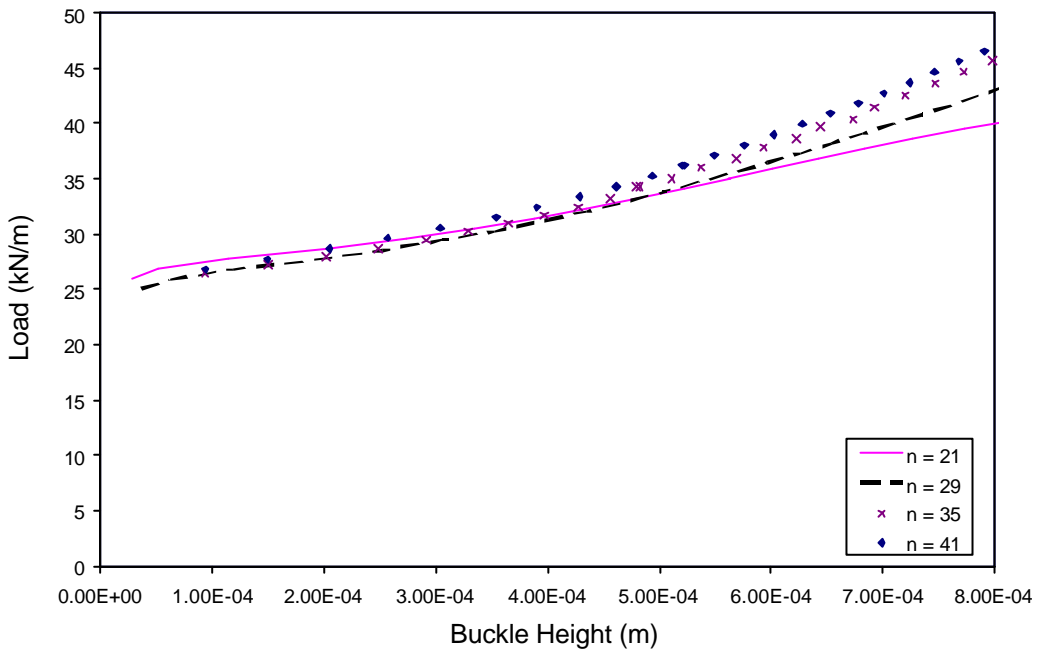


Figure 8.3.6 – Load versus disbond buckle height for various mesh densities

The difference between the highest loads plotted in Figure 8.3.6 for the 41×41 and 35×35 mesh densities was 2%. This was considered to be sufficiently converged and a mesh density of 35×35 was used in all of the model solutions. The solution time was also a large factor in this choice, being approximately proportional to the number of nodes to the third power.

8.3.5.2 LOAD INCREMENT STEP SIZE

The effect of various load increment sizes was checked. Expressed as a percentage of the buckling load the following figure shows increments of 1%, 2% and 4% and indicates that all increments produce the same result. Based on this result the maximum of the three increment sizes, 4%, was used for all model runs.

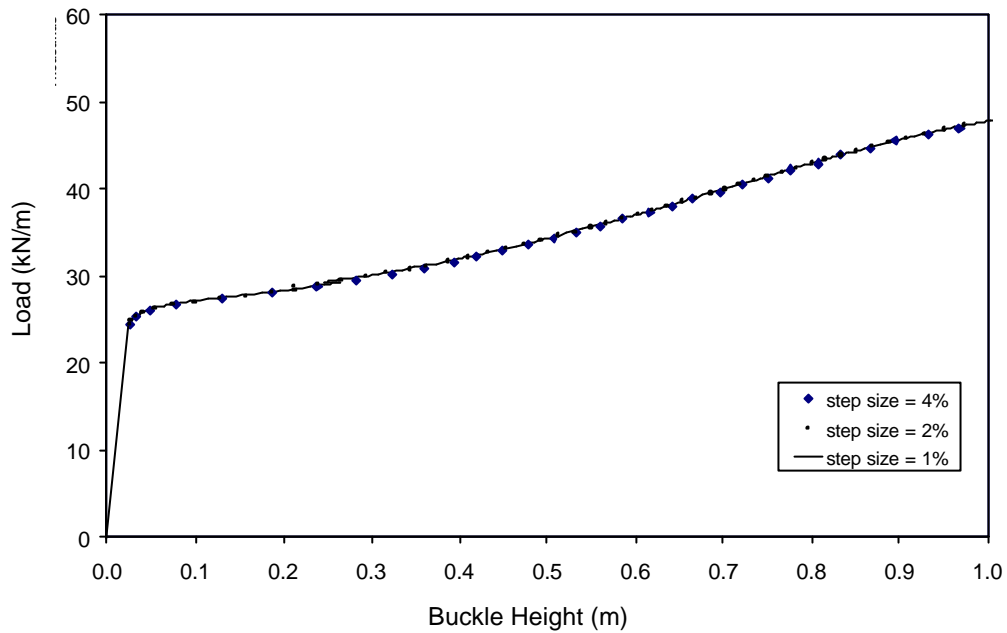


Figure 8.3.7 – Load versus disbond buckle height for various load increment sizes

8.4 COMPARISON WITH SPECIMEN TEST RESULTS

In this section the model results are compared with the specimen test results reported in Chapter Six. The first result comparison is the post-buckling in-plane stiffness for each configuration. This is an important aspect of the overall behaviour because it is required for a geometric failure condition, such as failure by gross deflection. The next comparison is between the model-predicted disbond growth initiation loads and those obtained from specimen testing. In the specimen test results of Chapter Six failure was caused by rapid disbond growth after an initial period of discrete growth increments. Therefore, this is the behaviour that governs the failure process and is the focus of the present model and the results presented in this Chapter.

A progressive damage propagation model is developed from the present model to predict complete specimen failure and the final comparison is between the failure loads of the model and specimen test results. A summary of the load comparisons is presented at the end of this section

8.4.1 POST-BUCKLING STIFFNESS COMPARISON

8.4.1.1 IN-PLANE STIFFNESS

The specimen testing of Chapter Six showed an almost imperceptible change in stiffness after buckling. This result was also observed in the model results. A typical result is shown in Figure 8.4.1 for a 50-G specimen (50mm disbond diameter and G-type face-sheet material).

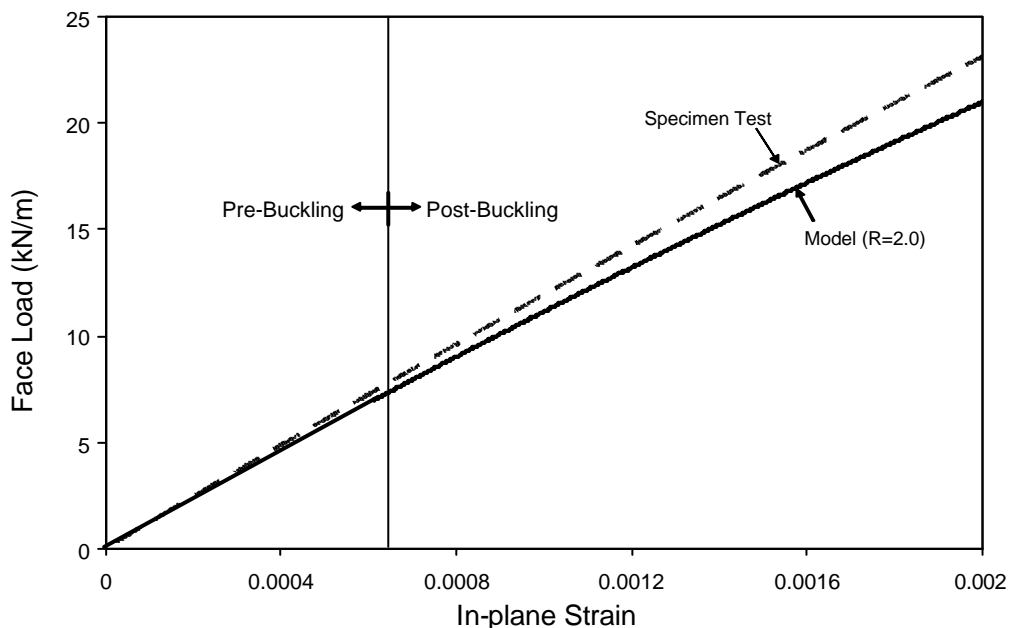


Figure 8.4.1 – Comparison between test and model in-plane stiffness results where the strain is the average value at the loaded boundary

Figure 8.4.1 shows firstly that the post-buckling in-plane stiffness is almost the same as the pre-buckling stiffness. This is in contrast to sandwich beam behaviour (Chapter Three), in which there is negligible post-buckling stiffness.

At twice the buckling load the model predicts a stiffness equal to 88% of the specimen test result. This under-prediction is due to the boundary conditions assumed in the model. There are two boundary conditions that could have been used at the loaded edge boundary, constant load or constant displacement (Figure 8.4.2). These conditions envelope the actual conditions experienced by the test specimens. The constant load direction was implemented in the model because it is an easier boundary condition to use. To implement the constant displacement condition and still maintain control of the solution by the load would require an iterative feedback loop in which the displacement was prescribed and the average load across the edge determined by integration, essentially resulting in a displacement controlled solution.

These boundary conditions were found to affect the post-buckling behaviour predicted by the model. The constant load condition results in a larger fraction of the total in-plane load being transferred in to the disbond region (reduced in-plane stiffness region). This is apparent by considering the sections defined by the dotted lines in Figure 8.4.2. For the constant load condition the load at the loaded edge is simply equal to the average load, whereas for the constant displacement condition the load at this section may be much less than the average load, depending on how much the stiffness is reduced in the disbond region.

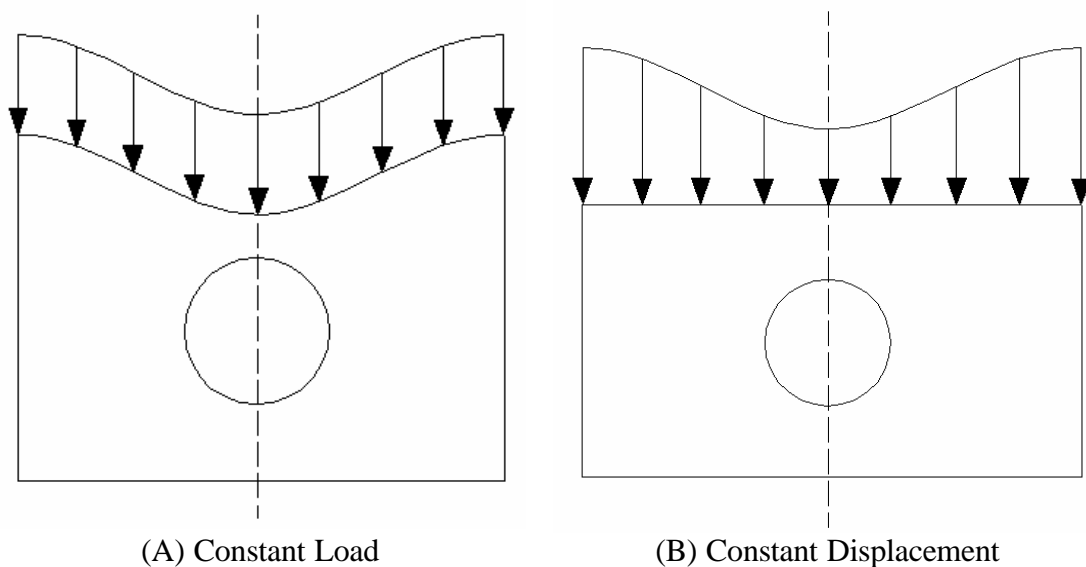


Figure 8.4.2 – Deformed shapes and load profiles of two panels having circular regions of reduced stiffness subjected to different boundary conditions

This effect is observable in the model result in Figure 8.4.3 for a 150mm square panel with a central 75mm disbond (deformations are exaggerated 50 times).

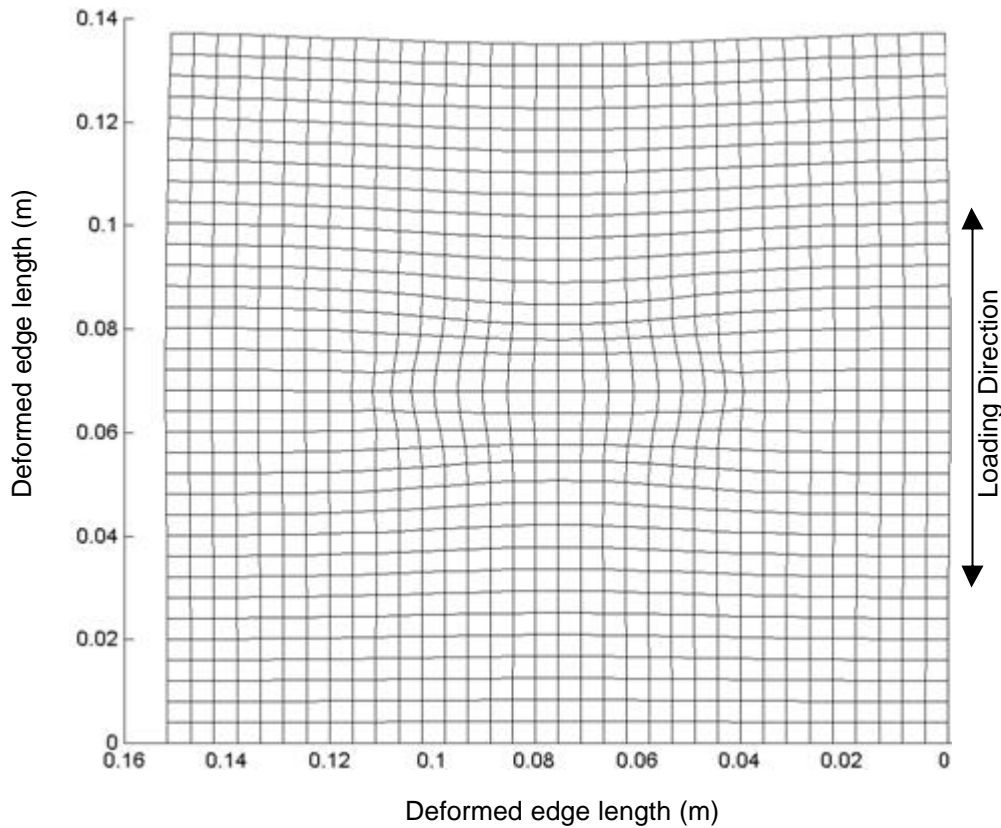


Figure 8.4.3 – Exaggerated deformed shape of a disbonded panel with a 75mm disbond and length ratios $R = Q = 2$ (see 8.4.1)

Increasing the length ratio, R , will reduce the effect shown in Figure 8.4.3. This is apparent by considering that in the limit case, for infinitely large R , the conditions of constant displacement and constant load at the boundary are mutually satisfied. This is because in the limit case the less stiff disbond region is infinitely small relative to the panel length and has negligible effect on the overall stiffness.

$$\begin{aligned}
 R &= \frac{L_x}{L_d} \\
 Q &= \frac{L_y}{L_d}
 \end{aligned}
 \tag{8.4.1}$$

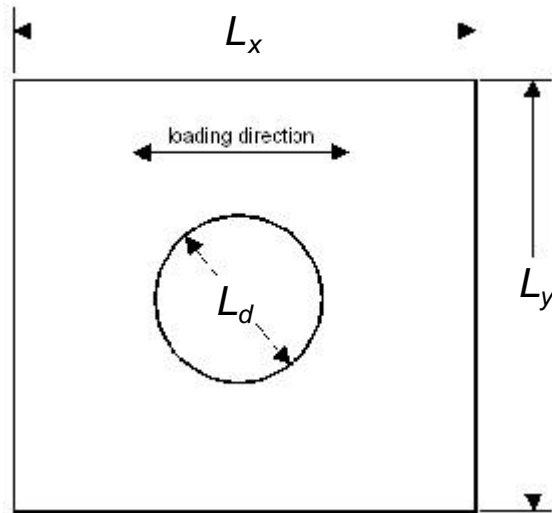


Figure 8.4.4 – Panel geometry definitions

Figure 8.4.5 demonstrates the effect of increasing R for the 50G specimen configuration that was plotted in Figure 8.4.1.

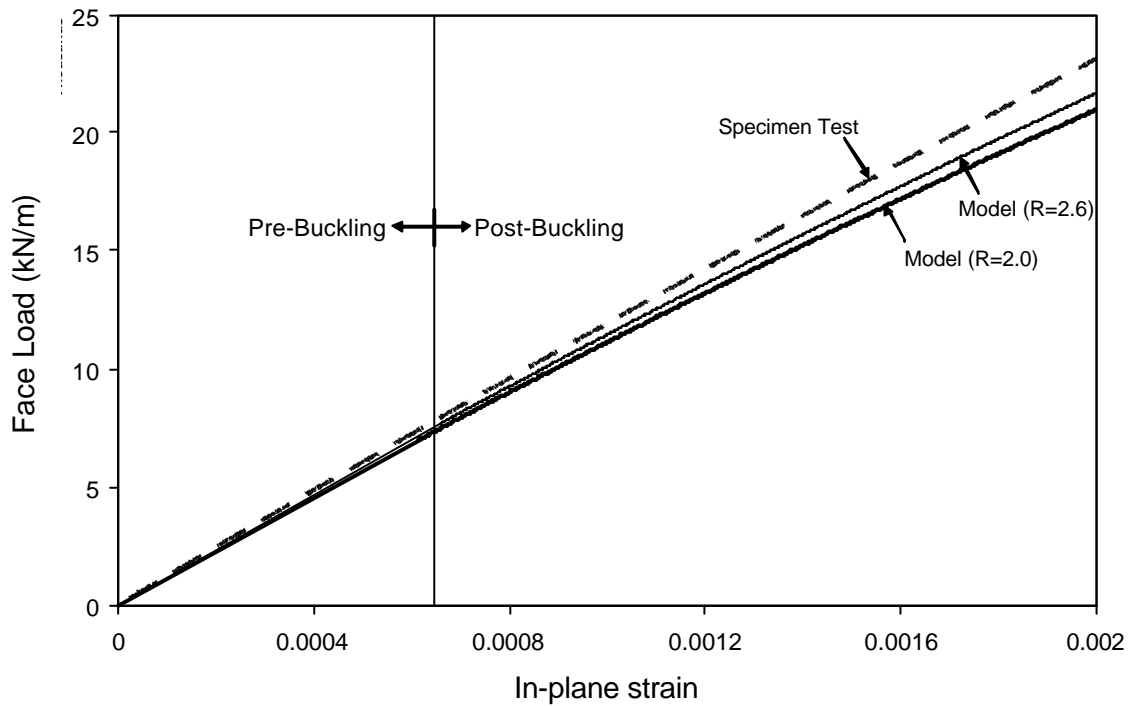


Figure 8.4.5 – Illustration of the increased in-plane stiffness resulting from an increased panel length ratio, R .

The original stiffness curve presented in Figure 8.4.1 was for a specimen with a 50mm disbond in a panel 100mm square ($R = 2$). This curve is presented in Figure 8.4.5 along with the stiffness curve for a 50mm disbond in a panel 125mm square ($R = 2.5$). As expected the stiffness increased with an

increase in R . At twice the buckling load the stiffness increased from 88% to 94% of the specimen test result.

The length of the actual specimen for which the test result is given in Figure 8.4.5 had a length of 175mm. The actual specimen dimensions were not replicated in each test because to do so would have resulted in very large models with unmanageably large solution times. Therefore the selection of panel size for input to the model was a compromise between accuracy and solution time, as with the selection of mesh density.

The comparison between the model result with increased panel dimensions and the specimen test result is very good, as would be expected of an in-plane displacement prediction. The next type of geometric behaviour to compare with test results is the predicted out-of-plane displacement and this is considered in the next section.

8.4.1.2 PREDICTING DISBOND BUCKLE HEIGHT

Another method of determining how well the geometric behaviour of the disbonded sandwich panel is predicted is to consider the buckled disbond height. The buckled disbond height is the maximum out-of-plane displacement of the post-buckling face-sheet, which was found in Chapter Six to be at the centre of the disbond. This was measured by the laser gauge described in Chapter Six testing and is an easily retrieved result from the present model. Specimen test results are compared with model predicted results in Figure 8.4.6 through Figure 8.4.10.

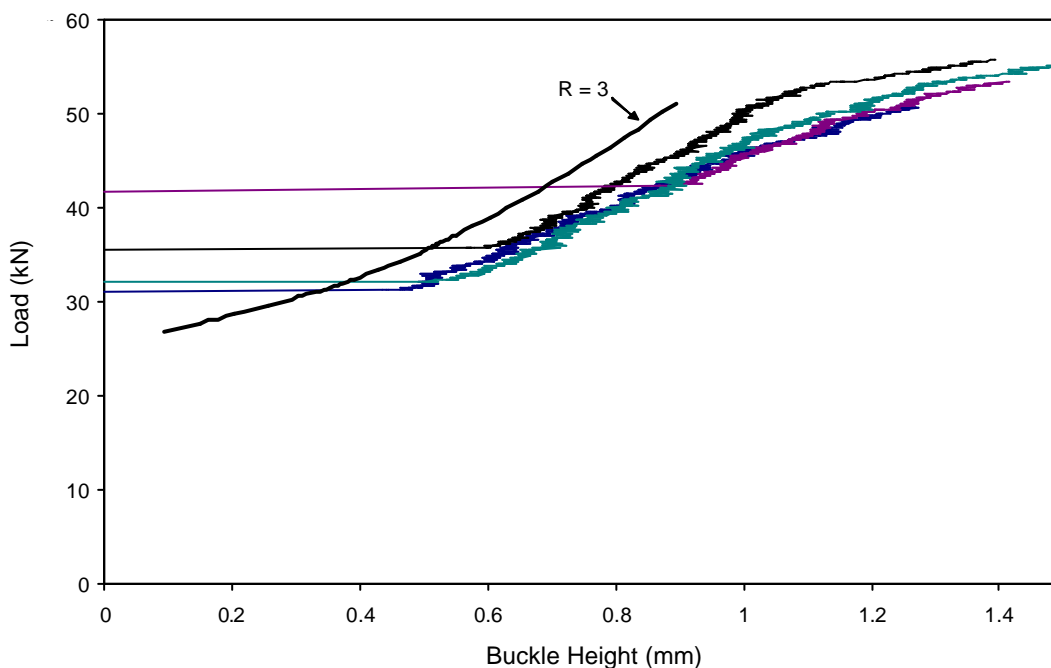


Figure 8.4.6 – Model versus specimen test results (25mm disbond diameter and G-type face-sheet)

As explained in Chapter Seven, the specimens with 25mm disbonds all exhibited snap buckling during testing. The model over-predicts the stiffness of these specimens and it is likely that the dynamic effects of snap buckling resulted in some disbond growth and generally larger buckle heights for the same load, effectively shifting the experimental plots in Figure 8.4.6 to the right.

The results for specimens designated 25-GH (25mm diameter disbond and GH-type face-sheet) could not be presented because the panel was not wide enough to support the laser gauge and therefore absolute displacement measurements were not possible. Note that displacements relative to the loading mechanism were used to determine the buckling loads.

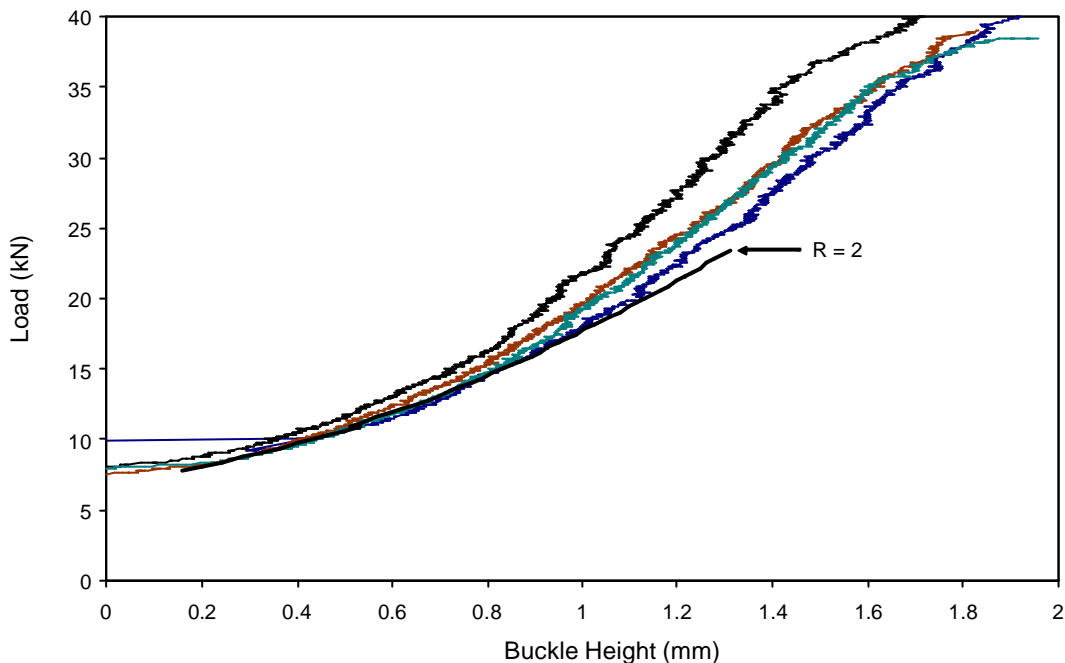


Figure 8.4.7 – Model versus specimen test results (50mm disbond diameter and G-type face-sheet)

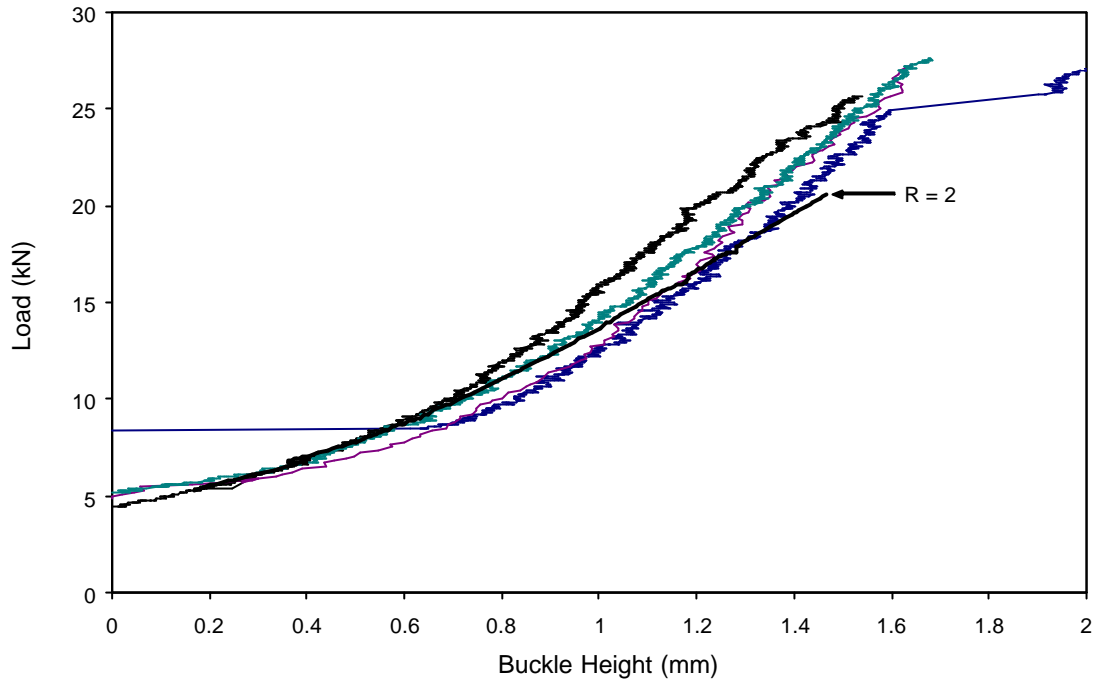


Figure 8.4.8 – Model versus specimen test results (50mm disbond diameter and GH-type face-sheet)

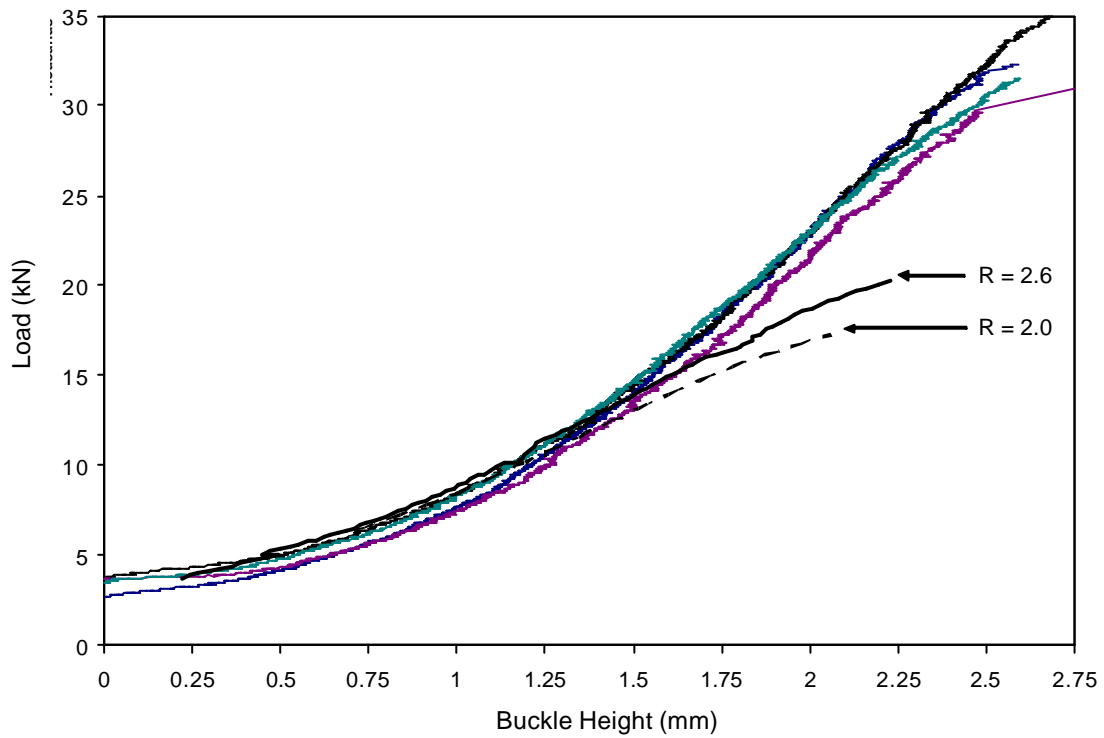


Figure 8.4.9 – Model versus specimen test results (75mm disbond diameter and G-type face-sheet)

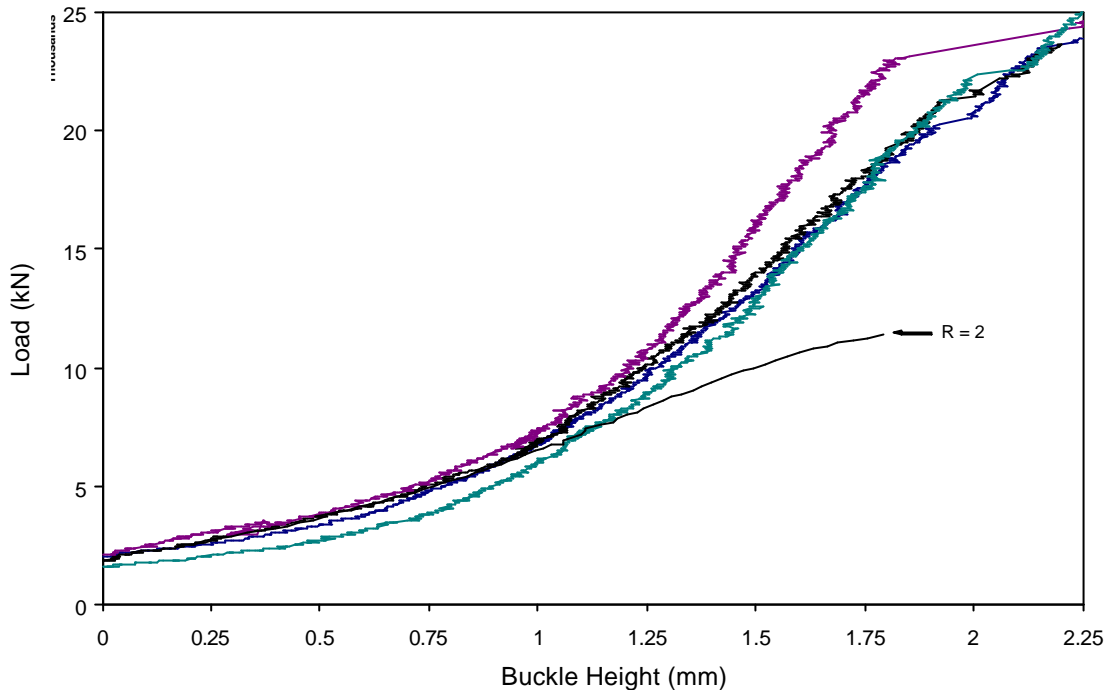


Figure 8.4.10 – Model versus specimen test results (75mm disbond diameter and GH-type face-sheet)

In all cases the initial (small-displacements) phase of post-buckling behaviour is very well predicted. The difference in behaviour increases as the post-buckling load increases. This effect is most noticeable for the specimens with 75mm disbonds. As explained in the previous section, a certain amount of this is due to the constant load boundary condition assumed at the loaded panel edge.

Figure 8.4.9 illustrates the effect of increasing the panel length ratio, R , from 2.0 to 2.6. The load is typically under-predicted for a given disbond buckle height and in addition to the effect of boundary conditions this may be due to several other effects. Material non-linearities, i.e. stiffening of the face-sheet and/or core under large strains, are not accounted for in the model and will cause some of the post-buckling stiffening observed in the specimen test results. Also, the model neglects shear tractions at the face-core interface. Shear tractions have negligible effect on the buckling load (Lin *et al.* 1996) however they may become significant in post-buckling and incorporating shear traction may improve the accuracy of the present model for large post-buckling loads.

The model assumes face-sheet rotations to be moderately small, i.e. less than approximately 15 degrees. An approximate check for the validity of this assumption was derived by considering a cross-section of the panel through the centre of the disbond (see Appendix H). Assuming a

sinusoidal buckle shape with a wavelength equal to the disbond diameter (8.4.2) is obtained as a condition to be satisfied to ensure that the maximum face-sheet rotation is less than 15 degrees.

$$h \leq \frac{L_d}{12} \quad (8.4.2)$$

For the three disbond diameters considered here, 25mm, 50mm and 75mm, the maximum buckle heights according to (8.4.2) are 2.1mm, 4.2mm and 6.3mm, respectively. This is an approximate criterion because the wavelength of the buckled shape is generally less than the disbond diameter due to the elliptical profile of the disbond in post-buckling (see Figure 8.4.14). However, even considering this effect, the assumption of small rotations is considered to be valid for all of the solutions obtained here.

Another behavioural result specific to specimens with 75mm disbonds was that the non-linear solution would reach a point at which the load reduced and then each load increment required significantly more iterations than early on in the solution. This was evident for both 75mm disbond specimens and was presumed to be due to the relative slenderness of the 75mm disbonds. Both face-sheets are less than 0.5mm thick and therefore the 75mm disbond is a very slender shell. At high loads there are considerably more deformed shape options in the form of higher buckling mode shapes for such a slender shell and this was presumed to be the cause of the instability of the solution for the 75mm disbond specimens at high load levels. For the 75-GH specimen configuration the buckling model of Chapter Seven was run and the first 20 buckling modes were captured. Of these only 4 were physically possible when considering contact, i.e. the other 16 had mode shapes with negative displacements. These four mode shapes are shown along with their respective loads in Figure 8.4.11.

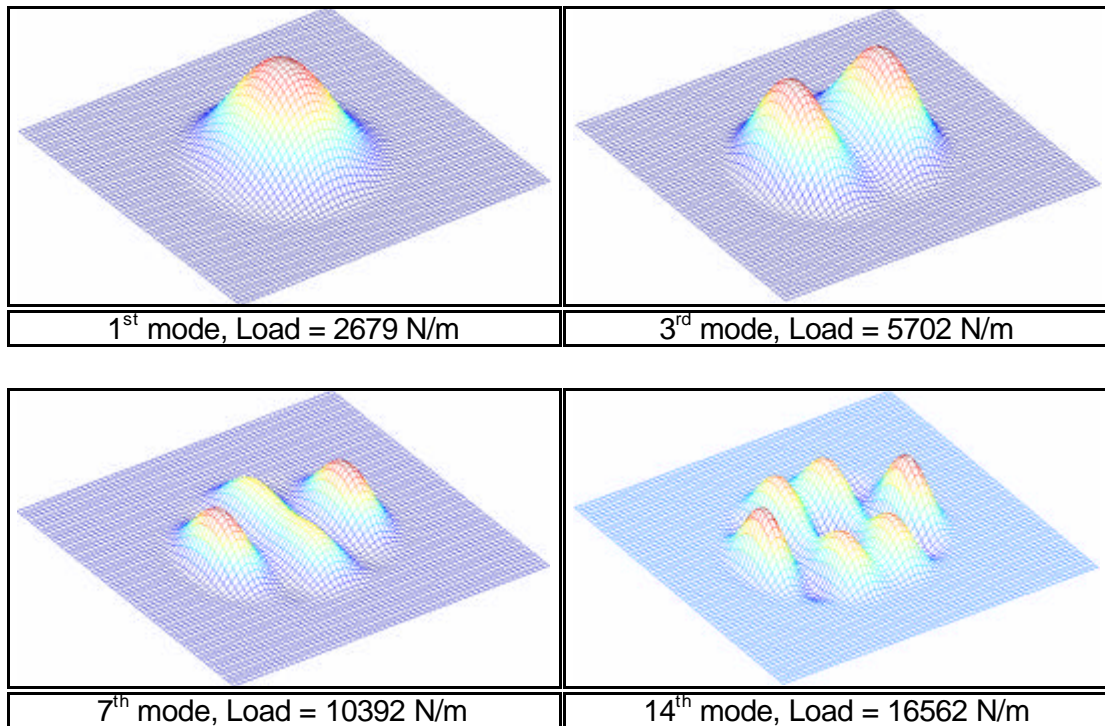


Figure 8.4.11 – Buckling modes of a specimen configuration with 75mm disbond diameter and GH-type face-sheet

This buckling result, combined with the load results from Table 8.4.1 in the following section, illustrates that the solution passes through a number of eigen-modes as the post-buckling solution progresses. These are linear eigen-modes and therefore the buckling loads at which they occur are not entirely accurate in the non-linear model because the geometry changes as the load is increased. For example, the third eigen-mode occurs at linear buckling load of 5702 N/m, whereas in a non-linear solution by the time the load had increased to this amount the geometry would have changed, if only slightly, from the original configuration and the corresponding change in the stiffness matrix would alter the buckling load. However it does illustrate why the solution may have difficulty converging for large loads and relatively large disbonds. This behaviour does not occur for small disbonds. For example, the 25-G specimen configuration did not pass through a second eigen-mode until well after the initiation of disbond growth and the solution was very stable.

Figure 8.4.12 and Figure 8.4.13 illustrate the face-sheet displacement shapes at disbond growth initiation for 2 of the 3 disbond sizes that were modelled.

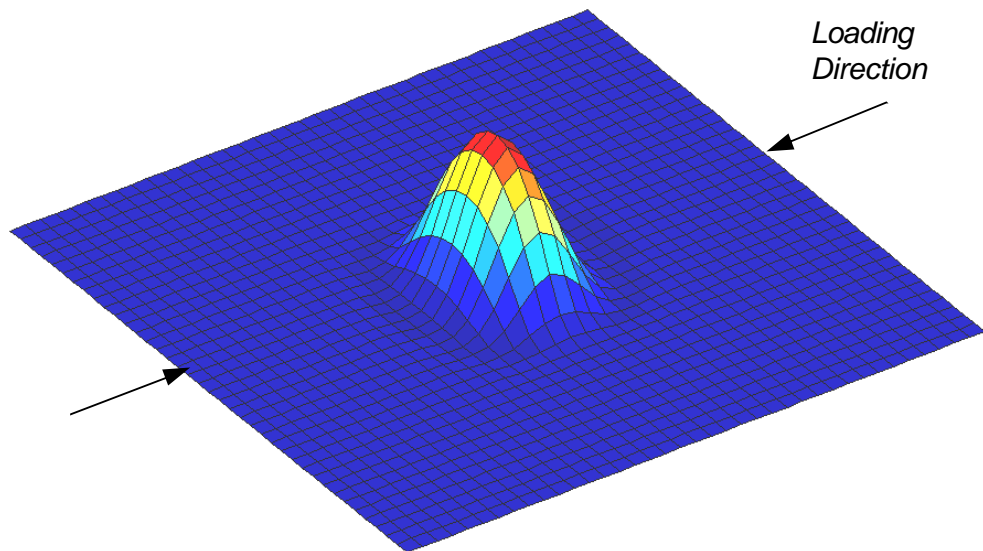


Figure 8.4.12 – Out-of-plane displacement at growth initiation for a specimen with 25mm disbond diameter and G-type face-sheet

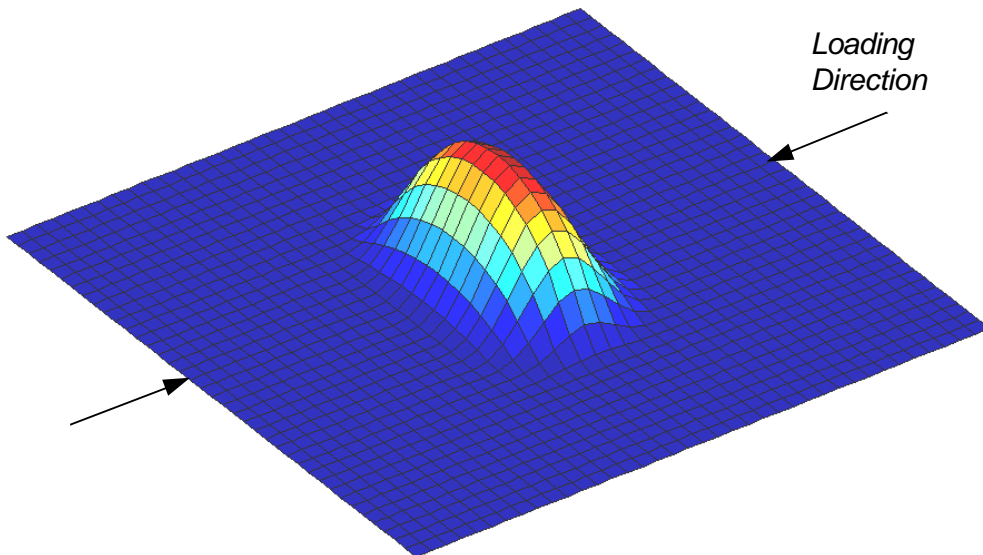


Figure 8.4.13 – Out-of-plane displacement at growth initiation for a specimen with 50mm disbond diameter and G-type face-sheet

If contour lines were used to connect similar out-of-plane displacements in Figure 8.4.12 and Figure 8.4.13, then the small disbond panel would display lines nearly circular in the disbond region, whereas the large disbond panel, 50mm (and similarly for 75mm), display a more elliptical profile, being elongated transverse to the direction of applied loading (Figure 8.4.14). This elliptical profile was particularly noticeable in the 75mm disbond specimens and resulted in large regions of contact as illustrated in Figure 8.4.14.

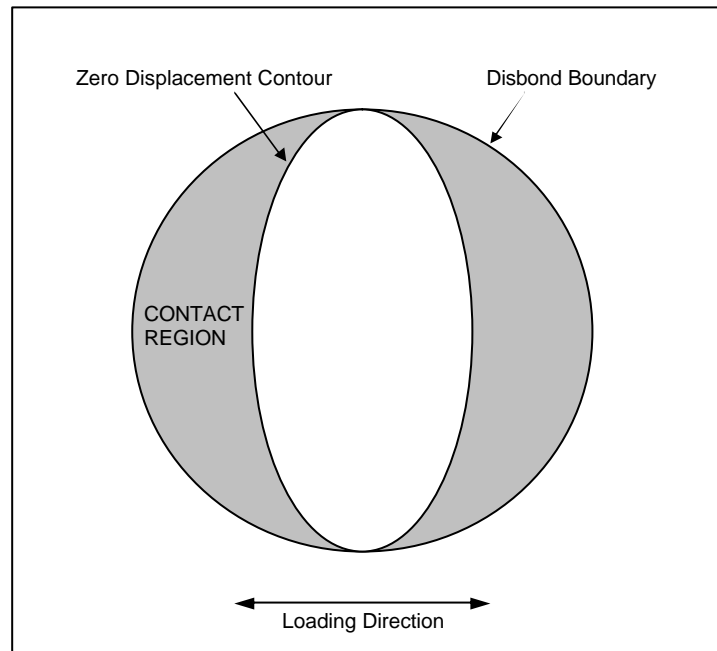


Figure 8.4.14 – Illustration of the elliptical profile observed in post-buckling, particularly for large disbonds, and the region of core contact

The conclusion of this section is that the model agrees very well with specimen test results provided appropriate boundary conditions are used. The agreement at high post-buckling loads might be improved by accounting for material non-linearity. The fundamental model assumption of small rotations was shown to be valid for all of the cases considered here.

8.4.2 DISBOND GROWTH INITIATION

The previous two sections showed that the geometrical post-buckling behaviour is well predicted. The next predictive capability to test by comparison with specimen test results is the load at which disbond growth initiates. This occurs when the strain energy release rate exceeds the critical value, which was determined by test in Chapter Three. Using the appropriate critical strain energy release rate in the present model the growth initiation loads were obtained (Table 8.4.1). As explained in the previous section, it was difficult to obtain large displacement results for the slender 75mm disbonds. The 75-GH specimen configuration has the most slender disbond and the solution was halted after a significant load reduction. The maximum load attained was 14200 N/m and this is quoted here as the estimate of growth initiation load.

Table 8.4.1 – Comparison of disbond growth initiation loads obtained from the model and specimen testing

Specimen Designation [#]	G _c (N/m)	Model Growth (N/m)	Exp. Growth (N/m)	Difference	Exp. Conf. Range (95%)
25-G	350	51000	42722	19.4 %	± 19.8%
25-GH	240	35900	26756	34.2 %	± 25.4%
50-G	350	28900	28000	3.2 %	± 25.4%
50-GH	240	20400	14242	43.2 %	± 62.8%
75-G	350	21000	21313	-1.5 %	± 13.2%
75-GH	240	14200*	14727	-3.6 %	± 18.7%
			Average	15.8 %	

[#] Refer to Chapter Six for specimen details

* Maximum obtainable load (occurred before growth initiation)

It is apparent from Table 8.4.1 that the present model predicts disbond growth initiation loads that for the most part lie within the statistical range of the experimental results, while generally being overestimates. Considering that this is a fracture problem in which the fracture toughness values have scatter in the order of 20%, the quality of the comparison is considered to be very good. The two figures below present loads normalised by the experimental wrinkling load (Aitken 2000) versus disbond diameter for the two types of face-sheet.

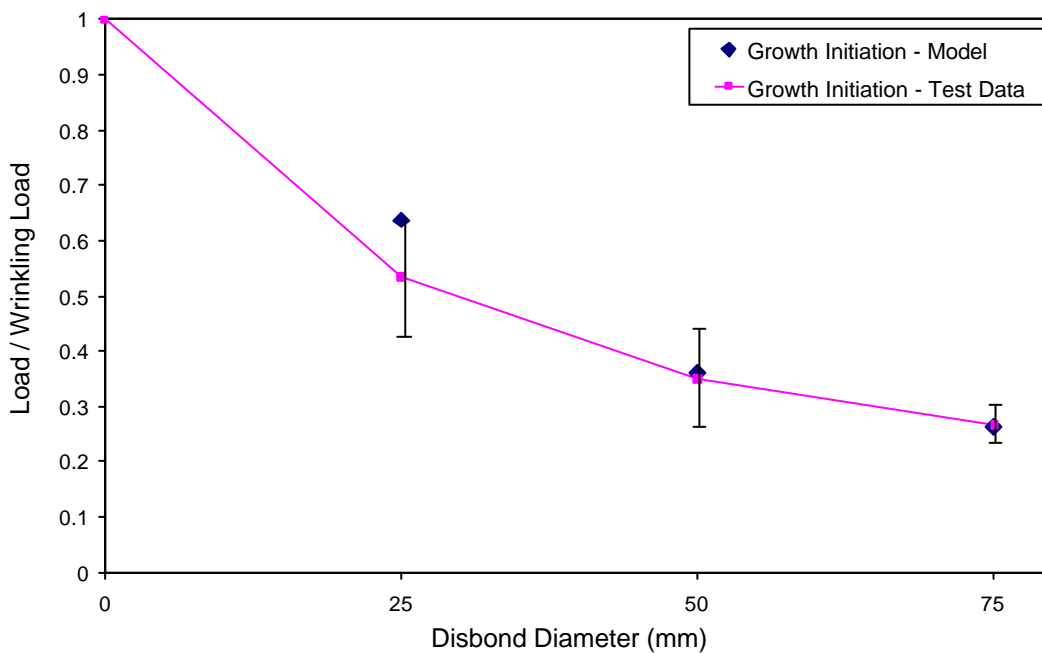


Figure 8.4.15 – Normalised disbond growth initiation loads for the G-type face-sheet (specimen test data also displays the 95% confidence range)

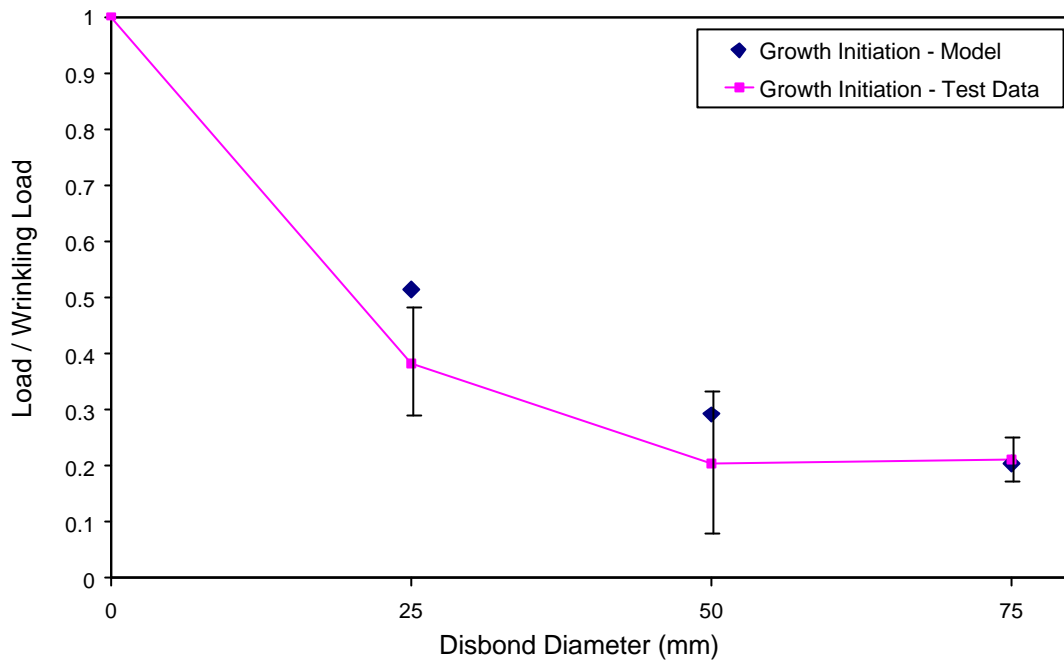


Figure 8.4.16 – Normalised disbond growth initiation loads for the GH-type face-sheet (specimen test data also displays the 95% confidence range)

It is apparent that the model provides good estimates of the load at which disbond growth initiates. This further validates the use of a Winkler-type model of a sandwich panel (in addition to the buckling load predictions of Chapter Seven agreeing to within 2.6% of specimen test results) as well as validating the present method of implementing the virtual crack closure technique in a Winkler plate model.

The growth initiation load results show the load at which the strain energy release rate at the disbond tip first exceeded the critical strain energy release rate. Figure 8.4.17 illustrates the variation of strain energy release rate (at the critical fracture node, see Figure 8.3.4) during the loading process. The load on the vertical axis is normalised to the disbond buckling load.

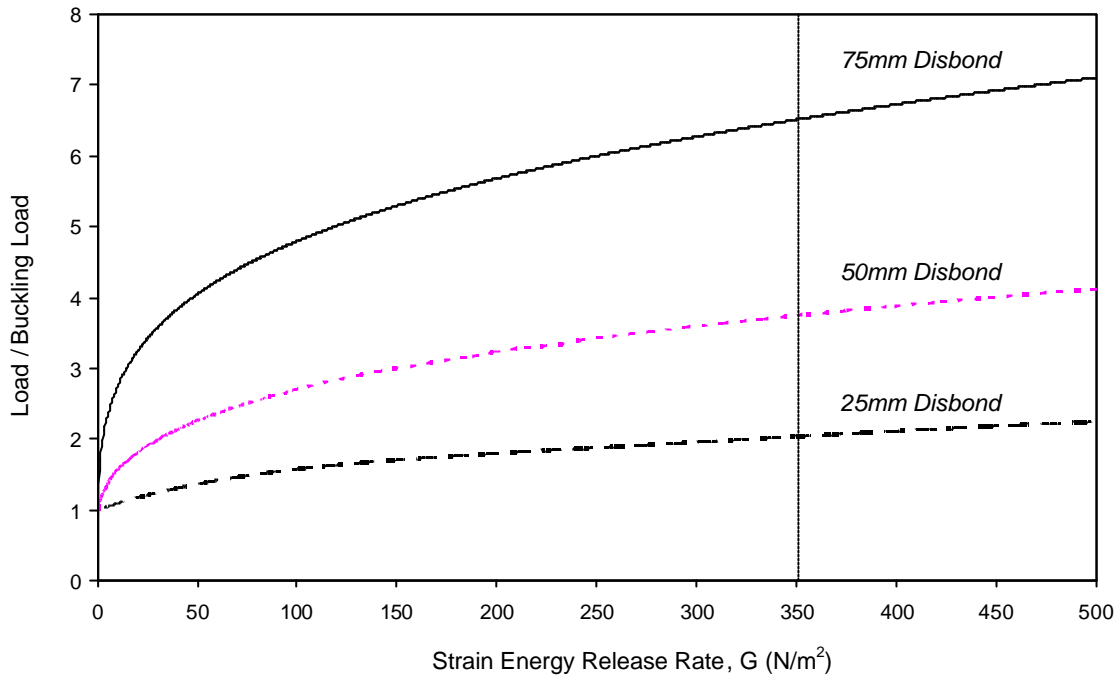


Figure 8.4.17 – Normalised load versus strain energy release rate for different disbond sizes

Figure 8.4.17 shows that the initiation of disbond growth occurs at load levels many times the buckling load for large disbonds. It also shows that the fraction of the buckling load at which fracture initiates decreases as the disbond size decreases.

In terms of predicting panel failure, the growth initiation load predictions of the present model provided a conservative estimate of the failure load in all cases (Table 8.4.2), with the best comparisons obtained for the specimens with small disbonds.

Table 8.4.2 – Comparison of experimental failure loads (Chapter Six) with model-predicted growth initiation loads

Specimen Designation	G_c (N/m)	Model Growth (N/m)	Exp. Failure (N/m)	Difference (%)
25-G	350	51000	54333	-6.1 %
25-GH	240	35900	38438	-6.6 %
50-G	350	28900	40092	-27.9 %
50-GH	240	20400	27992	-27.1 %
75-G	350	21000	33975	-38.2 %
75-GH	240	14200	25245	-43.8 %
			Average	-25.0 %

If the buckling load were used to obtain a conservative estimate of failure, it would result in under-estimates with an average difference of -77%, compared to the average under-estimate of -25% obtained using the growth initiation load. The next section describes an analysis of continued disbond growth to failure, to provide a more refined failure prediction.

8.4.3 PREDICTION OF CONTINUED DISBOND GROWTH

The present model calculates strain energy release rate at the disbond tip up to fracture and, at fracture, the stress at the fractured node is recorded and used from that point onwards as the tensile fracture strength of the core. By this method the disbond is able to propagate in any direction through the face-core interface. Disbond growth behaviour was very similar in form to that observed in specimen testing. Specifically, after the initiation of fracture several discrete fracture events occurred, spaced apart quite evenly in time. Then, at some point in all of the model runs, fracture became unstable. This was identified by a large number of fractured nodes occurring within consecutive increments and a corresponding reduction in load at each increment. This would typically cause the non-linear solution procedure to slow to a near halt as multiple load reductions were made. This sequence of events was defined as failure due to unstable disbond growth, as observed in Chapter Six specimen testing.

As previously discussed, it was found to be difficult to obtain convergence for the specimens with 75mm disbonds and these specimens were excluded from the analysis of continued disbond growth.

Table 8.4.3 – Comparison of model-predicted failure loads with experimental results

Specimen Designation	Model Failure (N/m)	Exp. Failure (N/m)	Difference (%)
25-G	62200	54333	14.5 %
25-GH	46200	38438	20.2 %
50-G	43600	40092	8.7 %
50-GH	31400	27992	12.2 %
		<i>Average</i>	<i>13.9 %</i>

These results show a very favourable comparison, with the difference between model and experimental failure loads having an average of +14%. These results are discussed further in the next section. The following figures illustrate a typical displacement profile evolution during loading, for the 50-G specimen, in which growth occurs perpendicular to the loading direction.

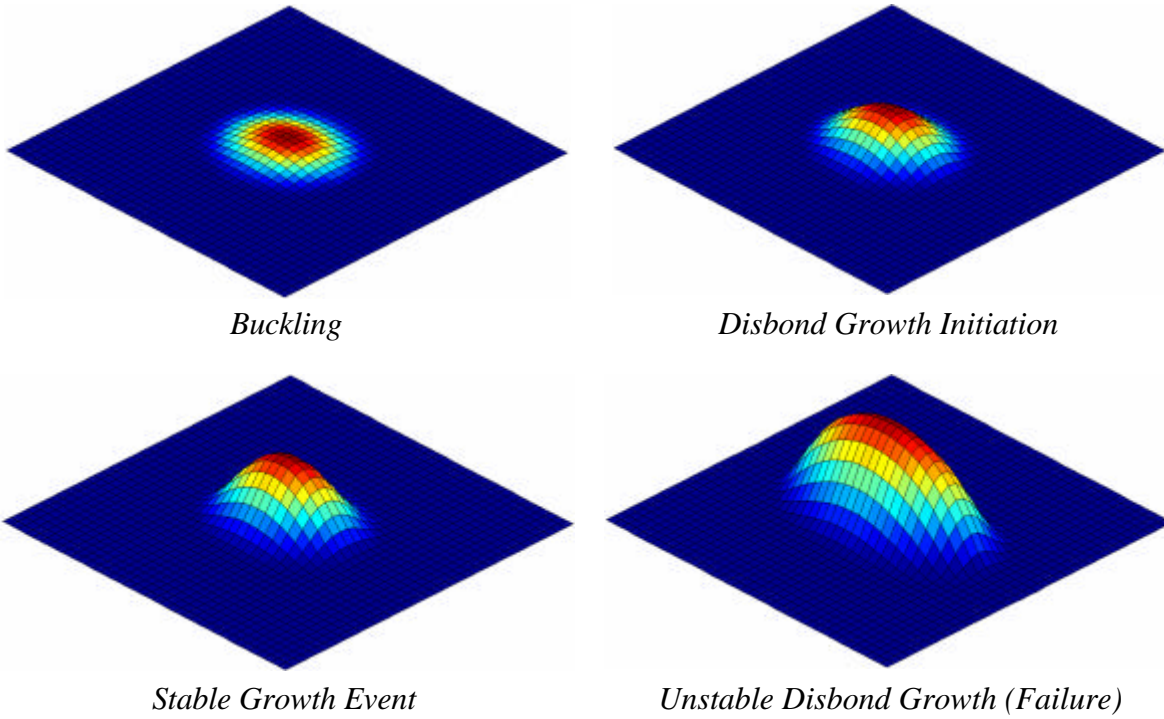


Figure 8.4.18 – Face-sheet displacements at various stages during loading

8.4.4 SUMMARY OF CRITICAL LOAD PREDICTIONS

The comparison between the specimen test results and the results of the present non-linear model are summarised in the following two figures.

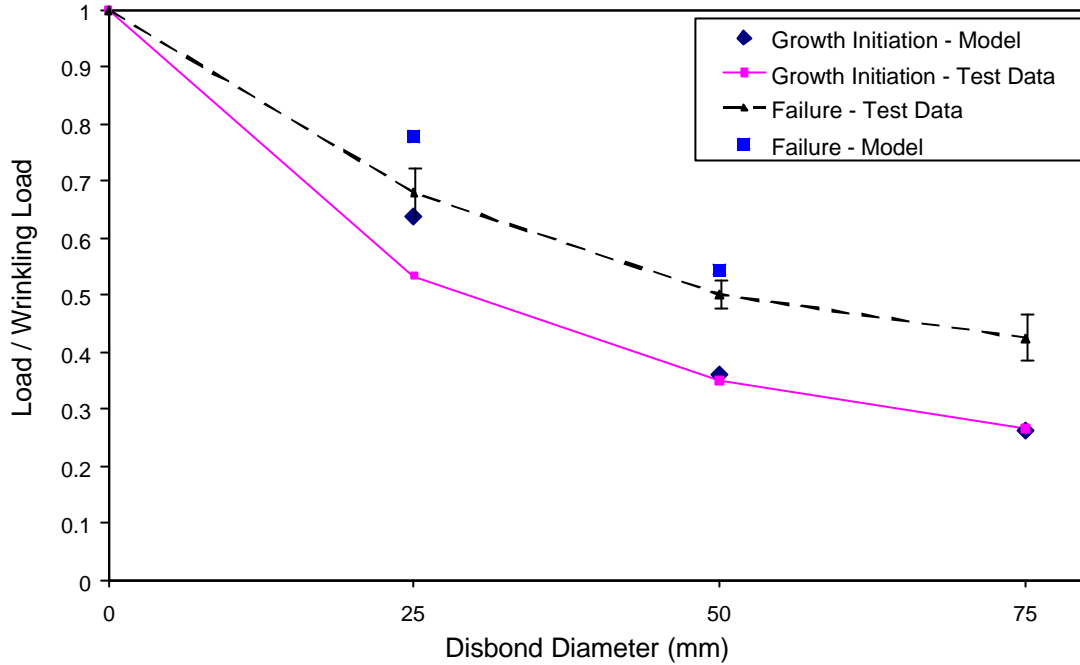


Figure 8.4.19 – Growth initiation and failure loads, from model and test results, for the G-type face-sheet material (test data includes the 95% confidence range)

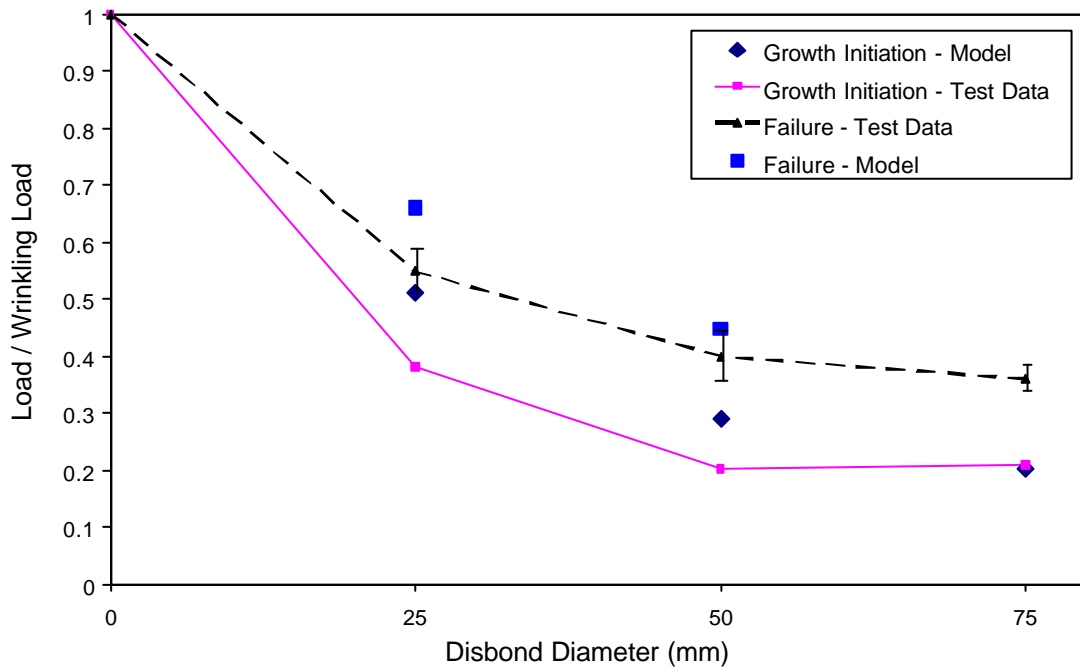


Figure 8.4.20 – Growth initiation and failure loads, experimental and model results, for the GH-type face-sheet material (test data includes the 95% confidence range)

Figures 8.4.19 and 8.4.20 show that the failure load is consistently over-predicted by the model and that the amount by which it is over-predicted is approximately the same as the amount by which the growth initiation load is over-predicted. This indicates that the post-growth behaviour is very well predicted and the main reason for the over-prediction is the growth initiation load prediction. Because the failure load is governed by disbond growth a more accurate growth initiation load would result in a more accurate failure load. The section at the end of Chapter Nine discusses possible improvements that could be made to the model to achieve more accurate growth initiation loads.

For practical purposes it is suggested that the growth initiation load be used as a conservative estimate of the failure load.

8.5 CONCLUSIONS

A non-linear Winkler plate model incorporating a circular central disbond has been developed. Core contact conditions were included and disbond growth initiation was modelled using the virtual crack closure technique. Continued disbond growth was modelled by switching from a fracture mechanics approach to a strength-based approach after the onset of growth. Pressure loading was also incorporated in the model and was used to establish a stable initial imperfection in the face-sheet.

The model was compared with specimen test results of disbond growth initiation and failure. With respect to predictions of disbond growth initiation the model consistently over-predicted but was within 15.8% of the specimen test data. This was considered to be an excellent result given the variability of fracture processes. These model results were also found to be conservative estimates of the failure load in all cases, with an average under-prediction of 25%. As a comparison, if the buckling load results presented in Chapter Seven were used as a conservative estimate of failure the average under-estimate would be 77%.

The analysis of continued disbond growth was performed for each specimen (except those with 75mm disbonds) and failure was defined by the initiation of unstable disbond growth, characterised by continuous fracture along with repeated load reductions. The specimens with 75mm disbonds were not used in this analysis because they were found to be too unstable to provide converged solutions at high loads. This behaviour was attributed to the slenderness of the disbonds allowing them to have multiple load paths. The failure loads were compared with specimen test data with an average error of +14%.

These results have shown that the computationally efficient Winkler plate model, incorporating moderate rotations, provides reasonably accurate failure load predictions. It is recommended for practical situations that the predicted disbond growth initiation load be used as a conservative estimate of the failure load.

The form of the growth behaviour was also very well predicted. Every run of the model exhibited several discrete increments of growth then, finally, initiation of unstable disbond growth through the width of the panel, which defined panel failure. This sequence of events agrees with specimen test results.

CHAPTER NINE

Conclusions

The aim of this research was to contribute significantly to the collective body of knowledge regarding failure of disbonded sandwich panels. This chapter reviews the results and findings of the thesis, summarising the most important findings from a damage tolerance perspective. Finally, the original contributions are summarised and suggestions are made for further research.

9.1 RESEARCH SUMMARY IN DAMAGE TOLERANCE TERMS

Two basic types of disbond were considered in the present research, through-width and embedded disbonds (Figure 9.1.1).

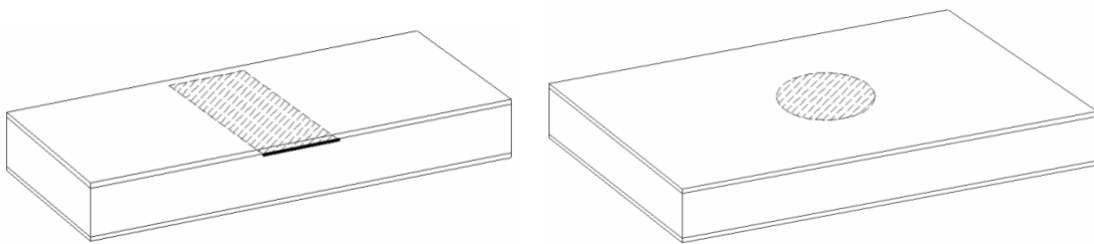


Figure 9.1.1 – Through-width (left) and embedded (right) disbonds

For each disbond type the failure behaviour was first determined by specimen testing and then predicted by two different models. In both cases buckling and disbond growth were identified as the critical events in the failure process. Therefore the models developed for each disbond type provided predictions of buckling load, disbond growth initiation load and disbond growth behaviour. In Chapter Two the basic concepts of damage tolerant design were presented with the aim that the present research would provide results that could fit into this general model and provide practical tools for damage tolerant design of sandwich structure. The model results presented in the various Chapters are summarised here in terms of the basic damage tolerance curve presented in Chapter Two (Figure 9.1.2).

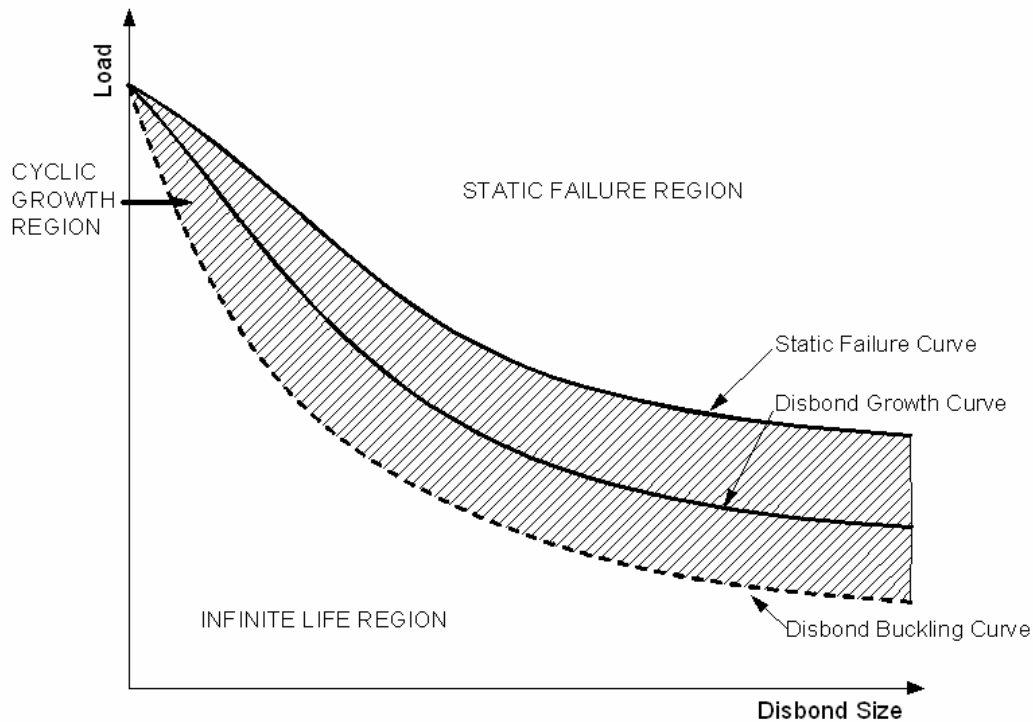


Figure 9.1.2 – A damage tolerance graph for disbonded sandwich structure

Figure 9.1.2 does not present cyclic loading curves but it does define a load range, for a given disbond size, within which cyclic loading may result in failure. The upper limit of the load carrying capacity of a panel is static failure. As discussed in Chapter Two, the endurance limit (maximum load that may be applied indefinitely without failure occurring) is equal to the buckling load.

9.1.1 SANDWICH BEAMS

9.1.1.1 DISBOND BUCKLING

Chapter Three identified the failure process as buckling followed by disbond growth, leading to failure by gross loss of stiffness. The buckling load was then predicted in Chapter Four using a Winkler beam model with modified core stiffness to incorporate orthotropic core properties. This model agreed with specimen test results within an average tolerance of 1.7%. A characteristic curve was developed from a regression analysis using dimensionless parameters (Figure 9.1.3).

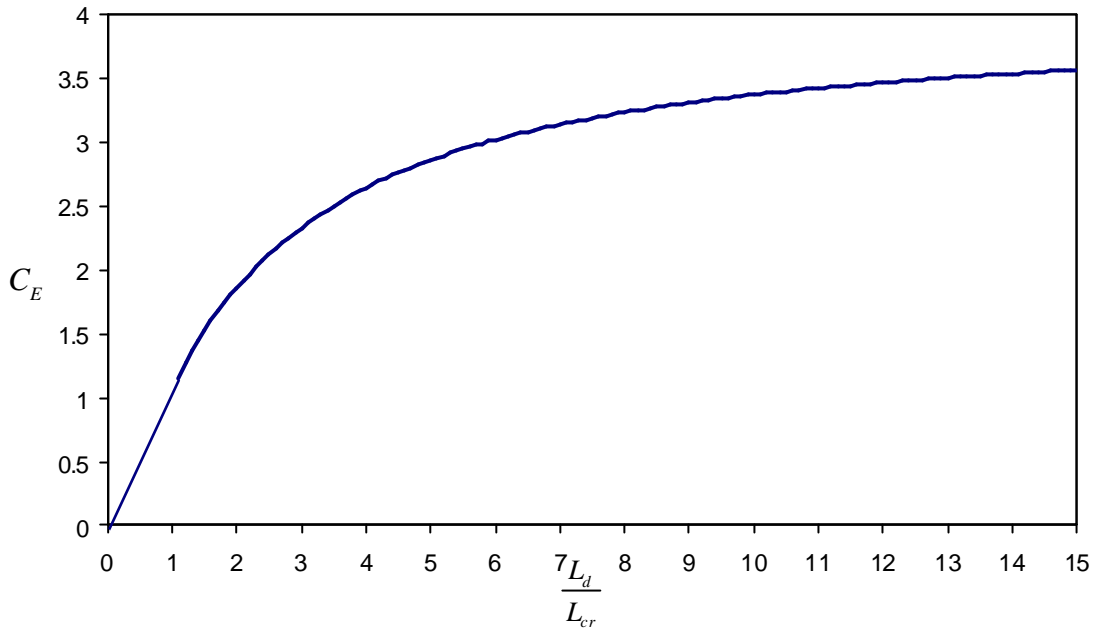


Figure 9.1.3 – Characteristic buckling curve for disbonded sandwich beams

The curve in Figure 9.1.3 represents a simple tool for determining the buckling load of a disbonded sandwich beam and agrees with the specimen test results within an average tolerance of 2.8%. This provides the lower of the three curves on the damage tolerance graph (Figure 9.1.2).

The buckling load is related to C_E in Figure 9.1.3 by:

$$P_{cr} = C_E \frac{P^2 D_f}{L_d^2} \quad (9.1.1)$$

9.1.1.2 DISBOND GROWTH

Having established the first of the three damage tolerance curves in Figure 9.1.2, the next to be determined is disbond growth initiation. Chapter Five tackled the issue of predicting disbond growth. The Winkler beam model used for buckling analysis was separated into two regions, the disbonded face-sheet and fully bonded sandwich. The fully bonded sandwich was treated as a Winkler beam with the same small displacement assumptions as the buckling model of Chapter Four. The disbonded face-sheet region was modelled as an Euler beam with arbitrarily large displacements and rotations. The virtual crack closure technique was adapted for use in a Winkler beam model and applied at the disbond edges to calculate the strain energy release rate. This provided a method of determining the initiation of disbond growth and hence the second curve in the damage tolerance graph was defined. Through a similar non-dimensional regression analysis to that of Chapter Four, a characteristic curve for disbond growth was found (Figure 9.1.4).

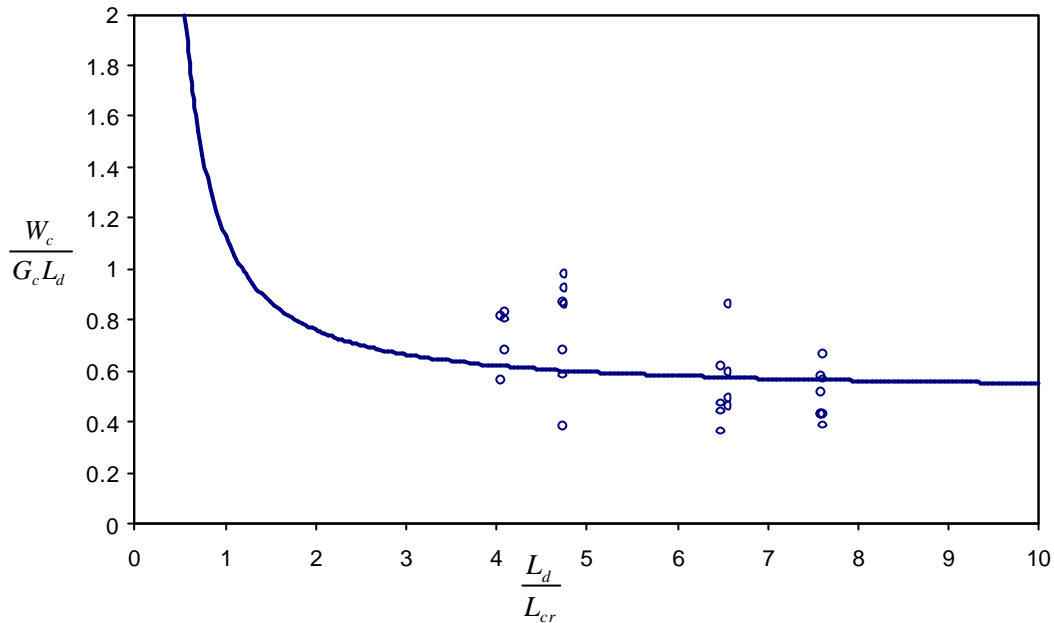


Figure 9.1.4 – Characteristic disbond growth curve for disbonded sandwich beams

This curve uses L_d/L_{cr} to define the specimen configuration, on the horizontal axis, and the vertical axis value is an energy ratio. The curve agrees with specimen test results with an average difference of 3.3% and standard deviation of 27.8%. This level of scatter is reasonable for fracture test results and the agreement is considered to be very good.

The work input required to initiate disbond growth is determined from Figure 9.1.4, for a specific specimen configuration, by finding the appropriate energy ratio on the vertical axis and multiplying it by $G_c L_d$. This can then be used to determine the post-buckling displacement that occurs before disbond growth by dividing the required work input by the buckling load.

$$\Delta = \frac{W_c}{P_{cr}} \quad (9.1.2)$$

This method assumes that the load remains constant after buckling, which was shown to be a reasonable assumption in Chapter Five. It should be noted that W_c is the work done in post-buckling only, i.e. it does not include work done up to buckling.

9.1.1.3 CONTINUED DISBOND GROWTH BEHAVIOUR

Although the model in Chapter Five did not allow the disbond to increase in size during loading, the characteristic disbond growth curve was used for an analysis of continued growth. The aim of this analysis was to predict static failure and the final damage tolerance curve. In the case of a sandwich beam static failure is defined by a gross loss of stiffness. Exactly how much stiffness must be lost

before it is defined as failure depends on the specific structural application. The characteristic disbond buckling and growth curves were combined to predict disbond growth behaviour. It was observed in the experimental results presented in Chapter Three that disbond growth proceeds as discrete fracture events rather than smooth, continuous growth. This was incorporated into the model with the assumption that the growth increments were equal to the cell size of the honeycomb core. The comparison in Figure 9.1.5 shows that the analysis closely predicts all of the following elements of disbond growth behaviour:

- Buckling load
- Overall load-displacement profile
- Load reduction at each growth increment
- Displacement between growth increments

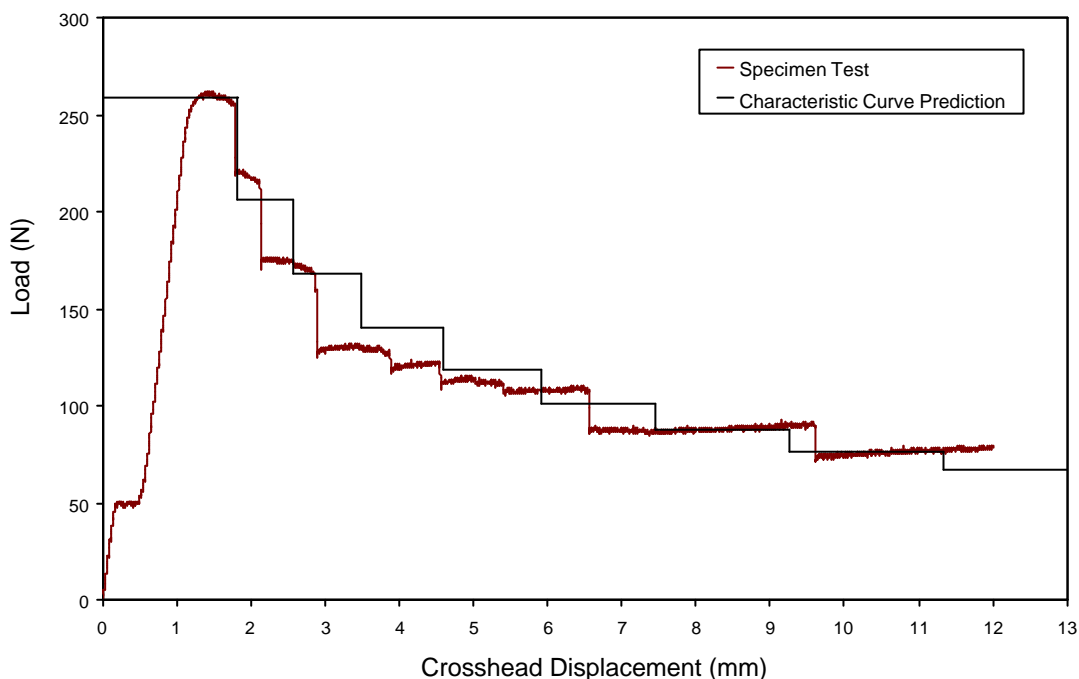


Figure 9.1.5 – Comparison between continued disbond growth analysis and a typical specimen test result

This result also verifies the assumption that growth occurs in increments approximately equal to the size of the honeycomb core cells.

The three analyses presented in Chapters Four and Five defined the damage tolerance behaviour of disbanded sandwich beams. The next consideration is the damage tolerance behaviour of sandwich panels with embedded disbonds.

9.1.2 SANDWICH PANELS

Specimen testing in Chapter Six identified the failure process of a sandwich panel containing an embedded disbond as; disbond buckling; continued loading where the stiffness of the structure remains virtually the same as in pre-buckling; several discrete growth increments followed by rapid unstable disbond growth to the panel edges, at which point failure is defined as a gross loss of structural stiffness.

The specimen tests showed that the primary difference between sandwich beams and the sandwich panels was that the sandwich panels continued to carry load after buckling with very little change in overall panel stiffness, whereas the sandwich beams had negligible post-buckling stiffness. Two models were developed for sandwich panels, one to predict disbond buckling and the other to predict disbond growth.

9.1.2.1 DISBOND BUCKLING

Chapter Seven described the development of a Winkler plate model to predict disbond buckling. In a similar analysis to that used for the sandwich beam model of Chapter Four, a characteristic buckling curve was determined (Figure 9.1.6) and agreed with specimen test results within an average tolerance of 3.7%.

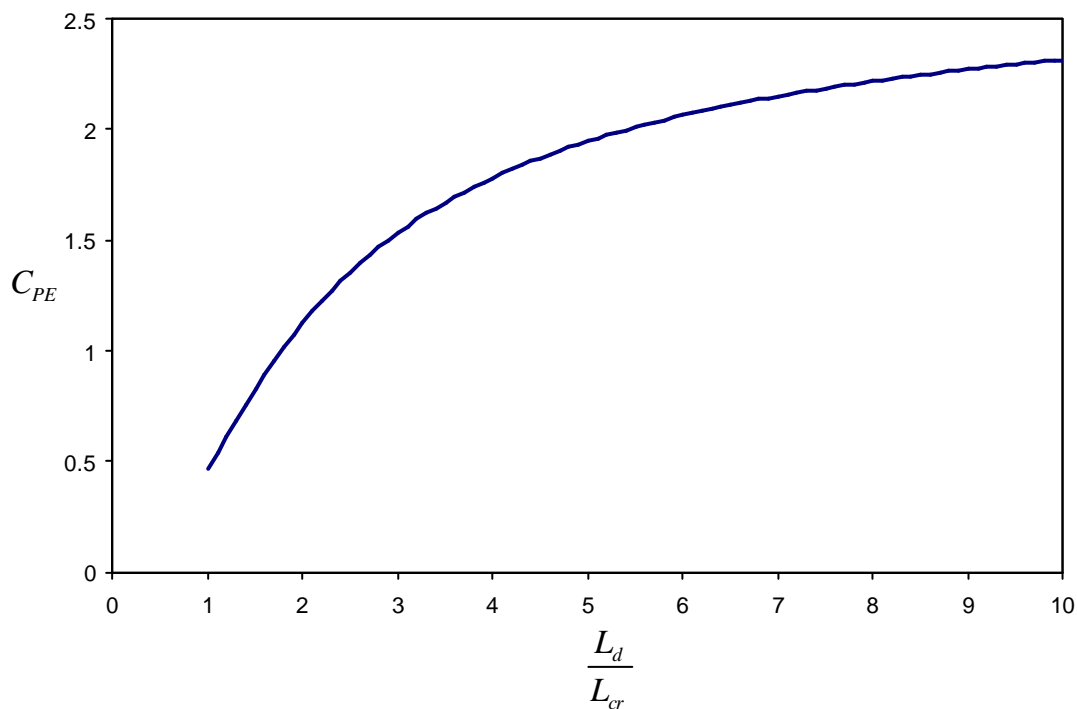


Figure 9.1.6 – Characteristic buckling curve for a sandwich panel with an embedded circular disbond of diameter L_d

This result provides the first of the damage tolerance curves. The Euler buckling coefficient on the vertical axis is defined as the coefficient C_{PE} in (9.1.3).

$$N_{cr} = C_{PE} \frac{4p^2 D_f}{L_d^2} \quad (9.1.3)$$

The effect of disbond proximity to a restrained edge was investigated and it was found that the wrinkling wavelength is a characteristic value for this analysis. The minimum distance between the disbond boundary a restrained panel edge must be greater than $2L_{cr}$ (the wrinkling wavelength) to ensure that the buckling load is unaffected. This minimum condition is illustrated in Figure 9.1.7.

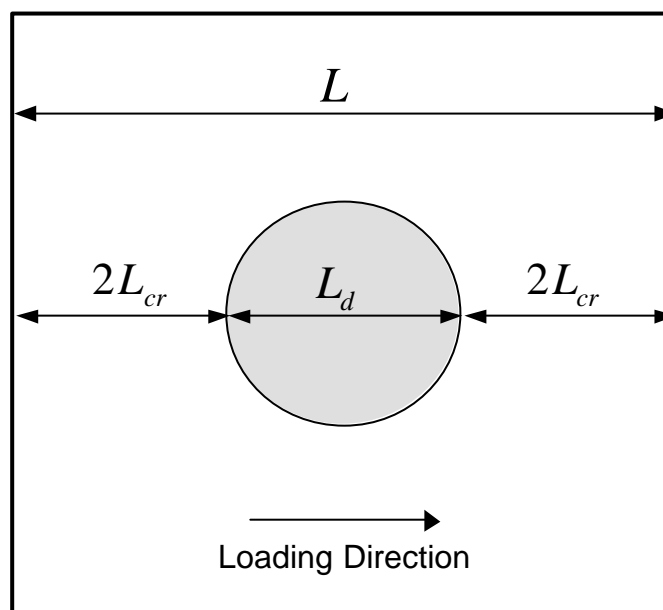


Figure 9.1.7 – An illustration of the minimum required panel size, to avoid edge effects.

The effect of the assumed disbond shape was also investigated. An actual disbond may be any shape and size and for analysis it is conservative to assume the disbond to be equal to the smallest circle that can completely enclose the actual disbond. However if the loading direction is known then it is more accurate to fit the smallest rectangle that encompasses the actual disbond, with edges of the rectangle parallel to the loading direction.

9.1.2.2 DISBOND GROWTH

Chapter Eight described a non-linear Winkler plate model incorporating the same fracture criteria as used in the non-linear Winkler beam model of Chapter Four. This analysis provided the remaining two curves in the damage tolerance graph; disbond growth initiation and static failure. The model predicted disbond growth initiation and included continuing disbond growth by releasing nodes that

exceeded the fracture strength. Failure was observed to be of the same form as the specimen test results, namely several small fracture events following by rapid unstable growth to failure.

Recall that the main aim of this research was to determine the three load curves required to define the damage tolerance behaviour of a disbanded sandwich. The first curve is the buckling load curve, the second is the disbond growth initiation curve and the last is the static failure curve. Buckling loads were predicted with an average difference of less than 4%. Growth initiation loads determined from the non-linear Winkler plate model of Chapter Eight agreed with specimen test results with an average difference of less than 16%, and failure loads obtained from the same model agreed to test results with an average difference of 14%. The 95% confidence intervals of the specimen test results were $\pm 11.8\%$, $\pm 27.6\%$ and $\pm 7.6\%$ for buckling, growth initiation and failure, respectively. Considering this level of scatter and the $\pm 31\%$ scatter in fracture toughness values used in the model the agreement was considered to be very good.

9.2 SUMMARY OF ORIGINAL CONTRIBUTIONS

This Chapter has identified the main findings of the present research in terms of the predictive capacity of the various models that were developed. The research presented here has increased the understanding of the failure process of compressively loaded disbanded sandwich panels and the models developed are efficient and accurate. Below is a table of the original contributions that this research has made.

Research Area	Original Contribution to the Field
Beam Testing	<ul style="list-style-type: none"> • Acoustic emission monitoring of disbond growth • New test method for face-core interfacial fracture properties • Testing of disbanded sandwich beams in bending
Through-width Disbond Buckling	<ul style="list-style-type: none"> • Modified foundation stiffness used in a Winkler beam model • Correlation with specimen test results
Through-width Disbond Growth	<ul style="list-style-type: none"> • The first non-linear model of disbanded sandwich beams in bending to incorporate transversely flexible core • A characteristic disbond growth curve validated by comparison to test results
Panel Testing	<ul style="list-style-type: none"> • Extensive testing of sandwich panels in bending with an embedded disbond • Accurate monitoring of the buckling event achieved by using a translating laser gauge • Acoustic emission monitoring of disbond growth and criteria for identifying face-core interfacial fracture acoustic events
Embedded Disbond Buckling	<ul style="list-style-type: none"> • Modified foundation stiffness resulting in the most accurate Winkler plate model developed to date • A characteristic buckling curve determined for circular embedded disbands • Identification of the wrinkling wavelength as a characteristic length regarding disbond proximity to a restrained boundary
Embedded Disbond Growth	<ul style="list-style-type: none"> • A non-linear Winkler plate model incorporating a disbond • Strain energy release rate used as a fracture criterion • Incorporated a failure model to account for continuing disbond growth to failure

9.3 SUGGESTIONS FOR FURTHER RESEARCH

During the course of this research several directions for further research were identified and they are described in this section, grouped under appropriate subject headings.

9.3.1 CYCLIC LOADING

The present research identified the load limits within which cyclic loading is a consideration but it did not include cyclic loading of test specimens. Based on the literature reviewed here there are no published experimental studies regarding cyclic loading of disbanded test specimens, having either through-width or embedded disbonds. It is recommended that research into this subject include the following:

- Identification of the endurance limit load. This could usefully be expressed as a fraction of the difference between buckling and failure loads due to static loading, as identified in the present research.
- Determine whether or not the experimental data can be reasonably represented by a Paris law relationship

9.3.2 REPAIR ANALYSIS

In practice a disbond region is repaired, or the part replaced, when it is discovered. Based on the present research more efficient repair methods might be developed and tested. The aim of a repair is typically to regain the stiffness and strength of the original structure. This research suggests that a reasonable method of quick repair may be to simply bond a circular face-sheet patch over the disbanded face-sheet region to increase the face-sheet thickness enough to restore original strength. This and other repair concepts could be developed and tested, both by analysis and by specimen testing, to validate an efficient repair for disbanded sandwich.

9.3.3 DEVELOPMENT OF A FAILURE MAP FOR DISBANDED SANDWICH

The beam and panel testing described in Chapters Three and Six, respectively, considered a specific range of specimen configurations. This might be expanded to develop a complete failure map for disbanded sandwich. In expanding the range of specimen configurations emphasis should be placed on face-sheet properties, as these were determined from the present research to have the most influence on failure. Specifically, a wider range of face-sheet thicknesses and material types could be included in an experimental plan. Such research would identify additional failure mechanisms

that should be incorporated into a disbond failure model, such as face-sheet or core failure (fracture or yielding). Different loading configurations might also be considered, such as shear and pure compression loading and multi-axial loading. Such an analysis would provide a map as to which type of analysis should be used for a particular loading situation.

9.3.4 MULTIPLE DISBONDS IN A SINGLE PANEL

Specifically regarding embedded disbonds it may often occur in practice that multiple disbonds occur in close proximity. In Chapter Seven the minimum distance required between multiple embedded disbonds to ensure independent buckling loads was presented. This was a linear analysis and did not consider in-plane strain effects, which may be significant when considering the effect of disbond proximity on failure load. The non-linear model presented in Chapter Eight could be used for this analysis and it should also be verified by testing of specimens having multiple embedded disbonds. This analysis would be valuable in practice because it would define a critical proximity, beyond which the disbonds could be considered independently by the present analysis. A method of treating disbonds in critical proximity might also be developed from such an analysis.

9.3.5 DEVELOPING THE NON-LINEAR MODEL PRESENTED IN CHAPTER EIGHT

The accuracy of the non-linear model presented in Chapter Eight might be improved by addition of the following:

- Shear tractions at the face-core interface
- Accounting for the variation of fracture toughness with core orientation
- A face-sheet damage model, such as that presented by Chen and Bai (2002)
- A refined mesh density at the disbond boundary (to achieve greater accuracy in the estimation of strain energy release rate)

These additions might prove particularly useful for achieving greater accuracy when considering specimen configurations outside of those presented in this research.

9.3.6 PROPERTIES OF HONEYCOMB CORE

Honeycomb core has many unique properties due to its cellular geometry. Two properties that are particularly relevant to the behaviour of debonded sandwich are fracture toughness and in-plane stiffness. Fracture toughness properties of honeycomb can be measured experimentally, however in the literature reviewed here there were no analytical models describing fracture through a face-sheet

to honeycomb core interface in which the cellular nature of the core was considered. The experimental fracture results obtained in Chapter Three identified a variation in fracture toughness of approximately 50% between fracture in the ribbon and transverse directions, however the cause of this variation is not known. Avery and Sankar (2000) noted similar variation according to honeycomb core orientation and only offered speculation that delamination of the honeycomb cell walls might cause higher toughness in the transverse direction. A detailed discrete model of honeycomb fracture could be used in a sandwich model such as the non-linear model presented in Chapter Eight to more accurately predict disbond growth behaviour.

The in-plane stiffness of honeycomb core when restrained by bonded face-sheets is significantly higher than honeycomb core alone (Becker 2000). As discussed in Chapter Two, more detailed cellular models are required to model in-plane stiffness more accurately. This is important because the in-plane core stiffness is a variable in the out-of-plane core stiffness used in the refined Winkler-type models.

9.3.7 THE EFFECT OF CORE THICKNESS ON CORE STIFFNESS

In Section 4.3.1 it was found that the core stiffness is a minimum when the thickness is equal to the wrinkling half-wavelength, L_{cr} , and below this thickness the stiffness increases rapidly. This behaviour is a function of the foundation stiffness term and further research is required to determine why the stiffness minimum occurs where it does and why the wrinkling wavelength should be a characteristic parameter of the core thickness when they are 90 degrees out of phase.

REFERENCES

- AFRL (Air Force Research Laboratory). 2002. *Handbook for Damage Tolerant Design*. AFRL/VASM. Retrieved: April 30th 2005, from <http://www.dtdesh.wpafb.af.mil>
- Aitken, R. R. 2000. Damage due to soft body impact on composite sandwich aircraft panels. PhD thesis. The University of Auckland, New Zealand.
- Ashby, M. F. & Gibson, L. J. 1997. *Cellular solids: structure and properties*. 2nd Edition. New York: Cambridge University Press.
- Avery, J. L., Sankar, B.V. 2000. Compressive failure of sandwich beams with debonded face-sheets. *Journal of Composite Materials*, 34: 1176-1199.
- Becker, W. 1998. The in-plane stiffnesses of a honeycomb core including the thickness effect. *Archive of Applied Mechanics*, 68(5): 334-341.
- Becker, W. 2000. Closed-form analysis of the thickness effect of regular honeycomb core material. *Composite Structures*, 48: 67-70.
- Beubl, R. 2004, *Damage tolerant design of fibre reinforced plastic sandwich structures*, BRITE/EURAM2. Retrieved: April 28, 2005, from http://dbs.cordis.lu/cordis-cgi/srchidadb?CALLER=RESUADVANCEDSRCH&ACTION=D&QF_EN_RCN_A=19093
- Bitzer, T. 1997. *Honeycomb Technology*. London: Chapman & Hall.
- Burman, M. 1998. Fatigue crack initiation and propagation in sandwich structures. PhD thesis. Royal Institute of Technology, Sweden.
- Cantwell, W. J., Davies, P. 1994. A test technique for assessing core-skin adhesion in composite sandwich structures. *Journal of Materials Science Letters*, 13: 203-205.
- Cantwell, W. J., Scudamore, R., Ratcliffe, J., Davies, P. 1999. Interfacial fracture in sandwich laminates. *Composites Science and Technology*, 59: 2079-2085.
- Carlsson, L. A., Sendlein, L.S., Merry, S.L. 1991. Characterisation of face sheet/core shear fracture of composite sandwich beams. *Journal of Composite Materials*, 25: 101-116.
- Chen, J. Y., Huang, Y. 1998. Fracture analysis of cellular materials: A strain gradient model. *Journal of Mechanics and Physics of Solids*, 46(5): 789-828.
- Chen, H., Bai, R. 2002. Post-buckling behaviour of face/core debonded composite sandwich plate considering matrix crack and contact effect. *Composite Structures*, 57: 305-313.
- Cheng, S.-H., Lin, C-C., Wang, J.T. 1997. Local buckling of delaminated sandwich beams using continuous analysis. *International Journal of Solids and Structures*, 34(2): 275-288.

- Cunningham, P. R., White, R.G. 2001. A new measurement technique for the estimation of core shear strain in closed sandwich structures. *Composite Structures*, 51: 319-334.
- Davidson, B. D. 1991. Delamination buckling: Theory and experiment. *Journal of Composite Materials*, 25: 1351-1379.
- Dennis, J. E., Schnabel, R.B. 1996. *Numerical methods for unconstrained optimisation and nonlinear equations*. PA: SIAM.
- Falk, L. 1994. Foam core sandwich panels with interface disbonds. *Composite Structures*, 28(4): 481-490.
- Frostig, Y. 1992. Behaviour of delaminated sandwich beam with transversely flexible core - higher order theory. *Composite Structures*, 20: 1-16.
- Frostig, Y., Sokolinsky, V. 1999. Buckling of debonded sandwich panels with transversely flexible core. *Advances in Aerospace Materials and Structures ASME*, 58: 23-40.
- Frostig, Y., Thomsen, O.T. 2004. Non-linear behaviour of delaminated unidirectional sandwich panels with partial contact and a transversely flexible core. *International Journal of Non-Linear Mechanics*, In-press.
- Gaudenzi, P., Perugini, P., Spadaccia, F. 1998. Post-buckling analysis of a delaminated composite plate under compression. *Composite Structures*, 40: 231-238.
- Gaudenzi, P., Perugini, P., Riccio, A. 2001. Post-buckling behaviour of composite panels in the presence of unstable delaminations. *Composite Structures*, 51: 301-309.
- Giordano, M., Calabro, A., Esposito, C., D'Amore, A., Nicolais, L. 1998. An acoustic-emission characterisation of the failure modes in polymer-composite materials. *Composites Science and Technology*, 58: 1923-1928.
- Goswami, S., Becker, W. 2000. Analysis of debonding fracture in a sandwich plate with hexagonal core. *Composite Structures*, 49: 385-392.
- Han, T.-S., Ural, A., Chen, G-S., Zehnder, A.T., Ingrassia, A.R., Billington, S.L. 2002. Delamination buckling and propagation analysis of honeycomb panels using a cohesive element approach. *International Journal of Fracture*, 115: 101-123.
- Hansen, U. 1998. Compression behaviour of frp sandwich specimens with interface debonds. *Journal of Composite Materials*, 32(4): 335-360.
- Haselbach, W., Lauke, B. 2003. Acoustic emission of debonding between fibre and matrix to evaluate local adhesion. *Composites Science and Technology*, 63: 2155-2162.
- Hetenyi, M. 1946. *Beams on elastic foundation*. Michigan: The University of Michigan Press.
- Horrigan, D. P. W. 2005. Personal Correspondence.
- Hwu, C., Hu, J.S. 1992. Buckling and postbuckling of delaminated composite sandwich beams. *AIAA Journal*, 30(7): 1901-1909.

- Kardomateas, G. A. 1990. Postbuckling characteristics in delaminated kevlar/epoxy laminates: An experimental study. *Journal of Composites Technology & Research*, 12(2): 85-90.
- Kassapoglou, C. 1988. Buckling, post-buckling and failure of elliptical delaminations in laminates under compression. *Composite Structures*, 9: 139-159.
- Kim, W. C., Dharan, C.K.H. 1992. Facesheet debonding criteria for composite sandwich panels under in-plane compression. *Engineering Fracture Mechanics*, 42(4): 642-652.
- Kim, W. C., Dharan, C.K.H., Miller, T.C. 1993. Strength of composite sandwich panels containing debonds. *International Journal of Solids and Structures*, 30: 211-223.
- Klug, J., Wu, X.X., Sun, C.T. 1996. Efficient modelling of post-buckling delamination growth in composite laminates using plate elements. *AIAA Journal*, 34(1): 178-184.
- Krueger, R., O'Brien, T. K. 2000. A shell/3D modeling technique for the analysis of delaminated composite laminates. *NASA technical memorandum TM-2000-210287, ARL-TR-2207*. Virginia: Langley Research Centre.
- Kulkarni, N., Mahfuz, H., Jeelani, S., Carlsson, L.A. 2003. Fatigue crack growth and life prediction of foam core sandwich composites under flexural loading. *Composite Structures*, 59: 499-505.
- Kyoung, W., Kim, C. 1995. Delamination buckling and growth of composite laminated plates with transverse shear deformation. *Journal of Composite Materials*, 29(15): 2047-2068.
- Lin, C.-C., Cheng, S.H., Wang, J.T-S. 1996. Local buckling of delaminated composite sandwich plates. *AIAA Journal*, 34(10): 2176-2183.
- Lusas Theory Manual, Lusas Finite Element software, version 13.5.
- Mackerle, J. 1995. Fracture mechanics parameters and finite element and boundary element methods - a bibliography (1992-1994). *Finite Elements in Analysis and Design*, 19: 209-223.
- Mason, R. L., Gunst, R.F., Hess, J.L. 1989. *Statistical design and analysis of experiments*. New York: Wiley.
- Minguet, P., Dugundji, J., Lagace, P.A. 1988. Buckling and failure of sandwich plates and graphite-epoxy faces and various cores. *Journal of Aircraft*, 25(4): 372-379.
- Nilsson, K.-F., Asp, L.E., Alpman, J.E., Nystedt, L. 2001. Delamination buckling and growth for delaminations at different depths in a slender composite panel. *International Journal of Solids and Structures*, 38: 3039-3071.
- Niu, K., Talreja, R. 1999. Buckling of a thin face layer on winkler foundation with debonds. *Journal of Sandwich Structures and Materials*, 1: 259-278.
- Okada, R., Kortschot, M.T. 2002. The role of the resin fillet in the delamination of honeycomb sandwich structures. *Composites Science and Technology*, 62: 1811-1819.

- Pappas, Y. Z., Kontsos, A., Loutas, T.H., Kostopoulos, V. 2004. On the characterisation of continuous fibres fracture by quantifying acoustic emission and acousto-ultrasonic waveforms. *NDT&E International*, 37: 389-401.
- Peck, S. O., Springer, G.S. 1991. The behaviour of delaminations in composite plates - analytical and experimental results. *Journal of Composite Materials*, 25: 907-925.
- Penzien, J., Didriksson, T. 1964. Effective shear modulus of honeycomb cellular structure. *AIAA Journal*, 2(3): 531-536.
- Pradhan, S. C., Tay, T.E. 1998. 3-dimensional finite element modelling of delamination growth in notched composite laminates under compression loading. *Engineering Fracture Mechanics*, 60(2): 157-171.
- Raju, I. S. 1987. Calculation of strain-energy release rates with higher order and singular finite elements. *Engineering Fracture Mechanics*, 28(3): 251-274.
- Reddy, J. N. 2004. *Mechanics of laminated composite plates and shells: theory and analysis*. 2nd Edition. Florida: CRC Press.
- Riccio, A., Perugini, P., Scaramuzzino, F. 2000. Modelling compression behaviour of delaminated composite panels. *Computers and Structures*, 78: 73-81.
- Riccio, A., Perugini, P., Scaramuzzino, F. 2001. Embedded delamination growth in composite panels under compressive load. *Composites: Part B*, 32: 209-218.
- Rinderknecht, S., Kroplin, B. 1997. A computational method for the analysis of delamination growth in composite plates. *Computers and Structures*, 64(1-4): 359-374.
- Sankar, B. V., Narayanan, M. 2001. Finite element analysis of debonded sandwich beams under axial compression. *Journal of Sandwich Structures and Materials*, 3: 197-219.
- Shenoi, R. A., Clark, S.D., Allen, H.G. 1995. Fatigue behaviour of polymer composite sandwich beams. *Journal of Composite Materials*, 29(18): 2423-2445.
- Shipsha, A. 2001. Failure of sandwich structures with sub-interface damage. PhD thesis. Royal Institute of Technology, Sweden.
- Sleight, D. W., Wang, J. T. 1995. Buckling analysis of debonded sandwich panel under compression. *NASA technical memorandum 4701*. Virginia: Langley Research Centre.
- Somers, M., Weller, T., Abramovich, H. 1991. Influence of predetermined delaminations on buckling and postbuckling behaviour of composite sandwich beams. *Composite Structures*, 17: 295-329.
- Tafreshi, A., Oswald, T. 2003. Global buckling behaviour and local damage propagation in composite plates with embedded delaminations. *International Journal of Pressure Vessels and Piping*, 80: 9-20.
- Thomson, R. S., Scott, M.L. 2000. Modelling delaminations in postbuckling stiffened composite shear panels. *Computational Mechanics*, 26: 75-89.
- Timoshenko, S. 1936. *Theory of elastic stability*. New York: McGraw-Hill.

-
- Toya, M., Aritomi, M., Chosa, A. 1997. Energy release rates for an interface crack embedded in a laminated beam subjected to 3-point bending. *Journal of Applied Mechanics*, 64: 375-382.
- Ural, A., Zehnder, A., Ingrassia, A. 2003. Fracture mechanics approach to facesheet delamination in honeycomb: Measurement of energy release rate of adhesive bond. *Engineering Fracture Mechanics*, 70: 93-103.
- Vizzini, A. J., Lagace, P.A. 1987. The buckling of a delaminated sublaminates on an elastic foundation. *Journal of Composite Materials*, 21: 1106-1117.
- Vonach, W. K., Rammerstorfer, F.G. 2000. Wrinkling of thick orthotropic sandwich plates under general loading conditions. *Archive of Applied Mechanics*, 70: 338-348.
- Whitcomb, J. D. 1989. Three-dimensional analysis of a postbuckled embedded delamination. *Journal of Composite Materials*, 23: 862-889.
- Whitcomb, J. D. 1992. Analysis of a laminate with a postbuckled embedded delamination - including contact effects. *Journal of Composite Materials*, 26(10): 1523-1534.
- White, F. M. 1994. *Fluid mechanics*. 3rd Edition. International Edition: McGraw-Hill.
- Xu, X. F., Qiao, P. 2002. Homogenised elastic properties of honeycomb sandwich with skin effect. *International Journal of Solids and Structures*, 39: 2153-2188.
- Yin, W. L., Sallam, S.N., Simitses, G.J. 1986. Ultimate axial load capacity of a delaminated beam-plate. *AIAA Journal*, 24(1): 123-128.
- Yin, W. L. 1988. The effects of laminated structure on delamination buckling and growth. *Journal of Composite Materials*, 22: 502-517.
- Zenkert, D. 1991. Strength of sandwich beams with interface debondings. *Composite Structures*, 17(4): 331-350.
- Zenkert, D. 1997. *The handbook of sandwich construction*. London: EMAS.

APPENDIX A

Specimen Manufacture and Testing

A.1 SPECIMEN MANUFACTURE

All test specimens were manufactured in the Composites Shop clean room of Air New Zealand Engineering Service (ANZES) from glass/epoxy laminate face-sheet (supplied as pre-impregnated sheets) and Nomex honeycomb core. The core was HRH78-1/8-3.0 (supplied by High Modulus Ltd.) and the face-sheets were 1581-38"-F155 and 120-38"-F155 (supplied by ANZES). Because the sheets were pre-impregnated with the F155 resin (pre-preg sheets), there was no additional adhesive used to bond the faces to the core. The complete manufacturing process was per aerospace recommended practice (SAE standards ARP5143 and ARP5144) and is detailed below:

1. Cut to size all core and face-sheet material
2. Lay the bottom face-sheets on the platen and then position the steel frame so as to locate the core centrally on the face-sheets
3. Place the core into the frame, locate the Teflon film centrally in the panel and layup the top face-sheets
4. Vacuum bag the platens per Figure A.1
5. Ensure that the vacuum seal will hold at least 10.7 psi consistently (manufacturer specified minimum vacuum for cure). The average vacuum pressure was approximately 12psi
6. Place specimens in the oven, ramping temperature up to 120°C at 1-4°C/min and maintaining this temperature for 90 minutes before ramping the temperature down again (Note: specialist composites technicians observed the entire cure process to ensure that nothing went wrong and to record the temperature profile, Figure A.2)
7. Once the panels are cured they are cut into the beam and panel specimens, as required, with a diamond edged table saw (Note: the disbonds were visible through the face-sheet, providing accurate reference points for the cutting process).

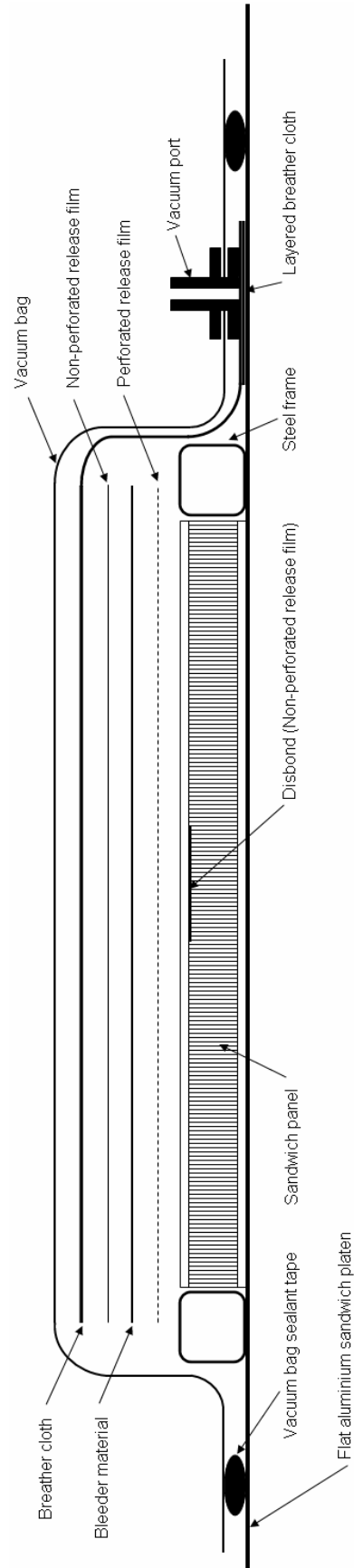


Figure A.1 – Lay-up sequence of sandwich test specimens

Document Name: Report Screen Print-out
 Document Info: File: Large-20031021-001.DAT, Tuesday, October 21, 2003, 9:52:23 PM
 Description: test piece

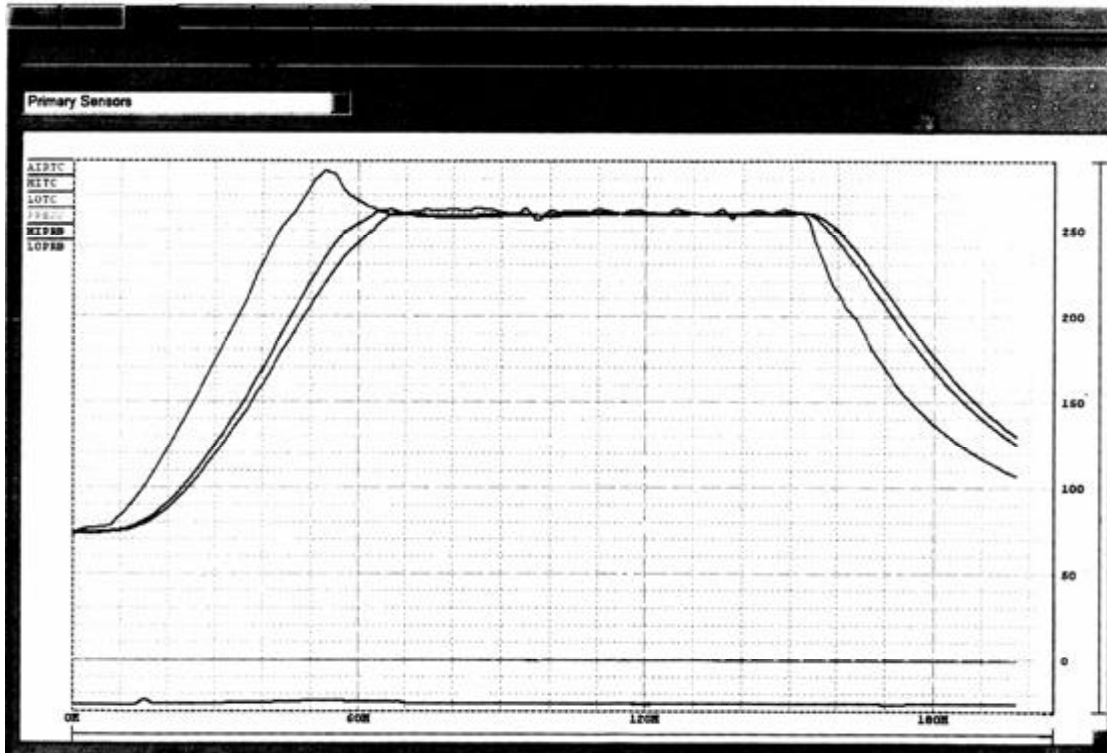


Figure A.2 – Sample temperature profile of a specimen cure (note: least controlled profile is the air temperature)

The manufacturer supplied face-sheet material properties are given in Figure A.3.



Physical Properties

	Property	Kevlar® Fabrics		Glass Fabrics		Carbon Tapes			Carbon Fabrics	
Prepreg	Material Description	K120	K285	120	1581	95 g/m ²	145 g/m ²	190 g/m ²	W3T282 or W3C282	F3T584 or F3C584
	%Flow @ 250°F 50 psi (121°C 345 kPa)	14-26	14-26	8-20	8-20	4-16	4-16	4-16	4-16	4-16
	% Resin Content (Dry)	54-60	49-55	42-48	36-40	38-40	38-40	38-40	40-44	40-44
Laminate	Cured Thickness per Ply - in (cm)	0.0045 (0.011)	0.0010 (0.0025)	0.0047 (0.012)	0.0104 (0.026)	0.0037 (0.0094)	0.0056 (0.014)	0.0074 (0.019)	0.0086 (0.022)	0.0150 (0.038)
	% Fiber Volume	42	46	38	45	57	57	57	50	51

Mechanical Properties

Property	Temp. T ₀ (°C)	Kevlar® 49 Fabrics		Glass Fabrics			Carbon Tapes			Carbon Fabrics
		120	285	120	220	181	T37056	T3C145	T2C100	W3T282
Tensile Strength, ksi (MPa)	75 (24)	62 (427)	62.8 (571)	57.0 (393)	60.3 (418)	70 (483)	225 (1552)	268 (1834)	225 (1518)	125 (848)
Tensile Modulus, mei (GPa)	75 (24)	3.9 (28.5)	4.4 (31.3)	3.0 (20.7)	3.0 (20.7)	2.4 (23.4)	18.3 (129.2)	15.3 (109.2)	18.1 (124.3)	8.4 (59)
Tensile Strain	75 (24)	15,800	---	---	---	---	10,180	10,370	10,470	10,480
Tensile Strength, ksi (MPa)	100 (71)	56 (401)	79.3 (547)	---	32.7 (227)	62 (427)	---	248 (1710)	226 (1556)	---
Tensile Modulus, mei (GPa)	100 (71)	3.7 (26)	3.9 (28.5)	---	2.7 (19.6)	3.1 (21.4)	---	17.2 (119)	17.3 (117)	---
Tensile Strain	100 (71)	---	---	---	---	---	---	---	---	---
Tensile Strength, ksi (MPa)	200 (138)	---	---	48.3 (313)	47.9 (333)	57 (393)	---	---	---	---
Tensile Modulus, mei (GPa)	200 (138)	---	---	2.6 (17.9)	2.6 (17.9)	2.6 (20)	---	---	---	---
Tensile Strain	200 (138)	---	---	---	---	---	---	---	---	---

Figure A.3 – Manufacturer supplied face-sheet properties for 120 and 1581 (also labelled 181) glass fabric laminae

A.2 ACOUSTIC EMISSION EQUIPMENT USED IN SANDWICH PANEL TESTING (CHAPTER SIX)

The acoustic emission equipment (provided by Industrial Research Laboratories) was a Vallens AMS-3, 4 channel acquisition unit with SE45-H transducers, having a sensitivity of -80 dB V/ μ bar at 150 kHz and a range of 25 kHz to approximately 260 kHz. AE event signals were recorded with a 5 MHz sampling rate and a 4k sample size by a designated transient sensor. There was minimal filtering on the transient recordings, the only requirement was a signal duration over 2 μ s. Acoustic gel was used to mount the sensors to the top and bottom faces of the specimens in the arrangement shown in Chapter Six. The acquisition software filtered events with an amplitude less than 35.6 dB (defined as the threshold amplitude).

APPENDIX B

Derivation of Non-dimensional Parameters

Refer to Chapter Five of White (1994) regarding all details of the methods described below for developing dimensionless parameters.

A.3 LINEAR WINKLER BEAM MODEL (CHAPTER FOUR)

The first step in the process of determining dimensionless parameters is establishing all of the variables in the problem. For the Winkler beam model these are defined below, along with the units for each variable. The MLT system unit system is used where M represents mass, L represents length and T represents time.

Variables	P	L_d	D_f	t_c	D_x	D_z	D_{xz}
Units	MT^{-2}	L	ML^2T^{-2}	L	$ML^{-1}T^{-2}$	$ML^{-1}T^{-2}$	$ML^{-1}T^{-2}$

There are 7 problem variables in 3 dimensions (M, L and T) therefore, according to the Buckingham-pi theorem, there could be as few as 4 dimensionless parameters, if there is a combination of three of the listed variables from which it is not possible to form a dimensionless group. For the variables shown this is not possible. As it happens, there are exactly 5 dimensionless parameters that can be derived from the 7 variables shown. Following the Buckingham-Pi theorem as described in White (1994), using disbond length, L_d , and face-sheet bending stiffness, D_f , as the scaling parameters:

$$\begin{aligned}
 \Pi_1 &= L_d^{x_1} D_f^{y_1} P & : (L)^{x_1} (ML^2T^{-2})^{y_1} (MT^{-2}) &= M^0 L^0 T^0 \\
 \Pi_2 &= L_d^{x_2} D_f^{y_2} t_c & : (L)^{x_2} (ML^2T^{-2})^{y_2} (L) &= M^0 L^0 T^0 \\
 \Pi_3 &= L_d^{x_3} D_f^{y_3} D_x & : (L)^{x_3} (ML^2T^{-2})^{y_3} (ML^{-1}T^{-2}) &= M^0 L^0 T^0 \\
 \Pi_4 &= L_d^{x_4} D_f^{y_4} D_z & : (L)^{x_4} (ML^2T^{-2})^{y_4} (ML^{-1}T^{-2}) &= M^0 L^0 T^0 \\
 \Pi_5 &= L_d^{x_5} D_f^{y_5} D_{xz} & : (L)^{x_5} (ML^2T^{-2})^{y_5} (ML^{-1}T^{-2}) &= M^0 L^0 T^0
 \end{aligned} \tag{A.1}$$

Solving for the powers in (A.1) results in the following non-dimensional parameters:

$$\Pi_1 = \frac{PL_d^2}{D_f}, \quad \Pi_2 = \frac{t_c}{L}, \quad \Pi_3 = \frac{D_x L_d^3}{D_f}, \quad \Pi_4 = \frac{D_z L_d^3}{D_f}, \quad \Pi_5 = \frac{D_{xz} L_d^3}{D_f} \quad (\text{A.2})$$

Because these parameters are dimensionless they may be scaled to provide a more meaningful number. In the case of Π_1 it is apparent that it may be rewritten as:

$$\Pi_1 = \frac{PL_d^2}{\mathbf{p}^2 D_f} \quad (\text{A.3})$$

Equation (A.3) represents the coefficient of Euler buckling, as explained in more detail in Chapter Five.

A.3.1 USING CORE STIFFNESS AS PROBLEM VARIABLE

The second analysis in Chapter Four considers using the core stiffness, k , as a problem parameter instead of the individual core properties, D_x , D_z , D_{xz} and t_c , that make up this final stiffness value. This analysis results in two dimensionless parameters as follows:

Variables	P	L_d	D_f	k
Units	MT^{-2}	L	ML^2T^{-2}	$ML^{-2}T^{-2}$

Using the same scaling parameters as the previous analysis:

$$\begin{aligned} \Pi_1 &= L_d^{x_1} D_f^{y_1} P && : (L)^{x_1} (ML^2T^{-2})^{y_1} (MT^{-2}) = M^0 L^0 T^0 \\ \Pi_2 &= L_d^{x_2} D_f^{y_2} k && : (L)^{x_2} (ML^2T^{-2})^{y_2} (ML^{-2}T^{-2}) = M^0 L^0 T^0 \end{aligned} \quad (\text{A.4})$$

Solving for the powers in the (A.4) results in the following two non-dimensional parameters:

$$\Pi_1 = \frac{PL_d^2}{D_f}, \quad \Pi_2 = \frac{kL_d^4}{D_f} \quad (\text{A.5})$$

Π_1 may be scaled as before, resulting in the Euler buckling coefficient:

$$\Pi_1 = \frac{PL_d^2}{\mathbf{p}^2 D_f} \quad (\text{A.6})$$

Π_2 may also be redefined by considering the definition of wrinkling wavelength (5.2.19). Taking Π_2 to the power $1/4$ and dividing by π results in a more meaningful dimensionless parameter:

$$\Pi_2 = \frac{L_d}{\mathbf{P}} \sqrt[4]{\frac{k}{D_f}} = \frac{L}{L_{cr}} \quad (\text{A.7})$$

A.4 NON-LINEAR WINKLER BEAM MODEL (CHAPTER FIVE)

The previous dimensional analysis highlighted that the wrinkling wavelength emerges as a variable in the disbonding problem. Therefore the problem variables are identified with their units as:

Variables	P	G	D	L_d	L_{cr}
Units	MT^{-2}	MT^{-2}	L	L	L

Using the wrinkling wavelength as a variable provides a means of lumping together the core and face-sheet values. Therefore, there are 5 variables in 3 dimensions (M, L and T). It is apparent by observation of the dimensions of the variables that it is only possible to find two scaling parameters that do not form a dimensionless group themselves. These are chosen to be load, P , and disbond length, L_d . The Buckingham-pi theorem is again used:

$$\begin{aligned} \Pi_1 = L_d^{x_1} P^{y_1} G & : (L)^{x_1} (MT^{-2})^{y_1} (MT^{-2}) = M^0 L^0 T^0 \\ \Pi_2 = L_d^{x_2} P^{y_2} \Delta & : (L)^{x_2} (MT^{-2})^{y_2} (L) = M^0 L^0 T^0 \\ \Pi_3 = L_d^{x_3} P^{y_3} L_{cr} & : (L)^{x_3} (MT^{-2})^{y_3} (L) = M^0 L^0 T^0 \end{aligned} \quad (\text{A.8})$$

Solving for the powers in (A.8) results in the following non-dimensional numbers:

$$\Pi_1 = \frac{G}{P} \quad , \quad \Pi_2 = \frac{\Delta}{L} \quad , \quad \Pi_3 = \frac{L_{cr}}{L} \quad (\text{A.9})$$

Π_3 is inverted so that it maintains the definition derived for the linear Winkler beam model:

$$\Pi_3 = \frac{L}{L_{cr}} \quad (\text{A.10})$$

A.5 LINEAR WINKLER PANEL MODEL (CHAPTER SEVEN)

Following the same procedure as above for the Winkler Plate model, the problem variables are first identified as:

Variables	N_x	L_d	k	H	D_{11}	D_{22}
Units	MT^{-2}	L	$ML^{-2}T^{-2}$	ML^2T^{-2}	ML^2T^{-2}	ML^2T^{-2}

H is a standard grouping of shear terms in the stiffness matrix, defined as:

$$H = D_{12} + 2D_{66} \quad (\text{A.11})$$

Choosing L_d and D_{11} as the scaling parameters:

$$\begin{aligned}
 \Pi_N &= L_d^{x_1} D_{11}^{y_1} N_x & : (L)^{x_1} (ML^2T^{-2})^{y_1} (MT^{-2}) &= M^0 L^0 T^0 \\
 \Pi_k &= L_d^{x_2} D_{11}^{y_2} k & : (L)^{x_2} (ML^2T^{-2})^{y_2} (ML^{-2}T^{-2}) &= M^0 L^0 T^0 \\
 \Pi_G &= L_d^{x_3} D_{11}^{y_3} H & : (L)^{x_3} (ML^2T^{-2})^{y_3} (ML^2T^{-2}) &= M^0 L^0 T^0 \\
 \Pi_D &= L_d^{x_4} D_{11}^{y_4} D_{22} & : (L)^{x_4} (ML^2T^{-2})^{y_4} (ML^2T^{-2}) &= M^0 L^0 T^0
 \end{aligned} \quad (\text{A.12})$$

Solving for the powers in (A.12) results in the following non-dimensional parameters:

$$\Pi_N = \frac{N_x L_d^2}{D_{11}}, \quad \Pi_k = \frac{k L_d^4}{D_{11}}, \quad \Pi_D = \frac{D_{22}}{D_{11}}, \quad \Pi_G = \frac{H}{D_{11}} = \frac{(D_{12} + 2D_{66})}{D_{11}} \quad (\text{A.13})$$

APPENDIX C

Strain Energy Release Rate Definitions for a Winkler Beam Model

As described in Chapter Five, Section 2.3.1, the derivation of an approximation to the strain energy release rate at the disbond edge in a Winkler beam model follows. The general expression for the Mode I strain energy release rate at a crack tip is:

$$G_I = \lim_{\Delta \rightarrow 0} \frac{1}{2\Delta} \int_0^{\Delta} \mathbf{s}_z(x,0) \cdot w(x-\Delta,0) dx \quad (\text{A.14})$$

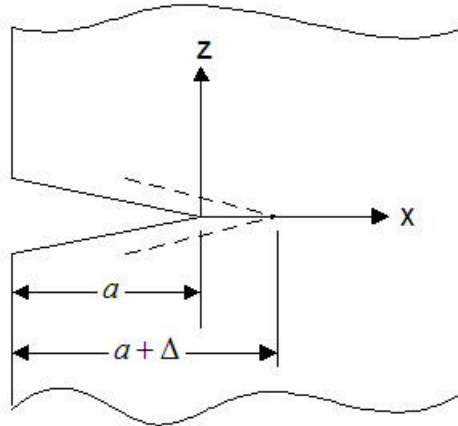


Figure C.4 – Reference for general strain energy release rate expression

For a Winkler beam:

$$\mathbf{s}_z = kw \quad (\text{A.15})$$

Therefore (A.15) can be rewritten for a discretised model:

$$G_I = \frac{k}{2\Delta} \int_0^{\Delta} w(x,0) \cdot w(x-\Delta,0) dx \quad (\text{A.16})$$

In order to implement this definition in the Winkler beam model, shown below, the face-sheet displacements are assumed to vary linearly between nodes. Therefore, two displacement functions can be defined for the two functions in (A.16):

$$\begin{aligned}
 w(x-\Delta, 0) &= \frac{w_n x + w_{n-1}(\Delta - x)}{\Delta} \\
 w(x, 0) &= \frac{w_{n+1} x + w_n(\Delta - x)}{\Delta}
 \end{aligned} \tag{A.17}$$

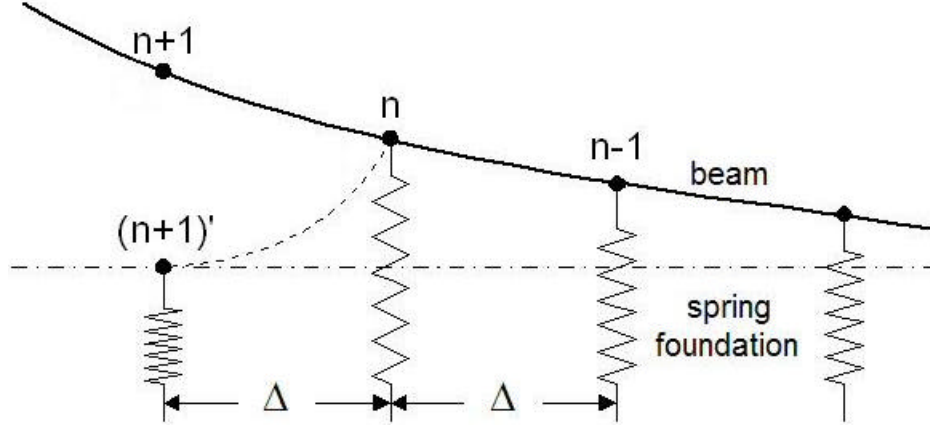


Figure C.5 – Discretised Winkler beam model

Equation (A.16) can be rewritten incorporating (A.17):

$$G_I = \frac{k}{2\Delta} \int_0^\Delta \left(\frac{w_{n+1}x + w_n(\Delta - x)}{\Delta} \right) \left(\frac{w_n x + w_{n-1}(\Delta - x)}{\Delta} \right) dx \tag{A.18}$$

Carrying out the integration of (A.18):

$$\begin{aligned}
 G_I &= \frac{k}{2\Delta} \int_0^\Delta \left(\frac{w_{n+1}x + w_n(\Delta - x)}{\Delta} \right) \left(\frac{w_n x + w_{n-1}(\Delta - x)}{\Delta} \right) dx \\
 &= \frac{k}{2\Delta^3} \int_0^\Delta \left(w_{n+1}w_n x^2 + w_{n+1}w_{n-1}\Delta x - w_{n+1}w_{n-1}x^2 + w_n^2 \Delta x + w_n w_{n-1} \Delta^2 - w_n w_{n-1} \Delta x + \dots \right. \\
 &\quad \left. \dots - w_n^2 x^2 - w_n w_{n-1} \Delta x + w_n w_{n-1} x^2 \right) dx \\
 &= \frac{k}{2\Delta^3} \left[w_{n+1}w_n \frac{x^3}{3} + w_{n+1}w_{n-1} \Delta \frac{x^2}{2} - w_{n+1}w_{n-1} \frac{x^3}{3} + w_n^2 \Delta \frac{x^2}{2} + w_n w_{n-1} \Delta^2 x + \dots \right. \\
 &\quad \left. \dots - w_n w_{n-1} \Delta \frac{x^2}{2} - w_n^2 \frac{x^3}{3} - w_n w_{n-1} \Delta \frac{x^2}{2} + w_n w_{n-1} \frac{x^3}{3} \right]_0^\Delta \\
 &= \frac{k}{2} \left(\frac{w_{n+1}w_n}{3} + \frac{w_{n+1}w_{n-1}}{2} - \frac{w_{n+1}w_{n-1}}{3} + \frac{w_n^2}{2} + w_n w_{n-1} - \frac{w_n w_{n-1}}{2} - \frac{w_n^2}{3} - \frac{w_n w_{n-1}}{2} + \frac{w_n w_{n-1}}{3} \right)
 \end{aligned} \tag{A.19}$$

Collecting similar terms results in the final expression:

$$G_I = \frac{k}{2} \left(\frac{w_{n+1}w_n}{3} + \frac{w_{n+1}w_{n-1}}{6} + \frac{w_n^2}{6} + \frac{w_n w_{n-1}}{3} \right) \quad (\text{A.20})$$

This is the expression given in Section 5.2.3 (Chapter Five).

APPENDIX D

Core Support Function at Disbond Boundaries

Variable definitions:

R	disbond radius
A	un-bonded nodal area
A'	bonded nodal area
Z	distance from disbond boundary to node
\mathbf{a}	bonded fraction of nodal area
x_n	x-coordinate of node n
y_n	y-coordinate of node n
\mathbf{D}	nodal spacing (equal in both x and y directions)

The method of modelling a circular disbond boundary in a square grid is described here. Figure D.6 is an illustration of the method, showing a region along the disbond boundary and defining the areas and lengths used to determine the stiffness value at a node. Nine nodes are shown with their rectangular areas of influence demarcated by dotted lines.

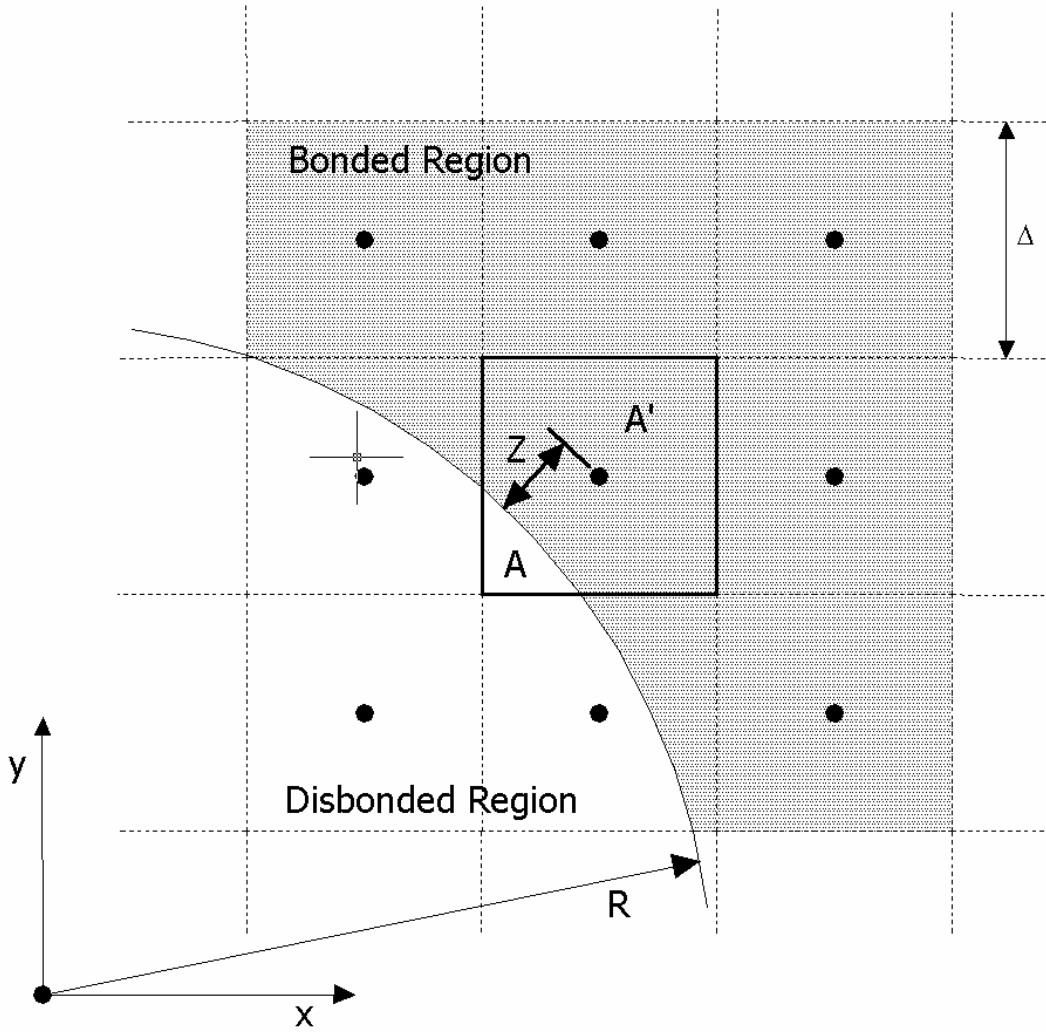


Figure D.6 – Method of defining stiffness at circular disbond boundary

The ratio α (refer Chapter Seven, Section 2.1.2) is determined for each node based on the following analysis. The exact definition of α is:

$$\mathbf{a} = \frac{A'}{A + A'} \quad (\text{A.21})$$

This is approximated at node n by defining the solution for the case where the disbond boundary is straight and parallel to one of the mesh directions (dotted lines in Figure D.6). This is done by defining the distance Z as:

$$Z = \sqrt{x_n^2 + y_n^2} - R \quad (\text{A.22})$$

Equation (A.21) is defined approximately by assuming:

$$A' = \left(\frac{\Delta}{2} + Z \right) \Delta \quad (\text{A.23})$$

This is exactly true when the disbond front is parallel to either the x or y axes. Note that $A+A'$ is the total area, Δ^2 .

$$\mathbf{a} \approx \frac{\left(\frac{\Delta}{2} + Z \right) \Delta}{\Delta^2} = 0.5 + \frac{Z}{\Delta} \quad (\text{A.24})$$

This method is applied to all nodes for which the disbond boundary intersects the associated nodal area. The maximum error in this approximate method occurs for nodes oriented at 45 degrees to the x and y axes and at this location the error in the approximated area fraction is 19%. The average error in the overall disbond area using this method was less than 0.2% for all test cases.

APPENDIX E

Derivation of Plane Strain Stiffness Terms used in Effective Core Stiffness Function

The stiffness terms used in the stress function of Vonach and Rammerstorfer (2000) (refer to Chapter Four, Section 2.2) were based on plane stress conditions within the core

$$\begin{aligned}
 D_z &= E_z \\
 D_x &= E_x \\
 D_{xz} &= \frac{2E_x G_{xz}}{(E_x - 2\nu_{xz} G_{xz})}
 \end{aligned}
 \tag{A.25}$$

The governing equation for a two-dimensional anisotropic solid is:

$$\left(\frac{1}{D_z} \right) \frac{\partial^4 \mathbf{f}}{\partial x^4} + \left(\frac{2}{D_{xz}} \right) \frac{\partial^4 \mathbf{f}}{\partial x^2 \partial z^2} + \left(\frac{1}{D_x} \right) \frac{\partial^4 \mathbf{f}}{\partial z^4} = 0
 \tag{A.26}$$

The equivalent terms for plane strain core conditions are derived for use in all of the Winkler-type models. Plane strain is assumed in the y-direction.

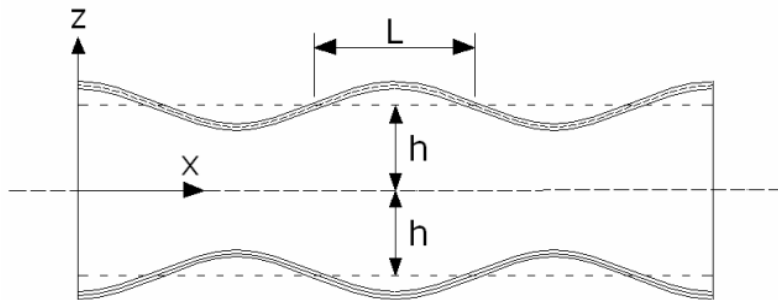


Figure E.7 – Sandwich beam in which the core stress function is being considered

The derivation begins by considering Hooke's Law for an orthotropic material:

$$\begin{aligned}
 \mathbf{e}_x &= \frac{\mathbf{s}_x}{E_x} - \frac{\mathbf{n}_{yx}\mathbf{s}_y}{E_y} - \frac{\mathbf{n}_{zx}\mathbf{s}_z}{E_z} \\
 \mathbf{e}_y &= \frac{\mathbf{s}_y}{E_y} - \frac{\mathbf{n}_{xy}\mathbf{s}_x}{E_x} - \frac{\mathbf{n}_{zy}\mathbf{s}_z}{E_z} \\
 \mathbf{e}_z &= \frac{\mathbf{s}_z}{E_z} - \frac{\mathbf{n}_{xz}\mathbf{s}_x}{E_x} - \frac{\mathbf{n}_{yz}\mathbf{s}_y}{E_y} \\
 \mathbf{g}_{xy} &= \frac{\mathbf{t}_{xy}}{G_{xy}} \\
 \mathbf{g}_{xz} &= \frac{\mathbf{t}_{xz}}{G_{xz}} \\
 \mathbf{g}_{yz} &= \frac{\mathbf{t}_{yz}}{G_{yz}}
 \end{aligned} \tag{A.27}$$

Under conditions of zero strain in y:

$$\begin{aligned}
 0 &= \frac{\mathbf{s}_y}{E_y} - \frac{\mathbf{n}_{xy}\mathbf{s}_x}{E_x} - \frac{\mathbf{n}_{zy}\mathbf{s}_z}{E_z} \\
 \Rightarrow \frac{\mathbf{s}_y}{E_y} &= \frac{\mathbf{n}_{xy}\mathbf{s}_x}{E_x} - \frac{\mathbf{n}_{zy}\mathbf{s}_z}{E_z}
 \end{aligned} \tag{A.28}$$

Using (A.27) in (A.26) develops the strain definitions:

$$\begin{aligned}
 \mathbf{e}_x &= \frac{\mathbf{s}_x}{E_x} - \frac{\mathbf{n}_{zx}\mathbf{s}_z}{E_z} - \frac{\mathbf{n}_{yx}\mathbf{n}_{xy}\mathbf{s}_x}{E_x} - \frac{\mathbf{n}_{yx}\mathbf{n}_{zy}\mathbf{s}_z}{E_z} \\
 &= \left(1 - \mathbf{n}_{yx}\mathbf{n}_{xy}\right) \frac{\mathbf{s}_x}{E_x} - \left(\mathbf{n}_{zx} + \mathbf{n}_{yx}\mathbf{n}_{zy}\right) \frac{\mathbf{s}_z}{E_z} \\
 &= A \frac{\mathbf{s}_x}{E_x} - B \frac{\mathbf{s}_z}{E_z} \\
 \mathbf{e}_z &= \frac{\mathbf{s}_z}{E_z} - \frac{\mathbf{n}_{xz}\mathbf{s}_x}{E_x} - \frac{\mathbf{n}_{yz}\mathbf{n}_{xy}\mathbf{s}_x}{E_x} - \frac{\mathbf{n}_{yz}\mathbf{n}_{zy}\mathbf{s}_y}{E_y} \\
 &= \left(1 - \mathbf{n}_{yz}\mathbf{n}_{zy}\right) \frac{\mathbf{s}_z}{E_z} - \left(\mathbf{n}_{xz} + \mathbf{n}_{yz}\mathbf{n}_{xy}\right) \frac{\mathbf{s}_x}{E_x} \\
 &= C \frac{\mathbf{s}_z}{E_z} - D \frac{\mathbf{s}_x}{E_x} \\
 \mathbf{g}_{xz} &= \frac{\mathbf{t}_{xz}}{G_{xz}}
 \end{aligned} \tag{A.29}$$

Based on the definition of Poisson's ratios as in (A.29) the constants B and D are redefined as in (A.30):

$$\mathbf{n}_{yx}\mathbf{n}_{zy} = \frac{\mathbf{e}_x \mathbf{e}_y}{\mathbf{e}_y \mathbf{e}_z} = \frac{\mathbf{e}_x}{\mathbf{e}_z} = \mathbf{n}_{zx} \quad (\text{A.30})$$

$$\begin{aligned} B &= 2\mathbf{n}_{zx} \\ D &= 2\mathbf{n}_{xz} \end{aligned} \quad (\text{A.31})$$

The strain compatibility condition is defined as:

$$\frac{\partial^2 \mathbf{e}_x}{\partial z^2} + \frac{\partial^2 \mathbf{e}_z}{\partial x^2} = \frac{\partial^2 \mathbf{g}_{xz}}{\partial x \partial z} \quad (\text{A.32})$$

Differentiating (A.28) and substituting in (A.31) yields:

$$\begin{aligned} &\frac{A}{E_x} \frac{\partial^2 \mathbf{s}_x}{\partial z^2} - \frac{B}{E_z} \frac{\partial^2 \mathbf{s}_z}{\partial z^2} + \frac{C}{E_z} \frac{\partial^2 \mathbf{s}_z}{\partial x^2} - \frac{D}{E_x} \frac{\partial^2 \mathbf{s}_x}{\partial x^2} = \frac{1}{G_{xz}} \frac{\partial^2 \mathbf{t}_{xz}}{\partial x \partial z} \\ \Rightarrow &\frac{A}{E_x} \frac{\partial^2 \mathbf{s}_x}{\partial z^2} - \frac{B}{E_z} \frac{\partial^2 \mathbf{s}_z}{\partial z^2} + \frac{C}{E_z} \frac{\partial^2 \mathbf{s}_z}{\partial x^2} - \frac{D}{E_x} \frac{\partial^2 \mathbf{s}_x}{\partial x^2} + \frac{1}{2G_{xz}} \frac{\partial^2 \mathbf{s}_x}{\partial x^2} + \frac{1}{2G_{xz}} \frac{\partial^2 \mathbf{s}_z}{\partial z^2} = 0 \\ \Rightarrow &\left(\frac{A}{E_x} \right) \frac{\partial^2 \mathbf{s}_x}{\partial z^2} + \left(\frac{C}{E_z} \right) \frac{\partial^2 \mathbf{s}_z}{\partial x^2} + \left(\frac{1}{2G_{xz}} - \frac{D}{E_x} \right) \frac{\partial^2 \mathbf{s}_x}{\partial x^2} + \left(\frac{1}{2G_{xz}} - \frac{B}{E_z} \right) \frac{\partial^2 \mathbf{s}_z}{\partial z^2} = 0 \end{aligned} \quad (\text{A.33})$$

The stresses are defined in terms of the stress function as:

$$\begin{aligned} \mathbf{s}_x &= \frac{\partial^2 \mathbf{f}}{\partial z^2} \\ \mathbf{s}_z &= \frac{\partial^2 \mathbf{f}}{\partial x^2} \end{aligned} \quad (\text{A.34})$$

Substituting (A.33) into (A.32) and expanding the constants, A , B , C and D , results in the governing equation:

$$\left(\frac{1 - \mathbf{n}_{yx}\mathbf{n}_{xy}}{E_x} \right) \frac{\partial^4 \mathbf{f}}{\partial z^4} + 2 \left(\frac{1}{2G_{xz}} - \frac{2\mathbf{n}_{xz}}{E_x} \right) \frac{\partial^4 \mathbf{f}}{\partial x^2 \partial z^2} + \left(\frac{1 - \mathbf{n}_{yz}\mathbf{n}_{zy}}{E_z} \right) \frac{\partial^4 \mathbf{f}}{\partial x^4} = 0 \quad (\text{A.35})$$

From which the definitions of the plane strain constants in (A.25) are:

$$\begin{aligned} D_z &= \frac{E_z}{1 - \mathbf{n}_{yz}\mathbf{n}_{zy}} \\ D_x &= \frac{E_x}{1 - \mathbf{n}_{yx}\mathbf{n}_{xy}} \\ D_{xz} &= \frac{2E_x G_{xz}}{E_x - 4\mathbf{n}_{xz} G_{xz}} \end{aligned} \quad (\text{A.36})$$

APPENDIX F

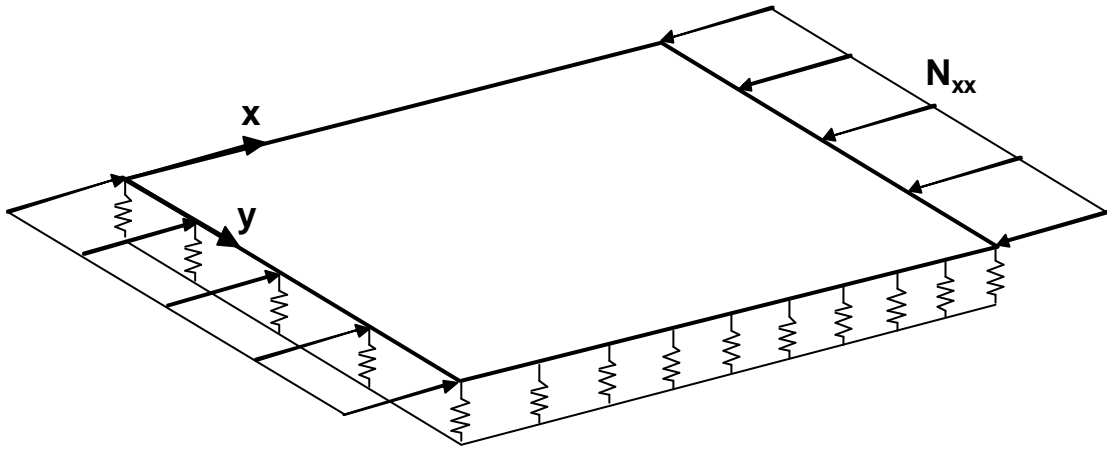
Non-linear Winkler Plate Modelling

A.6 PLATE EQUATIONS WITH MODERATE ROTATIONS

The governing equations are:

$$\begin{aligned} \frac{\partial N_{xx}}{\partial x} + \frac{\partial N_{xy}}{\partial y} &= 0 \\ \frac{\partial N_{yy}}{\partial y} + \frac{\partial N_{xy}}{\partial x} &= 0 \\ \frac{\partial^2 M_{xx}}{\partial x^2} + 2 \frac{\partial^2 M_{xy}}{\partial x \partial y} + \frac{\partial^2 M_{yy}}{\partial y^2} + \frac{\partial}{\partial x} \left(N_{xx} \frac{\partial w_0}{\partial x} + N_{xy} \frac{\partial w_0}{\partial y} \right) + \frac{\partial}{\partial y} \left(N_{xy} \frac{\partial w_0}{\partial x} + N_{yy} \frac{\partial w_0}{\partial y} \right) + k w_0 &= 0 \end{aligned} \quad (\text{A.37})$$

With reference to the following diagram of a Winkler plate in uniaxial compression:



The strain definitions are given as:

$$\begin{aligned} \mathbf{e}_{xx} &= \frac{\partial u_0}{\partial x} + \frac{1}{2} \left(\frac{\partial w_0}{\partial x} \right)^2 \\ \mathbf{e}_{yy} &= \frac{\partial v_0}{\partial y} + \frac{1}{2} \left(\frac{\partial w_0}{\partial y} \right)^2 \\ \mathbf{e}_{xy} &= \frac{\partial u_0}{\partial y} + \frac{\partial v_0}{\partial x} + \frac{\partial w_0}{\partial x} \frac{\partial w_0}{\partial y} \end{aligned} \quad (\text{A.38})$$

The force and moment definitions are, respectively:

$$\begin{aligned} N_{xx} &= A_{11}\mathbf{e}_x + A_{12}\mathbf{e}_y \\ N_{yy} &= A_{12}\mathbf{e}_x + A_{22}\mathbf{e}_y \\ N_{xy} &= A_{66}\mathbf{e}_{xy} \end{aligned} \quad (\text{A.39})$$

$$\begin{aligned} M_{xx} &= -D_{11} \frac{\partial^2 w}{\partial x^2} - D_{12} \frac{\partial^2 w}{\partial y^2} \\ M_{yy} &= -D_{12} \frac{\partial^2 w}{\partial x^2} - D_{22} \frac{\partial^2 w}{\partial y^2} \\ M_{xy} &= -2D_{66} \frac{\partial^2 w}{\partial x \partial y} \end{aligned} \quad (\text{A.40})$$

Rewriting the governing equation in terms of displacements u , v , and w :

$$A_{11} \left(\frac{\partial^2 u_0}{\partial x^2} + \frac{\partial w_0}{\partial x} \frac{\partial^2 w_0}{\partial x^2} \right) + A_{12} \left(\frac{\partial^2 v_0}{\partial x \partial y} + \frac{\partial w_0}{\partial y} \frac{\partial^2 w_0}{\partial x \partial y} \right) + A_{66} \left(\frac{\partial^2 u_0}{\partial y^2} + \frac{\partial^2 v_0}{\partial x \partial y} + \frac{\partial^2 w_0}{\partial x \partial y} \frac{\partial w_0}{\partial y} + \frac{\partial w_0}{\partial x} \frac{\partial^2 w_0}{\partial y^2} \right) = 0 \quad (\text{A.41})$$

$$A_{12} \left(\frac{\partial^2 u_0}{\partial x \partial y} + \frac{\partial w_0}{\partial x} \frac{\partial^2 w_0}{\partial x \partial y} \right) + A_{22} \left(\frac{\partial^2 v_0}{\partial y^2} + \frac{\partial w_0}{\partial y} \frac{\partial^2 w_0}{\partial y^2} \right) + A_{66} \left(\frac{\partial^2 u_0}{\partial x \partial y} + \frac{\partial^2 v_0}{\partial x^2} + \frac{\partial^2 w_0}{\partial x^2} \frac{\partial w_0}{\partial y} + \frac{\partial w_0}{\partial x} \frac{\partial^2 w_0}{\partial x \partial y} \right) = 0 \quad (\text{A.42})$$

$$\begin{aligned} &D_{11} \frac{\partial^4 w_0}{\partial x^4} + 2D_{12} \frac{\partial^4 w_0}{\partial x^2 \partial y^2} + 4D_{66} \frac{\partial^4 w_0}{\partial x^2 \partial y^2} + D_{22} \frac{\partial^4 w_0}{\partial y^4} + k w_0 - A_{11} \left(\frac{\partial u_0}{\partial x} + \frac{1}{2} \left(\frac{\partial w_0}{\partial x} \right)^2 \right) \frac{\partial^2 w_0}{\partial x^2} + \dots \\ &\dots - A_{12} \left(\frac{\partial v_0}{\partial y} + \frac{1}{2} \left(\frac{\partial w_0}{\partial y} \right)^2 \right) \frac{\partial^2 w_0}{\partial x^2} - 2A_{66} \left(\frac{\partial u_0}{\partial y} + \frac{\partial v_0}{\partial x} + \frac{\partial w_0}{\partial x} \frac{\partial w_0}{\partial y} \right) \frac{\partial^2 w_0}{\partial x \partial y} - A_{12} \left(\frac{\partial u_0}{\partial x} + \frac{1}{2} \left(\frac{\partial w_0}{\partial x} \right)^2 \right) \frac{\partial^2 w_0}{\partial y^2} + \dots \\ &\dots - A_{22} \left(\frac{\partial v_0}{\partial y} + \frac{1}{2} \left(\frac{\partial w_0}{\partial y} \right)^2 \right) \frac{\partial^2 w_0}{\partial y^2} = 0 \end{aligned} \quad (\text{A.43})$$

Using a central finite differencing scheme to discretise these equations leads to three equations in u , v and w to be solved at each node. The plate is divided into a square nodal grid with boundary conditions applied per Chapter Eight.

A.7 NONLINEAR SOLUTION PROCEDURE

The basic formulation of the Newton-Raphson procedure for any multi-dimensional problem is as follows (Dennis and Schnabel 1996). Given a set of N equations in N unknowns;

$$f_i(x_1, x_2, x_3 \dots x_N) = f_i(X) = 0$$

where; $i = 1, 2, 3, \dots, N$ (A.44)

The procedure continues generally with a Taylor series expansion of these equations:

$$f_i(X + \Delta X) \approx f_i(X) + \sum_{j=1}^N \frac{\partial f_i}{\partial x_j} \Delta x_j$$
(A.45)

The procedure starts with an initial guess of X and finds the required change in X (ΔX) to make the entire set of functions zero:

$$f_i(X + \Delta X) = 0$$
(A.46)

$$\Rightarrow 0 = f_i(X) + \sum_{j=1}^N \frac{\partial f_i}{\partial x_j} \Delta x_j$$

$$\Rightarrow \sum_{j=1}^N a_{ij} \Delta x_j = \mathbf{b}_i$$
(A.47)

where $a_{ij} = \frac{\partial f_i}{\partial x_j}$ and $\mathbf{b}_i = -f_i(X)$

Rewriting in matrix notation:

$$[\mathbf{A}] = \sum_{j=1}^N a_{ij}$$
(A.48)

$$\underline{\mathbf{b}} = -f_i(X)$$

This is a matrix equation:

$$[\mathbf{A}]\underline{\Delta X} = \underline{\mathbf{b}}$$
(A.49)

In the present research, matrix $[\mathbf{A}]$ (the Jacobian matrix) was determined by differentiating the finite differenced governing equations with respect to each nodal variable (refer to the previous section of this Appendix for the governing equations). To avoid an ill-conditioned Jacobian matrix, which would result in inaccurate solution of (A.48), the Jacobian was scaled to unity. This was done by multiplying each row in the Jacobian matrix (and the corresponding entry in the residual vector, \mathbf{b}) by the inverse of the maximum value on that row.

Equation (A.48) is solved and the new displacement vector is found:

$$\underline{X}_+ = \underline{X}_c + \underline{\Delta X} \quad (\text{A.50})$$

This process continues until a convergence criterion is met.

A.7.1 LINE SEARCHES AND BACKTRACKING

Recalling that the non-linear process aims to solve:

$$f_i(X) = 0 \quad (\text{A.51})$$

The iterative step given by the NR method with line searches is given as:

$$X_+ = X_c - \mathbf{I} \frac{f_i(X_c)}{J(X_c)} \quad (\text{A.52})$$

$J(X)$ is the Jacobian of $f_i(X)$ and \mathbf{I} is the line search parameter (a positive real number). The line search method defines a criterion that determines if X_+ is a reasonable next step (i.e. is it closer to the actual solution than X_c). Using the sum of the squares of each vector entry (L2-norm) a natural criteria to ensure that the solution is converging would be:

$$\|f_i(X_+)\|_2 < \|f_i(X_c)\|_2 \quad (\text{A.53})$$

With the following two definitions:

$$\begin{aligned} F(X) &= f_i(X) \\ \|f_i(X)\|_2 &= F(X)^T F(X) \end{aligned} \quad (\text{A.54})$$

It is now apparent that (A.52) is equivalent to a minimisation criteria for $g(X)$, defined as:

$$g(X) = F(X)^T F(X) \quad (\text{A.55})$$

However, (A.52) is not a sufficient criterion as there are cases where this criterion does not ensure convergence to the minimum of $g(X)$ (Dennis and Schnabel 1996). With backtracking the only modification required to (A.52) is:

$$g(X_+) \leq g(X_c) + \mathbf{aI} \frac{\nabla g(X_c) F(X)}{J(X)} \quad (\text{A.56})$$

After simplification this becomes:

$$g(X_+) \leq g(X_c) - \mathbf{aI} F(X)^T F(X) \quad (\text{A.57})$$

This condition ensures that the average rate of decrease from $g(X_c)$ to $g(X_+)$ is at least some prescribed fraction, $\alpha \in (0,1)$, of the initial rate of decrease in that direction. The condition eliminates the possibility of monotonically decreasing iterates that do not converge to the minimiser. See Dennis and Schnabel (1996) for more details.

A.7.2 CONVERGENCE CRITERIA

Any iterative solution procedure requires convergence criteria to define when the solution is sufficiently accurate. Popular finite element packages such as Abaqus and Lusas typically require that the average residual is sufficiently small and that the incremental displacements are small, i.e. the displacements are changing by a small amount per iteration. The same approach was taken in the present model, where two convergence criteria were used, one for displacement and one for the residual.

A.7.2.1 INCREMENTAL DISPLACEMENT NORM

The first convergence criterion is the incremental displacement norm ($L2DISP$), which defines the limit of the sum of the squares of the iterative displacements as a fraction of the sum of the squares of the total displacements:

$$L2DISP = \frac{\|\Delta X\|_2}{\|X\|_2} \quad (A.58)$$

The Lusas FEA user manual describes this convergence criterion;

This is a useful measure of how much the structure has moved during an iteration. Being a scaled norm it is not affected by units but convergence is not guaranteed. Typical values of slack, reasonable and tight norms are (5% – 1%), (1% – 0.1%) and (0.1% – 0.001%) respectively.

The default value for this convergence criterion in both Abaqus FEA and Lusas FEA software is 1%. The default in the present analysis was 10^{-6} (0.0001%). Such a tight value was chosen to balance the residual convergence criteria, which was less stringent.

A.7.2.2 RESIDUAL CONVERGENCE

The second convergence criterion is the RMS residual ($RMSRES$). Typically the RMS residual convergence criterion defines the limit of the square root of the mean of the squares of all the residuals (Lusas FEA user manual). However this results in a convergence condition that is

dependant on the units of the problem and selecting an appropriate limit becomes problem dependent. The RMS residual was modified here by expressing it as a fraction of the average applied stress, σ_{av} :

$$RMSRES = RMS(\underline{b}) \tag{A.59}$$

A default value for *RMSRES* of 10^{-8} was chosen and found to coincide in most cases to convergence of the incremental displacement norm, although unlike *L2DISP*, *RMSRES* is not dimensionless. In the present model the residual vector is scaled by the maximum value of the corresponding row of the Jacobian matrix. While this does not create a dimensionless residual it does provide a decreased sensitivity to the units being used.

APPENDIX G

Two Measures of Scatter in Experimental Results

The standard deviation is one of the simplest and most common measures of scatter and is often presented alongside the mean. A more refined method of presenting this is to scale the standard deviation to the mean. This is defined here as the coefficient of variance (COV):

$$COV = \frac{\text{standard deviation}}{\text{mean}} \quad (\text{A.60})$$

The downfall of this method is that it does not account for the sample size. A COV based on a sample size of 1000 is considerably more reliable than the same COV based on a sample size of 3. A method of accounting for sample size is to consider confidence intervals. Statistical confidence intervals, based on a T-distribution, can be determined for any sample set of data. Equation (A.61) defines the range within which the population mean is expected to lie, with a given level of confidence, based on a sample mean, standard deviation and size.

- s** sample mean
- $(1-\alpha)$ confidence level
- $t_{\alpha/2}$ double sided T-distribution value for the specified confidence level
- s sample standard deviation
- n sample size
- m** population mean

$$s - t_{\alpha/2} \frac{s}{\sqrt{n}} < m < s + t_{\alpha/2} \frac{s}{\sqrt{n}} \quad (\text{A.61})$$

This range is then expressed as a percentage of the mean and labelled the confidence range:

$$\text{Confidence Range} = \pm t_{\alpha/2} \frac{s}{s\sqrt{n}} \quad (\text{A.62})$$

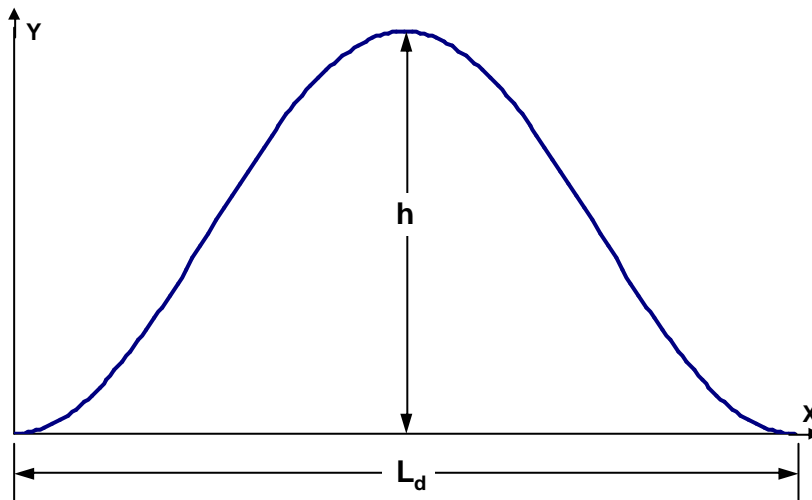
The confidence level used for all statistical analysis in this thesis is 95%.

APPENDIX H

Criterion for Assessing the Validity of a Small Rotations Assumption

A section through the centre of the disbond was considered because the largest out-of-plane displacement occurs at the disbond centre. Assuming a sinusoidal displacement function of the form:

$$y = \frac{h}{2} - \frac{h}{2} \cos\left(\frac{2px}{L_d}\right) \quad (\text{A.63})$$



The gradient is defined by:

$$\frac{dy}{dx} = \frac{ph}{L_d} \sin\left(\frac{2px}{L_d}\right) \quad (\text{A.64})$$

The maximum gradient is 15 degrees and occurs when the sine function is unity:

$$\left. \frac{dy}{dx} \right|_{\max} = \frac{ph}{L_d} \leq \frac{15p}{180} \quad (\text{A.65})$$

$$\Rightarrow h \leq \frac{L_d}{12} \quad (\text{A.66})$$